UNIVERSITY OF BIRMINGHAM

Synthesis and Characterisation of Novel Oxyanion Doped Materials for Use in Solid Oxide Fuel Cells

By

Alaric Smith

Supervisors: Prof. Peter Slater &
Prof. Colin Greaves

A thesis submitted to the
University of Birmingham for the
degree of Doctor of Philosophy

School of Chemistry
College of Engineering and Physical Sciences
University of Birmingham
July 2014

Abstract

In this thesis the work presented focussed on the doping of oxyanions, borate, silicate, sulfate and phosphate, into different materials with the perovskite structure for use as electrolytes or cathodes in solid oxide fuel cells.

Phosphate and sulfate doping was shown to have been carried out successfully on gallium doped barium and strontium scandates. They all adopted the cubic perovskite structures with the presence of oxyanions confirmed by Raman spectroscopy. These samples were found to have improved stability to CO_2 atmospheres with increasing gallium content.

Phosphate doping was also carried out on doped barium cerates and was found to lower the conductivity while not leading to improved stability. Oxyanion doped barium stannates were investigated and showed a lower conductivity on oxyanion doping and borate doped samples showed an improved stability in reducing atmospheres.

Following on from earlier work on silicate doping in perovskite cathode materials silicon doping was carried out on $(Ca/Sr)_2MnFe_{1-x}Si_xO_{6-\delta}$ which resulted in the formation of cubic perovskites with a mixed oxidation state on the B site. Conductivity and area specific resistance data were collected for the samples showing an initial improvement on silicon doping for two of the series.

Acknowledgements

First of all I would like to thank my supervisor Peter Slater for taking me on in the first place and giving me this project. Thanks also for all the help you've given me over the past 3 and a half years, the numerous coffee and pub trips, the beer festivals and for having to be persuaded to go the all-you-can-eat fried meat place.

I would also like to thank Jackie Deans for all the help she has given me with the machines and also whenever I've asked for help always going above and beyond what I've asked for, it's been much appreciated.

Thanks also to past and present members of the Slater group for all the enjoyable times and making the lab a fun place to work, especially Cathryn for all the help she gave me when I started.

Also thanks to Ben, James and Luke for all the good times right from when I started.

Thanks to the rest of Floor 5 for again making this an enjoyable place to work.

I would also like to thank Annabelle for all the help and support you have provided over the last 2 and a half years, it's been great.

I'd also like to thank my family for all the support over the years and also for being such great people to spend time with.

Also a 4 year late thanks to Paul, Jade, Diane, Suz, Hannah and Chris for all the past and continuing great times.

And finally thanks to EPSRC for funding and Advantage West Midlands for providing funding for equipment.

Contents

Chapter 1 Introduction

1.1 Fuel Cells

1.1.1 History of Fuel Cells

Research into areas related to fuel cells has been occurring for over 200 years and is traced back to two British scientists, William Nicholson and Anthony Carlisle, who discovered the process, known as electrolysis, of using electricity to convert water into hydrogen and oxygen, the reverse reaction of the electrochemical reaction occurring in fuel cells.[1, 2] William Grove found that by placing the ends of two platinum electrodes in sulphuric acid and the other ends separately in sealed containers of hydrogen and oxygen, with both also containing water, a current would flow between the electrodes and the water level would rise. When he combined several sets of these electrodes in series he created what he termed a "gas battery" or the first fuel cell.[1, 3]

Friedrich Wilhelm Oswalt experimentally determined the interconnection of various components of these fuel cells, and this helped him confirm where the action in Grove's fuel cell occurred.[4] William W. Jacques in 1896 developed the first fuel cell with practical applications and 4 years later Walther Nernst first used zirconium dioxide as a solid electrolyte.[5] In the 1930s, Thomas Francis Bacon began investigating alkaline fuel cells that employed air and hydrogen, and managed to develop a fuel cell that was used aboard World War II submarines. This work was then acquired by Pratt & Whitney and was used in the Apollo space missions.

Research continued in the area and fuel cells are now available for a number of practical uses, including automobiles and for stationary power uses.

1.1.2 How a Fuel Cell Works and Types of Fuel Cells

In all types of fuel cell the basic structure is the same; they contain two electrodes, a cathode and an anode, which are separated by an electrolyte. They operate in the same way as a battery, as an electrochemical reaction takes place. However, the difference is that in a fuel cell the oxidant and the fuel are continuously supplied, whereas in a battery they are stored in limited amounts in the electrodes.

In a fuel cell there are separate half-cell reactions occurring at each of the cathode and anode depending on the type of fuel cell used. These reactions cause the formation of electrons at the anode which are unable to transfer through the electrolyte and so pass through an external circuit, producing power for use in a number of different applications. An ionic species is produced at either the cathode or anode that then travels through the electrolyte before acting in the half-cell reaction at the other electrode. The 5 main types of fuel cell are listed in Table 1.1 and Figure 1.1 with their operating temperatures and half-cell reactions.

Table 1.1 Summary of the 5 main types of fuel cell with their half-cell reactions and operation temperatures

Fuel Cell Type	Anode Reaction	Cathode Reaction	Temperature of Operation
Alkaline Fuel Cell (AFC)	$2H_2 + 4OH^- \rightarrow 4H_2O + 4e^-$	$O_2 + 4e^- + 2H_2O \rightarrow 4OH^-$	90-100 °C
Molten Carbonate Fuel Cell (MCFC)	$2H_2 + 2CO_3^{2-} \rightarrow 2H_2O + 2CO_2 + 4e^-$	$O_2 + 4e^- + 2CO_2 \rightarrow 2CO_3^{2-}$	600-700 °C
Phosphoric Acid Fuel Cell (PAFC)	$2H_2 \rightarrow 4H^+ + 4e^-$	$O_2 + 4e^- + 4H^+ \rightarrow 2H_2O$	150-200 °C
Polymer Electrolyte Membrane Fuel Cell (PEMFC)	$2H_2 \rightarrow 4H^+ + 4e^-$	$O_2 + 4e^- + 4H^+ \rightarrow 2H_2O$	50-100 °C
Solid Oxide Fuel Cell (SOFC)	$2H_2 + 2O^{2-} \rightarrow 2H_2O + 4e^-$	$O_2 + 4e^- \rightarrow 2O^{2-}$	500-1000 °C

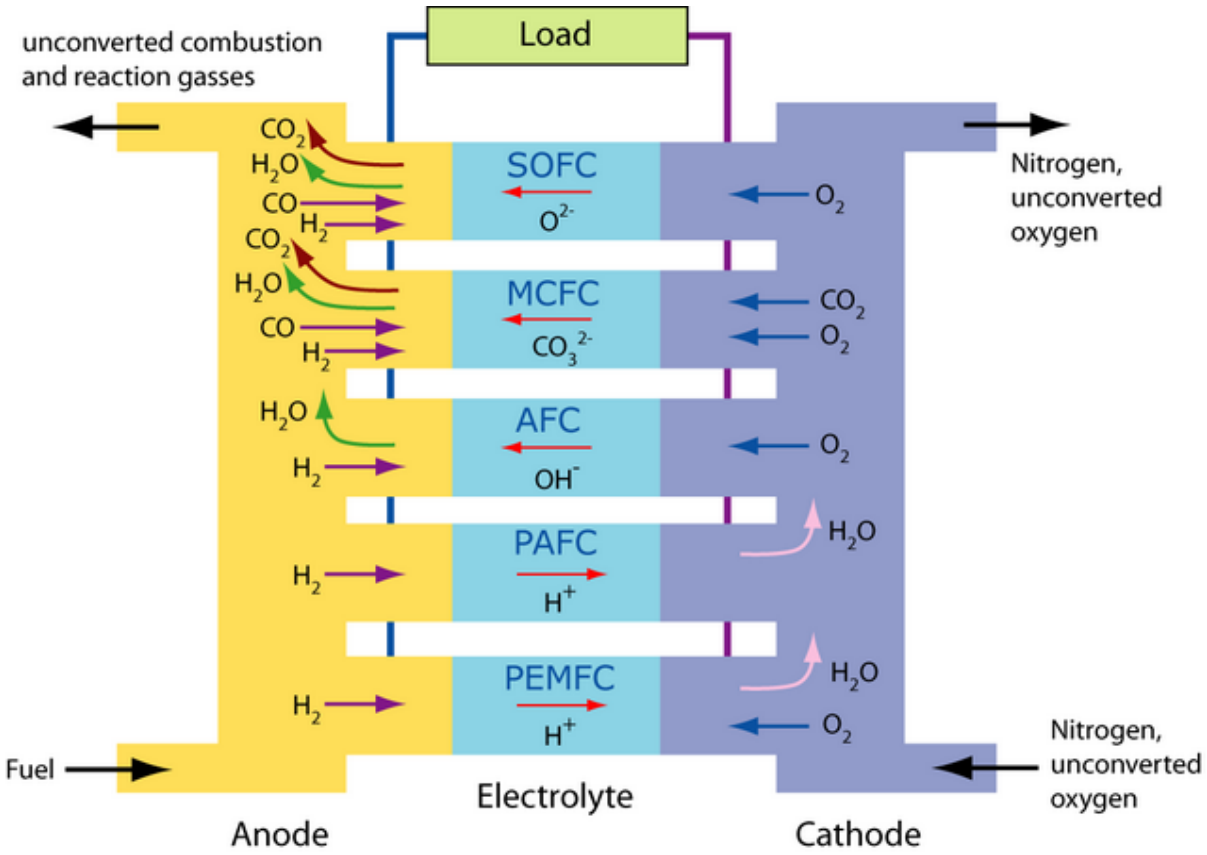

Figure 1.1 Summary of the different fuel types and their ionic species [6]

In this PhD, work has focused on new materials developed for use in solid oxide fuel cells, and so these will be covered in more detail.

1.1.3 Solid Oxide Fuel Cells (SOFCs)

Solid oxide fuel cells (SOFCs) are fuel cells that operate at high temperatures, 500-1000 °C, and are of particular interest due to their high efficiency, compared to combustion-based technologies, low emissions and fuel flexibility. This fuel flexibility, due to their high operational temperatures, allows SOFCs to act as a bridging technology as natural gas can be used as a source of fuel.[7-13] The ionic species that travels through the electrolyte is the oxide ion, O^{2-}.

The electrolyte is a dense solid specifically a hard non porous ceramic compound. Due to the high temperatures in SOFCs these materials can conduct ionically to give good fuel cell

performance, although lowering the operating temperature is being researched as this would hasten implementation by reducing sealing problems, as well as long term degradation.

The most common crystal structure for the electrolyte is the fluorite structure, Figure 1.2, and the two main fluorite electrolytes are doped ZrO_2 and doped CeO_2.

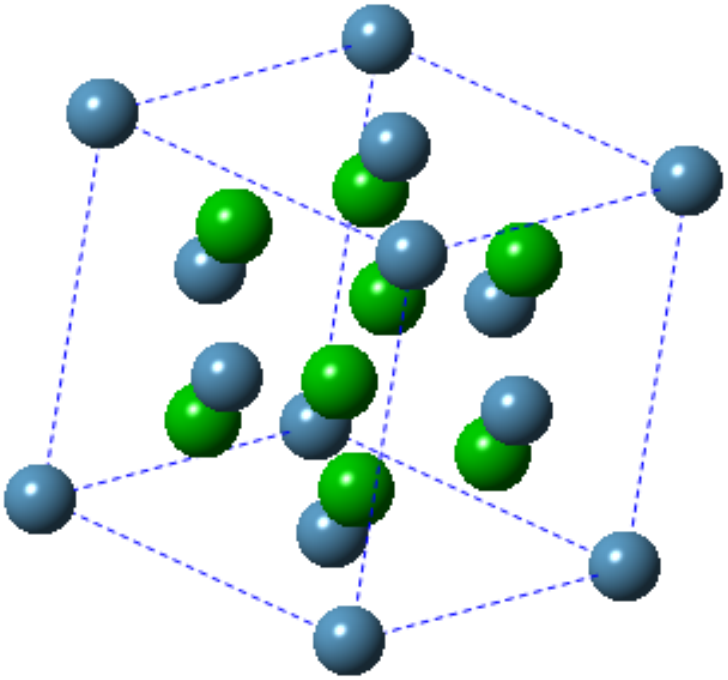

Figure 1.2 Fluorite Crystal Structure (AO_2); with the cation in blue and the anion in green

Pure zirconia, ZrO_2, is not a good ion conductor at room temperature and only adopts the cubic fluorite structure above 2300 °C.[14] The cubic structure is stabilised at lower temperatures by acceptor dopants, which also has the added benefit of introducing oxygen vacancies into the structure, required for ionic conductivity through a vacancy hopping mechanism.[15-20] Yttria-stabilised zirconia (YSZ) is the most favoured system commercially due to its low cost, availability, good mechanical and electrical properties, despite not having the highest ionic conductivity; it needs to operate between 800 and 1000 °C to ensure a high enough performance. Scandium doped zirconia has a superior conductivity than YSZ but its

use is restricted due to the higher cost of scandium.[21] A potential route to lowering the operating temperature is the fabrication of very thin film YSZ.[22-24]

Doped CeO_2 has also been shown to have a good ionic conductivity.[25-35] Gadolinia-doped ceria (CGO) and samaria-doped ceria (SDC) have a much higher conductivity than YSZ, especially at lower temperatures (500-700 °C). However at low oxygen partial pressures and above 600 °C the cerium is partially reduced to Ce^{3+}, which leads to a small amount of n-type conductivity lowering the fuel cell performance. Despite this, SOFCs with a solid ceria electrolyte have been shown to operate well at a working temperature of 500-700 °C although it has a lower voltage at elevated temperatures due to aforementioned reduction of cerium.[36, 37]

Another issue with these fluorite systems is their susceptibility to silica impurities, which are common impurities in the reagents. These impurities can form a siliceous intergranular phase which significantly reduces grain boundary conductivity, and methods to trap these phases and overcome this conductivity reduction are being investigated.[38]

Other crystal structures studied for use as electrolytes in SOFCs are the perovskite structure, apatites and series based on $La_2Mo_2O_9$.[39-42]

The anode in SOFCs is usually a cermet of Ni and the electrolyte. Generally the electrolyte used in the anode is the same as that for the electrolyte in the fuel cell, i.e. YSZ/Ni anode is used with a YSZ electrolyte.[2] NiO is used as the Ni metal source as at SOFC operating temperatures (>500 °C) it is reduced to Ni providing the required electronic conductivity as well as the catalytic performance. In addition reducing NiO to Ni increases the porosity of the anode.

In a SOFC the cathode has to be stable at high temperatures in oxidising atmospheres. Therefore only electronic conducting oxides and noble metals can be used. Due to the high cost of the noble metals and their poor long term stability, electronic conducting oxides have been principally researched for cathode materials. In particular materials with the perovskite structure have been found to have the most promise for use as cathode materials due to their generally high electronic conductivities and catalytic activity.[43-47]

In a conventional cathode, a composite of the cathode material and the electrolyte is used, and it is believed that the electrochemical reaction can only occur at the triple phase boundary, where the electrolyte, air and electrode meet. At this boundary the oxygen from the air is reduced and incorporated into the electrolyte as the oxide ion according to the following equation (Kröger-Vink notation)[181]

Equation 1.1

$$\frac{1}{2}O_{2(g)} + 2e'_{cathode} + V_o^{\bullet\bullet} \rightarrow O^{2-}_{electrolyte}$$

This limits the electrochemical reaction to a very small area. However one potential option to improve the performance of a SOFC is to have a cathode with a mixed conductivity, ionic and electronic, allowing the reduction of oxygen to occur at the surface of the cathode and then have the oxide ion move through the cathode to the electrolyte.

$LaMnO_3$ based oxides have been researched for use as cathode materials and they are generally formulated as $La_{1-x}A_xMnO_{3\pm\delta}$ (A is a divalent cation such as Sr^{2+} or Ca^{2+}).[48-51] Usually strontium is used as the dopant (i.e. $La_{1-x}Sr_xMnO_{3-\delta}$, LSM) as its size matches with lanthanum however it does not increase the oxygen vacancy concentration but rather oxidises the manganese.[52] This oxidation of the manganese improves the electrical conductivity, however LSM has been found at high temperature to undergo reaction with YSZ forming

$La_2Zr_2O_7$.[53-55] Strontium substitution decreases this reactivity; however $SrZrO_3$ forms when the strontium concentration is above the 30% dopant level.[54, 56-58] Both $La_2Zr_2O_7$ and $SrZrO_3$ are insulating phases and therefore lower the performance of the cathode material. The lack of oxygen vacancies in this structure limits the reduction of oxygen to the triple-phase boundary and this in turn typically limits the operation temperatures to above 800 °C. The lack of oxygen vacancies is the main reason why performance is too low at lower temperatures and to overcome this a second ionically conducting phase can be added or to replace manganese with other transition metal elements, such as cobalt and iron, which promote the formation of oxygen vacancies.[59]

Strontium doped $LaCoO_3$ has also been studied as a potential cathode material due to its higher ionic and electronic conductivities.[60] On strontium doping some of the cobalt is oxidised from 3+ to 4+ in addition with the formation of oxygen vacancies. $La_{1-x}Sr_xCoO_{3-\delta}$ has a high oxygen diffusivity and a high dissociation catalytic activity for the oxygen molecules leading to a marked improved electrode activity. Increasing the amount of cobalt leads to an increased thermal expansion coefficient, which may result in cracking of the electrolyte and delamination at the cathode/electrolyte interface.[61] This increased thermal expansion is due the weaker Co-O bond compared to the Mn-O bond, the formation of oxygen vacancies, and the spin-state transitions associated with Co^{3+}.[62, 63] These cobaltite cathodes also react readily with YSZ, forming insulating phases during the sintering process, lowering their performance. Therefore, a diffusion barrier is typically necessary if cobaltite cathodes are to be used with YSZ.[64, 65]

Lanthanum ferrite, $LaFeO_3$, is expected to be more stable than its cobalt counterpart due to the stability of Fe^{3+} caused by its $3d^5$ electronic configuration. Strontium doped $LaFeO_3$ (LSF) has shown promising performance with respect to the power density and stability at 750 °C.[66,

[67] Doping with strontium, as outlined in the paragraphs above, causes some of the iron to oxidise to Fe^{4+} as well as oxygen vacancies to form, in order to accommodate the lower charge of strontium compared to lanthanum. At high temperatures LSF loses oxygen forming oxygen vacancies and decreasing the amount of Fe^{4+} present. In this system the electrons have a much higher mobility than the oxygen ions so the conductivity is dominated by a hole-conduction mechanism. The thermal expansion coefficient of LSF closely matches those of the CGO and YSZ electrolyte.

The electrochemical performance of LSF is, however, inferior compared to cobalt containing systems. A compromise system is $La_{1-x}Sr_xFe_{1-y}Co_yO_3$ (LSCF).[68, 69] LSCF does not react with ceria based electrolytes and has a similar thermal expansion coefficient to commonly used electrolytes.[34, 70, 71] The ionic conductivity is influenced more by the strontium concentration on the A-site and the iron and cobalt concentration influences the electronic conductivity more. LSCF has a superior performance compared to cathodes based on LSM but as LSCF reacts with YSZ a protective CGO diffusion barrier is typically needed to prevent insulating phase formation.[72, 73]

1.1.4 Proton Conducting Ceramic Fuel Cells

In attempting to lower the operation temperature of SOFCs there has been a growing interest in proton conducting ceramics. The compounds originally identified with this property were oxides with a perovskite-type structure, ABO_3 (A = Sr, Ba; B = Ce, Zr).[74] Doping these systems with a trivalent element, for example yttrium, leads to the formation of oxide-ion vacancies allowing water incorporation to occur according to the following equation

Equation 1.2

$$V_O^{\bullet\bullet} + O_O^{x} + H_2O \leftrightarrow 2\ OH_O^{\bullet}$$

The protons incorporated into the structure migrate by hopping from one oxide ion to the next, and this easy migration means they can achieve high proton conductivities at a low temperature (350-600 °C) taking advantage of the relatively low activation energy for proton migration (0.3-0.6 eV).[75-78] In addition as the protons move through the electrolyte rather than oxide ions, water formation occurs at the cathode side of the fuel cell meaning fuel dilution does not occur as in SOFCs leading to potentially higher fuel utilisation.

Iwahara *et al*. first observed proton conduction in doped strontium and barium cerates in the 1980s.[74, 79] Undoped barium cerate adopts the orthorhombic structure at room temperature, and as the temperature increases it undergoes a phase transformation at ≈ 260 °C to another orthorhombic structure (*P m c n* to *I n c n*) followed by a transition to a rhombohedral structure at ≈ 380 °C (*F -3 2/n*) and to a cubic structure at ≈ 900 °C (*P m -3 m*).[80, 81] As described above doping barium cerate with a trivalent cation was carried out to introduce oxygen vacancies into the structure that could be filled with water and has been attempted for a number of trivalent cations, Yb, Pr, Nd, Sm, Eu, Gd, Tb, Dy, Ho, Er, Tm, Lu and In.[82-94] The conductivity of the system was found to increase with increasing dopant level up to a dopant level of 10-25 mol% depending on the nature of the dopant. This occurs as increasing the dopant level increases the amount of oxygen vacancies until a point is reached where the vacancies start to associate thus lowering the amount of free vacancies and hence the conductivity.[95, 96] Barium cerate based materials are promising materials for use in proton conducting ceramic fuel cells as a result of their high proton conductivity, however their usage is limited due to their low stability to CO_2 and water vapour containing atmospheres, with the following chemical reactions occurring:

$$BaCeO_3 + CO_2 \rightarrow BaCO_3 + CeO_2$$

$$BaCeO_3 + H_2O \rightarrow Ba(OH)_2 + CeO_2$$

To overcome this co-doping niobium into yttrium doped barium cerate was carried out by Radojkovic *et al.*[97] This was shown to improve the CO_2 stability of barium cerate, however the transport properties decreased, due to the average grain size decreasing and the reduction in free vacancies. Niobium, tin, titanium, gallium and other elements have also been studied to analyse their effect on the stability of barium cerate.[98-105] Cerium is also reduced under reducing conditions from Ce^{4+} to Ce^{3+} causing fuel cell efficiency losses due to electronic conduction in the electrolyte.

Doped and undoped $BaZrO_3$ adopts the cubic perovskite structure although Kreuer *et al.* found $BaZr_{1-x}Y_xO_{3-\delta}$ adopted the tetragonal structure for $0.05 < x < 0.25$ while remaining cubic at other concentrations.[106-108] Compared to doped barium cerates, doped barium zirconates have an excellent chemical stability in standard operation conditions for fuel cells.[77, 78, 109-111] While having an improved stability, doped barium zirconates have a conductivity that is in general one order of magnitude lower than their barium cerate analogues at the same temperature.[77, 78, 110, 112] This lower conductivity is caused by the poor sinterability of the material and the poor conduction of the grain boundary regions. This low grain boundary conductivity is most likely due to barium deficiency due to barium evaporation. If these problems with the sinterability and large grain boundary are overcome then the high bulk proton conductivity may enable barium zirconates to be used as electrolytes in proton conducting ceramic fuel cells. To overcome this poor sinterability some advances have been made with the use of sintering aids.[113, 114]

As barium cerate and zirconate can form a solid solution, mixed cerate-zirconates are being investigated to develop a system with the high proton conductivity of barium cerates

combined with the improved stability of barium zirconates. This was first carried out by Ruy and Haile. who found that the mixed phase had an improved stability in water and CO_2 containing atmospheres than barium cerates but a lower protonic conductivity than barium cerates.[115] This work also showed that increasing the zirconium content improved the stability of the system to CO_2 atmospheres. These mixed systems have been most extensively studied with yttrium doping. This doping strategy has been carried out on a number of mixed barium cerate-zirconate systems and found that the CO_2 stability improved although the proton conductivity fell, while the sintering temperature required for these systems also increased with increasing zirconium content.[116-122] This fall in conductivity with increasing zirconium content in most cases is due to an increasing grain boundary resistance as outlined above for doped barium zirconate.

Other perovskite systems studied for their use as electrolytes in proton conducting SOFCs are $Ba_2SnYO_{5.5}$, $Ba_2In_2O_5$ and $Ba_3Ca_{1.18}Nb_{1.82}O_{8.73}$.[123-125] Other structures studied for their proton conductivity are doped $LaPO_4$ and orthoniobates and orthotantalates with the formula $RE_{1-x}A_xMO_4$ (RE = rare earth metal).[126, 127]

For anode materials with these proton conducting electrolytes, Ni-electolyte cermets are used. For cathode materials there have been a few steps towards the development of a mixed proton/electron conducting oxides and the substitution of zirconate with praseodymium was found to produce a system that conducted protons and electrons, however stability to CO_2 is an issue with this system.[128, 129] Work has also been carried on composite materials with the electrolyte and a mixed oxide ion and electron conductor to provide a mixed proton/electron conducting oxide and improve fuel cell performance.[130-134]

1.2 Perovskites

The perovskite structure takes its name from the mineral $CaTiO_3$, known as perovskite, and this mineral was named after Russian mineralogist L. A. Perovski by Gustav Rose.

Ideal perovskite oxides have a general formula of ABO_3, Figure 1.3, with the A cation sitting in the centre of the unit cell, and is 12 coordinate with respect to the anions around it. The A cation is larger than the B cation, which is commonly a transition metal, and the B cation sits on the corners of the unit cell and has an octahedral arrangement of the anions around it; these octahedra are corner sharing throughout the structure.

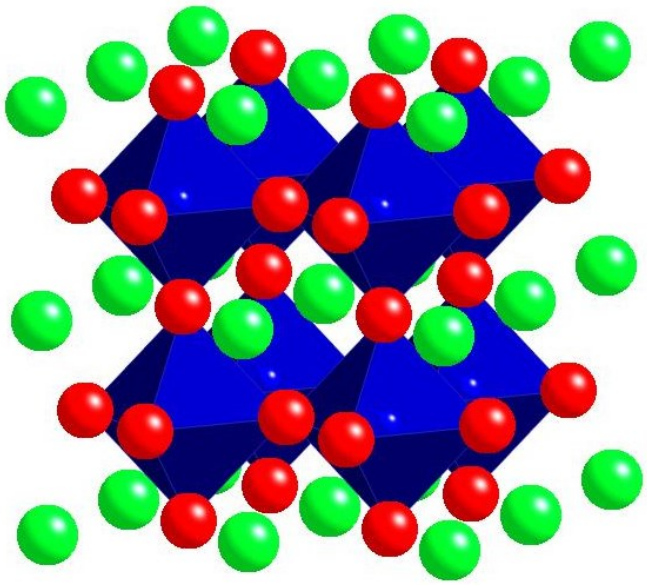

Figure 1.3 Perovskite Crystal Structure (ABO_3); where the A cation is green, B cation is navy and O is red

To determine if the perovskite structure is likely to form for a certain crystal stoichiometry the Goldschmidt tolerance factor can be calculated from the ionic radii of the constituent atoms according to the formula below.[135-137]

Equation 1.3

$$t = \frac{(R_a + R_o)}{\sqrt{2}(R_b + R_o)}$$

Many compositions with the perovskite structure, including the original mineral $CaTiO_3$, do not adopt the ideal perovskite structure.[138] The tolerance factor is a guide and there are a number of exceptions to the following. If $0.8 < t < 0.9$, the B cation is too big, and to release the strain, the octahedra around the B cation can tilt resulting in a lower symmetry unit cell, an orthorhombic unit cell, in $GdFeO_3$.[139] However if $t > 1$, the B cation is too small, e.g. $BaNiO_3$, and in such cases a hexagonal cell with face sharing of octahedra can form, rather than the edge sharing octahedra seen in the ideal structure.[135-137, 140]

There can also be deviations from the ideal perovskite structure due to a change in stoichiometry, as the perovskite structure can readily incorporate ion vacancies. These vacancies can cause a change in the properties of a system as shown by introducing oxygen vacancies into $BaZrO_3$ through doping on the cation site, which causes an increase in the proton conductivity through water incorporation.[141] While yttrium doped $BaZrO_3$ retains the cubic structure, these oxygen vacancies can potentially order giving rise to other structures as seen for $SrFeO_{3-\delta}$, where oxygen vacancies order at low values of δ (= 0.5) to give the brownmillerite structure, with alternating layers of octahedral and tetrahedral coordination around the B cation. This structure is also adopted by $Ba_2In_2O_5$, among others.[124, 142] The ratio of A:B cations can also be altered to give Ruddlesden Popper phases with a general formula $A_{n+1}BO_{3n+1}$. These systems have the rock salt layer (AO) in between n consecutive perovskite layers (ABO_3).[143]

Perovskites are used as both electrolytes and electrodes in ceramic fuel cells as outlined in sections 1.1.3 and 1.1.4.

1.3 Oxyanion Doping

Traditional strategies employed for SOFCs to optimize the conductivities have entailed doping with aliovalent cations of similar size, for example ZrO_2 doped with Y_2O_3. However prior work on perovskite-type cuprate superconductors showed that they were able to incorporate oxyanions (nitrate, phosphate, carbonate and sulfate) into their structure.[144-149] This doping strategy could also be used to stabilise phases that could not otherwise be obtained under ambient pressure conditions, for example the Sr analogue of $YBa_2Cu_3O_{7-x}$.

Further work showed that oxyanions could be incorporated into other perovskite systems. Borate and carbonate have been incorporated into manganese containing systems; resulting in $Sr_5Mn_4CO_3O_{10}$ and $Sr_4Mn_{3+x}B_{1-x}O_{10}$.[150, 151] Carbonate doped Ruddlesden Popper $Sr_4Fe_{3-x}(CO_3)_xO_{10-4x}$ has also been reported.[152-154]

More recently, it has been shown that oxyanions (phosphate, silicate and sulfate) can be incorporated into $Ba_2In_2O_5$.[155-157] $Ba_2In_2O_5$ adopts the brownmillerite structure with alternating layers of octahedral and tetrahedral indium at room temperature. Increasing the temperature to ~930 °C $Ba_2In_2O_5$ forms a tetragonal structure causing the oxygen sublattice to disorder, resulting in a corresponding jump in the oxide ion conductivity; further heating to 1140 °C causes cubic $Ba_2In_2O_5$ to form.[158, 159] As the disordered temperature states of $Ba_2In_2O_5$ have a much higher oxide ion conductivity there have been numerous attempts to lower the structural transition temperatures through doping. Doping an isovalent element with a smaller ionic radius for In has been shown to lower the transition temperature.[159] Doping with the higher valent cations Sn, Ti, W, V and Mo has also been shown to have much better results at lowering the transition temperature.[160-162] However doped $Ba_2In_2O_5$ has also been

shown to have instability in humid atmospheres, reactivity with CO_2 at operating temperatures as well as easy reducibility.

It has been shown that phosphate groups, PO_4^{3-}, can be doped onto the In sites in $Ba_2In_2O_5$ to give $Ba_2In_{2-x}P_xO_{5+x}$, for values of x = 0.1, 0.2, 0.3.[155, 157] X-ray powder diffraction data showed that on increasing the phosphate concentration the structure changed from orthorhombic to cubic at room temperature. The cubic structure, unlike the orthorhombic structure, has disordered oxide ions, which improves ionic conductivity. Ionic conductivity was found to increase greatly at lower temperatures on phosphate doping. This is due to the disordering of the oxide ion vacancies from the structural change. This series was also found to show proton conductivity due to water incorporation, but the level of water incorporation was found to decrease on increasing the concentration of phosphate. Phosphate doping of $Ba_2In_2O_5$ was also shown to increase the stability towards CO_2 at operating temperatures.

It was also found that $Ba_2In_2O_5$ could incorporate silicate, SiO_4^{4-}, into the structure resulting in the structure changing from orthorhombic to cubic at room temperature, as in the case with phosphate, with increasing oxygen disorder for $Ba_2In_{1.8}Si_{0.2}O_{5.1}$ due to this change in structure.[156] At higher dopant composition there is the formation of an impurity, Ba_2SiO_4, indicating the solubility limit is around 10%. As noted earlier silicon is generally seen as a poison in SOFC electrolytes, whereas for these compositions the introduction of silicate leads to an increase in the ionic conductivity at lower temperatures.[163-165] This increase in ionic conductivity, in the same way as in phosphate doped $Ba_2In_2O_5$, is due to the increase in oxide ion disorder in the doped compositions at these temperatures. At higher temperatures $Ba_2In_{1.9}Si_{0.1}O_{5.05}$ was found to exhibit a slightly higher ionic conductivity than $Ba_2In_{1.8}Si_{0.2}O_{5.1}$. This is because both doped phases have similar oxide ion disorder at these temperatures with the higher doped composition having fewer oxygen vacancies and most

likely more defect trapping occurring. As with phosphate doping there is proton conductivity for $Ba_2In_{2-x}Si_xO_{5+x/2}$ at lower temperatures due to water incorporation.

Sulphate can also be doped into $Ba_2In_2O_5$ to give $Ba_2In_{2-x}S_xO_{5+3x/2}$, leading to an increase in cell symmetry to cubic for x = 0.3.[157] Conductivity data showed an increase in conductivity at lower temperatures upon doping with sulphate, consistent with the increase in disorder of the oxygen sublattice. There was also an increase in conductivity in a wet atmosphere due to a protonic contribution upon doping with sulphate. The conductivities for $Ba_2In_{2-x}S_xO_{5+3x/2}$ were lower than those for the related phosphate doped compositions, which may be due to the higher oxygen content or to increased defect trapping of the sulphate group.

This work was then extended to $Ba_2Sc_2O_5$ by Shin *et al.*[166] $Ba_2Sc_2O_5$ had been shown by prior studies to be unstable above 1000 °C, as on heating above this temperature $Ba_3Sc_4O_9$ formed.[167, 168] This thermal instability was shown to be caused by the presence of carbonate groups in $Ba_2Sc_2O_5$, ascertained from Raman spectroscopy. Phosphate doped $Ba_2Sc_2O_5$ was found to form a perovskite structure for $Ba_2Sc_{1.6}P_{0.4}O_{5.4}$ and $Ba_2Sc_{1.5}P_{0.5}O_{5.5}$, and for lower phosphate contents $Ba_3Sc_4O_9$ impurity formed. Conductivity measurements carried out showed evidence for proton conduction in wet atmospheres and a p-type contribution to the conductivities at elevated temperatures. Also the CO_2 stability of these phosphate doped systems was found to be superior to barium cerate systems. Silicate doped analogues were attempted to be prepared, however while the synthesis of a cubic perovskite was achieved, this could not be prepared phase-pure.

Further work has demonstrated the potential for use of this doping strategy for electrode materials. $SrMnO_3$ and $SrCoO_3$ both adopt the hexagonal perovskite structure at room temperature. On incorporation of 3% silicon for cobalt in $SrCoO_3$ a cubic cell was observed,

with single phase samples seen up to 7% silicon doping.[169] The data showed that on silicon doping some of the Co^{4+} was reduced to Co^{3+}, and this reduction led to an increase in conductivity of 2 orders of magnitude on silicon doping; the best conductivity was seen for the 3% silicon content composition as on further silicon doping there is most likely a partial disruption of the electronic conduction pathway by the silicon lowering the conductivity. However, on heating overnight at 750 °C the samples became hexagonal perovskites again also resulting in a decrease in conductivity to the levels seen for non-doped $SrCoO_3$, showing these samples were most likely metastable. For $SrMnO_3$ silicon doping was found to give a pure cubic perovskite for $SrMn_{0.85}Si_{0.15}O_{3-\delta}$ and $SrMn_{0.8}Si_{0.2}O_{3-\delta}$.[169] These compositions did not change structure to the hexagonal structure on heating like the $SrCoO_3$ samples showing that the higher silicon content stabilised the cubic structure in this system. The conductivities of the silicon doped $SrMnO_3$ were shown to be superior to undoped $SrMnO_3$ due to the change in structure from hexagonal to cubic, and the mixed valency of manganese that arises due to silicon doping. The change in structure in both these systems is due to silicon being incorporated as tetrahedral silicon causing the introduction of oxygen vacancies. These oxygen vacancies lead to a fall in the oxygen level causing a reduction of the manganese and the cobalt leading to an increase in the average ionic size of the B cation in the perovskite altering the tolerance factor in favour of the cubic perovskite. This improvement in conductivity on silicon doping is interesting as silicon is usually seen as detrimental to the conductivity of SOFC materials as it has been previously reported to congregate at the grain boundaries to give insulating siliceous phases, thus decreasing the conductivity and lowering the performance. [19, 170-175] The results here, however, have shown that improvements in performance can occur provided silicon is accommodated into the structure.

It was later shown by Hancock *et al.* that phosphate and sulfate could also be incorporated into $SrCoO_3$ at the same levels seen for silicate doping.[176] The conductivity results were very similar to those found for silicate doping as the conductivity was markedly better than the non-doped $SrCoO_3$ and at higher phosphate and sulfate contents the Co-O pathways were partially disrupted. However the conductivity decreased after thermal cycling and the samples were also found to be non-stable at fuel cell operating temperatures as seen for the silicate doped compositions.

Both $CaMnO_3$ and $La_{1-y}Sr_yMnO_{3-\delta}$ have also been successfully doped with oxyanions.[177] Some of the manganese in both cases was found to reduce to Mn^{3+} from Mn^{4+} due to the reasons outlined in the paragraphs above. The conductivity of $CaMnO_3$ was found to improve on oxyanion doping however for LSM the conductivity decreased. However area specific resistance (ASR) tests carried out on all the samples showed an improvement in the ASR values which was attributed to the increased oxygen vacancy content which was believed to promote ionic conduction.

Porras-Vazquez *et al.* also showed that phosphate and borate could be doped into $Ba_{1-y}Sr_yCo_{0.8}Fe_{0.2}O_{3-\delta}$.[178] The results showed that the phosphate doped compositions were more stable than their non-doped analogues as they retained the cubic structure after long term heating, in contrast to the undoped samples which transformed to a hexagonal perovskite. The conductivities of both phosphate and borate doped samples was found to improve relative to the parent non-oxyanion containing composition and the conductivity did not worsen for the phosphate doped composition after long term annealing unlike its parent composition.

In other studies it was found that LSCF and $Sr_{0.9}Y_{0.1}Co_{3-\delta}$ could also incorporate small amounts of oxyanions, up to a maximum of 5 mol% for borate and 2.5 mol% for silicate in LSCF and 2.5 mol% for silicate, phosphate and borate in $Sr_{0.9}Y_{0.1}Co_{3-\delta}$. All the compositions showed a decrease in the cobalt and iron oxidation state on oxyanion doping and the electronic conductivity was found to improve for oxyanion doped LSCF relative to the parent composition while the electronic conductivity decreased for oxyanion doped $Sr_{0.9}Y_{0.1}CoO_{3-\delta}$. All the oxyanion samples studied showed an improvement in the ASR values on oxyanion doping compared to the parent attributed to the increased amount of oxygen vacancies leading to an improved ionic conductivity. Also oxyanion doped $Sr_{0.9}Y_{0.1}CoO_{3-\delta}$ was found to have an increased stability to CO_2 atmospheres compared to undoped $Sr_{0.9}Y_{0.1}CoO_{3-\delta}$.

Further work on the manganese based systems showed that silicate could be doped into the $Sr_{1-y}Ca_yMnO_{3-\delta}$ with the level of silicate required to stabilise the cubic structure shown to decrease with increasing calcium content.[179] As seen in previous work the conductivities were found to improve on silicon doping for low levels, due to the reduction of manganese, compared to their parent compounds, which then worsens due to the partial disruption of the Mn-O conductivity pathway at higher silicon levels. All the compositions examined showed an improvement in their ASR values compared to their parent compounds.

Silicon doped $SrFeO_{3-\delta}$ was also studied and showed that silicon could be incorporated up to 15 mol%.[180] Undoped $SrFeO_{3-\delta}$ has a tetragonal structure which became cubic on silicon doping. It was also shown that the silicon doped compositions were stable under reducing conditions indicating that these materials could potentially be used in a symmetrical fuel cell. The conductivities were found to improve initially with silicon doping, then worsen as the silicon content increased. Conductivities in reducing atmospheres showed a decrease

compared to the conductivities in air with an improvement for higher silicon contents as they are more stable in these conditions. The same results were seen for the ASR values.

1.4 Project Aims

As oxyanion doping in perovskite materials has been shown to be successful, the primary aim of this research was to synthesise and analyse a number of new oxyanion doped perovskites. This doping strategy was utilised to create new phases that are stable towards the conditions found in fuel cells while retaining the conductivity properties required for an efficient fuel cell.

For the electrolyte materials studied, the initial work carried out will build on the research of Shin *et al.* into $Ba_2Sc_2O_5$ in the hope of improving the chemical stability of this phase even further, while reducing the scandium content and hence lowering the cost and maintaining the high conductivities observed.[166] Following on from this, known electrolyte materials, $BaCe_{1-x}M_xO_{3-\delta}$ and Ba_2SnYO_5, with poor stability in either CO_2 or reducing atmospheres were studied in the hope of improving their stability when doped with oxyanions and retaining their high ionic conductivities.

To try and develop stable cathode materials, silicon doping was also carried out on $(Ca/Sr)_2MnFe_{1-x}Si_xO_{6-\delta}$, with silicon doping having already been shown to be successful in a number of related phases.

In all cases principle characterisation would be carried out by powder X-ray diffraction, Raman spectroscopy and thermogravimetric analysis, and if pure phases were obtained impedance spectroscopy or 4-probe direct current conductivity measurements were carried out. The stability of the phases was analysed using powder X-ray diffraction and thermogravimetric analysis.

1.5 References

1. E. I. Ortiz-Rivera, A. L. Reyes-Hernandez, R. A-Febo and Ieee, *Understanding the history of fuel cells*, I.E.E.E., New York, 2007.
2. A. B. Stambouli and E. Traversa, *Renew. Sust. Energ. Rev.*, 2002, **6**, 433-455.
3. J. M. Andujar and F. Segura, *Renew. Sust. Energ. Rev.*, 2009, **13**, 2309-2322.
4. http://americanhistory.si.edu/fuelcells/origins/origins.htm, (April 2014)
5. A. J. Appleby, *J. Power Sources*, 1990, **29**, 3-11.
6. http://www.doitpoms.ac.uk/tlplib/fuel-cells/printall.php, (April 2014)
7. B. C. H. Steele and A. Heinzel, *Nature*, 2001, **414**, 345-352.
8. J. B. Goodenough, *Ann. Rev. Mater. Res.*, 2003, **33**, 91-128.
9. S. M. Haile, *Acta Mater.*, 2003, **51**, 5981-6000.
10. D. J. L. Brett, A. Atkinson, N. P. Brandon and S. J. Skinner, *Chem. Soc. Rev.*, 2008, **37**, 1568-1578.
11. A. Orera and P. R. Slater, *Chem. Mat.*, 2010, **22**, 675-690.
12. A. J. Jacobson, *Chem. Mat.*, 2010, **22**, 660-674.
13. J. A. Kilner, *Faraday Discuss.*, 2007, **134**, 9-15.
14. H. G. Scott, *J. Mater. Sci.*, 1975, **10**, 1527-1535.
15. A. W. Smith, F. W. Meszaros and C. D. Amata, *J. Am. Ceram. Soc.*, 1966, **49**, 240.
16. K. Kitazawa and R. L. Coble, *J. Am. Ceram. Soc.*, 1974, **57**, 360-363.
17. L. D. Burke, H. Rickert and R. Steiner, *Zeitschrift für Physikalische Chemie-Frankfurt*, 1971, **74**, 146.
18. S. Q. Hui, J. Roller, S. Yick, X. Zhang, C. Deces-Petit, Y. S. Xie, R. Maric and D. Ghosh, *J. Power Sources*, 2007, **172**, 493-502.
19. X. Guo and R. Waser, *Prog. Mater. Sci.*, 2006, **51**, 151-210.
20. T. I. Politova and J. T. S. Irvine, *Solid State Ion.*, 2004, **168**, 153-165.
21. A. Lashtabeg and S. J. Skinner, *J. Mater. Chem.*, 2006, **16**, 3161-3170.
22. E.-O. Oh, C.-M. Whang, Y.-R. Lee, J.-H. Lee, K. J. Yoon, B.-K. Kim, J.-W. Son, J.-H. Lee and H.-W. Lee, *Journal of the European Ceramic Society*, 2012, **32**, 1733-1741.
23. R. Nedelec, S. Uhlenbruck, D. Sebold, V. A. C. Haanappel, H. P. Buchkremer and D. Stover, *J. Power Sources*, 2012, **205**, 157-163.
24. M. V. F. Schlupp, M. Prestat, J. Martynczuk, J. L. M. Rupp, A. Bieberle-Hutter and L. J. Gauckler, *J. Power Sources*, 2012, **202**, 47-55.
25. K. Eguchi, T. Setoguchi, T. Inoue and H. Arai, *Solid State Ion.*, 1992, **52**, 165-172.
26. H. L. Tuller and A. S. Nowick, *J. Electrochem. Soc.*, 1975, **122**, 255-259.
27. J. A. Kilner, *Chem. Lett.*, 2008, **37**, 1012-1015.
28. M. Mogensen, N. M. Sammes and G. A. Tompsett, *Solid State Ion.*, 2000, **129**, 63-94.
29. M. Mogensen, D. Lybye, N. Bonanos, P. V. Hendriksen and F. W. Poulsen, *Solid State Ion.*, 2004, **174**, 279-286.
30. T. Inoue, T. Setoguchi, K. Eguchi and H. Arai, *Solid State Ion.*, 1989, **35**, 285-291.
31. O. A. Marina, C. Bagger, S. Primdahl and M. Mogensen, *Solid State Ion.*, 1999, **123**, 199-208.
32. K. Zheng, B. C. H. Steele, M. Sahibzada and I. S. Metcalfe, *Solid State Ion.*, 1996, **86-8**, 1241-1244.
33. M. Sahibzada, B. C. H. Steele, K. Zheng, R. A. Rudkin and I. S. Metcalfe, *Catal. Today*, 1997, **38**, 459-466.
34. B. C. H. Steele, *Solid State Ion.*, 2000, **129**, 95-110.

35. H. Inaba and H. Tagawa, *Solid State Ion.*, 1996, **83**, 1-16.
36. T. Kudo and H. Obayashi, *J. Electrochem. Soc.*, 1976, **123**, 415-419.
37. C. Milliken, S. Guruswamy and A. Khandkar, *J. Am. Ceram. Soc.*, 2002, **85**, 2479-2486.
38. J. H. Lee, *Mon. Chem.*, 2009, **140**, 1081-1094.
39. T. Ishihara, H. Matsuda and Y. Takita, *J. Am. Chem. Soc.*, 1994, **116**, 3801-3803.
40. E. Kendrick, M. S. Islam and P. R. Slater, *J. Mater. Chem.*, 2007, **17**, 3104-3111.
41. P. Lacorre, F. Goutenoire, O. Bohnke, R. Retoux and Y. Laligant, *Nature*, 2000, **404**, 856-858.
42. F. Goutenoire, O. Isnard, R. Retoux and P. Lacorre, *Chem. Mat.*, 2000, **12**, 2575-2580.
43. A. Tarancon, S. J. Skinner, R. J. Chater, F. Hernandez-Ramirez and J. A. Kilner, *J. Mater. Chem.*, 2007, **17**, 3175-3181.
44. P. Plonczak, M. Gazda, B. Kusz and P. Jasinski, *J. Power Sources*, 2008, **181**, 1-7.
45. Y. Shimakawa, *Inorganic Chemistry*, 2008, **47**, 8562-8570.
46. L. Qiu, T. Ichikawa, A. Hirano, N. Imanishi and Y. Takeda, *Solid State Ion.*, 2003, **158**, 55-65.
47. J. Tulloch and S. W. Donne, *J. Power Sources*, 2009, **188**, 359-366.
48. J. Nowotny and M. Rekas, *J. Am. Ceram. Soc.*, 1998, **81**, 67-80.
49. J. Mizusaki, N. Mori, H. Takai, Y. Yonemura, H. Minamiue, H. Tagawa, M. Dokiya, H. Inaba, K. Naraya, T. Sasamoto and T. Hashimoto, *Solid State Ion.*, 2000, **129**, 163-177.
50. S. Miyoshi, J. O. Hong, K. Yashiro, A. Kaimai, Y. Nigara, K. Kawamura, T. Kawada, J. Mizusaki and J. Mizusaki, *Solid State Ion.*, 2002, **154**, 257-263.
51. M. B. Phillipps, N. M. Sammes and O. Yamamoto, *J. Mater. Sci.*, 1996, **31**, 1689-1692.
52. J. M. Ralph, A. C. Schoeler and M. Krumpelt, *J. Mater. Sci.*, 2001, **36**, 1161-1172.
53. O. Yamamoto, Y. Takeda, R. Kanno and M. Noda, *Solid State Ion.*, 1987, **22**, 241-246.
54. C. Clausen, C. Bagger, J. B. Bildesorensen and A. Horsewell, *Solid State Ion.*, 1994, **70**, 59-64.
55. T. Kenjo and M. Nishiya, *Solid State Ion.*, 1992, **57**, 295-302.
56. G. Stochniol, E. Syskakis and A. Naoumidis, *J. Am. Ceram. Soc.*, 1995, **78**, 929-932.
57. T. Setoguchi, T. Inoue, H. Takebe, K. Eguchi, K. Morinaga and H. Arai, *Solid State Ion.*, 1990, **37**, 217-221.
58. H. Yokokawa, N. Sakai, T. Kawada and M. Dokiya, *Solid State Ion.*, 1990, **40-1**, 398-401.
59. T. L. Wen, H. Tu, Z. Xu and O. Yamamoto, *Solid State Ion.*, 1999, **121**, 25-30.
60. K. Q. Huang, M. Feng, J. B. Goodenough and M. Schmerling, *J. Electrochem. Soc.*, 1996, **143**, 3630-3636.
61. A. Weber and E. Ivers-Tiffee, *J. Power Sources*, 2004, **127**, 273-283.
62. K. T. Lee and A. Manthiram, *J. Electrochem. Soc.*, 2006, **153**, A794-A798.
63. K. Huang, H. Y. Lee and J. B. Goodenough, *J. Electrochem. Soc.*, 1998, **145**, 3220-3227.
64. C. Rossignol, J. M. Ralph, J. M. Bae and J. T. Vaughey, *Solid State Ion.*, 2004, **175**, 59-61.
65. M. Shiono, K. Kobayashi, T. L. Nguyen, K. Hosoda, T. Kato, K. Ota and M. Dokiya, *Solid State Ion.*, 2004, **170**, 1-7.

66. S. P. Simner, J. F. Bonnett, N. L. Canfield, K. D. Meinhardt, V. L. Sprenkle and J. W. Stevenson, *Electrochemical and Solid State Letters*, 2002, **5**, A173-A175.
67. S. P. Simner, J. R. Bonnett, N. L. Canfield, K. D. Meinhardt, J. P. Shelton, V. L. Sprenkle and J. W. Stevenson, *J. Power Sources*, 2003, **113**, 1-10.
68. H. Yokokawa, N. Sakai, T. Horita, K. Yamaji, M. E. Brito and H. Kishimoto, *J. Alloy. Compd.*, 2008, **452**, 41-47.
69. A. Mai, V. A. C. Haanappel, S. Uhlenbruck, F. Tietz and D. Stover, *Solid State Ion.*, 2005, **176**, 1341-1350.
70. L. Kindermann, D. Das, H. Nickel, K. Hilpert, C. C. Appel and F. W. Poulson, *J. Electrochem. Soc.*, 1997, **144**, 717-720.
71. G. C. Kostogloudis and C. Ftikos, *Solid State Ion.*, 1999, **126**, 143-151.
72. S. Uhlenbruck, T. Moskalewicz, N. Jordan, H. J. Penkalla and H. P. Buchkremer, *Solid State Ion.*, 2009, **180**, 418-423.
73. A. Mai, M. Becker, W. Assenmacher, F. Tietz, D. Hathiramani, E. Ivers-Tiffee, D. Stoever and W. Mader, *Solid State Ion.*, 2006, **177**, 1965-1968.
74. H. Iwahara, H. Uchida, K. Ono and K. Ogaki, *J. Electrochem. Soc.*, 1988, **135**, 529-533.
75. R. C. T. Slade and N. Singh, *Solid State Ion.*, 1993, **61**, 111-114.
76. D. A. Stevenson, N. Jiang, R. M. Buchanan and F. E. G. Henn, *Solid State Ion.*, 1993, **62**, 279-285.
77. E. Fabbri, A. D'Epifanio, E. Di Bartolomeo, S. Licoccia and E. Traversa, *Solid State Ion.*, 2008, **179**, 558-564.
78. K. Katahira, Y. Kohchi, T. Shimura and H. Iwahara, *Solid State Ion.*, 2000, **138**, 91-98.
79. H. Iwahara, *Solid State Ion.*, 1988, **28**, 573-578.
80. A. J. Jacobson, B. C. Tofield and B. E. F. Fender, *Acta Crystallographica Section B-Structural Crystallography and Crystal Chemistry*, 1972, **B 28**, 956-&.
81. K. S. Knight, *Solid State Ion.*, 1994, **74**, 109-117.
82. S. Yamaguchi and N. Yamada, *Solid State Ion.*, 2003, **162**, 23-29.
83. M. Y. Wang and L. G. Qiu, *Chin. J. Chem. Phys.*, 2008, **21**, 286-290.
84. N. V. Sharova and V. P. Gorelov, *Russ. J. Electrochem.*, 2005, **41**, 1001-1007.
85. E. Gorbova, V. Maragou, D. Medvedev, A. Demin and P. Tsiakaras, *J. Power Sources*, 2008, **181**, 207-213.
86. N. Maffei, L. Pelletier, J. P. Charland and A. McFarlan, *J. Power Sources*, 2006, **162**, 165-167.
87. C. Chen and G. L. Ma, *J. Alloy. Compd.*, 2009, **485**, 69-72.
88. N. I. Matskevich and T. A. Wolf, *J. Chem. Thermodyn.*, 2010, **42**, 225-228.
89. W. B. Wang, J. W. Liu, Y. D. Li, H. T. Wang, F. Zhang and G. L. Ma, *Solid State Ion.*, 2010, **181**, 667-671.
90. M. Y. Wang, L. G. Qiu and G. L. Ma, *Chin. J. Chem.*, 2007, **25**, 1273-1277.
91. J. L. Yin, X. W. Wang, J. H. Xu, H. T. Wang, F. Zhang and G. L. Ma, *Solid State Ion.*, 2011, **185**, 6-10.
92. L. G. Qiu and M. Y. Wang, *Chin. J. Chem. Phys.*, 2010, **23**, 707-712.
93. N. I. Matskevich, T. Wolf, M. Y. Matskevich and T. I. Chupakhina, *Eur. J. Inorg. Chem.*, 2009, 1477-1482.
94. F. Giannici, A. Longo, A. Balerna, K. D. Kreuer and A. Martorana, *Chem. Mat.*, 2007, **19**, 5714-5720.
95. J. A. Kilner, *Solid State Ion.*, 2000, **129**, 13-23.

96. K. Yashiro, I. Suzuki, A. Kaimai, H. Matsumoto, Y. Nigara, T. Kawada, J. Mizusaki, J. Sfeir and J. Van Herle, *Solid State Ion.*, 2004, **175**, 341-344.
97. A. Radojkovic, M. Zunic, S. M. Savic, G. Brankovic and Z. Brankovic, *Ceramics International*, 2013, **39**, 307-313.
98. K. Xie, R. Yan, X. Chen, S. Wang, Y. Jiang, X. Liu and G. Meng, *J. Alloy. Compd.*, 2009, **473**, 323-329.
99. K. Xie, R. Yan, X. Chen, D. Dong, S. Wang, X. Liu and G. Meng, *J. Alloy. Compd.*, 2009, **472**, 551-555.
100. K. Xie, R. Yan, X. Xu, X. Liu and G. Meng, *J. Power Sources*, 2009, **187**, 403-406.
101. R. Yan, Q. Wang, G. Chen, W. Huang and K. Xie, *Ionics*, 2009, **15**, 749-752.
102. R. Yan, Q. Wang and K. Xie, *Ionics*, 2009, **15**, 501-505.
103. Z. Tao, Z. Zhu, H. Wang and W. Liu, *J. Power Sources*, 2010, **195**, 3481-3484.
104. L. Bi, Z. Tao, C. Liu, W. Suna, H. Wang and W. Liu, *Journal of Membrane Science*, 2009, **336**, 1-6.
105. X.-M. Liu, Y.-J. Gu, Z.-G. Liu, J.-H. Ouyang, F.-Y. Yan and J. Xiang, *Bulletin of Materials Science*, 2013, **36**, 395-401.
106. A. K. Azad, C. Savaniu, S. Tao, S. Duval, P. Holtappels, R. M. Ibberson and J. T. S. Irvine, *J. Mater. Chem.*, 2008, **18**, 3414-3418.
107. Y. Yamazaki, P. Babilo and S. M. Haile, *Chem. Mat.*, 2008, **20**, 6352-6357.
108. K. D. Kreuer, S. Adams, W. Munch, A. Fuchs, U. Klock and J. Maier, *Solid State Ion.*, 2001, **145**, 295-306.
109. A. D'Epifanio, E. Fabbri, E. Di Bartolomeo, S. Licoccia and E. Traversa, *Fuel Cells*, 2008, **8**, 69-76.
110. K. D. Kreuer, *Ann. Rev. Mater. Res.*, 2003, **33**, 333-359.
111. S. M. Haile, G. Staneff and K. H. Ryu, *J. Mater. Sci.*, 2001, **36**, 1149-1160.
112. F. M. M. Snijkers, A. Buekenhoudt, J. Cooymans and J. J. Luyten, *Scripta Materialia*, 2004, **50**, 655-659.
113. P. Babilo and S. M. Haile, *J. Am. Ceram. Soc.*, 2005, **88**, 2362-2368.
114. S. B. C. Duval, P. Holtappels, U. Stimming and T. Graule, *Solid State Ion.*, 2008, **179**, 1112-1115.
115. K. H. Ryu and S. M. Haile, *Solid State Ion.*, 1999, **125**, 355-367.
116. J. S. Fish, S. Ricote, F. Lenrick, L. R. Wallenberg, T. C. Holgate, R. O'Hayre and N. Bonanos, *J. Mater. Sci.*, 2013, **48**, 6177-6185.
117. M. Della Negra, W. Zhang, N. Bonanos and S. Ricote, *J. Mater. Sci.*, 2014, **49**, 2588-2595.
118. J. Lv, L. Wang, D. Lei, H. Guo and R. V. Kumar, *J. Alloy. Compd.*, 2009, **467**, 376-382.
119. W. Zajac, E. Hanc, A. Gorzkowska-Sobas, K. Swierczek and J. Molenda, *Solid State Ion.*, 2012, **225**, 297-303.
120. S. Zhan, X. Zhu, W. Wang and W. Yang, in *Advances in Chemistry Research Ii, Pts 1-3*, eds. S. Chen, Z. T. Liu and Q. Z. Zeng, 2012, vol. 554-556, pp. 404-407.
121. S. Ricote, N. Bonanos, A. Manerbino and W. G. Coors, *Int. J. Hydrog. Energy*, 2012, **37**, 7954-7961.
122. P. Sawant, S. Varma, B. N. Wani and S. R. Bharadwaj, *Int. J. Hydrog. Energy*, 2012, **37**, 3848-3856.
123. P. Murugaraj, K. D. Kreuer, T. He, T. Schober and J. Maier, *Solid State Ion.*, 1997, **98**, 1-6.
124. J. B. Goodenough, J. E. Ruizdiaz and Y. S. Zhen, *Solid State Ion.*, 1990, **44**, 21-31.

125. B. Gross, S. Marion, R. Hempelmann, D. Grambole and F. Herrmann, *Solid State Ion.*, 1998, **109**, 13-23.
126. T. Norby, *Solid State Ion.*, 1999, **125**, 1-11.
127. R. Haugsrud and T. Norby, *Nat. Mater.*, 2006, **5**, 193-196.
128. E. Fabbri, I. Markus, L. Bi, D. Pergolesi and E. Traversa, *Solid State Ion.*, 2011, **202**, 30-35.
129. I. Antunes, G. C. Mather, J. R. Frade, J. Gracio and D. P. Fagg, *J. Solid State Chem.*, 2010, **183**, 2826-2834.
130. J. Chen, F. Liang, L. Liu, S. Jiang, B. Chi, J. Pu and J. Li, *J. Power Sources*, 2008, **183**, 586-589.
131. E. Fabbri, S. Licoccia, E. Traversa and E. D. Wachsman, *Fuel Cells*, 2009, **9**, 128-138.
132. E. Fabbri, L. Bi, D. Pergolesi and E. Traversa, *Energy & Environmental Science*, 2011, **4**, 4984-4993.
133. B. Lin, H. Ding, Y. Dong, S. Wang, X. Zhang, D. Fang and G. Meng, *J. Power Sources*, 2009, **186**, 58-61.
134. L. Yang, C. D. Zuo, S. Z. Wang, Z. Cheng and M. L. Liu, *Advanced Materials*, 2008, **20**, 3280-+.
135. M. T. Weller, *Inorganic Materials Chemistry*, Oxford Chemistry Primers, Oxford, 1994.
136. C. Li, K. C. K. Soh and P. Wu, *J. Alloy. Compd.*, 2004, **372**, 40-48.
137. S. Svarcova, K. Wiik, J. Tolchard, H. J. M. Bouwmeester and T. Grande, *Solid State Ion.*, 2008, **178**, 1787-1791.
138. S. Sasaki, C. T. Prewitt, J. D. Bass and W. A. Schulze, *Acta Crystallographica Section C*, 1987, **43**, 1668-1674.
139. P. Coppens and M. Eibschutz, *Acta Crystallographica*, 1965, **19**, 524-531.
140. J. Lander, *Acta Crystallographica*, 1951, **4**, 148-156.
141. H. Iwahara, T. Yajima, T. Hibino, K. Ozaki and H. Suzuki, *Solid State Ion.*, 1993, **61**, 65-69.
142. J. P. Hodges, S. Short, J. D. Jorgensen, X. Xiong, B. Dabrowski, S. M. Mini and C. W. Kimball, *J. Solid State Chem.*, 2000, **151**, 190-209.
143. E. E. McCabe and C. Greaves, *Chem. Mat.*, 2006, **18**, 5774-5781.
144. C. Greaves and P. R. Slater, *Physica C*, 1991, **175**, 172-178.
145. C. Greaves and P. R. Slater, *J. Mater. Chem.*, 1991, **1**, 17-21.
146. P. R. Slater, C. Greaves, M. Slaski and C. M. Muirhead, *Physica C*, 1993, **208**, 193-196.
147. Y. Miyazaki, H. Yamane, N. Ohnishi, T. Kajitani, K. Hiraga, Y. Morii, S. Funahashi and T. Hirai, *Physica C*, 1992, **198**, 7-13.
148. A. Maignan, M. Hervieu, C. Michel and B. Raveau, *Physica C*, 1993, **208**, 116-120.
149. K. Kinoshita and T. Yamada, *Nature*, 1992, **357**, 313-315.
150. V. Caignaert, B. Domenges and B. Raveau, *J. Solid State Chem.*, 1995, **120**, 279-289.
151. D. Pelloquin, M. Hervieu, C. Michel, N. Nguyen and B. Raveau, *J. Solid State Chem.*, 1997, **134**, 395-408.
152. Y. Breard, C. Michel, M. Hervieu and B. Raveau, *J. Mater. Chem.*, 2000, **10**, 1043-1045.
153. Y. Breard, C. Michel, M. Hervieu, N. Nguyen, A. Ducouret, V. Hardy, A. Maignan, B. Raveau, F. Bouree and G. Andre, *Chem. Mat.*, 2004, **16**, 2895-2905.
154. B. Raveau, M. Hervieu, D. Pelloquin, C. Michel and R. Retoux, *Zeitschrift Fur Anorganische Und Allgemeine Chemie*, 2005, **631**, 1831-1839.

155. J. F. Shin, L. Hussey, A. Orera and P. R. Slater, *Chemical Communications*, 2010, **46**, 4613-4615.
156. J. F. Shin, D. C. Apperley and P. R. Slater, *Chem. Mat.*, 2010, **22**, 5945-5948.
157. J. F. Shin, A. Orera, D. C. Apperley and P. R. Slater, *J. Mater. Chem.*, 2011, **21**, 874-879.
158. S. A. Speakman, J. W. Richardson, B. J. Mitchell and S. T. Misture, *Solid State Ion.*, 2002, **149**, 247-259.
159. T. Q. Ta, T. Tsuji and Y. Yamamura, *J. Alloy. Compd.*, 2006, **408**, 253-256.
160. T. Schober, *Solid State Ion.*, 1998, **109**, 1-11.
161. V. Jayaraman, A. Magrez, M. Caldes, O. Joubert, M. Ganne, Y. Piffard and L. Brohan, *Solid State Ion.*, 2004, **170**, 17-24.
162. A. Rolle, R. N. Vannier, N. V. Giridharan and F. Abraham, *Solid State Ion.*, 2005, **176**, 2095-2103.
163. M. Aoki, Y. M. Chiang, I. Kosacki, I. J. R. Lee, H. Tuller and Y. P. Liu, *J. Am. Ceram. Soc.*, 1996, **79**, 1169-1180.
164. S. P. S. Badwal, F. T. Ciacchi, S. Rajendran and J. Drennan, *Solid State Ion.*, 1998, **109**, 167-186.
165. C. C. Appel and N. Bonanos, *Journal of the European Ceramic Society*, 1999, **19**, 847-851.
166. J. F. Shin, K. Joubel, D. C. Apperley and P. R. Slater, *Dalton Transactions*, 2012, **41**, 261-266.
167. W. Kwestroo, H. A. M. Vanhal and Langerei.C, *Mater. Res. Bull.*, 1974, **9**, 1623-1630.
168. T. Omata, T. Fuke and S. Otsuka-Yao-Matsuo, *Solid State Ion.*, 2006, **177**, 2447-2451.
169. C. A. Hancock and P. R. Slater, *Dalton Transactions*, 2011, **40**, 5599-5603.
170. D. Ivanova, E. Lima, A. Kovalevsky, F. M. L. Figueiredo, V. V. Kharton and F. M. B. Marques, *Ionics*, 2008, **14**, 349-356.
171. M. J. Verkerk, A. J. A. Winnubst and A. J. Burggraaf, *J. Mater. Sci.*, 1982, **17**, 3113-3122.
172. S. P. S. Badwal and J. Drennan, *J. Mater. Sci.*, 1987, **22**, 3231-3239.
173. M. L. Mecartney, *J. Am. Ceram. Soc.*, 1987, **70**, 54-58.
174. S. P. S. Badwal and J. Drennan, *J. Mater. Sci.*, 1989, **24**, 88-96.
175. D. Ivanova, A. Kovalevsky, V. V. Kharton and F. M. B. Marques, *Boletin De La Sociedad Espanola De Ceramica Y Vidrio*, 2008, **47**, 201-206.
176. C. A. Hancock, R. C. T. Slade, J. R. Varcoe and P. R. Slater, *J. Solid State Chem.*, 2011, **184**, 2972-2977.
177. J. M. Porras-Vazquez, T. F. Kemp, J. V. Hanna and P. R. Slater, *J. Mater. Chem.*, 2012, **22**, 8287-8293.
178. J. M. Porras-Vazquez and P. R. Slater, *J. Power Sources*, 2012, **209**, 180-183.
179. J. M. Porras-Vazquez, E. R. Losilla, P. J. Keenan, C. A. Hancock, T. F. Kemp, J. V. Hanna and P. R. Slater, *Dalton Transactions*, 2013, **42**, 5421-5429.
180. J. M. Porras-Vazquez, T. Pike, C. A. Hancock, J. F. Marco, F. J. Berry and P. R. Slater, *Journal of Materials Chemistry A*, 2013, **1**, 11834-11841.
181. F. A. Kröger, H. J. Vink; *Solid State Physics*, 1956, **3**, 307-435

Chapter 2 Experimental Techniques

2.1 Solid State Synthesis

The solid state synthesis method is the most common synthesis method used in materials science due to its simplicity. High purity starting materials are weighed out using the correct stoichiometry, as required for the specific chemical reaction. The sample is then ground until a homogenous powder is obtained; this process distributes the reactants throughout the mixture and reduces the grain size, increasing the reaction rate. The temperature used is generally above 750 °C and heating occurs for generally a few days; the high temperatures are used to enable the atoms to have energy to migrate to the reaction site by breaking their bonds and form new bonds at the reaction site. Purity of reagents is vital to ensure high purification of the product, as separation of the intended phase from the other phases formed is almost impossible; chemical suppliers provide high purity reagents that are easily available and the reagents must be chosen carefully to ensure the correct stoichiometry. However care must be taken if the reagent is hygroscopic (although this can be overcome by heating the reagent above the dehydration temperature) or air sensitive, as this can lead to incorrect calculations of the mass required.

In solid state synthesis the reaction occurs at the interface of the reagents. Therefore once the product has started to form at the interface, the reagents must now move through the product phase to react. Point defects that are present, such as vacancies or interstitial atoms, can improve the reaction process. As the product layer increases in size the length of the diffusion path increases causing a lowering of the rate of reaction. To overcome this, intermittent grinding of the sample can be used. This breaks up the product layer that formed at the interface and creates new reaction sites at the newly formed interface between reagents.

Pressing the sample into a pellet can improve the reaction by increasing the contact between the reagents.

Starting reagents for the alkaline earth metals generally are carbonates rather than oxides, as the carbonates are more stable at room temperature than the oxides, which can react with CO_2, forming the carbonate, as well as being hygroscopic. In this project the carbonates $SrCO_3$ and $BaCO_3$ were used and decomposed to the oxides under the heating, producing a reactant with a high reactivity.

A high reaction temperature can result in the evaporation of some the reagents if they are volatile, such as barium, as seen by Omata *et al*.[1] To overcome this common issue a sealed vessel can be used, however this is not always possible due to high temperatures being used. Pressing the sample into a pellet to reduce the surface area can reduce reagent evaporation; the top deficient layer can be removed after heating by sanding. Other ways to overcome this evaporation are to use excess reactant initially, placing a lid over the crucible and covering the pellet in sacrificial powder, all of these were used in this project to prevent barium loss.

2.2 Structural Characterisation [2-4]

2.2.1 Crystallography

Crystals are solids that possess long range order. Crystals with this long range order are best described by using a lattice description. This lattice is made up of repeating blocks called the unit cell; the crystal structure can be made by translating or shifting the unit cells along one, two or three directions independently. A three-dimensional lattice or the unit cell can be described fully by three noncoplanar vectors

$$\boldsymbol{q} = u\boldsymbol{a} + v\boldsymbol{b} + w\boldsymbol{c}$$

Where $u + v + w = 0$ is taken as the origin and positive and negative values of u, v and w define positive and negative directions. Instead of using these noncoplanar vectors the unit cell can be completely described by six scalar quantities, known as the lattice parameters. a, b and c describe of the length of the edges of the unit cell and α, β and γ describe the angles between them, Figure 2.1.

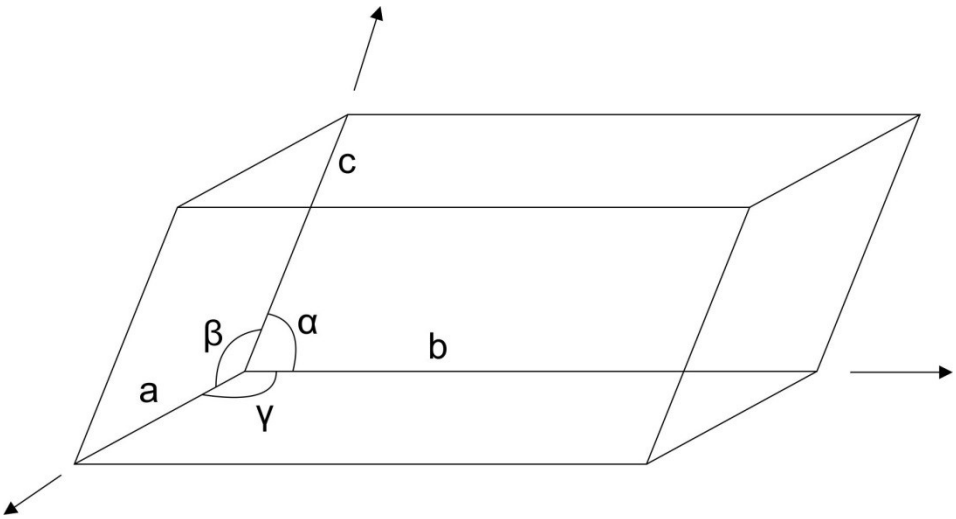

Figure 2.1 Lattice parameters of a unit cell

There are 7 different crystal systems, summarised in Table 2.1, with different relationships between the lengths and angles of the unit cell. There are also 4 different lattice types; primitive (P), lattice points at each corner, body-centred (I), lattice points at each corner and the centre of the unit cell, face-centred (F), lattice points at each corner and the middle of each face, and base-centred (C), lattice points at each corner and in the middle of two opposite faces. Combining these with the 7 crystal systems gives rise to the Bravais lattices, Figure 2.2.

Table 2.1 The seven crystal systems

Crystal System	Axial Relationships
Cubic	$a = b = c$
	$\alpha = \beta = \gamma = 90°$
Tetragonal	$a = b \neq c$
	$\alpha = \beta = \gamma = 90°$
Orthorhombic	$a \neq b \neq c$
	$\alpha = \beta = \gamma = 90°$
Monoclinic	$a \neq b \neq c$
	$\alpha = \gamma = 90°, \beta \neq 90°$
Triclinic	$a \neq b \neq c$
	$\alpha \neq 90°, \beta \neq 90°, \gamma \neq 90°$
Hexagonal	$a = b \neq c$
	$\alpha = \beta = 90°, \gamma = 120°$
Rhombohedral	$a = b = c$
	$\alpha = \beta = \gamma \neq 90°$

There are 7 symmetry elements that can be used to convert a group of atoms in a unit cell into each other; These symmetry elements are rotation axis, centre of inversion, mirror plane, translation vector, roto-inversion/improper rotation (rotation followed by inversion), screw axis (rotation followed by translation) and glide plane (reflection followed by translation). Regular stacking of the unit cells that can be translated but not reflected or rotated imposes a constraint on the symmetry elements allowed in the lattice. The only symmetry operators allowed in a Bravais lattice are the centre of symmetry, $\bar{1}$, mirror operator, m, proper rotation axes, 1, 2, 3, 4, and 6, and the improper rotation axes, $\bar{1}$, $\bar{2}$, $\bar{3}$, $\bar{4}$ and $\bar{6}$. This results in 32 crystallographic point groups and when combined with the 14 Bravais lattices, and including screw axes, results in the 230 crystallographic space groups.

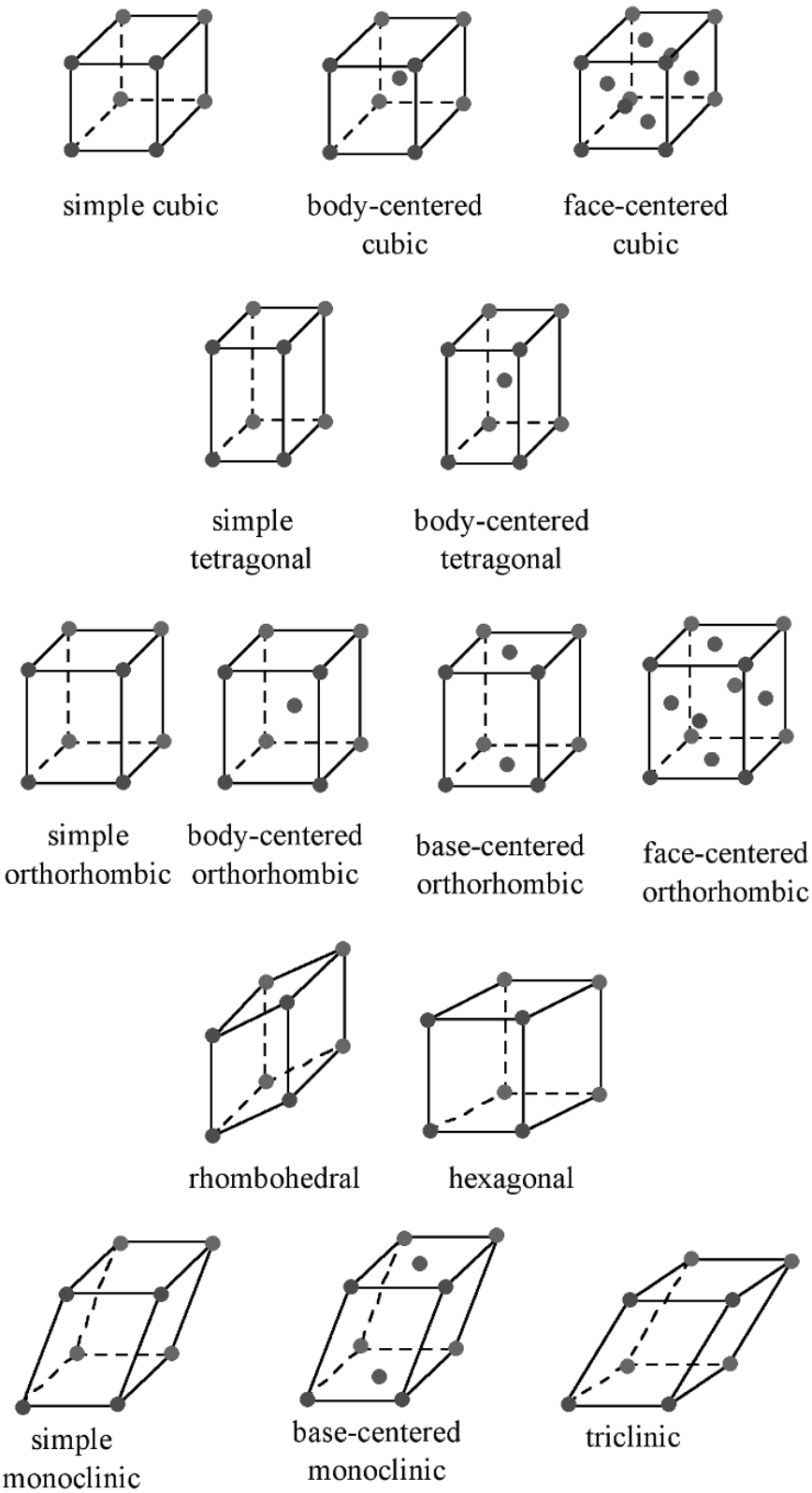

Figure 2.2 The Bravais lattices [5]

To determine atom positions in a unit cell, atomic coordinates are used; these describe how far along each vector ***a***, ***b*** and ***c*** the atom is, and are recorded as (***a***, ***b***, ***c***).

Miller indices are used to specify planes in a lattice and are defined as the inverse of the fractional intercept along *a*, *b* and *c* and placed in round brackets in the form (hkl), Figure 2.3.

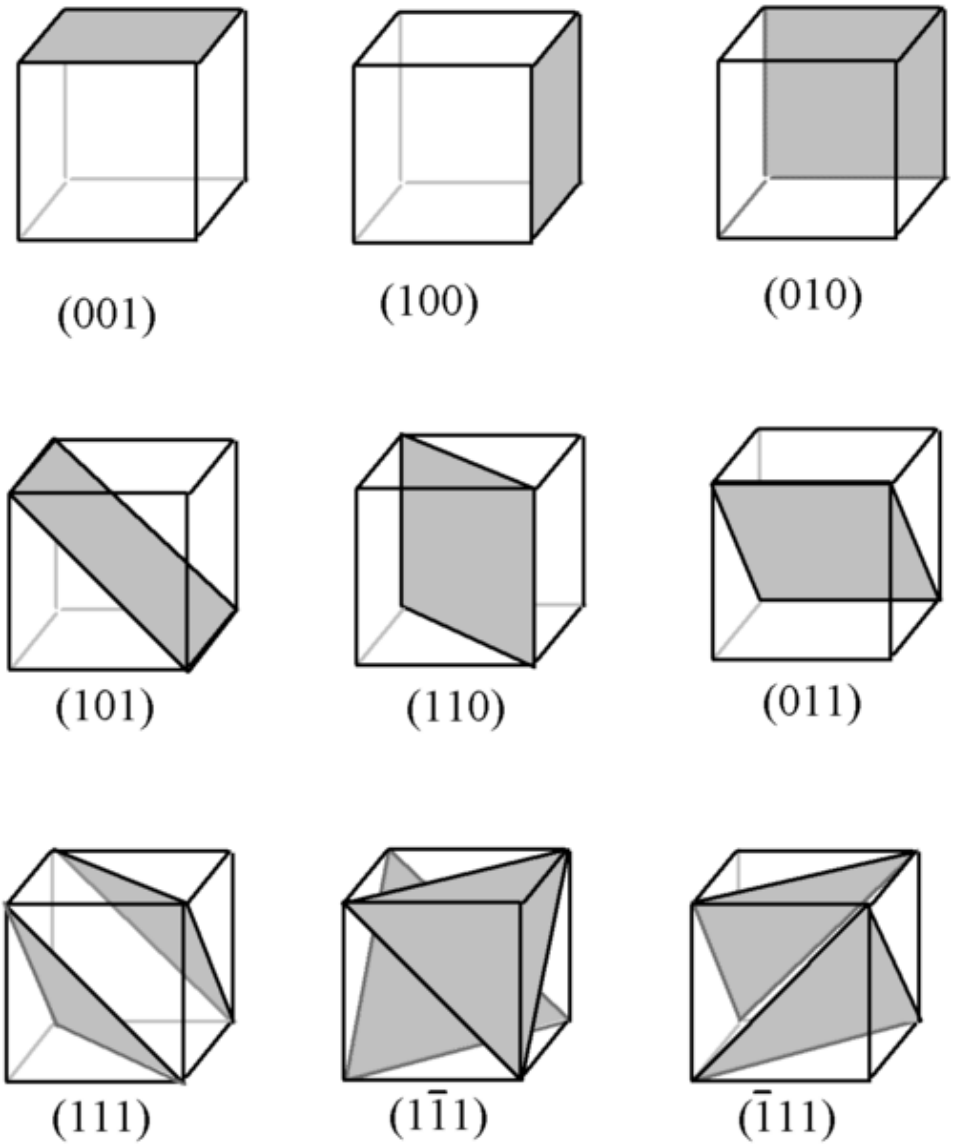

Figure 2.3 Miller indices [6]

The separation between the lattice planes is known as d_{hkl} and in a cubic cell is given by

Equation 2.1

$$\frac{1}{{d_{hkl}}^2} = \frac{h^2 + k^2 + l^2}{{a_0}^2}$$

Where a_0 is the lattice constant. This equation can be adjusted to any of the crystal systems, as detailed in the next section.

2.2.2 Powder X-ray Diffraction

The periodic array of atoms in a crystal has an interatomic spacing of around 1 Å. As X-rays have this wavelength they can be scattered to give a diffraction pattern, which can be obtained for single crystals or a crystalline powder. The position and intensities of these diffracted beams are a function of the arrangements of the atoms in space and the atomic number of the atoms. For a peak to be observed constructive interference of the reflected radiation must occur. To meet this criteria planes defined by the Miller indices must fulfil Bragg's law, Figure 2.4.

Equation 2.2

$$Path\ Difference = AB + BC = 2d \sin\theta$$

$$\therefore n\lambda = 2d_{hkl} \sin\theta$$

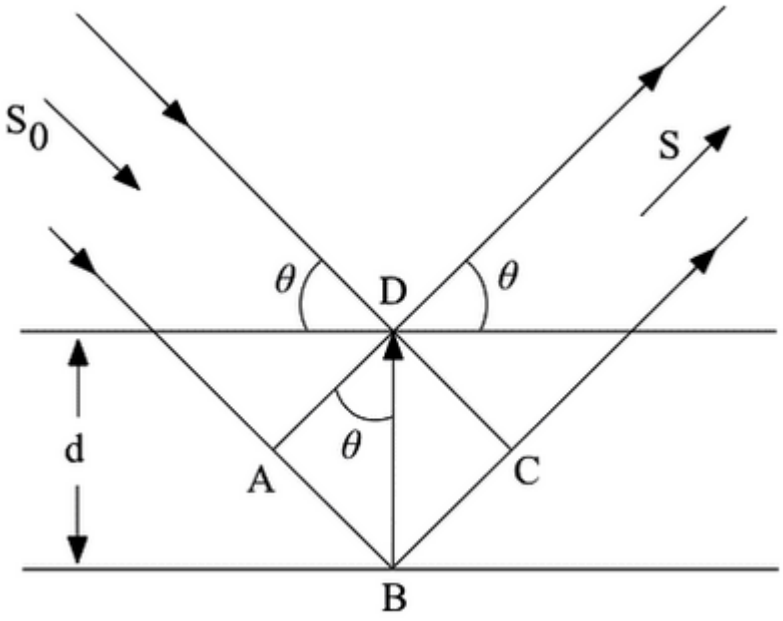

Figure 2.4 Derivation of Bragg's law [7]

From Equation 2.1 the lattice parameter can be calculated from the d_{hkl}-spacing for a cubic system and therefore the lattice parameter can be calculated from the incident X-ray radiation, λ, and the diffraction angle, θ, along with the Miller indices giving

Equation 2.3

$$a_0{}^2 = \frac{\lambda^2}{4\sin^2\theta}(h^2 + k^2 + l^2)$$

The lattice parameters for the other crystal systems, excluding triclinic, can be calculated from

Crystal System	Expression for d_{hkl} in terms of lattice parameters and Miller indices
Tetragonal	$\frac{1}{d_{hkl}{}^2} = \frac{h^2 + k^2}{a_0{}^2} + \frac{l^2}{c_0{}^2}$
Orthorhombic	$\frac{1}{d_{hkl}{}^2} = \frac{h^2}{a_0{}^2} + \frac{k^2}{b_0{}^2} + \frac{l^2}{c_0{}^2}$
Hexagonal	$\frac{1}{d_{hkl}{}^2} = \frac{4}{3}\left(\frac{h^2 + hk + k^2}{a_0{}^2}\right) + \frac{l^2}{c_0{}^2}$
Monoclinic	$\frac{1}{d_{hkl}{}^2} = \frac{1}{\sin^2\beta}\left(\frac{h^2}{a_0{}^2} + \frac{k^2\sin^2\beta}{b_0{}^2} + \frac{l^2}{c_0{}^2} - \frac{2hl\cos\beta\, a_0}{a_0 c_0}\right)$

In powder X-ray diffraction monochromatic X-rays hit the samples and are diffracted according to Bragg's law. The resulting beams form a cone of diffracted radiation with a cone angle equal to 4θ, Figure 2.5. These cones are formed by all the lattice spacings allowed, with the innermost cones having the largest d_{hkl}-spacing. A detector is then rotated around the sample cutting through all the diffraction cones determining the intensity as a function of 2θ.

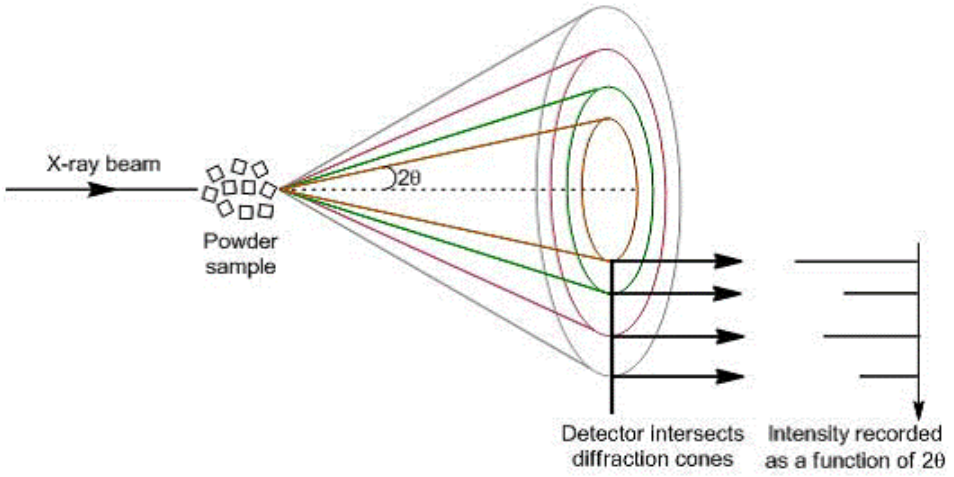

Figure 2.5 Schematic representation of diffracted X-ray beam cone formation and XRD pattern collection

The intensities of the diffracted beam depend on:

1. The Bragg angle of the diffracted beam
2. The atomic scattering factor
3. The structure factor
4. The temperature factor
5. The polarisation of the beam
6. The form factor
7. The multiplicity
8. The absorption factor

The scattering of the X-ray beam increases with increasing electrons as X-rays are scattered by the electron cloud. Therefore heavier elements will scatter more strongly than lighter elements and the scattering factor, f_a, is given by

Equation 2.4

$$f_a = \sum_{i=1}^{4} a_i e^{\left[-b_i\left(\frac{\sin\theta}{\lambda}\right)^2\right]} + c$$

The constants are called the Cromer-Mann coefficients and the scattering is strongly angle dependent, $\frac{\sin\theta}{\lambda}$.

The structure factor depends on the scattering from the unit cell and contains some of the other factors, and is given by the equation

Equation 2.5

$$F_{hkl} = \sum_{n=1}^{N} f_n exp[2\pi i(hx_n + ky_n + lz_n)]$$

$$F_{hkl} = \sum_{n=1}^{N} f_n \cos[2\pi(hx_n + ky_n + lz_n)] + if_n \sin[2\pi(hx_n + ky_n + lz_n)]$$

Where f_n is the atomic scattering factor of each atom contributing to the reflection. In a centrosymmetric unit cell the sin term is zero and can be ignored. The square of the structure factor is proportional to the intensity.

The temperature factor, also known as the Debye-Waller factor, is caused by the thermal motion of the atoms and ions in a solid. This motion has the effect of making the crystal "a slightly fuzzy diffraction grating" reducing the intensity of the diffraction peak. It has a strong 2θ dependence and becomes most noticeable at large angles. It is given by

Equation 2.6

$$f_{th} = f_n exp\left[-B\left(\frac{\sin\theta}{\lambda}\right)^2\right]$$

$$B = 8\pi^2 U$$

U is the isotropic temperature factor. The overall magnitude of the thermal vibrations is not usually isotropic and so U is replaced by anisotropic factors that define the size and orientation of the thermal ellipsoid.

The incident beam of the X-ray is unpolarised and the diffracted beam is partially polarised as not all polarisation orientations are reflected equally and is given by

Equation 2.7

$$P_\theta \propto \frac{1 + \cos^2 2\theta}{2}$$

The Lorentz factor is defined by the geometry of diffraction. It is caused by the finite size of the reciprocal lattice points and the variable radii of the Debye rings, both functions of θ. It is given by

Equation 2.8

$$L_\theta \propto \frac{1}{\cos\theta \sin^2\theta}$$

It can be combined with the polarisation factor to give a single correction term

Equation 2.9

$$\frac{1 + \cos^2 2\theta}{\cos\theta \sin^2\theta}$$

Diffraction occurs over a small range of θ values rather than a precise value due to crystal imperfections and the approximate range over which diffraction occurs is given as

Equation 2.10

$$\delta\theta \approx \frac{\lambda}{D_{hkl} \cos\theta}$$

Where D_{hkl} is the crystal thickness in the direction normal to the (hkl) planes diffracting the radiation. D_{hkl} is a multiple of d_{hkl} so

Equation 2.11

$$md_{hkl} \approx \frac{\lambda}{\delta\theta \cos\theta}$$

Therefore a sharp line indicates a well ordered crystal and a broad line an extremely disordered or very small crystallite.

In a cubic lattice the d_{hkl}-spacing of a reflection is given by Equation 2.1. Therefore (111), (-111), (1-11), (11-1), (-1-11), (-11-1), (1-1-1) and (-1-1-1) all have the same d_{hkl}-spacing, $\frac{a_0}{\sqrt{3}}$. Therefore these 8 reflections will all have the same θ values and the intensity observed will be 8 times greater than that observed for the (111) plane alone. This is known as the reflection multiplicity.

The absorption factor can also affect the intensity but can generally be ignored unless samples contain strongly absorbing elements and the effect is most noticeable at low 2θ values. It can be overcome by changing the wavelength of the radiation used.

Systematic absences can occur in the diffraction pattern due to the symmetry operations present in the unit cell and these can be calculated from the structural factor as shown below for a body centred unit cell, atomic positions (0,0,0) and (0.5,0.5,0.5).

Equation 2.12

$$F_{hkl} = \sum_{All\ atoms} f_n \cos[2\pi(hx_n + ky_n + lz_n)] + if_n \sin[2\pi(hx_n + ky_n + lz_n)]$$

$$F_{hkl} = \sum_{All\ atoms} f_n \cos[2\pi(hx_n + ky_n + lz_n)]$$

due to a centrosymmetric unit cell

$$F_{hkl} = f_n \cos[2\pi i(0)] + f_n \cos\left[2\pi i\left(\frac{1}{2}h + \frac{1}{2}k + \frac{1}{2}l\right)\right]$$

$$h + k + l = 2n, F_{hkl} = 2f_n$$

$$h + k + l \neq 2n, F_{hkl} = 0$$

Therefore $h + k + l$ must be even for a reflection to be observed for a body centred cell and if $h + k + l$ is odd then there will be no reflection intensity observed.

X-ray beams are generally generated using an X-ray tube. A tungsten filament is electrically heated and generates electrons. These electrons are then fired at a metal target by using a high electrostatic potential between the target and filament. The high energy electrons ionise electrons from the 1s orbitals, which causes electrons in higher energy orbitals to drop into the empty 1s holes, emitting X-rays and these X-rays exit the tube through beryllium windows. X-ray tubes are very inefficient due to the amount of heat generated during this process and this heat also requires the metal target to be continually cooled. The X-ray spectrum for copper, used as the metal target in this project, is shown in Figure 2.6.

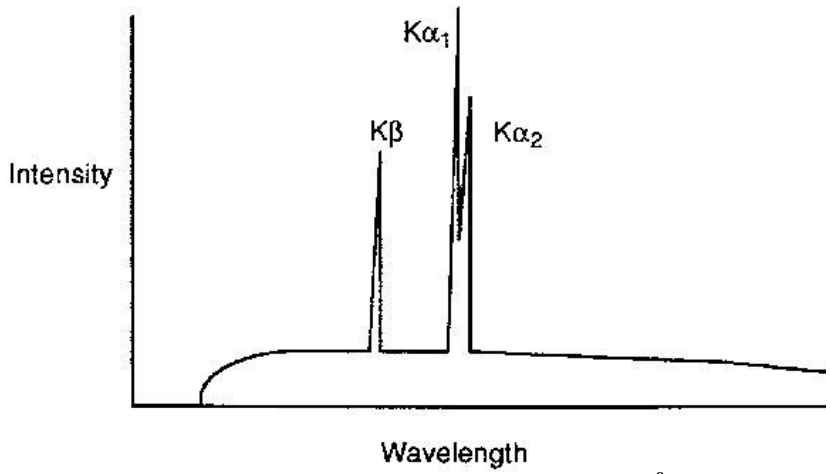

Figure 2.6 X-ray spectrum from a copper target [8]

The intense peaks are caused by electron falling from the 2p, K_α, and the 3p , K_β, to the 1s orbital. The peak from the K_α radiation is split due to the different possible spin states of the electron. The background X-ray radiation emitted (known as Bremsstrahlung radiation) is caused by electrons decelerating on hitting the target giving a wide range of wavelengths not dependent of the nature of the metal target.

For X-ray diffraction experiments to be performed a single wavelength of X-rays is necessary. This can be obtained through monochromation. The X-ray beam after passing through the beryllium windows hits a single crystal with a fixed orientation and a single wavelength of this beam is then reflected according to Bragg's law. This gives a purely monochromatic beam, only one of $K_{\alpha1}$ and $K_{\alpha2}$ is obtained, however the beam intensity is reduced. A metal filter with a lower atomic number than the metal target source can also be used, i.e. a nickel filter is used with a copper metal target and this removes the K_β radiation, although both $K_{\alpha1}$ and $K_{\alpha2}$ are still present in the X-ray beam.

2.2.3 Rietveld Analysis

This technique was developed by Hugo Rietveld in the 1960s.[9-12] Before this only high symmetry compositions were resolved using powder X-ray diffraction due to the peaks overlapping such that separating them was impossible. Single crystal X-ray diffraction could be used to overcome this issue as this allows three-dimensional data to be extracted from the diffraction pattern, such that the intensities of individual reflections could be determined, however large single crystals for some materials are hard if not impossible to grow.

Major advances in structure determination were made when the Rietveld method was developed.[9] To enable the powder diffraction data to be used in a computer the collected data must be in digitised form. The data is therefore collected in digitised form by collecting data

at thousands of individual incremental steps; in this project these steps were collected in 2θ as constant wavelength X-rays were used. The Rietveld method uses a starting model; this model must be close to the actual structure of the sample for the method to work. This model is used to calculate the intensity at each point from the unit cell parameters, the atomic positions, occupancy and thermal motion and the experimental parameters. This model is then modified using the least-squares method until the differences between the observed and calculated diffraction patterns are minimised. This is done by minimising S_y from the equation below

Equation 2.13

$$S_y = \sum_i w_i (y_i - y_{ci})^2$$

y_i is the observed intensity at the i^{th} point

y_{ci} is the calculated intensity at the i^{th} point

w_i is the weighting of each data point and is equivalent to $1/y_i$.

The majority of powder diffraction patterns of crystalline materials contain overlapping peaks that each contribute a specific peak intensity, peak position, peak shape and integrated area that is proportional to the Bragg intensity. As a number of Bragg reflections can contribute to the observed intensity at a point i the calculated intensities are determined using the following equation

$$y_{ci} = \left[s \sum_K L_K |F_K|^2 \varphi(2\theta_i - 2\theta_K) P_K A \right] + y_{bi}$$

s is the scale factor

K represents the Miller indices

L_K contains the Lorentz, polarisation and multiplicity factors

F_K is the structure factor for reflection K

φ is the peak profile function

P_K is the preferred orientation

A is the sample absorption

y_{bi} is the background intensity at the i^{th} step

Normal equations are set up that involve the derivates of all the y_{ci} with respect to each of the variable parameters. These parameters include atomic coordinates, profile parameters, site occupancies, background, lattice parameters, atomic thermal parameters, scale, preferred orientation, detector zero-point among others. The best solution is found by an iterative process and the calculated shifts are applied to the initial parameters to produce new parameters each cycle that then form the starting point for the new cycle. As the relationship between the variable parameters and intensities are mostly non-linear the starting model used must be close to the correct model. This process is continued until S_y is minimised, although care should be taken to avoid a local minimum being obtained rather than the global minimum. The visual representation of the fit is the best way of determining the success of the fit and there are numerical measures of following the refinement, known as R-factors, as shown below

$$R_p = \frac{\sum_i |y_i - y_{ci}|}{\sum_i y_i}$$

$$R_{wp} = \left[\frac{\sum_i w_i (y_i - y_{ci})^2}{\sum_i w_i (y_i)^2}\right]^{\frac{1}{2}}$$

$$R_{exp} = \left[\frac{(N - P - C)}{\sum_i w_i (y_i)^2}\right]^{\frac{1}{2}}$$

N is the total number of data points measured in the diffraction pattern

P is the number of refined parameters

C is the number of constraints

$$\chi^2 = \left[\frac{R_{wp}}{R_{exp}}\right]^2$$

$$R_I = \frac{\sum_K |I_{Ki} - I_{Kci}|}{\sum_K I_{Ki}}$$

R_{wp} is commonly reported as its numerator is also used in the minimisation of S_y. However R_{wp} can give misleading results as a high background in the diffraction pattern can lead to a low value of R_{wp} and R_{wp} values can be seriously affected by impurities. R_{exp} gives an indication of the quality of the data as the denominator will be larger if the data was collected for a long time due to the errors not being dominated by counting statistics. χ^2 values of less than 1 are not an indicator of an excellent fit but of a model that contains more parameters than can be justified by the quality of the data. R_I can be used to give an indication of the reliability of the structural model.

There are a number of computer programs available for Rietveld refinement and in this project the GSAS suite of programs was used for Rietveld refinement.[13] GSAS can work with both X-ray and neutron data from both fixed wavelength and time of flight measurements. It can work with multiple data sets simultaneously and both hard and soft constraints can be used.

The background function used in this project is type 2 in GSAS to approximate the background. This is a cosine Fourier series with a leading constant term.

$$I_b = B_1 + \sum_{j=2}^{N} B_j \cos[P * (j-1)]$$

Where P is in degrees 2θ and is just the detector position for the step.

Up to 36 coefficients can be used although fewer terms were used in this work so as not to bias the R factors and to make sure the background function is not fitting Bragg intensity.

The peak profile function 3 was used to fit the peak shape. This is a Thompson modified pseudo-Voigt function, which uses a mixing coefficient η to combine Gaussian and Lorentzian functions and employs a multi-term Simpson's rule integration.[14, 15] This function models asymmetry due to axial divergence as described by Finger *et al*.[16] The benefit of using this function is the ability to separate the Gaussian and Lorentzian contributions to the peak shape.

2.3 Raman Spectroscopy [17]

Raman spectroscopy was discovered by C. V. Raman and K. S. Krishnan in 1928 who used sunlight to observe the Raman effect.[18] This technique was used to catalogue molecular vibrational frequencies and its usage decreased when commercial IR spectrometers became available. With the advent of the laser in the 1960s Raman spectroscopy became more popular as the time required to obtain spectra decreased considerably.

Raman spectroscopy is a type of vibrational spectroscopy which is used to probe the bonding that occurs in materials. The sample is irradiated with a single wavelength of radiation (monochromatic). The photon interacts with the molecule polarising the electron cloud

surrounding the constituent nuclei of the molecule, raising the energy of the molecule to a "virtual state". The excited molecule relaxes immediately releasing a photon which can have the same or a different energy. The majority of these emitted photons have the same energy and this scattering process is known as Rayleigh scattering. This is where the molecule, after excitation and relaxation, has the same vibrational state as when it started so the process is elastic. If the vibrational state of the molecule after relaxation is different, then the emitted photon will have a different energy and hence wavelength, this is known as Raman scattering. If the molecule returns to a higher vibrational state the emitted photon will have a lower energy than the incident photon and this is called Stokes scattering, whereas if a molecule is in an excited vibrational state and returns to a lower vibrational state the emitted photon will have a higher energy and this is called anti-Stokes scattering, Figure 2.7.

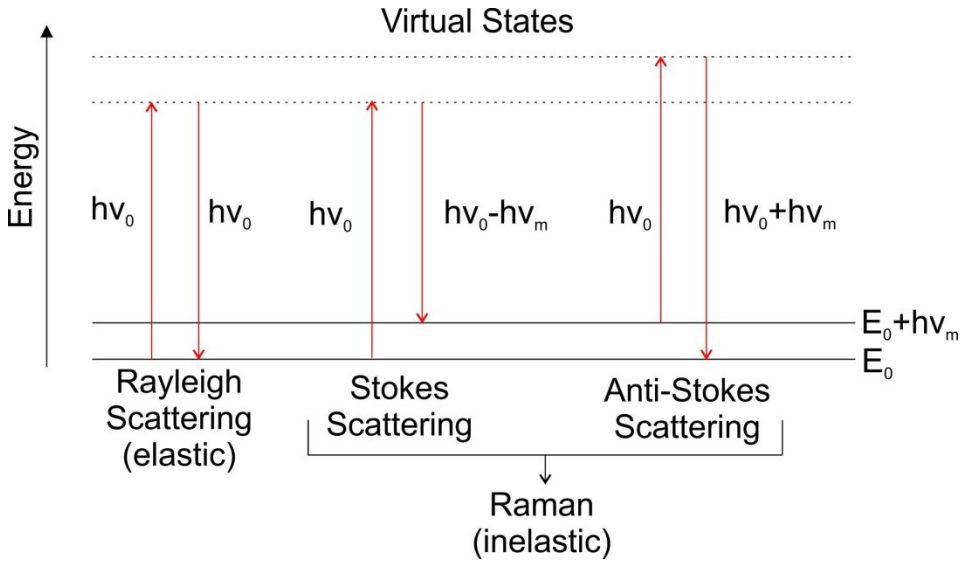

Figure 2.7 Energy transitions for Raman and Rayleigh scattering

For a molecular vibration to be Raman active the vibration must cause a change in the magnitude or direction of the polarisability of the molecule. Symmetrical vibrations generally give the most intense bands compared with asymmetric vibrations which are relatively weak. The molecular symmetry determines which vibrations are Raman active.

The intensities of the Stokes and anti-Stokes scattering are proportional to the occupancy of the original vibrational states. At room temperature most of the molecules are in the ground vibrational state so Stokes scattering will have a higher intensity than anti-Stokes scattering. Increasing the temperature will result in an increase in intensity of anti-Stokes scattering; this allows the temperature of the sample to be calculated using the Boltzmann equation and the relative intensities of the Stokes and anti-Stokes bands, Equation 2.14.[19]

Equation 2.14

$$\frac{N_1}{N_0} = \left(\frac{g_1}{g_0}\right) exp \frac{-(\Delta E)}{kT}$$

N_1 = Number of molecules in higher vibrational energy level

N_0 = Number of molecules in lower vibrational energy level

g_1 = Degeneracy of the higher vibrational energy

g_0 = Degeneracy of the lower vibrational energy

ΔE = Energy difference between higher and lower vibrational energy levels

k = Boltzmann constant

T = Temperature (K)

Raman spectra were collected on a Renishaw inVia Raman microscope with excitation using a Cobolt Samba CW532 nm DPSS laser on powdered samples.

2.4 Thermogravimetric Analysis [20]

Thermogravimetric analysis (TGA) is a technique used to measure the change in mass of a sample when heated to a specific temperature at a specific rate over time.

The sample is placed in an accurately weighed alumina or platinum crucible and the mass of the sample is then determined. The crucible is then placed on a precision thermobalance and subjected to a pre-set programme controlling the temperature and rate of temperature change while measuring the mass change of the sample. This is usually recorded by a computer coupled to a thermal analyser producing a graph as shown in Figure 2.8. A correction file can also be created, where no sample is in the crucible, from which the data with the sample can be subtracted to remove the change in mass of the crucible under the conditions, thus increasing the accuracy. Sometimes the furnace can be programmed for the heating to acquire a constant mass loss, which is much less common but used to probe specific reaction kinetics.

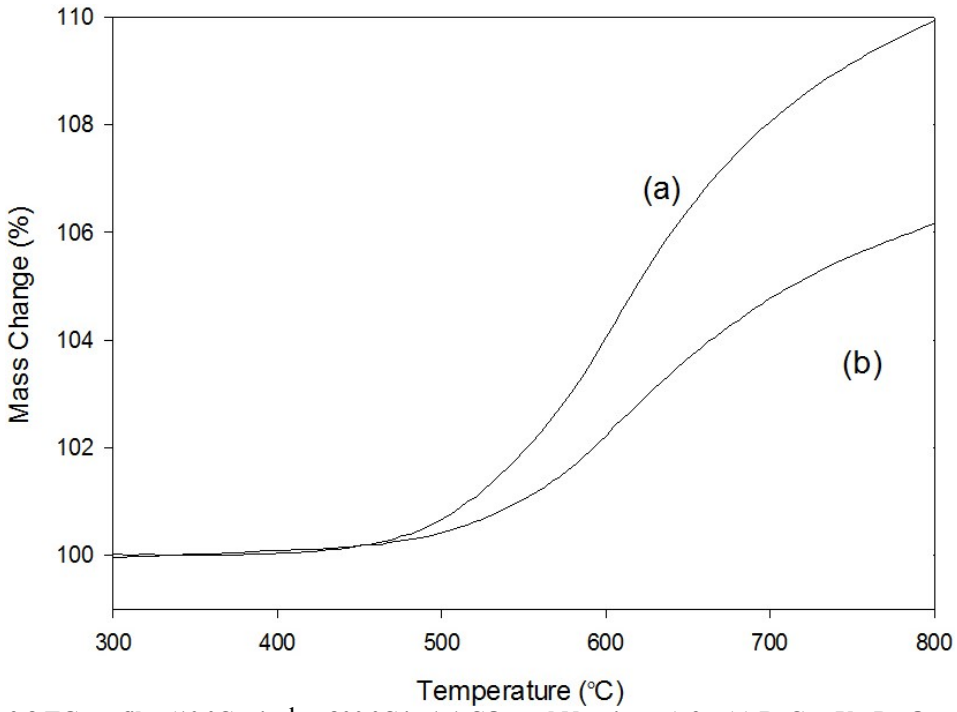

Figure 2.8 TG profiles (10 °C min^{-1} to 800 °C in 1:1 CO_2 and N_2 mixture) for (a) $BaCe_{0.6}Y_{0.3}P_{0.1}O_{2.9}$ and (b) $BaCe_{0.6}Yb_{0.3}P_{0.1}O_{2.9}$

If the relative molecular mass of a sample of the starting material or at a certain point of the temperature programme is known, then the relative molecular mass of the sample at all stages can be calculated.

TGA can also be carried out under different flowing gases, e.g. N_2, Ar, CO_2, O_2 etc., to determine the relative stability of the sample to these gases under heating conditions. The TGA can be coupled with a mass spectrometer or infrared spectrometer to give information about the gases given off during the experiment. This is especially useful during decomposition reactions as in the example below the mass loss due to water can be specifically assigned, Figure 2.9.

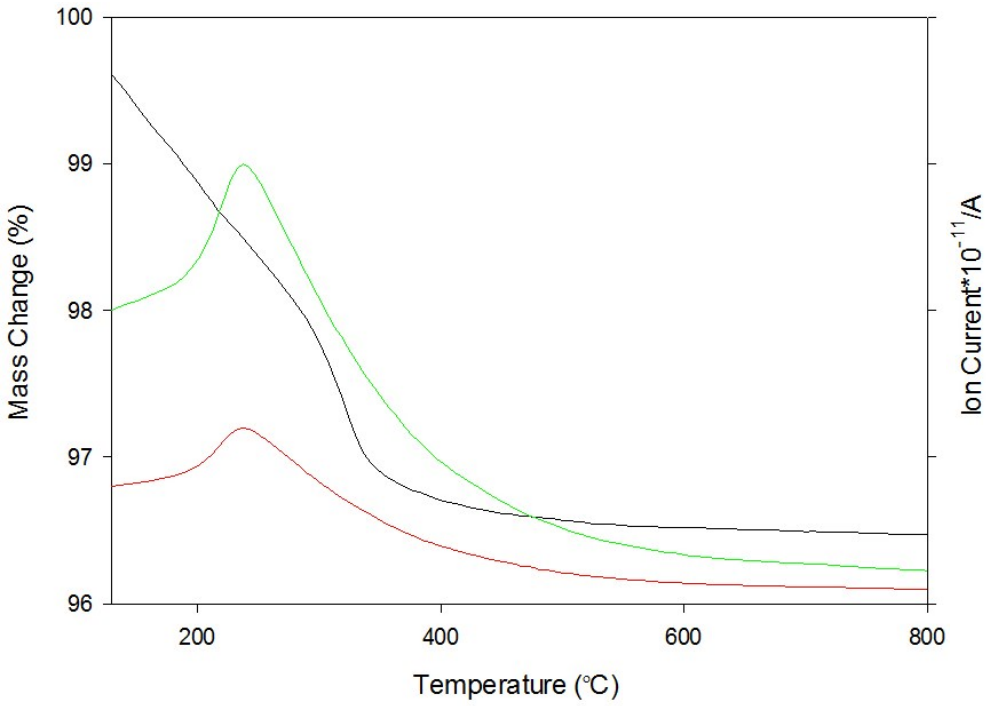

Figure 2.9 TG profiles (10 °C min^{-1} to 800 °C in N_2) for hydrated $BaFeO_{2.5}$ with the green line (m=18) and red line (m=17) showing the mass loss of their respective masses against temperature

Most TGAs now incorporate differential thermal analysis (DTA) so both mass loss and thermal information can be analysed. DTA uses an inert reference which undergoes the same thermal programme simultaneously as the sample, and the difference in temperature is recorded. This allows changes in the sample that are endothermic or exothermic relative to the reference to be observed providing data on transformations that occur, such as phase transitions.

The instrument used in this project was a Netzsch STA 449 F1 Jupiter Thermal Analyser coupled with a Netzsch MS 403C Aëolos Mass Spectrometer, and this was used to probe water incorporation, metal oxidation states and CO_2 stability in this study.

2.5 Electrical 4 Probe Conductivity Measurements [21]

There are two different types of four probe method, the Van de Pauw and the four probe DC method.

Using the Van de Pauw method four platinum wires are attached at 90° angles on the pellet, which can be circular or square, and the resistance is measured twice across the pellet, Figure 2.10.[22, 23]

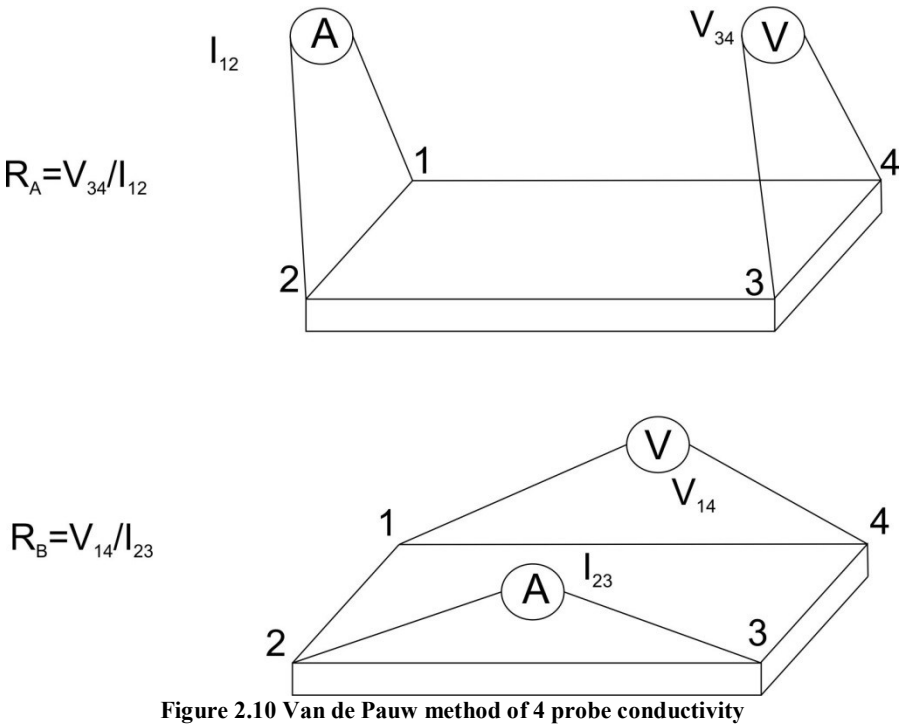

Figure 2.10 Van de Pauw method of 4 probe conductivity

The conductivity is then calculated using the following equation

$$\frac{1}{\sigma} = \frac{\pi t}{\ln 2} * \frac{RA + RB}{2} f(r)$$

Where t is the sample thickness and $f(r)$ only depends on the ratio RA/RB. If RA and RB are equal within 1% $f(r)$ can be neglected.

The other method used also attaches 4 platinum electrodes to the pellet in a different configuration as shown below.

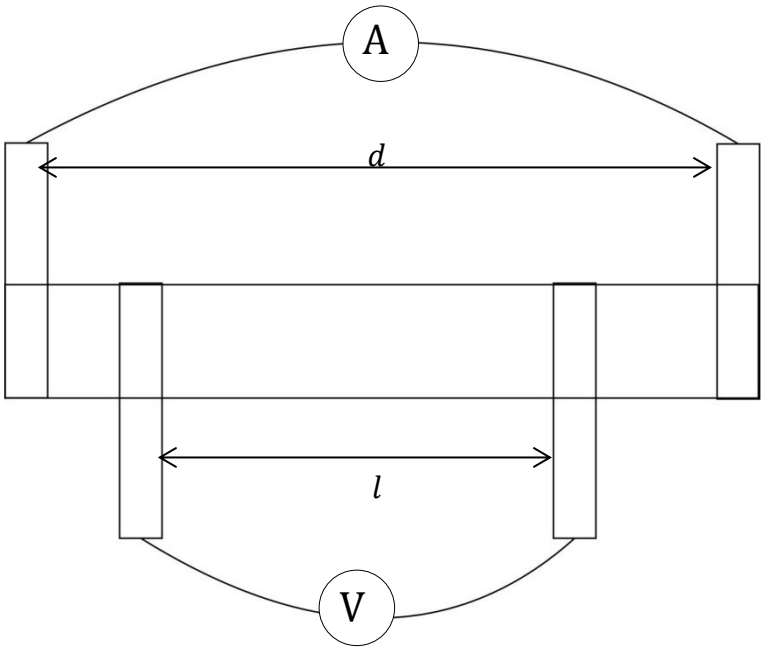

Figure 2.11 4 probe DC conductivity method

The conductivity is then calculated by

$$\sigma = \frac{l}{dt} * \frac{I}{V}$$

Where t is the sample thickness. A current is passed through the two outer electrodes while the voltage is measured using the two inner electrodes, i.e. there are two circuits in parallel.

The four probe method was used in this project as it is simpler and work on similar series had shown that the two methods provided similar results.[21]

2.6 AC Impedance Conductivity Measurements [24-26]

Sluyters first started using AC impedance for electrochemical analysis in 1960 in his studies of aqueous cell polarization phenomena; this was then extended by Bauerle in 1969 to use on a solid sample of yttria stabilised zirconia using platinum electrodes to analyse its polarisation behaviour.[27, 28] Over the following years work was carried out and impedance analysis was used in a number of fields. In this work AC impedance was carried out on sintered pellets with platinum paste coated on both faces and platinum foil pieces attached to these faces. The data collected allowed the conductivities and activation energies of the samples to be obtained.

A sinusoidal voltage can be expressed as

Equation 2.15

$$e = E \sin \omega t$$

Where e is the observed voltage at time t, E the amplitude, ω is 2π times the frequency in Hz. The observed voltage can be thought of as a rotating vector and be as shown below in Figure 2.12.

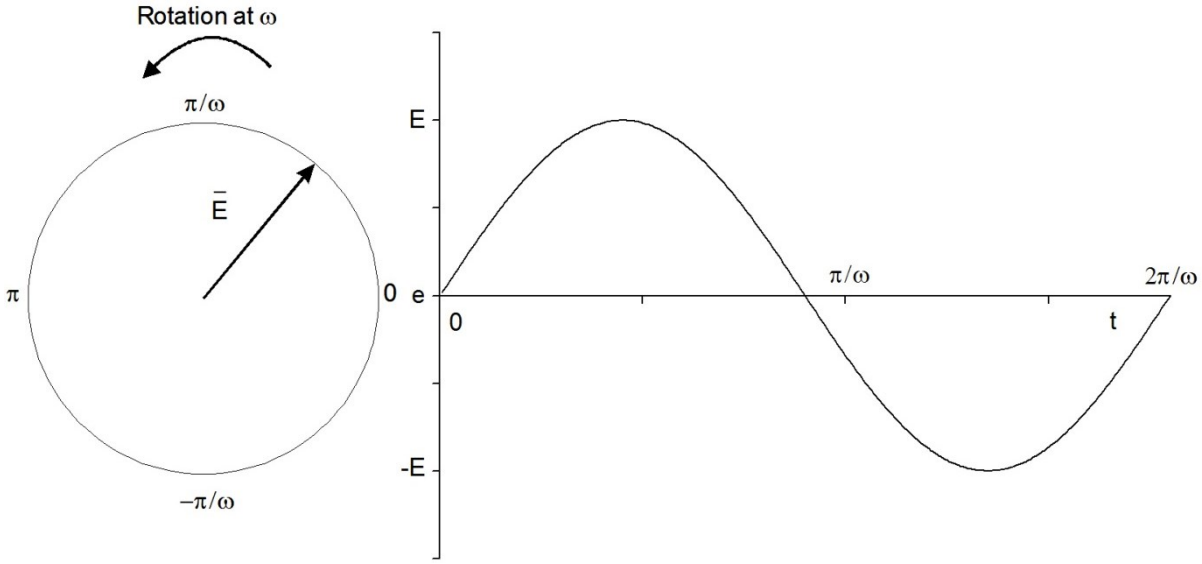

Figure 2.12 Phasor diagram for an AC voltage

Electrochemical impedance involves applying an AC voltage across a sample and measuring the current response. This current response will be sinusoidal if the voltage is sinusoidal and generally they will not be in phase with each other. Therefore a phase angle (φ) indicating this phase shift is used, Equation 2.16.

Equation 2.16

$$i = I\sin(\omega t + \varphi)$$

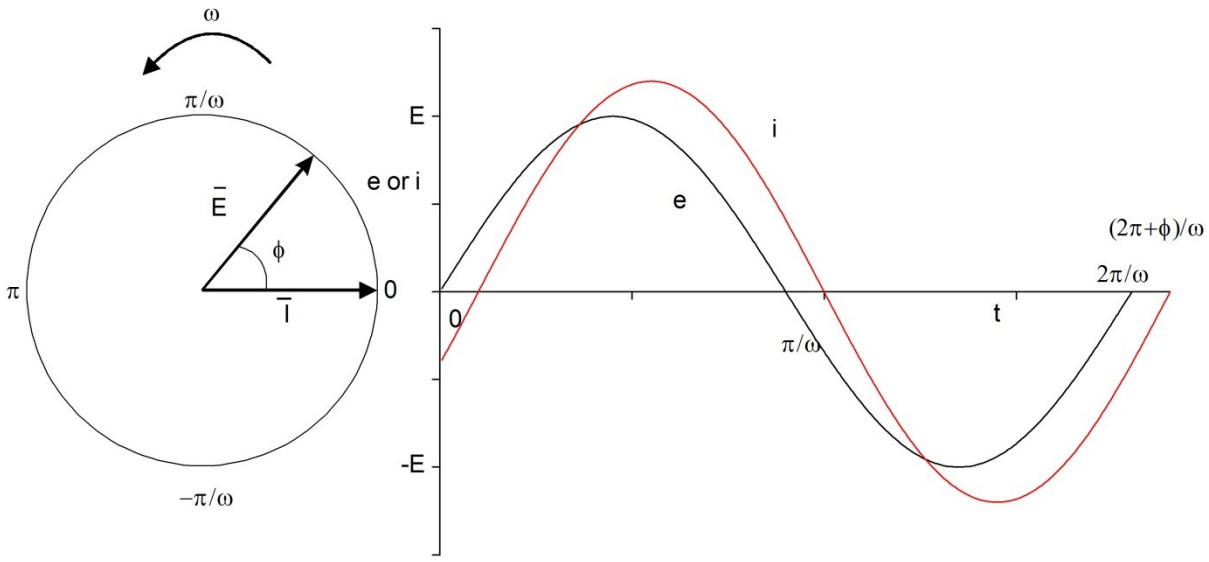

Figure 2.13 Phasor diagram showing the shift in phase between voltage and current at frequency ω

One of the phasors, generally the voltage E, is used as a reference from which φ is measured from. The sign of the phase angle varies depending on whether the current is ahead or lags behind the voltage.

The phase angle between E and I typically remains constant leaving the phasors to be plotted as vectors from a common origin separated by the phase angle φ.

If a sinusoidal voltage, Equation 2.15, is applied across a pure resistor the current can be considered to be Equation 2.17 where R is the resistance and Ohm's law ($V = IR$) is obeyed.

Equation 2.17

$$i = \frac{E}{R}\sin(\omega t)$$

For a pure resistor there is no phase separation between the voltage and the current. Replacing the resistor with a pure capacitor results in the relationship

Equation 2.18

$$i = C\left(\frac{de}{dt}\right)$$

Equation 2.19

$$i = \frac{E}{X_c}\sin(\omega t + \frac{\pi}{2})$$

Where X_c is the capacitive reactance, $X_c = 1/\omega C$. The vector relationship between the current and the voltage is perpendicular for a pure capacitor. Therefore if the current is plotted horizontally and if it leads the voltage, as in Equation 2.19, voltage would be plotted vertically and so complex notation can be used, however both components are still real. This allows the voltage to be described as

Equation 2.20

$$\bar{E} = -jX_c\bar{I}$$

Where $j = \sqrt{-1}$. As $V = IR$ X_c must carry a resistive component. If a capacitance and a resistance are in series and a voltage $\bar{E}$ is applied across them then it must equal the sum of the individual voltage drops giving

Equation 2.21

$$\bar{E} = \overline{E_R} + \overline{E_c}$$

Equation 2.22

$$\bar{E} = \bar{I}(R - jX_c)$$

Equation 2.23

$$\bar{E} = \bar{I}\bar{Z}$$

This gives the vector *Z*, the impedance, and this is comprised of two parts, a real and imaginary part.

Equation 2.24

$$\bar{Z} = \bar{Z}_{Re} - j\bar{Z}_{Im}$$

Here $\bar{Z}_{Re} = R$ and $\bar{Z}_{Im} = X_c = 1/\omega C$. The magnitude of $Z(|Z|)$ is given by

Equation 2.25

$$|\bar{Z}| = \sqrt{R + X_c} = \sqrt{Z_{Re} + Z_{Im}}$$

The phase angle is given by

Equation 2.26

$$\tan\varphi = \frac{\bar{Z}_{Im}}{\bar{Z}_{Re}} = \frac{X_c}{R}$$

The impedance can be considered as a sort of generalised resistance and therefore Equation 2.23 can be considered as a generalised form of Ohm's law. The impedance changes with frequency and this information is plotted on a Nyquist plot displaying Z_{Im} vs Z_{Re} for values of ω. An example of this plot is shown in Figure 2.14.

Circuits using a resistor and capacitor in parallel, RC circuit, are often used to describe the electrochemical behaviour of an ionic conductor. Its characteristic relaxation time can be calculated, τ, which is the product of the resistance and the capacitance.

Equation 2.27

$$\tau = RC = \frac{1}{\omega_{max}}$$

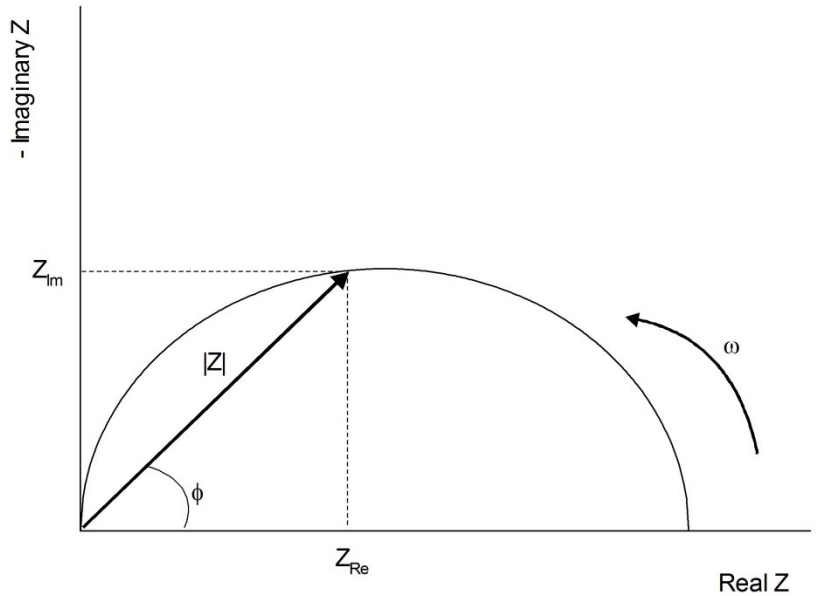

Figure 2.14 A Nyquist plot showing the quantities involved in a complex impedance plot

Both R and C can be calculated from the complex impedance plot. If the time constants are different by several orders of magnitude then the contributions are distinguishable and separate semicircles are seen, although if the time constants are close together the semi circles overlap making it difficult to resolve the individual RC components. The R values can be

calculated from the intercept with x axis on a Nyquist plot, while the C values can be calculated using Equation 2.27. Generally computer software is used to fit a semi-circle to the data giving the values of R and C. In this project the programme Zview v2.9b was used. The determined C values can help assign a component to a physical feature of the sample, Table 2.2.

Table 2.2 Capacitance values and links to physical phenomena [29]

Capacitance (F)	Phenomenon Responsible
10^{-12}	Bulk
10^{-11}	Minor, second phase
10^{-11}-10^{-8}	Grain boundary
10^{-10}-10^{-9}	Bulk ferroelectic
10^{-9}-10^{-7}	Surface layer
10^{-7}-10^{-5}	Sample-electrode interface
10^{-4}	Electrochemical reactions

For the electrolyte materials studied in this project the capacitance values that are of the most interest are those relating to the bulk and grain boundary of the sample; for the potential cathode materials a much higher capacitance was observed for the electrode processes, i.e. the O^{2-} transport through the cathode and cathode-electrolyte interface and competitive reaction at the triple phase boundary (adsorption, transfer of species and surface diffusion). The density of the pellet can partially affect the grain boundary contribution as well as other factors, and the bulk contribution is indicative of the conductivity through the grains, dependent on the material being studied. For the grain boundary high capacitance values generally relate to high density samples, i.e. a small gap between grains, and lower capacitance values can relate to a poorly sintered samples. The density can be improved by using sintering aids, such as NiO, or using higher temperatures.[30, 31] An ideal spectrum should show 2 distinct semicircles that can be assigned to the bulk (higher frequency) and the grain boundary (lower frequency) Figure 2.15.

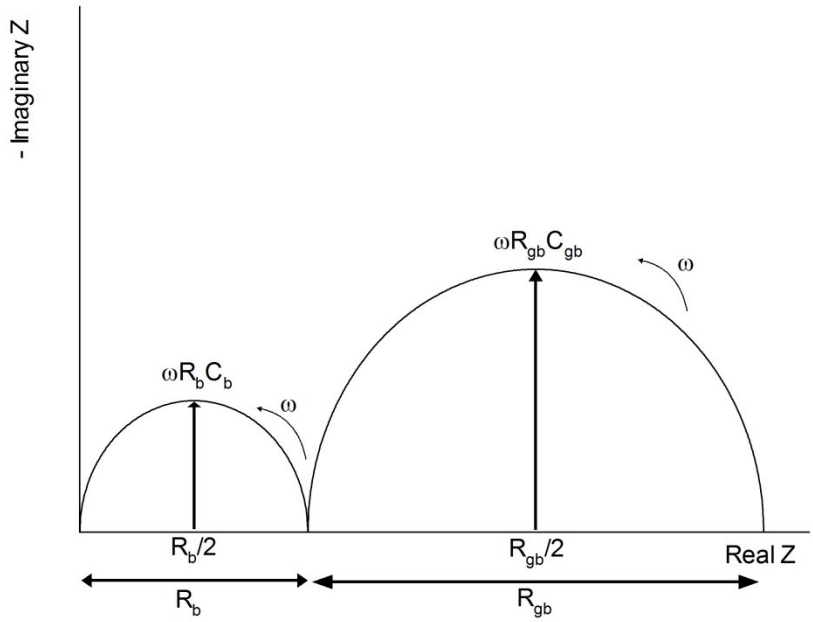

Figure 2.15 Ideal representation of an impedance spectrum for a solid electrolyte material showing bulk and grain boundary components

The conductivity, σ, of the sample is obtained using the following equation; where R is the resistance, l the sample thickness (cm) and A is the sample surface are (cm^2)

Equation 2.28

$$\sigma = \frac{1}{R} \times \frac{l}{A}$$

If impedance spectra are collected over a range of temperatures the activation energy can be calculated as the temperature dependence of the conductivity, and is generally denoted by

Equation 2.29

$$\sigma T = Ae^{\frac{-E_a}{RT}}$$

This is an Arrhenius type function and the activation energy can be calculated from the slope of a plot of Log_{10} (σT / S cm^{-1} K) against T^{-1} /K^{-1}.

The instrument used in the analysis of the electrolyte materials was a Hewlett Packard 4092A impedance analyser; spectra were measured over the range 0.1 to 10^3 kHz with AC signal amplitude of 100 mV. For the electrode materials a PSM 1735 NumertriQ 35MHz phase

sensitive multimeter was used in the range 0.0001 to 10^3 kHz with AC signal amplitude of 100 mV.

2.7 References

1. T. Omata, T. Fuke and S. Otsuka-Yao-Matsuo, *Solid State Ion.*, 2006, **177**, 2447-2451.
2. R. J. D. Tilley, *Crystals and Crystal Structures*, John Wiley & Sons, Chichester, 2007.
3. V. K. Pecharsky and P. Y. Zavalij, *Fundamentals of Powder Diffraction and Structural Characterization of Materials*, Springer, New York, 2009.
4. R. A. Young, *The Rietveld Method*, Oxford University Press, Oxford, 1995.
5. http://cnx.org/content/m16927/latest/, (March 2014)
6. http://en.wikipedia.org/wiki/Miller_index, (March 2014)
7. http://ictwiki.iitk.ernet.in/wiki/index.php/Unit-2:_Introduction_to_X-ray_diffraction#BRAGG_LAW, (March 2014)
8. http://ruby.colorado.edu/~smyth/G30105.html, (March 2014)
9. H. M. Rietveld, *Acta Crystallographica*, 1966, **S 21**, A228.
10. H. M. Rietveld, *Acta Crystallographica*, 1966, **20**, 508.
11. H. M. Rietveld, *Acta Crystallographica*, 1967, **22**, 151.
12. H. M. Rietveld, *Journal of Applied Crystallography*, 1969, **2**, 65.
13. B. H. Toby, *Journal of Applied Crystallography*, 2001, **34**, 210-213.
14. C. J. Howard, *Journal of Applied Crystallography*, 1982, **15**, 615-620.
15. P. Thompson, D. E. Cox and J. B. Hastings, *Journal of Applied Crystallography*, 1987, **20**, 79-83.
16. L. W. Finger, D. E. Cox and A. P. Jephcoat, *Journal of Applied Crystallography*, 1994, **27**, 892-900.
17. S. A. Maher *Raman Spectroscopy for Soft Matter Application*, Wiley and Sons, New York, 2008.
18. C. V. Raman and K. S. Krishnan, *Nature*, 1928, **121**, 501-502.
19. M. Pelletier, *Analytical Applications of Raman Spectroscopy*, Blackwell Publishing, 1999.
20. P. J. Haines, *Principles of Thermal Analysis and Calorimtery*, Royal Society of Chemistry, Cambridge, 2002.
21. C. A. Hancock, *Anion substitution in Perovskite related materials for fuel cell applications*, University of Birmingham, 2013.
22. G. Rietveld, C. V. Koijmans, L. C. A. Henderson, M. J. Hall, S. Hannon, P. Warnecke and B. Schumacher, *IEEE Trans. Instrum. Meas.*, 2003, **52**, 449-453.
23. R. Bissessur, W. White and D. C. Dahn, *Mater. Lett.*, 2006, **60**, 248-251.
24. J. R. Macdonald, *Impedance Spectroscopy*, John Wiley & Sons, New York, 2005.
25. J. F. Shin, University of Birmingham, 2013.
26. J. Percival, *Novel Crystalline Lithium Battery Materials*, University of Surrey, 2009.
27. J. H. Sluyters, *Recl. Trav. Chim. Pays-Bas-J. Roy. Neth. Chem. Soc.*, 1960, **79**, 1092-1100.
28. J. E. Bauerle, *J. Phys. Chem. Solids*, 1969, **30**, 2657.
29. J. T. S. Irvine, D. C. Sinclair and A. R. West, *Advanced Materials*, 1990, **2**, 132.
30. Z. G. Liu, J. H. Ouyang and Y. Zhou, *J. Power Sources*, 2013, **243**, 836-840.
31. Z. G. Liu, J. H. Ouyang, K. N. Sun and Y. Zhou, *J. Power Sources*, 2013, **228**, 1-6.

Chapter 3 Synthesis and Characterisation of Oxyanion Doped $Ba_2Sc_{2-y}Ga_yO_5$

3.1 Introduction

Barium containing perovskites, for example $BaZrO_3$ and $BaCeO_3$, have attracted considerable interest for use as proton conducting electrolyte materials in fuel cells.[1-3] An integral aspect to the optimisation of these samples for use as an electrolyte system is the introduction of oxide ion vacancies which allow the conduction of oxide ions or the incorporation of water to introduce protons. The traditional doping strategy to vary the anion content in perovskite systems is to dope with aliovalent cations of a similar ionic radius, e.g. $Ba(Ce/Zr)O_3$ doped with Y on the Ce/Zr site.[4-6] In this work we have focused on an alternative strategy, doping with a smaller cation P^{5+} and S^{6+}, which are expected to be accommodated as phosphate and sulfate respectively. Prior work from our group has found that the incorporation of oxyanions results in the stabilization of some materials in different packing arrangements to their undoped analogue, or the stabilization of a phase that does not exist without oxyanion doping. For example $Ba_2In_2O_5$ adopts the brownmillerite structure, where the oxide ion vacancies are ordered giving alternating layers of tetrahedral and octahedral In^{3+} hence lowering the ionic conductivity.[7-10] Doping $Ba_2In_2O_5$ with Si^{4+}, P^{5+} and S^{6+} was found to lead to disorder on the oxygen sublattice and an increase in cell symmetry from orthorhombic to cubic. This oxide ion disorder resulted in an increase in the conductivity of the system, with proton conduction observed in wet atmospheres due to water incorporation into the oxide ion vacancies.[11-13] It has been subsequently shown that a cubic perovskite is formed for $Ba_2Sc_2O_5$ upon doping with phosphate which leads to a high conductivity, along with a protonic component, and improved CO_2 stability.[14] Moreover, the parent "$Ba_2Sc_2O_5$" was actually shown to be an oxide carbonate, emphasising the importance of oxyanions to stabilise the structure. In this

thesis the work has been extended to gallium doping into these phosphate doped barium scandate systems with a view reducing the scandium content and hence the cost. Analysis of the conductivity and CO_2 stability of these Ga containing phases has been performed, along with a study into the effect of sulfate substitution for phosphate.

3.2 Experimental Procedure

$Ba_2Sc_{2-x-y}Ga_yP_xO_{5+x}$ and $Ba_2Sc_{2-x-y}Ga_yS_xO_{5+3x/2}$ were synthesised using the standard ceramic synthesis method. Stoichiometric amounts of $BaCO_3$ (≥99%), Sc_2O_3 (99.995%), Ga_2O_3 (99.9%), $NH_4H_2PO_4$ (≥98%) and $(NH_4)_2SO_4$ (99+%) were ground together in an agate pestle and mortar and heated at 1000 °C for 12 hours. A 3% excess of $BaCO_3$ was used to overcome Ba loss at elevated temperatures and eliminate Ba deficient impurities, for example $Ba_3Sc_4O_9$, as has been seen in other studies.[13] The mixtures were then ball-milled (350 rpm for 1 hour, Fritsch Pulverisette 7 Planetary Mill) and reheated to 1100 °C for 12 hours. The resulting powders were then ball-milled (350 rpm for 1 hour, Fritsch Pulverisette 7 Planetary Mill) a second time and pressed into pellets using a 13 mm die set and sintered at 1400 °C for 12 hours. The pellets were covered in sample powder and the crucibles had lids placed on them to lower Ba loss during the sintering process. When powder X-ray diffraction (Bruker D8 diffractometer with Cu-$K\alpha_1$ radiation) confirmed the presence of a single phase, the GSAS suite of programs was used to obtain unit cell parameters from the X-ray diffraction data.[15]

Raman spectroscopy measurements were carried out to confirm the presence of phosphate and sulfate in the compositions. These measurements utilised a Renishaw inVia Raman microscope with excitation using a Cobolt Samba CW532 nm DPSS laser.

The samples were hydrated by heating up to 800 °C under flowing wet N_2 and then slow cooling (0.4 °C min^{-1}). The water contents of these hydrated samples were ascertained using

thermogravimetric analysis (Netzsch STA 449 F1 Jupiter Thermal Analyser), where samples were heated at 10 °C min^{-1} to 1000 °C in N_2 and the resulting mass loss was used to calculate the water content.

For conductivity measurements the sintered pellets were coated on either side with platinum paste, platinum electrodes were attached to both faces, with the sample then heated at 800°C for 1 hour to ensure bonding to the pellet. The conductivities were then measured in a temperature range of 350 °C to 800 °C by AC impedance measurements (Hewlett Packard 4192A impedance analyser) in the range 0.1 to 10^3 kHz with ac signal amplitude of 100 mV. Measurements were carried out in dry and wet N_2 (in which gas was bubbled at room temperature through water) to identify any protonic contribution to the conductivity. Measurements were also made in dry O_2 to determine if there was a p-type contribution to the conductivity. The data showed a single broad semicircle indicative of an overlapping of bulk and grain boundary arcs, and so the conductivity reported represents total conductivity, Figure 3.1.

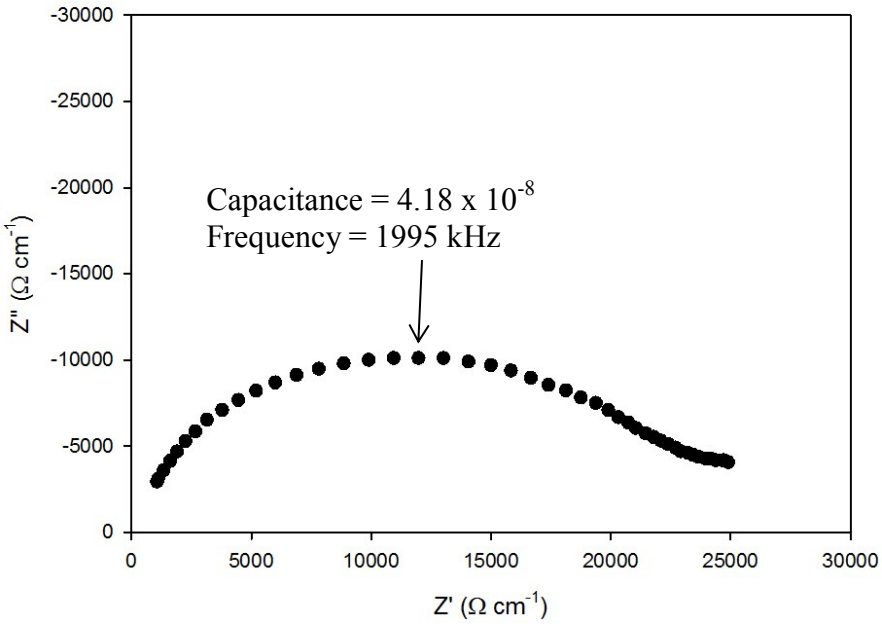

Figure 3.1 Impedance spectra for $Ba_2ScGa_{0.8}P_{0.2}O_{5.2}$ at 500 °C in wet N_2

The CO_2 stabilities of the phases were determined using 2 methods. The first was thermogravimetric analysis with a Netzsch STA 449 F1 Jupiter Thermal Analyser. Samples were heated at 10 °C min^{-1} to 1000°C in a 1:1 CO_2 and N_2 mixture to determine at what temperature CO_2 pick up occurred. The second method involved heating the samples at 600 °C and 800 °C for 12 hours in a tube furnace under flowing CO_2 gas. The samples were then analysed for partial decomposition by X-ray diffraction.

3.3 Results and Discussion

3.3.1 Phosphate Doping

3.3.1.1 Structural Characterisation

3.3.1.1.1 Powder X-ray Diffraction

Prior work had shown that 20% and 25% phosphate doping for scandium could be achieved with the higher conductivity observed for the 20% composition, $Ba_2Sc_{1.6}P_{0.4}O_{5.4}$, and

therefore this level of phosphate doping was used initially for the gallium containing systems.[14] It was found that to stabilise a cubic perovskite with 20% phosphate doping up to 10% gallium doping for scandium was possible, Figure 3.2, as at higher gallium levels impurities, such as Ba_2ScGaO_5 formed, and unreacted Sc_2O_3 was present, Figure 3.3. Phosphate rich impurities were not seen as phosphorus was assumed to have evaporated from the powder during the heating periods or to be present as part of an additional amorphous impurity.

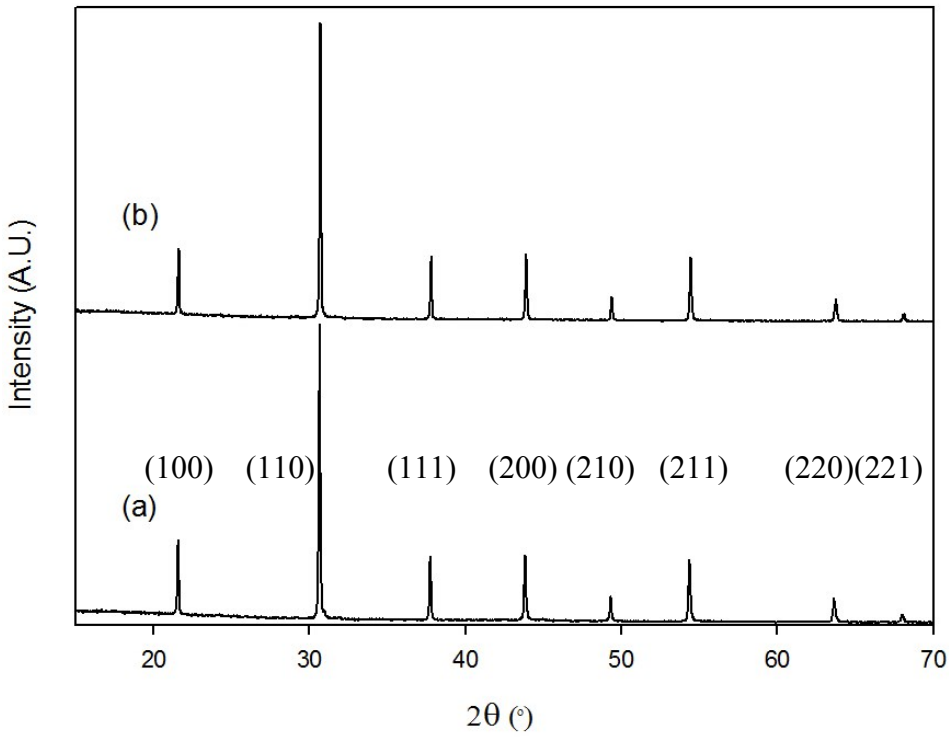

Figure 3.2 Powder X-ray diffraction data of (a) $Ba_2Sc_{1.5}Ga_{0.1}P_{0.4}O_{5.4}$ and (b) $Ba_2Sc_{1.4}Ga_{0.2}P_{0.4}O_{5.4}$

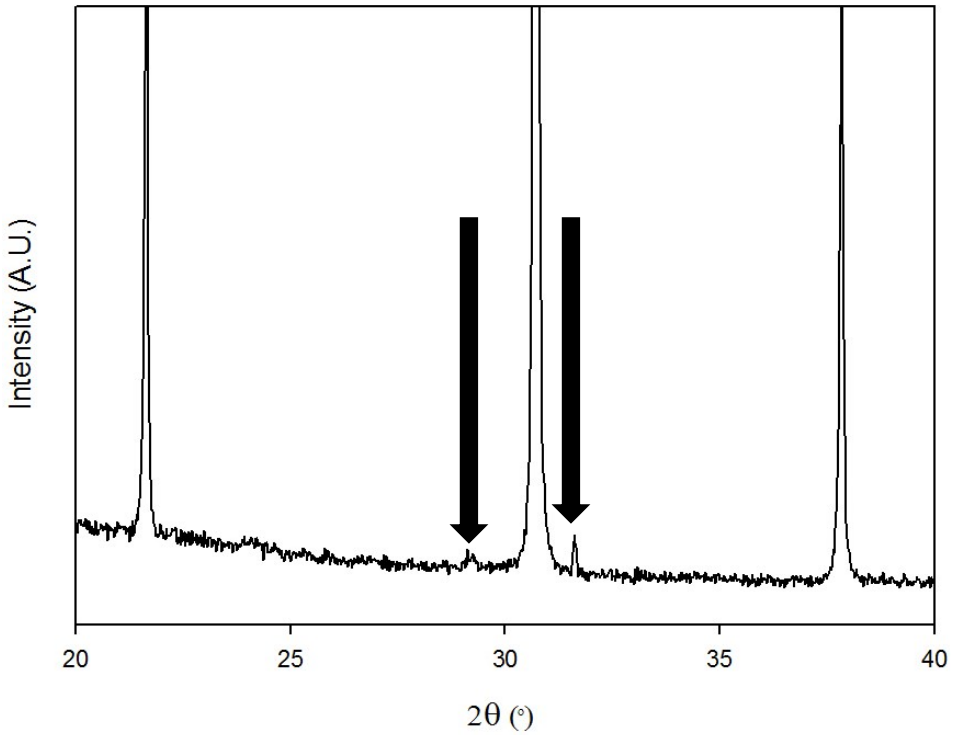

Figure 3.3 Powder X-ray diffraction data of attempted synthesis of "$Ba_2Sc_{1.3}Ga_{0.3}P_{0.4}O_{5.4}$" with impurity peaks indicated

Further work showed that to increase the gallium content phase, lower amounts of phosphate had to be used to stabilise a single phase cubic perovskite, resulting in the single phase compositions $Ba_2Sc_{1.3}Ga_{0.4}P_{0.3}O_{5.3}$, $Ba_2Sc_{1.3}Ga_{0.5}P_{0.2}O_{5.2}$, $Ba_2Sc_{1.2}Ga_{0.6}P_{0.2}O_{5.2}$, $Ba_2Sc_{1.1}Ga_{0.7}P_{0.2}O_{5.2}$ and $Ba_2ScGa_{0.8}P_{0.2}O_{5.2}$, Figure 3.4. The lower phosphate content required on increased gallium doping is most likely due to the gallium as well as the phosphorus preferring tetrahedral coordination and also possibly an increase in the tolerance factor on the replacement of Sc^{3+} (0.745 Å) with Ga^{3+} (0.62 Å) favouring a lower phosphate incorporation to balance.[16, 17]

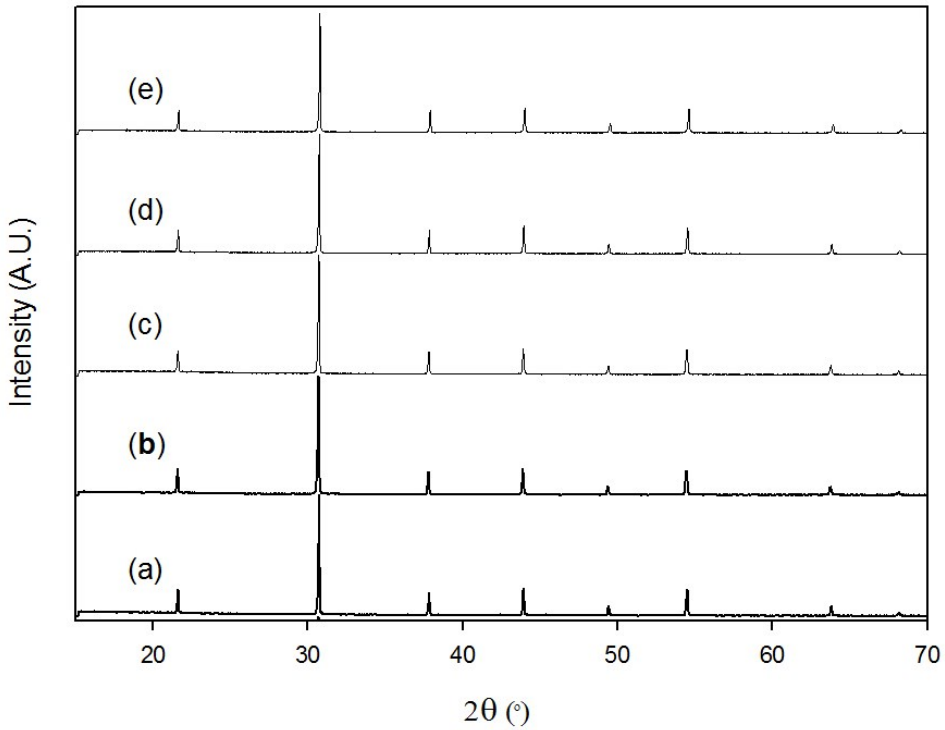

Figure 3.4 Powder X-ray diffraction data of (a) $Ba_2Sc_{1.3}Ga_{0.4}P_{0.3}O_{5.3}$, (b) $Ba_2Sc_{1.3}Ga_{0.5}P_{0.2}O_{5.2}$, (c) $Ba_2Sc_{1.2}Ga_{0.6}P_{0.2}O_{5.2}$, (d) $Ba_2Sc_{1.1}Ga_{0.7}P_{0.2}O_{5.2}$ and (e) $Ba_2ScGa_{0.8}P_{0.2}O_{5.2}$

3.3.1.1.2 Rietveld Refinement

A structural model with a space group *P m -3 m* was refined against the collected powder X-ray diffraction of the pure phases using the GSAS suite of programs.[15] A structure with this space group and composition has mixed occupancy on the B cation site, so the scandium, gallium and phosphorus were all put on the same site with the expected values from the weighed out stoichiometric amounts. The oxygen occupancy was set to the correct values for the oxidation states of the cations and not refined throughout the refinement due to the lack of sensitivity of powder X-ray diffraction techniques to light atoms. The initial refinement gave a good agreement with the collected powder X-ray diffraction data and was deemed complete when convergence was achieved. The following lattice parameters were obtained, Table 3.1 with the visual representation and the complete description of the refined model of $Ba_2Sc_{1.3}Ga_{0.4}P_{0.3}O_{5.3}$ shown in Figure 3.5 and Table 3.2.

Table 3.1 Lattice parameters for phosphate doped $Ba_2Sc_{2-y}Ga_yO_5$

Composition	a (Å)
$Ba_2Sc_{1.5}Ga_{0.1}P_{0.4}O_{5.4}$	4.14269(7)
$Ba_2Sc_{1.4}Ga_{0.2}P_{0.4}O_{5.4}$	4.13745(6)
$Ba_2Sc_{1.3}Ga_{0.4}P_{0.3}O_{5.3}$	4.13439(6)
$Ba_2Sc_{1.3}Ga_{0.5}P_{0.2}O_{5.2}$	4.14012(7)
$Ba_2Sc_{1.2}Ga_{0.6}P_{0.2}O_{5.2}$	4.13524(9)
$Ba_2Sc_{1.1}Ga_{0.7}P_{0.2}O_{5.2}$	4.13203(8)
$Ba_2ScGa_{0.8}P_{0.2}O_{5.2}$	4.1233(1)

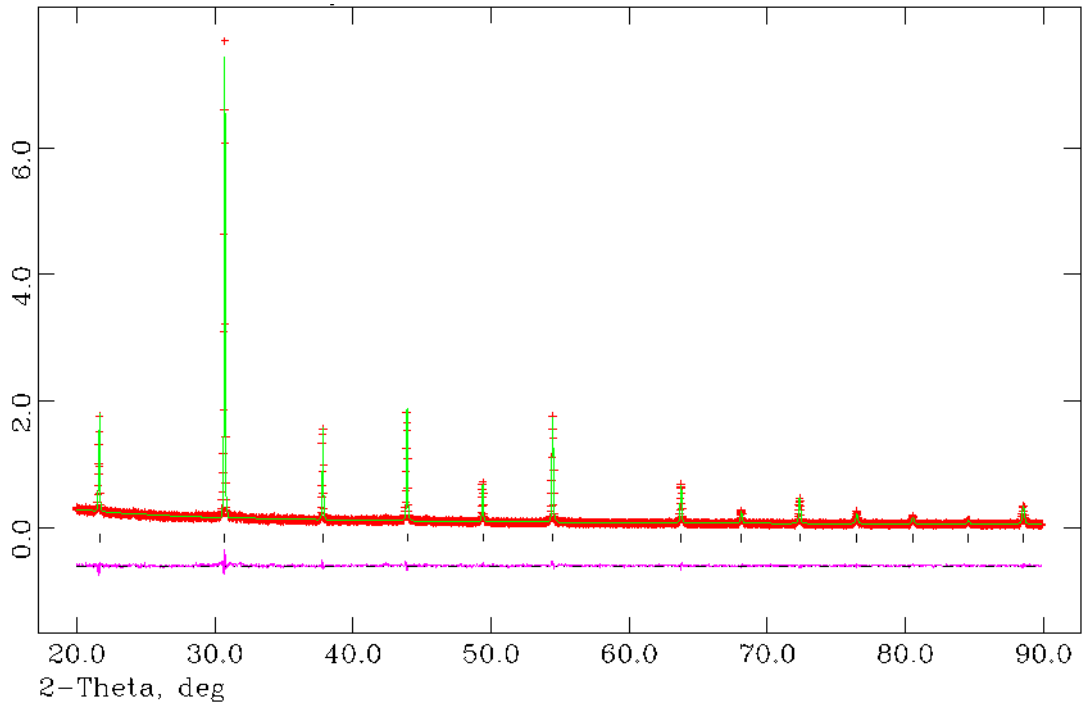

Figure 3.5 Observed, calculated and difference plots for structural refinement of $Ba_2Sc_{1.3}Ga_{0.4}P_{0.3}O_{5.3}$ using X-ray powder diffraction data

Table 3.2 Structural detail for $Ba_2Sc_{1.3}Ga_{0.4}P_{0.3}O_{5.3}$

	Site	x	y	z	Fraction	100 U (Å^2)
Ba	1b	0.5	0.5	0.5	1	3.06(6)
Sc	1a	0	0	0	0.65	4.8(1)
Ga	1a	0	0	0	0.2	4.8(1)
P	1a	0	0	0	0.15	4.8(1)
O	3d	0.5	0	0	0.8833	5.4(3)
Space Group = *P m -3 m*, a = 4.13439(6) Å wR_p = 7.11%, R_p = 6.47%, χ^2 = 1.270						

The refinements showed a decrease in the lattice parameter on increased gallium doping for scandium, in agreement with Ga^{3+}, 0.62 Å, having a smaller ionic radius than Sc^{3+}, 0.745 Å.[17]

The data also showed that substituting gallium for phosphorus led to an increase in the lattice parameter as P^{5+} is a smaller ion than Ga^{3+} regardless of the local coordination of the cations.[17] We were unable to determine the local coordination of the B site cations using powder X-ray diffraction data due to the previously mentioned lack of sensitivity to oxygen, and the complexity associated with multiple cations on this site.

3.3.1.1.3 Raman Spectroscopy

To provide further confirmation for the presence of phosphate in this perovskite system, Raman data were collected on all the samples, all of which showed bands at 415 cm^{-1} and 940 cm^{-1} consistent with the incorporation of phosphate, Figure 3.6.

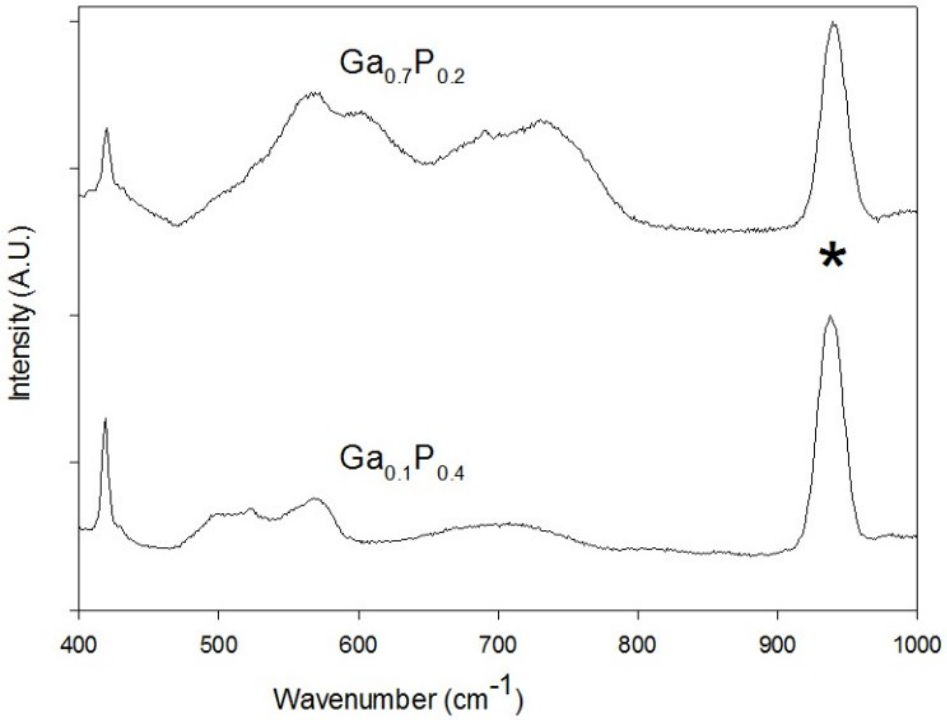

Figure 3.6 Raman spectra of $Ba_2Sc_{1.5}Ga_{0.1}P_{0.4}O_{5.4}$ and $Ba_2Sc_{1.1}Ga_{0.7}P_{0.2}O_{5.2}$ with the main peak showing the presence of phosphate indicated.

The band at 415 cm^{-1} is due to a bending mode of phosphate and the band at 940 cm^{-1} comes from the internal stretching mode.[18] A perfect cubic perovskite should have no bands present as the cubic symmetry results in all the lattice sites having inversion symmetry, thus causing first order Raman scattering to be forbidden, however the presence of phosphate, i.e.

tetrahedral coordination, on the B site also negates perfect cubic symmetry – hence why the peak due to phosphate is much more intense as there is no inversion symmetry for a cation with a tetrahedral coordination. The broad peaks from 450 cm^{-1} to 760 cm^{-1} show that the system is not perfectly cubic and in this respect, Mancini *et al*. showed from total scattering studies that the related phosphate doped $Ba_2In_2O_5$ was locally not cubic, despite XRD indicating an average cubic cell in agreement with the data collected, Cervera *et al*. also found similar bands in cubic $BaScO_2(OH)$.[19, 20]

3.3.1.1.4 Water Incorporation

The water uptake of hydrated samples was then determined by TGA analysis by using the resulting mass loss, with the results shown in Table 3.3.

Table 3.3 Water content for $Ba_2Sc_{2-x-y}Ga_yP_xO_{5+x}$

Composition	% Mass Loss	Amount of water per formula unit
$Ba_2Sc_{1.5}Ga_{0.1}P_{0.4}O_{5.4}$	0.46	0.11(1)
$Ba_2Sc_{1.4}Ga_{0.2}P_{0.4}O_{5.4}$	0.38	0.10(1)
$Ba_2Sc_{1.3}Ga_{0.4}P_{0.3}O_{5.3}$	0.43	0.11(1)
$Ba_2Sc_{1.3}Ga_{0.5}P_{0.2}O_{5.2}$	0.42	0.11(1)
$Ba_2Sc_{1.2}Ga_{0.6}P_{0.2}O_{5.2}$	0.45	0.12(1)
$Ba_2Sc_{1.1}Ga_{0.7}P_{0.2}O_{5.2}$	0.53	0.14(1)
$Ba_2ScGa_{0.8}P_{0.2}O_{5.2}$	0.41	0.11(1)

As the amount of water and oxygen per formula unit does not equal 6 there is a lack of oxygen vacancies available to be filled with water, which can be explained by the fact that the phosphate is incorporated into the structure with a tetrahedral coordination trapping some of the oxygen vacancies around it, as has been noted by Shin *et al*. in related studies on oxyanion doped $Ba_2In_2O_5$.[13, 14] All the compositions have similar water contents despite differing amounts of phosphate, and this supports the assumption that gallium preferentially has a tetrahedral coordination, which would limit water incorporation. However for the higher gallium content samples, statistically not all the gallium can be tetrahedral, indicating there

must be some octahedral gallium at least in these cases. This may therefore indicate that the key issue limiting water incorporation is the unfavourability for the hydration of the vacant sites around gallium.

3.3.1.2 Conductivity Measurements

Conductivity data were collected on $Ba_2Sc_{1.5}Ga_{0.1}P_{0.4}O_{5.4}$, $Ba_2Sc_{1.4}Ga_{0.2}P_{0.4}O_{5.4}$, $Ba_2Sc_{1.3}Ga_{0.4}P_{0.3}O_{5.3}$, $Ba_2Sc_{1.3}Ga_{0.5}P_{0.2}O_{5.2}$ and $Ba_2ScGa_{0.8}P_{0.2}O_{5.2}$ in N_2 atmospheres to eliminate additional p-type contribution, to the conductivity, and under dry and wet conditions to observe potential proton conduction. P-type conductivity may lead to an increase in conductivity due to hole formation caused by an increase in oxygen pressure, an example is shown in Figure 3.7 for Frenkel defects in the oxygen sublattice. For the wet samples water may ingress into the grain boundaries which can affect the grain boundary conductivity.

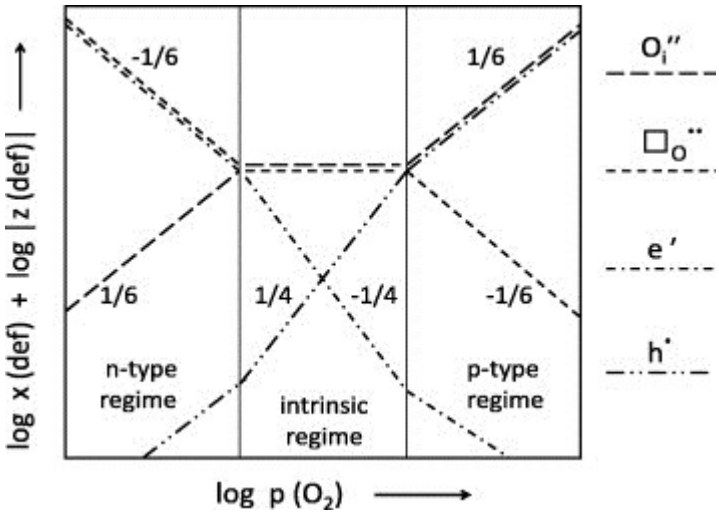

Figure 3.7 Brouwer plot diagram showing how the oxygen pressure affects the number of interstitials and holes in a substance

All compositions for which data were collected exhibited high total conductivities with a significant protonic contribution, Table 3.4, Figure 3.8, Figure 3.9 and Figure 3.10.

Table 3.4 Total conductivity data for $Ba_2Sc_{2-x-y}Ga_yP_xO_{5+x}$

Sample (nominal composition)	Conductivity (S cm^{-1})			
	500 °C		800 °C	
	Dry N_2	Wet N_2	Dry N_2	Wet N_2
$Ba_2Sc_{1.5}Ga_{0.1}P_{0.4}O_{5.4}$	1.13×10^{-3}	1.19×10^{-3}	3.39×10^{-3}	3.38×10^{-3}
$Ba_2Sc_{1.4}Ga_{0.2}P_{0.4}O_{5.4}$	6.06×10^{-4}	7.76×10^{-4}	2.25×10^{-3}	2.26×10^{-3}
$Ba_2Sc_{1.3}Ga_{0.4}P_{0.3}O_{5.3}$	3.53×10^{-4}	6.41×10^{-4}	2.88×10^{-3}	1.51×10^{-3}
$Ba_2Sc_{1.3}Ga_{0.5}P_{0.2}O_{5.2}$	8.31×10^{-4}	1.24×10^{-3}	3.48×10^{-3}	2.04×10^{-3}
$Ba_2ScGa_{0.8}P_{0.2}O_{5.2}$	8.23×10^{-6}	4.28×10^{-5}	5.86×10^{-5}	1.38×10^{-4}

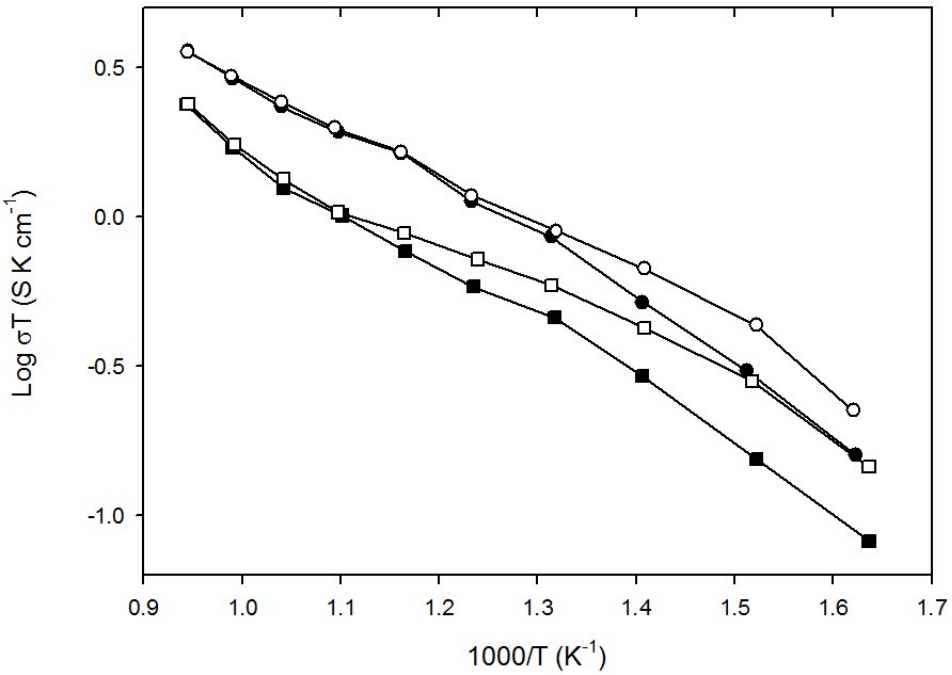

Figure 3.8 Conductivity data for $Ba_2Sc_{1.5}Ga_{0.1}P_{0.4}O_{5.4}$ (circle) and $Ba_2Sc_{1.4}Ga_{0.2}P_{0.4}O_{5.4}$ (square) in dry (filled) and wet (empty) N_2

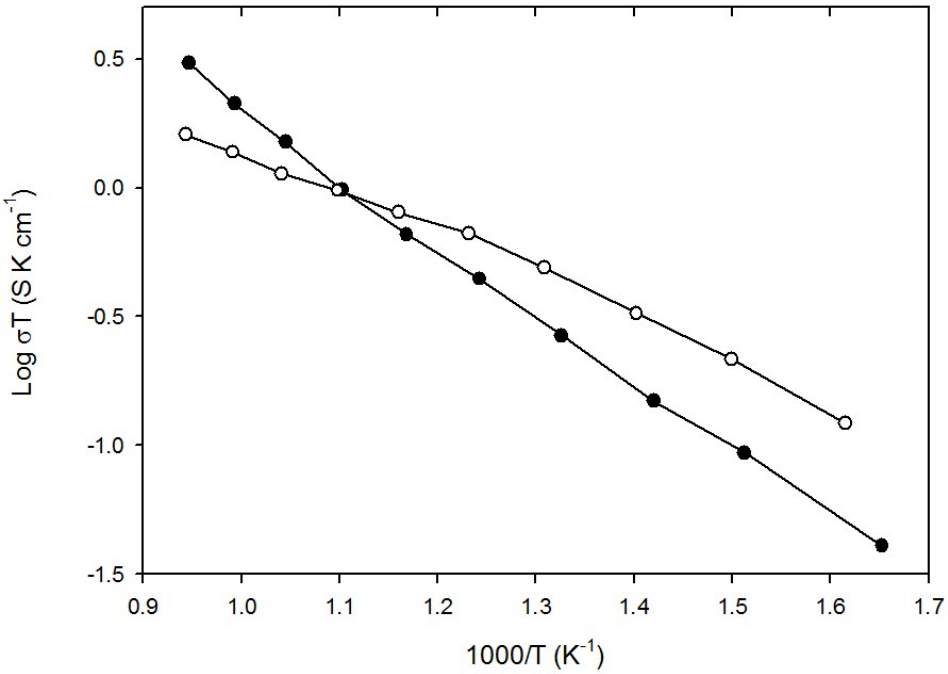

Figure 3.9 Conductivity data for $Ba_2Sc_{1.3}Ga_{0.4}P_{0.3}O_{5.3}$ in dry (filled) and wet (empty) N_2

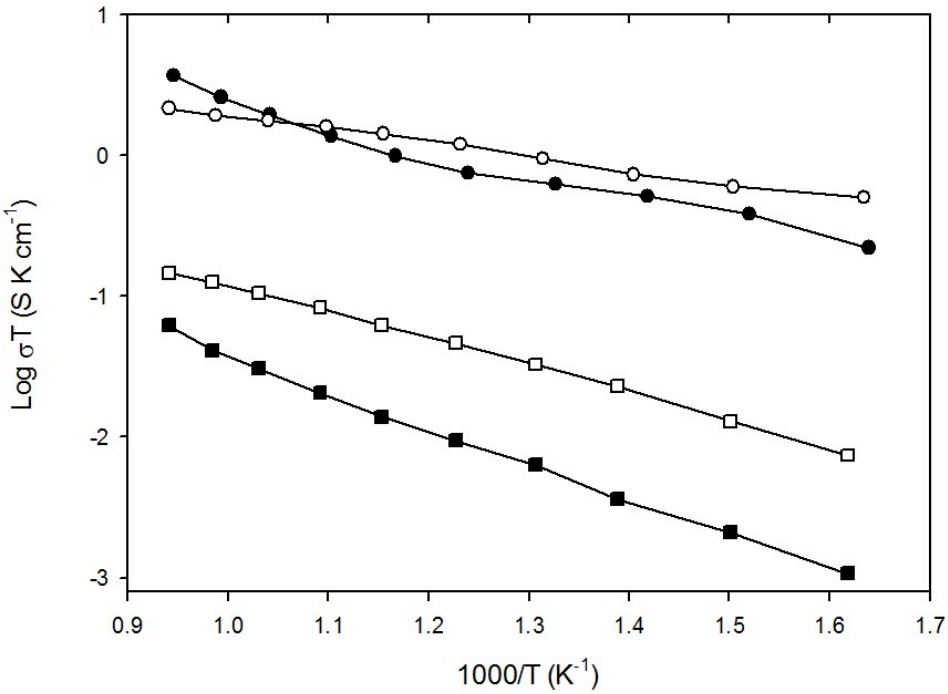

Figure 3.10 Conductivity data for $Ba_2Sc_{1.3}Ga_{0.5}P_{0.2}O_{5.2}$ (circle) and $Ba_2ScGa_{0.8}P_{0.2}O_{5.2}$ (square) in dry (filled) and wet (empty) N_2

The data showed that there was a decrease in the conductivity on increasing the gallium content which may indicate some trapping of the oxide ion vacancy/ proton defects around the gallium, in agreement with the suggestion earlier that gallium preferentially adopts a lower coordination, along with lack of hydration of vacancies surrounding gallium. While there is a

decrease as a result of the gallium content it can be shown that decreasing the phosphate content improves the conductivity, as the amount of free oxide ion vacancies increases (the vacancies are not trapped due to a tetrahedral coordination), eg. $Ba_2Sc_{1.3}Ga_{0.5}P_{0.2}O_{5.2}$ has a higher conductivity than $Ba_2Sc_{1.3}Ga_{0.4}P_{0.3}O_{5.3}$.[12] The activation energies were in the range expected for ceramic protonic conductors, $Ba_2Sc_{1.3}Ga_{0.4}P_{0.3}O_{5.3}$ has an activation energy of 0.27 eV and 0.22 eV for $Ba_2ScGa_{0.8}P_{0.2}O_{5.2}$. For $Ba_2Sc_{1.3}Ga_{0.4}P_{0.3}O_{5.3}$ and $Ba_2Sc_{1.3}Ga_{0.5}P_{0.2}O_{5.2}$ at higher temperatures the conductivity collected in dry N_2 was greater than the conductivity collected in wet N_2 suggesting a potential p-type contribution to the conductivity even under dry N_2. To confirm that this was the case conductivities were collected in dry O_2, Figure 3.11.

The data confirmed the presence of p-type conductivity at elevated temperatures leading to an increase in the conductivity. The origin of the p-type conductivity can be explained by O_2 incorporation into the vacancies according to $V_O^{\bullet\bullet} + O_O^x + \frac{1}{2}O_2 \leftrightarrow 2O_O^{\bullet}$.

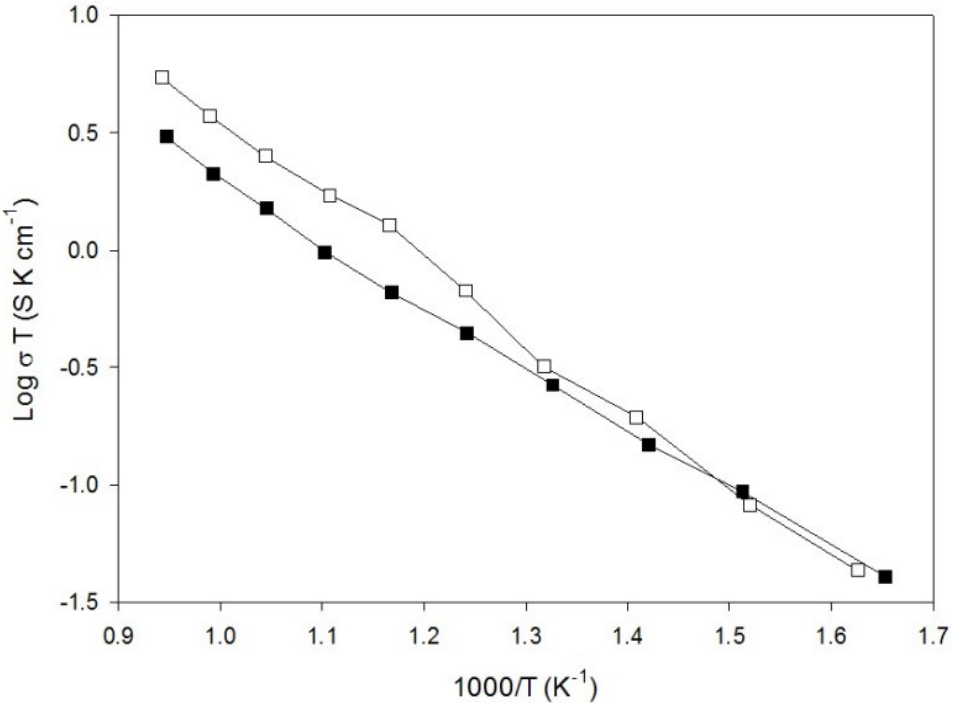

Figure 3.11 Conductivity data for $Ba_2Sc_{1.3}Ga_{0.4}P_{0.3}O_{5.3}$ in dry N_2 (filled square) and dry O_2 (empty square)

3.3.1.3 CO_2 Stability

The stability of the phases to CO_2 atmospheres was tested across the operating temperature range for solid oxide fuels cells using two experiments. The first experiment involved heating the samples to 1000 °C at 10 °C min^{-1} under flowing 1:1 CO_2 and N_2 mixture and observing the resulting mass gain. The results are summarised in Table 3.5.

Table 3.5 Temperature for uptake of CO_2 for $Ba_2Sc_{2-x-y}Ga_yP_xO_{5+x}$ from TGA studies up to 1000 °C

Composition	Temperature of Mass Gain
$Ba_2Sc_{1.5}Ga_{0.1}P_{0.4}O_{5.4}$	750 °C
$Ba_2Sc_{1.4}Ga_{0.2}P_{0.4}O_{5.4}$	800 °C
$Ba_2Sc_{1.3}Ga_{0.4}P_{0.3}O_{5.3}$	825 °C
$Ba_2Sc_{1.3}Ga_{0.5}P_{0.2}O_{5.2}$	850 °C
$Ba_2Sc_{1.2}Ga_{0.6}P_{0.2}O_{5.2}$	No mass gain
$Ba_2Sc_{1.1}Ga_{0.7}P_{0.2}O_{5.2}$	No mass gain
$Ba_2ScGa_{0.8}P_{0.2}O_{5.2}$	No mass gain

The data collected shows $Ba_2Sc_{2-x-y}Ga_yP_xO_{5+x}$ starts to gain mass in a CO_2 atmosphere at temperatures at, or in excess, of 750 °C which is superior to $BaCe_{0.9}Y_{0.1}O_{2.95}$ (this phase gains mass at 500 °C).[14] Samples with a gallium content greater than 0.5 showed no mass gain at any of the temperatures measured. These results therefore indicate that gallium improves the stability of the phase to CO_2 containing atmospheres. The phosphate content seemed to have little effect on the temperature of mass gain, although it is hard to be completely certain of this, as the different phosphate compositions have different gallium contents.

The second experiment involved placing the samples in a furnace for 12 hours at 600 °C and 800 °C under flowing CO_2 and then using powder X-ray diffraction to analyse if partial decomposition had occurred. The powder X-ray diffraction data for the lowest and highest gallium content compositions after heating at 600 °C are shown in Figure 3.12.

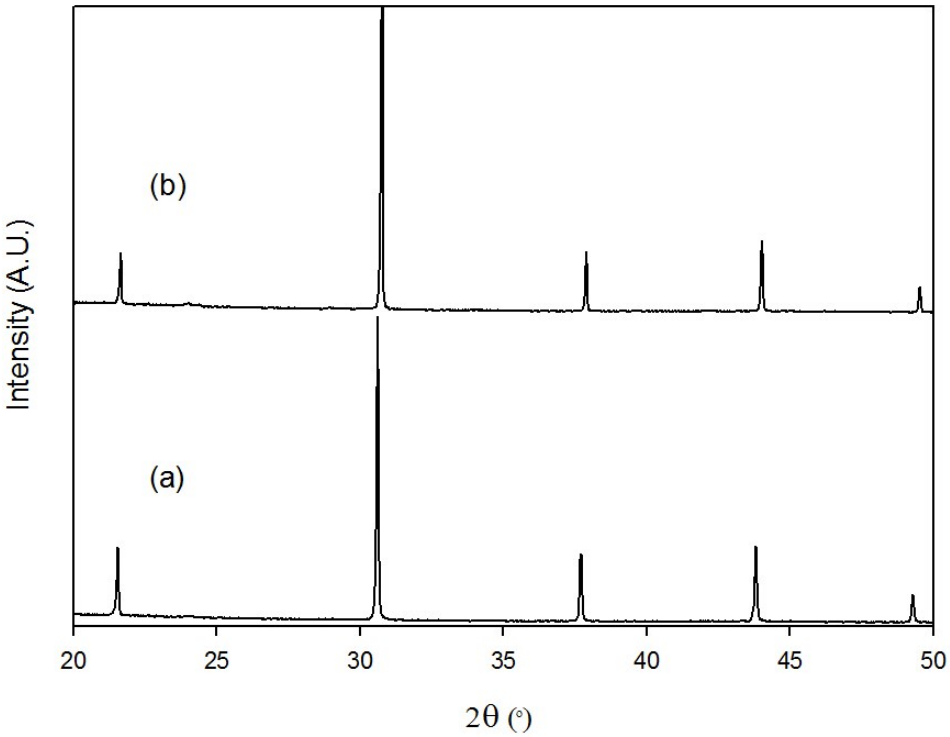

Figure 3.12 Powder X-ray diffraction data of (a) $Ba_2Sc_{1.5}Ga_{0.1}P_{0.4}O_{5.1}$ and (b) $Ba_2ScGa_{0.8}P_{0.2}O_{5.2}$ after heating for 12 hours at 600 °C under flowing CO_2

The data collected showed that at these conditions there was no decomposition occurring for all samples highlighting the stability of these samples to CO_2. Data were then collected at 800 °C with the same two compositions shown in Figure 3.13.

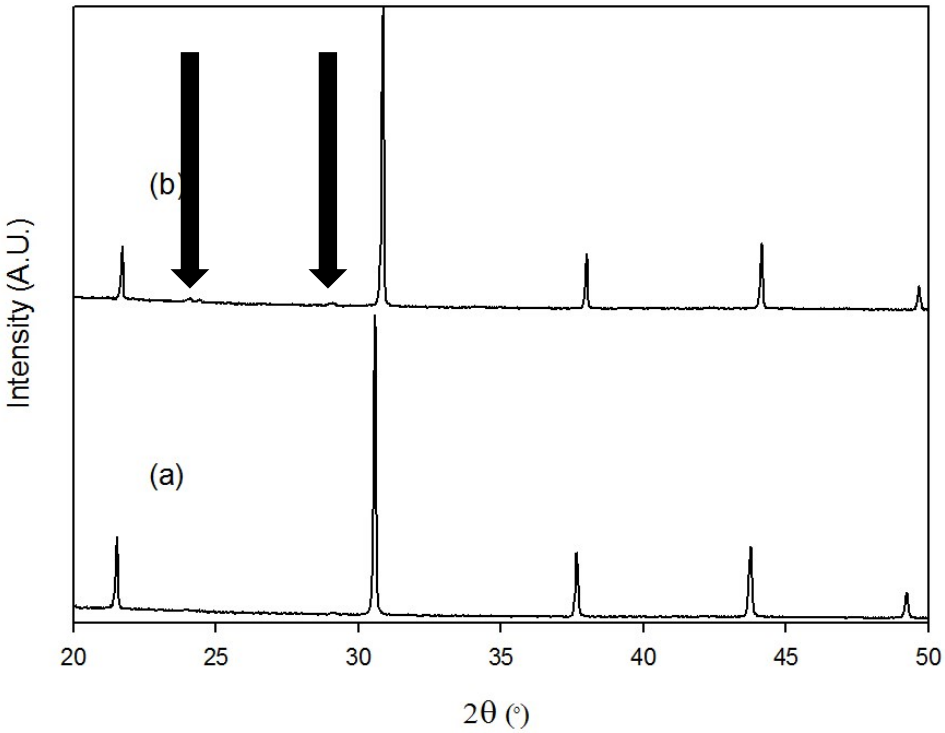

Figure 3.13 Powder X-ray diffraction data of (a) $Ba_2Sc_{1.5}Ga_{0.1}P_{0.4}O_{5.1}$ and (b) $Ba_2ScGa_{0.8}P_{0.2}O_{5.2}$ after heating for 12 hours at 800 °C under flowing CO_2 with peaks for $BaCO_3$ indicated

After heating at 800 °C for 12 hours small peaks of $BaCO_3$, at 2θ = 24° and 29° respectively, started to appear for all compositions showing that even the higher gallium containing samples do show some reactivity to CO_2 under these extreme conditions, although it is possible that these weak $BaCO_3$ impurities may be from some excess barium on the surface reacting with CO_2 due to the small amount of excess barium used in the synthesis. In addition, it should be noted that these conditions are very extreme compared to the atmospheres found in operating SOFCs and so the results do indicate that $Ba_2Sc_{2-x-y}Ga_yP_xO_{5+x}$ phases are relatively stable to CO_2 and superior to $BaCe_{0.9}Y_{0.1}O_{2.95}$ in this respect.

3.3.2 Sulfate Doping

3.3.2.1 Structural Characterisation

3.3.2.1.1 Powder X-ray Diffraction

As for the phosphate doped samples, initial work focused on 20% substitution of sulfate. At this dopant level we were unable to form a pure cubic perovskite for any gallium content, see Figure 3.14 for examples.

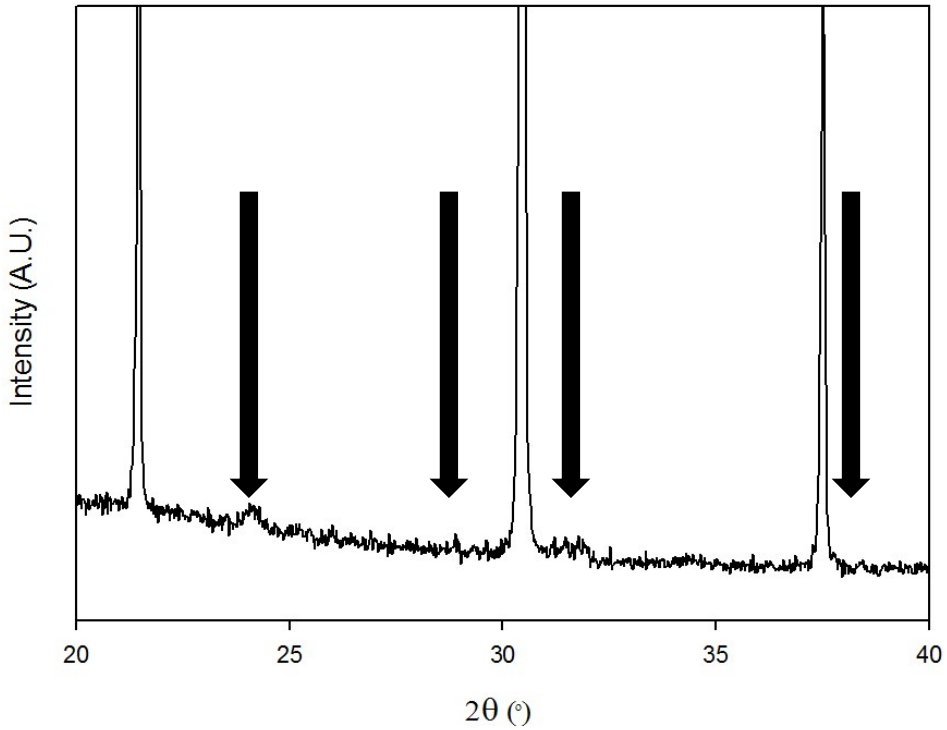

Figure 3.14 Powder X-ray diffraction data of attempted synthesis of "$Ba_2Sc_{1.4}Ga_{0.2}S_{0.4}O_{5.6}$" with impurity peaks from $Sc_2(SO_4)_3$ indicated

The impurity phase was identified as $Sc_2(SO_4)_3$ indicating that sulfate could not be doped into this structure at the 20% level on gallium doping. There are two possible reasons why sulfate cannot be doped into the structure at the same level as phosphate; namely the different ionic size, P (0.17 Å) and S (0.12 Å), and the different oxygen contents required.[17] The higher oxygen content, 5.6 per formula unit compared to 5.4, is the most likely reason for the non-purity of 20% sulfate doped barium scandate. This increased oxygen content makes it harder for gallium to adopt a lower coordination, compared with the phosphate analogue.

Lowering the sulfate doping level to 15% and 10% was found to lead to pure cubic perovskite phases for similar gallium contents to the phosphate doped analogues. The single phase compositions were $Ba_2Sc_{1.4}Ga_{0.3}S_{0.3}O_{5.45}$, $Ba_2Sc_{1.3}Ga_{0.4}S_{0.3}O_{5.45}$, $Ba_2Sc_{1.2}Ga_{0.6}S_{0.2}O_{5.3}$, $Ba_2Sc_{1.1}Ga_{0.7}S_{0.2}O_{5.3}$ and $Ba_2ScGa_{0.8}S_{0.2}O_{5.3}$, Figure 3.15.

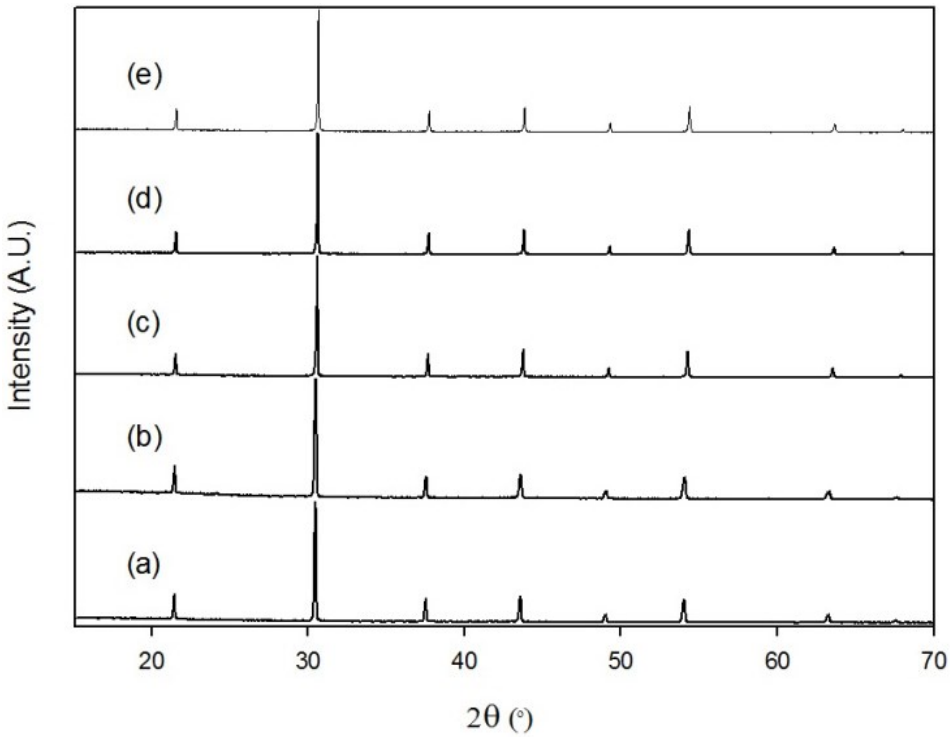

Figure 3.15 Powder X-ray diffraction data of (a) $Ba_2Sc_{1.4}Ga_{0.3}S_{0.3}O_{5.45}$, (b) $Ba_2Sc_{1.3}Ga_{0.4}S_{0.3}O_{5.45}$, (c) $Ba_2Sc_{1.2}Ga_{0.6}S_{0.2}O_{5.3}$, (d) $Ba_2Sc_{1.1}Ga_{0.7}S_{0.2}O_{5.3}$ and (e) $Ba_2ScGa_{0.8}S_{0.2}O_{5.3}$

As in the case of the phosphate doped compositions, a higher gallium content is required to stabilise the cubic perovskite phase for lower sulfate contents, which is most likely due to the preference of gallium as well as sulfate to have a tetrahedral coordination with respect to the oxygen.[16, 17]

3.3.2.1.2 Rietveld Refinement

The same structural model was examined using the collected X-ray diffraction data as for the phosphate doped compositions; the structure with space group *P m -3 m* was refined using the GSAS suite of programs.[15] The B site cations, scandium, gallium and sulfur, have a mixed occupancy so the expected stoichiometric amounts were used. Using the oxidation states of

the cations the oxygen content was set to the expected value, and this parameter was then not refined due to the lack of sensitivity of powder X-ray diffraction to oxygen. The initial refinement gave a good agreement with the collected powder X-ray diffraction data and was deemed complete when convergence was achieved. The following lattice parameters were obtained, Table 3.6, with the visual representation and the complete description of the refined model of $Ba_2ScGa_{0.8}S_{0.2}O_{5.3}$ shown in Figure 3.16 and Table 3.7.

Table 3.6 Lattice parameters and goodness of fit parameters for sulfate doped $Ba_2Sc_{2-y}Ga_yO_5$

Composition	a (Å)
$Ba_2Sc_{1.4}Ga_{0.3}S_{0.3}O_{5.45}$	4.16770(9)
$Ba_2Sc_{1.3}Ga_{0.4}S_{0.3}O_{5.45}$	4.1656(1)
$Ba_2Sc_{1.2}Ga_{0.6}S_{0.2}O_{5.3}$	4.14827(8)
$Ba_2Sc_{1.1}Ga_{0.7}S_{0.2}O_{5.3}$	4.14056(7)
$Ba_2ScGa_{0.8}S_{0.2}O_{5.3}$	4.13952(6)

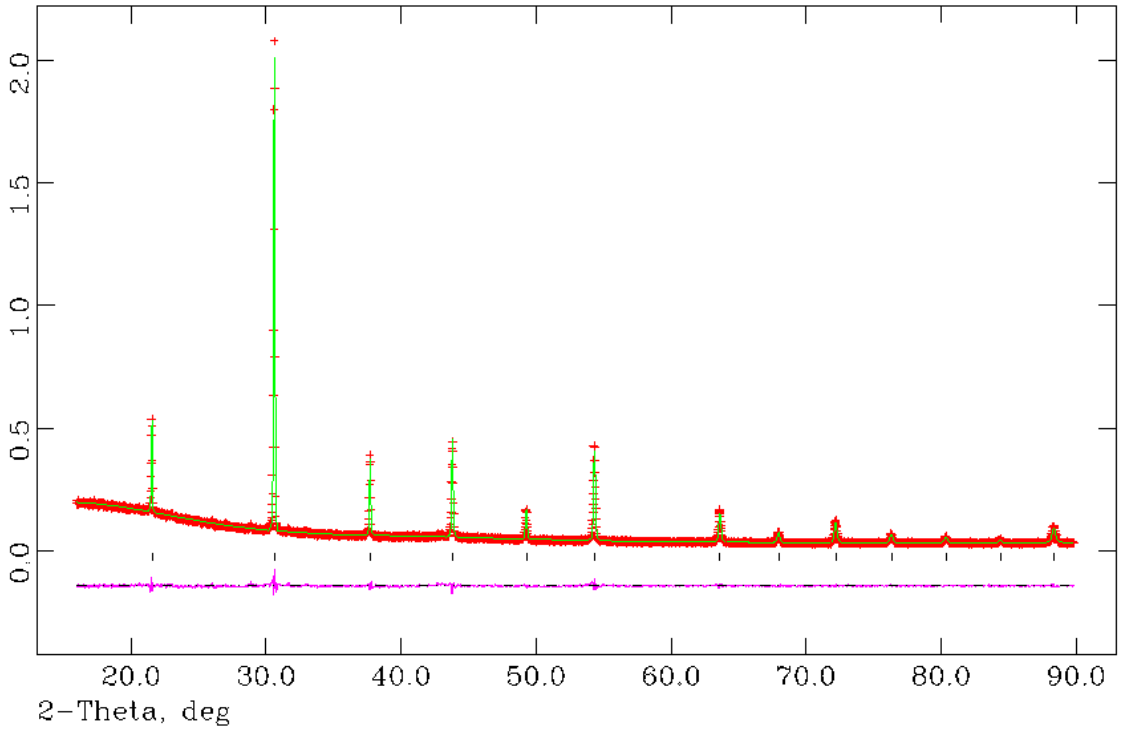

Figure 3.16 Observed, calculated and difference plots for structural refinement of $Ba_2ScGa_{0.8}S_{0.2}O_{5.3}$ using X-ray powder diffraction data

Table 3.7 Structural detail for $Ba_2ScGa_{0.8}S_{0.2}O_{5.3}$

	Site	x	y	z	Fraction	100 U ($Å^2$)
Ba	1b	0.5	0.5	0.5	1	2.79(4)
Sc	1a	0	0	0	0.5	5.5(1)
Ga	1a	0	0	0	0.4	5.5(1)
S	1a	0	0	0	0.1	5.5(1)
O	3d	0.5	0	0	0.8667	6.3(2)
Space Group = *P m -3 m*, a = 4.13952(6) Å wR_p = 4.90%, R_p = 3.65%, χ^2 = 1.728						

The refinements showed that, as for of the phosphate doped samples, increasing the gallium content decreased the lattice parameter, as Ga^{3+} (0.62 Å) is smaller than Sc^{3+} (0.745 Å).[17] On increasing the sulfate content the lattice parameter decreases, opposite to the phosphate compositions. At first glance this is unexpected as S^{6+} has a smaller ionic radius than both Ga^{3+} and Sc^{3+}, however the decrease in cell parameters may be related to the higher oxidation state of sulfur leading to a larger decrease in the oxygen content with decreasing sulfate content. The results may also indicate some loss of sulfate and hence a lower sulfate content than expected. The local coordination of the gallium and scandium was unable to be determined due to previously mentioned lack of sensitivity of X-rays to oxygen, and the presence of multiple cations on the B site.

3.3.2.1.3 Raman Spectroscopy

To provide confirmation that sulfate has been incorporated into the structure Raman data were collected, Figure 3.17.

All the data contained peaks at 450 cm^{-1} (symmetric bend), 610 cm^{-1} (asymmetric bend) and 990 cm^{-1} (symmetric stretch) characteristic of the presence of sulfate.[21] There are also additional bands from 450 cm^{-1} to 760 cm^{-1}, as seen in section 3.3.1.1.3, associated with the scandium/gallium oxygen bonds.[19, 20]

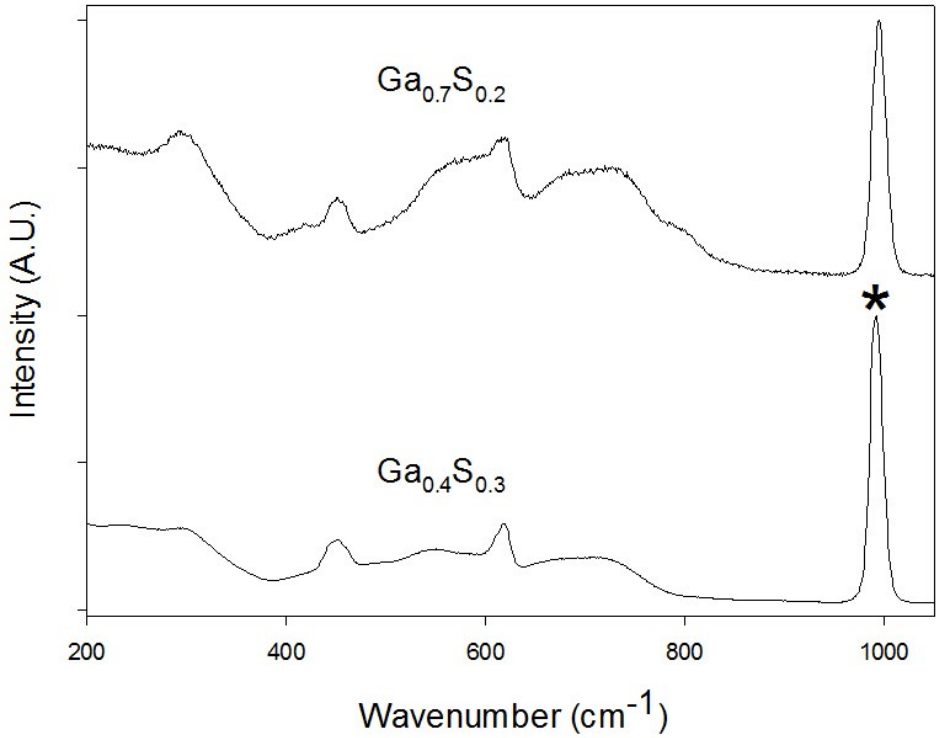

Figure 3.17 Raman spectra of $Ba_2Sc_{1.3}Ga_{0.4}S_{0.3}O_{5.45}$ and $Ba_2Sc_{1.1}Ga_{0.7}S_{0.2}O_{5.3}$ with the main peak showing the presence of sulfate indicated.

3.3.2.1.4 Water Incorporation

The mass losses from hydrated samples were determined by TGA and used to calculate the amount of water per formula unit, Table 3.8.

Table 3.8 Water content for $Ba_2Sc_{2-x-y}Ga_yS_xO_{5+3x/2}$

Composition	% Mass Loss	Amount of water per formula unit
$Ba_2Sc_{1.4}Ga_{0.3}S_{0.3}O_{5.45}$	0.26	0.07(1)
$Ba_2Sc_{1.3}Ga_{0.4}S_{0.3}O_{5.45}$	0.31	0.08(1)
$Ba_2Sc_{1.2}Ga_{0.6}S_{0.2}O_{5.3}$	0.30	0.08(1)
$Ba_2Sc_{1.1}Ga_{0.7}S_{0.2}O_{5.3}$	0.31	0.08 (1)
$Ba_2ScGa_{0.8}S_{0.2}O_{5.3}$	0.22	0.06(1)

As with the phosphate doped samples, not all the oxygen vacancies could be filled which can partially be explained by the fact that sulfate is incorporated into structure with a tetrahedral coordination as has been noted by Shin *et al*. such that the oxide ion vacancies around the sulfate group cannot be filled.[13] In addition, all the samples have a similar amount of water per formula unit despite different sulfate compositions suggesting that gallium also

preferentially adopts a lower coordination than octahedral coordination as well as a resistance to incorporate water around it. All the sulfate containing compositions have a lower amount of water per formula unit than the phosphate containing compositions which may be related to the fact that sulfate has a higher oxidation state than phosphate and so the oxygen content is higher and therefore there are less oxygen vacancies as has been reported by Shin *et al* for sulfate doped $Ba_2In_2O_5$.[13]

3.3.2.2 Conductivity Measurements

Conductivities were collected in N_2 atmospheres to remove any p-type contribution to the conductivity, and in dry and wet atmospheres to observe the protonic contribution to the conductivity. Data were collected for $Ba_2Sc_{1.4}Ga_{0.3}S_{0.3}O_{5.45}$, $Ba_2Sc_{1.3}Ga_{0.4}S_{0.3}O_{5.45}$, $Ba_2Sc_{1.2}Ga_{0.6}S_{0.2}O_{5.3}$ and $Ba_2ScGa_{0.8}S_{0.2}O_{5.3}$. All the compositions showed high total conductivities as for the phosphate doped samples, Table 3.9, Figure 3.18 and Figure 3.19.

Table 3.9 Total conductivity data for $Ba_2Sc_{2-x-y}Ga_yS_xO_{5+3x/2}$

Sample (nominal composition)	Conductivity (S cm^{-1})			
	500 °C		800 °C	
	Dry N_2	Wet N_2	Dry N_2	Wet N_2
$Ba_2Sc_{1.4}Ga_{0.3}S_{0.3}O_{5.45}$	3.79×10^{-4}	8.66×10^{-4}	1.57×10^{-3}	2.98×10^{-3}
$Ba_2Sc_{1.3}Ga_{0.4}S_{0.3}O_{5.45}$	2.21×10^{-4}	5.21×10^{-4}	1.03×10^{-3}	2.04×10^{-3}
$Ba_2Sc_{1.3}Ga_{0.6}S_{0.2}O_{5.3}$	1.51×10^{-4}	5.99×10^{-4}	4.34×10^{-4}	1.06×10^{-3}
$Ba_2ScGa_{0.8}S_{0.2}O_{5.3}$	4.64×10^{-5}	1.96×10^{-4}	1.89×10^{-4}	5.21×10^{-4}

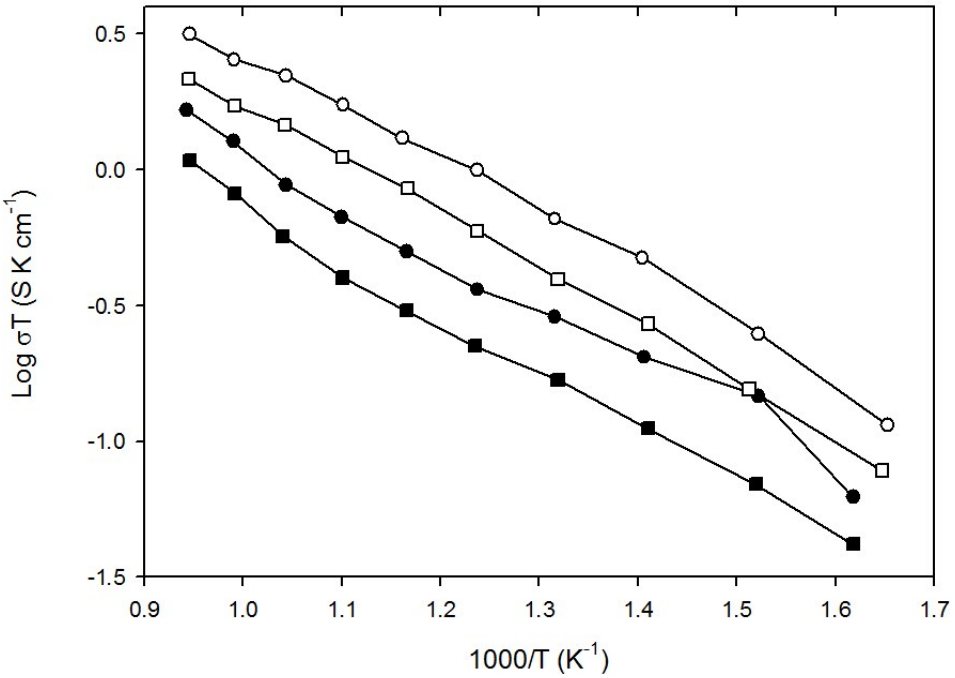

Figure 3.18 Conductivity data for $Ba_2Sc_{1.4}Ga_{0.3}S_{0.3}O_{5.45}$ (circle) and $Ba_2Sc_{1.3}Ga_{0.4}S_{0.4}O_{5.45}$ (square) in dry (filled) and wet (empty) N_2.

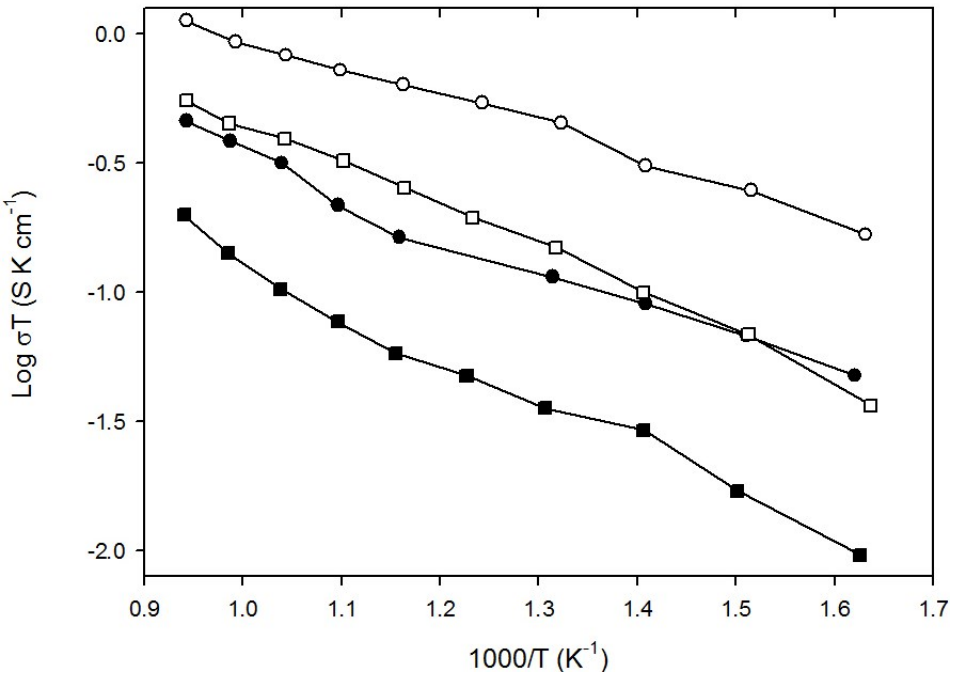

Figure 3.19 Conductivity data for $Ba_2Sc_{1.2}Ga_{0.6}S_{0.2}O_{5.3}$ (circle) and $Ba_2ScGa_{0.8}S_{0.2}O_{5.3}$ (square) in dry (filled) and wet (empty) N_2.

As for the phosphate doped compositions there was a decrease in conductivity upon increasing gallium content. As noted earlier, this may indicate that there is some defect trapping of the oxygen vacancies around the gallium, agreeing with the earlier suggestion that the gallium adopts a lower coordination, The conductivities collected in dry N_2 atmospheres

were lower for the sulfate doped compositions than for the phosphate doped compositions, whereas the conductivities in wet N_2 were similar. This is despite the sulfate containing samples having a lower water content than the phosphate compositions. To determine if there was a p-type contribution to the conductivity, as seen in the phosphate doped compositions, conductivities were collected in a dry O_2 atmosphere, Figure 3.20.

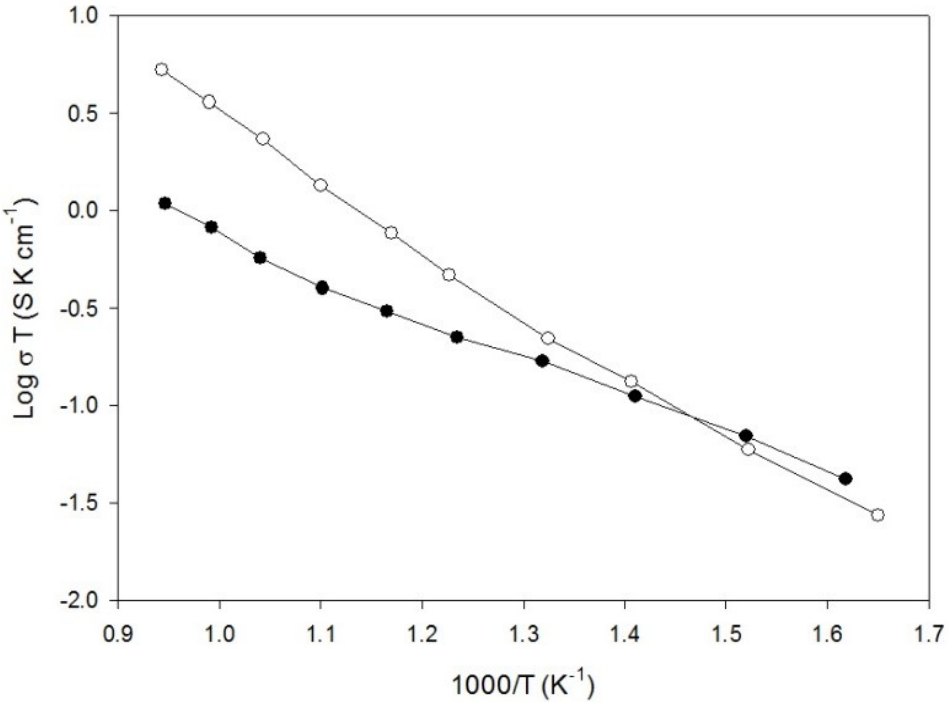

Figure 3.20 Conductivity data between 500 °C and 800 °C for $Ba_2Sc_{1.3}Ga_{0.4}S_{0.3}O_{5.45}$ in dry N2 (filled circle) and dry O2 (empty circle).

These collected data confirmed the presence of a p-type contribution to the conductivity at elevated temperatures.

3.3.2.3 CO_2 Stability

To determine the CO_2 stability of the compositions two experiments were carried out as for the phosphate doped systems. The first experiment involved heating the samples up to 1000°C at 10°C min^{-1} under flowing 1:1 CO_2 and N_2 and using TGA to measure the temperature at which mass uptake, formation of $BaCO_3$, occurred, Table 3.10.

Table 3.10 Temperature for uptake of CO_2 for $Ba_2Sc_{2-x-y}Ga_yS_xO_{5+3x/2}$ from TGA studies up to 1000°C

Composition	Temperature of Mass Gain
$\mathbf{Ba_2Sc_{1.4}Ga_{0.3}S_{0.3}O_{5.45}}$	800 °C
$\mathbf{Ba_2Sc_{1.3}Ga_{0.4}S_{0.3}O_{5.45}}$	850 °C
$\mathbf{Ba_2Sc_{1.2}Ga_{0.6}S_{0.2}O_{5.3}}$	950 °C
$\mathbf{Ba_2Sc_{1.1}Ga_{0.7}S_{0.2}O_{5.3}}$	950 °C
$\mathbf{Ba_2ScGa_{0.8}S_{0.2}O_{5.3}}$	No mass gain

The results showed that all the compositions only started to gain mass after 800°C in flowing CO_2, thus showing superior chemical stability to CO_2 than $BaCe_{0.9}Y_{0.1}O_{2.95}$, which gains mass in this experiment at 500 °C.[14] Furthermore the composition with the most gallium, $Ba_2ScGa_{0.8}S_{0.2}O_{5.3}$, showed no mass gain up to 1000 °C.

The second experiment involved heating the samples at 600 °C and 800 °C for 12 hours and then observing if any decomposition had taken place using powder X-ray diffraction. The powder X-ray diffraction patterns for $Ba_2Sc_{1.4}Ga_{0.3}S_{0.3}O_{5.45}$ and $Ba_2ScGa_{0.8}S_{0.2}O_{5.3}$ are shown in Figure 3.21.

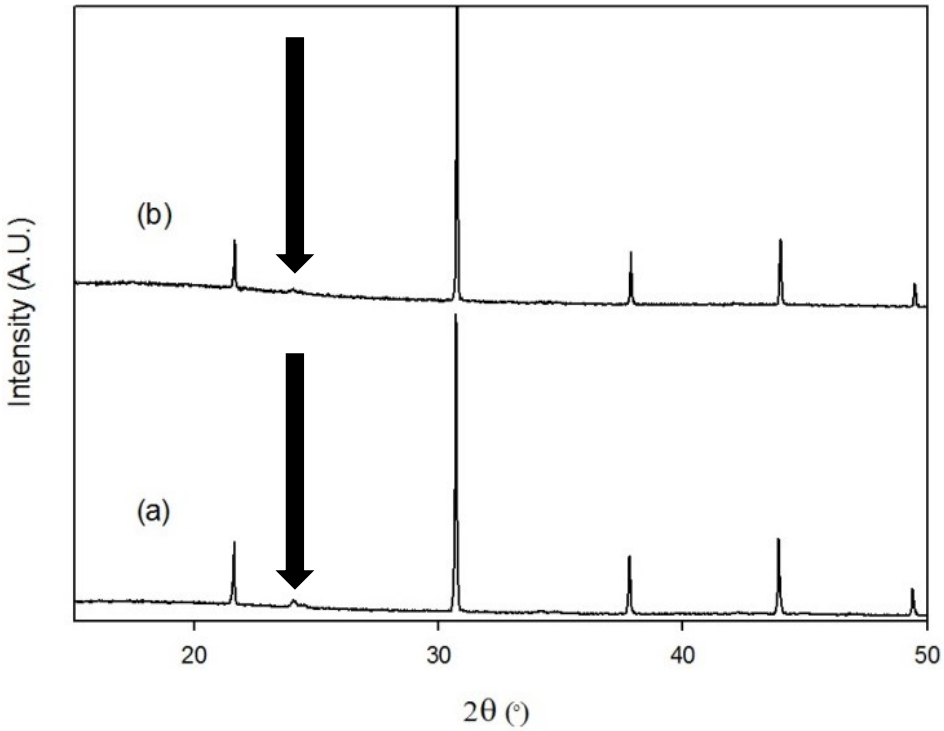

Figure 3.21 Powder X-ray diffraction data of (a) $Ba_2Sc_{1.4}Ga_{0.3}S_{0.3}O_{5.45}$ and (b) $Ba_2ScGa_{0.8}S_{0.2}O_{5.3}$ after heating for 12 hours at 600 °C under flowing CO_2

Unlike the phosphate doped compositions initial results suggested that the sulfate samples were not stable, $BaCO_3$ was formed, in a pure CO_2 atmosphere on heating for an extended period of time at 600 °C. The same results were seen for heating at 800 °C, Figure 3.22, however surprisingly there was no increase in the level of $BaCO_3$ for this more extreme temperature condition. This is most likely explained by the presence of a small amount of amorphous $BaO/Ba(OH)_2$ (either from the Ba excess, or due to loss of some sulfate on synthesis) which then picks up CO_2 to form $BaCO_3$, rather than CO_2 pick up from the perovskite itself.

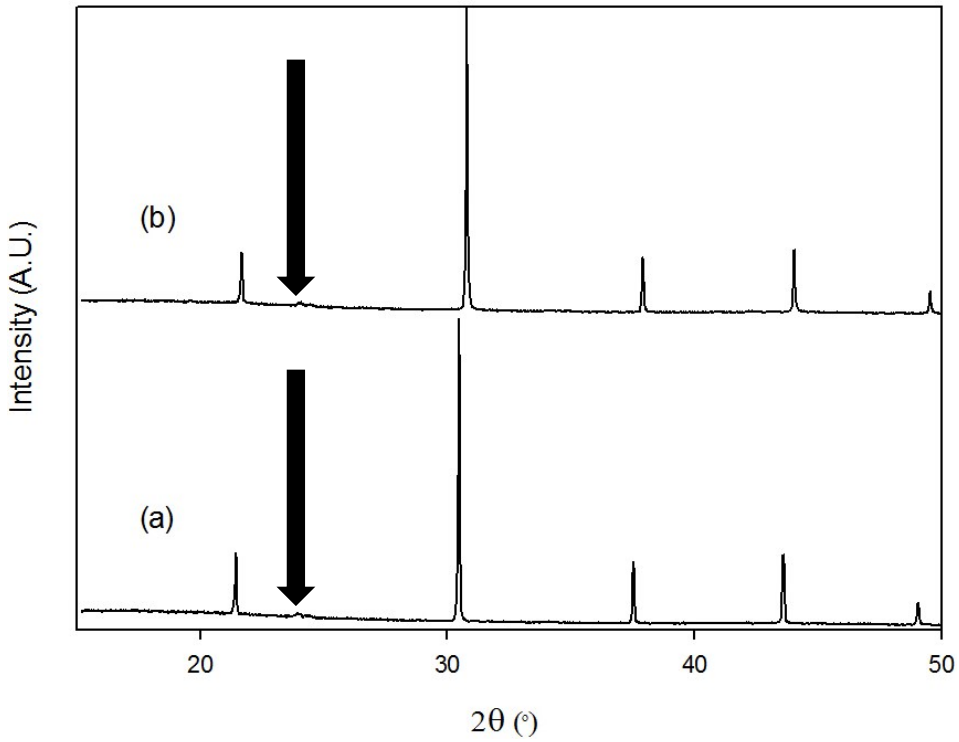

Figure 3.22 Powder X-ray diffraction data of (a) $Ba_2Sc_{1.4}Ga_{0.3}S_{0.3}O_{5.45}$ and (b) $Ba_2ScGa_{0.8}S_{0.2}O_{5.3}$ after heating for 12 hours at 800 °C under flowing CO_2

This suggests that the perovskite systems are stable to CO_2 atmospheres at SOFC operating temperatures.

3.4 Conclusions

Powder X-ray diffraction data on $Ba_2Sc_{2-x-y}Ga_yP_xO_{5+x}$ and $Ba_2Sc_{2-x-y}Ga_yS_xO_{5+3x/2}$ showed that both compositions adopt a cubic perovskite structure with space group *P m -3 m* and a lattice parameter in the range 4.12 Å to 4.17 Å.

Raman spectroscopy data confirmed the presence of phosphate and sulfate in the structure.

The water occupancies of hydrated samples were measured and found to be lower than expected which may be due to a resistance of gallium to accommodate water into the oxide ion vacancies around it. This was unable to be confirmed due to the lack of sensitivity of powder X-ray diffraction to oxygen atoms and further work using gallium NMR would need

to carried out to confirm this. Modelling studies would also be of interest to examine the energetics of the hydration reaction around the scandium and gallium in these phases.

The conductivities of selected samples were determined and it was found that they displayed high total conductivities with a significant protonic contribution, albeit lower than the samples without gallium doping. The samples were also found to exhibit a p-type contribution to the conductivity at elevated temperatures in high $p(O_2)$.

The relative stabilities towards CO_2 were measured, and increasing the gallium content was found to improve the stability of the samples to CO_2, suggesting that despite the lower conductivities, these phases could be used in technological applications.

3.5 References

1. T. Norby, *Solid State Ion.*, 1999, **125**, 1-11.
2. K. D. Kreuer, *Solid State Ion.*, 1997, **97**, 1-15.
3. A. Orera and P. R. Slater, *Chem. Mat.*, 2010, **22**, 675-690.
4. H. Iwahara, H. Uchida, K. Ono and K. Ogaki, *Journal of the Electrochemical Society*, 1988, **135**, 529-533.
5. T. Yajima, H. Kazeoka, T. Yogo and H. Iwahara, *Solid State Ion.*, 1991, **47**, 271-275.
6. H. Iwahara, T. Yajima, T. Hibino, K. Ozaki and H. Suzuki, *Solid State Ion.*, 1993, **61**, 65-69.
7. J. B. Goodenough, J. E. Ruizdiaz and Y. S. Zhen, *Solid State Ion.*, 1990, **44**, 21-31.
8. A. Rolle, R. N. Vannier, N. V. Giridharan and F. Abraham, *Solid State Ion.*, 2005, **176**, 2095-2103.
9. E. Quarez, S. Noirault, M. T. Caldes and O. Joubert, *J. Power Sources*, 2010, **195**, 1136-1141.
10. M. Karlsson, A. Matic, C. S. Knee, I. Ahmed, S. G. Eriksson and L. Borjesson, *Chem. Mat.*, 2008, **20**, 3480-3486.
11. J. F. Shin, D. C. Apperley and P. R. Slater, *Chem. Mat.*, 2010, **22**, 5945-5948.
12. J. F. Shin, L. Hussey, A. Orera and P. R. Slater, *Chemical Communications*, 2010, **46**, 4613-4615.
13. J. F. Shin, A. Orera, D. C. Apperley and P. R. Slater, *J. Mater. Chem.*, 2011, **21**, 874-879.
14. J. F. Shin, K. Joubel, D. C. Apperley and P. R. Slater, *Dalton Transactions*, 2012, **41**, 261-266.
15. A. C. Larson and R. B. Von Dreele, (1994), Los Alomos National Laboratory, Los Alomos NM.
16. L. J. Gillie, H. M. Palmer, A. J. Wright, J. Hadermann, G. Van Tendeloo and C. Greaves, *Journal of Physics and Chemistry of Solids*, 2004, **65**, 87-93.
17. R. D. Shannon, *Acta Crystallographica Section A*, 1976, **32**, 751-767.
18. K. Popa, R. J. M. Konings, O. Benes, T. Geisler and A. F. Popa, *Thermochimica Acta*, 2006, **451**, 1-4.
19. A. Mancini, J. F. Shin, A. Orera, P. R. Slater, C. Tealdi, Y. Ren, K. L. Page and L. Malavasi, *Dalton Transactions*, 2012, **41**, 50-53.
20. R. B. Cervera, S. Miyoshi, Y. Oyama, Y. E. Elammari, T. Yagi and S. Yamaguchi, *Chem. Mat.*, 2013, **25**, 1483-1489.
21. P. Vargas Jentzsch, B. Kampe, V. Ciobota, P. Rosch and J. Popp, *Spectrochimica acta. Part A, Molecular and biomolecular spectroscopy*, 2013, **115**, 697-708.

Chapter 4 Synthesis and Characterisation of Oxyanion Doped $Sr_2Sc_{2-y}Ga_yO_5$

4.1 Introduction

Acceptor doped $SrCeO_3$ has also been examined as an electrolyte material for proton conducting SOFCs due to its high proton conductivity upon water incorporation.[1] However, this system has an inferior conductivity to acceptor doped $BaCeO_3$ while having a similar stability to CO_2, although the reaction speed is lower for $SrCeO_3$ compared to $BaCeO_3$.[2, 3]

Oxyanion doping of strontium based perovskite materials for use in electrolytes has not been previously examined, however silicon doping of electrode materials has been studied. It has been shown that silicon can be incorporated into $SrAO_3$ (A = Mn, Fe, Co) and results in an improvement in the electrical conductivity and the stability of these phases.[4-9] Phosphate and sulfate have also been successfully doped into $SrCoO_3$ leading to a structural change from a hexagonal perovskite phase to a cubic perovskite phase and an improvement in the electrical conductivity of this phase.[10]

Therefore in this work, the extension of oxyanion doping to potential strontium based electrolytes was attempted. In this respect while $Sr_2Sc_2O_5$ does not exist, Sr_2ScGaO_5 has been reported.[11] The latter adopts a brownmillerite-type structure, similar to $Ba_2In_2O_5$, with the scandium and gallium perfectly ordered over the octahedral and tetrahedral sites respectively. Chernov *et al* extended this series and found that by substituting scandium for more gallium to give Sr $Sc_{0.25}Ga_{0.75}O_{2.5}$, a cubic perovskite phase (some of the gallium now occupies the octahedral site) with a disordered oxygen lattice formed and conductivity studies showed a protonic contribution to the conductivity.[12]

In this chapter the effects of oxyanion doping $Sr_2Sc_{2-y}Ga_yO_5$ are analysed and the conductivities and chemical stabilities are measured and compared with the data collected previously for oxyanion doped $Ba_2Sc_{2-y}Ga_yO_5$.

4.2 Experimental Procedure

$SrCO_3$ (≥99.9%), Sc_2O_3 (99.995%), Ga_2O_3 (99.9%), $NH_4H_2PO_4$ (≥98%), and $(NH_4)_2SO_4$ (99+%) were used to prepare $Sr_2Sc_{2-x-y}Ga_yP_xO_{5+x}$ and $Sr_2Sc_{2-x-y}Ga_yS_xO_{5+3x/2}$ samples. The powders were intimately ground in an agate pestle and mortar and heated initially to 1000 °C for 12 hours. They were then reground and reheated to 1500 °C for 12 hours. The resulting powders were then reground a second time and pressed as pellets (1.3 cm diameter) and sintered at 1500 °C for 12 hours. Powder X-ray diffraction (Bruker D8 diffractometer with Cu $K\alpha_1$ radiation) was used to demonstrate phase purity as well as for preliminary structure determination. For the latter, the GSAS suite of programs was used.[13]

Raman spectroscopy measurements were made in order to provide further evidence for the successful incorporation of phosphate, or sulfate. These measurements utilised a Renishaw inVia Raman microscope with excitation using a Cobolt Samba CW 532 nm DPSS Laser.

The samples were hydrated by heating up to 800°C under flowing wet N_2 and then slow cooling (0.4 °C min^{-1}). The water contents of these hydrated samples were determined from thermogravimetric analysis (Netzsch STA 449 F1 Jupiter Thermal Analyser). Samples were heated at 10 °C min^{-1} to 1000 °C in N_2, and the water content was determined from the observed mass loss.

For the conductivity measurements, the sintered pellets were coated with Pt paste, and then heated to 800 °C for 1 hour to ensure bonding to the pellet. Conductivities were then

measured by AC impedance measurements (Hewlett Packard 4192A impedance analyser) in the range from 0.1 to 10^3 kHz with ac signal amplitude of 100 mV. The conductivities reported are the total conductivity as it was not possible to reliably separate the bulk and grain boundary arcs, Figure 4.1. Measurements were made in dry N_2 and wet N_2 (in which the gas was bubbled at room temperature through water) to identify any protonic contribution to the conductivity. Measurements were also made in dry O_2 to determine if there was a p-type electronic contribution to the conductivity.

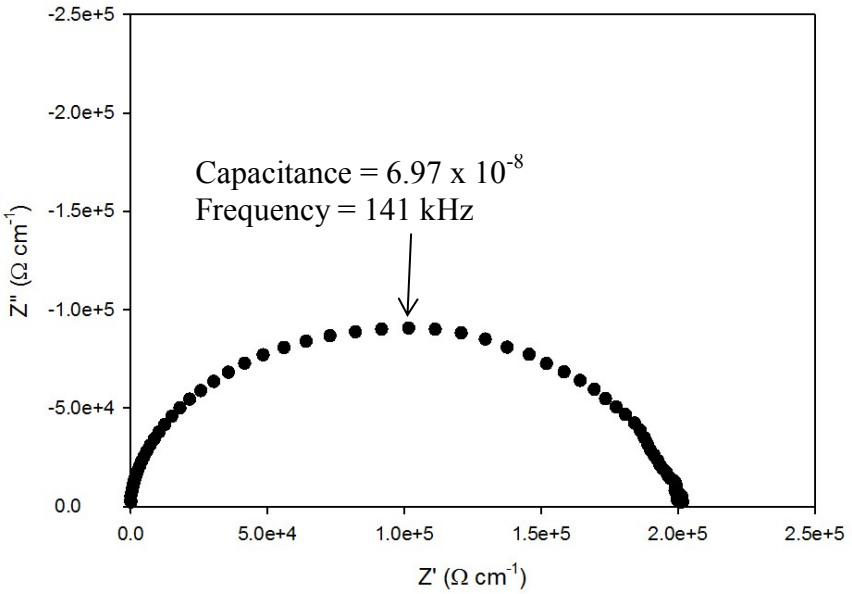

Figure 4.1 Impedance spectrum for $Sr_2ScGa_{0.7}P_{0.2}O_{5.2}$ at 440 °C in dry N_2

The CO_2 stability of samples was determined using two experiments, the first involved thermogravimetric analysis on a Netzsch STA 449 F1 Jupiter Thermal Analyser. Samples were heated at 10 °C min^{-1} to 1000 °C in a 1:1 CO_2 and N_2 mixture to determine at what temperature CO_2 pick up occurred. The second experiment involved heating at 800 °C for 12 hours in a tube furnace under flowing dry and wet CO_2 gas (in which the gas was bubbled at room temperature through water). The samples were then analysed for partial decomposition by X-ray diffraction.

4.3 Results and Discussion

4.3.1 Phosphate Doping

4.3.1.1 Structural Characterisation

4.3.1.1.1 Powder X-ray Diffraction

Initial attempts to prepare phosphate doped $Sr_2Sc_2O_5$ were carried out, as any attempt at the synthesis of the undoped $Sr_2Sc_2O_5$ composition led to a mixture of phases containing the starting materials, SrO and Sc_2O_3, Figure 4.2. A pure perovskite phase was obtained for 25% phosphate doping, while for lower amounts of phosphate, impurity phases, such as $SrSc_2O_4$ and SrO, were observed, Figure 4.3.

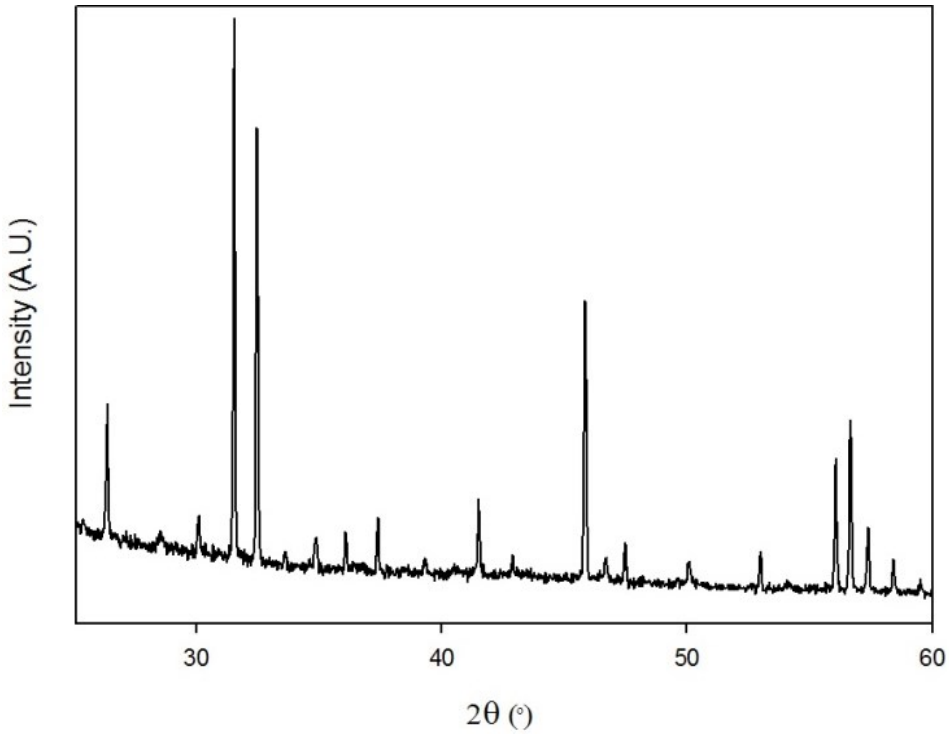

Figure 4.2 Powder X-ray diffraction data of attempted synthesis of "$Sr_2Sc_2O_5$" showing starting materials alongside other phases

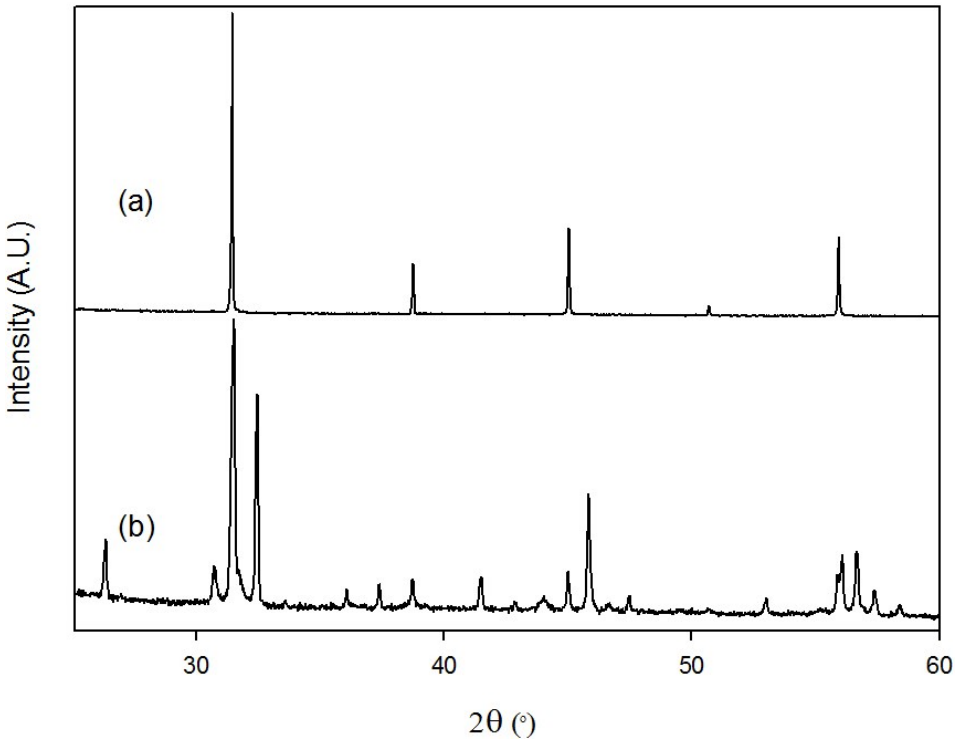

Figure 4.3 Powder X-ray diffraction data of (a) $Sr_2Sc_{1.5}P_{0.5}O_{5.5}$ and (b) attempted synthesis of "$Sr_2Sc_{1.8}P_{0.2}O_5$" showing the presence of peaks from $SrSc_2O_4$ and SrO along with a cubic perovskite phase

Rietveld refinement using the GSAS suite of programs was carried out on the collected powder X-ray diffraction data to obtain lattice parameters and provide evidence in support of the presence of phosphate. A structural model with space group *P m -3 m* was used with the phosphorus and scandium atoms both placed on the *1a* site with the expected stoichiometric weighed used as a starting point. The oxygen content was set to the expected value and the occupancy was not refined due to the lack of sensitivity of oxygen to powder X-ray diffraction. The refinement gave a good agreement with the collected powder X-ray diffraction data. The refined phosphorus content was also in good agreement with the value expected. The visual representation and the complete description of the refined model of $Sr_2Sc_{1.5}P_{0.5}O_{5.5}$ is shown in Figure 4.4 and Table 4.1.

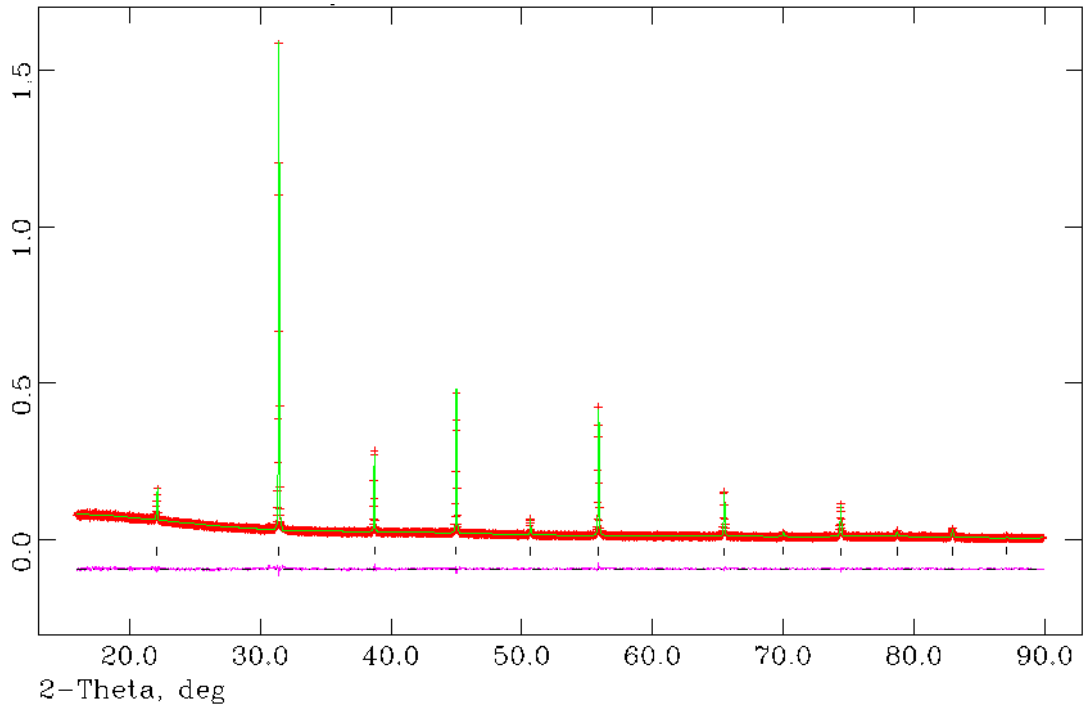

Figure 4.4 Observed, calculated and difference plots for structural refinement of $Sr_2Sc_{1.5}P_{0.5}O_{5.5}$ using X-ray powder diffraction data

Table 4.1 Structural data for $Sr_2Sc_{1.5}P_{0.5}O_{5.5}$

	Site	x	y	z	Fraction	100 U (Å^2)
Ba	1b	0.5	0.5	0.5	1	3.04(6)
Sc	1a	0	0	0	0.76(2)	2.2(1)
P	1a	0	0	0	0.24(2)	2.2(1)
O	3d	0.5	0	0	0.9167	8.3(2)
Space Group = *P m -3 m*, a = 4.03361(7) Å wR_p = 4.75%, R_p = 4.48%, χ^2 = 1.228						

The data showed a decrease in lattice parameter of $Sr_2Sc_{1.5}P_{0.5}O_{5.5}$ compared to $Ba_2Sc_{1.5}P_{0.5}O_{5.5}$ in agreement with the smaller ionic size of Sr^{2+} compared with Ba^{2+}.[14] The local coordination of the B site cations was unable to be determined due to the aforementioned lack of sensitivity of oxygen to X-rays and the presence of both scandium and phosphorus on this site.

After the successful synthesis of $Sr_2Sc_{1.5}P_{0.5}O_{5.5}$, oxyanion doped $Sr_2Sc_{2-y}Ga_yO_5$ compositions were attempted. 15% phosphate doped compositions were attempted as this resulted in single

phase compositions for the barium analogues, however multiple phases were obtained, including a perovskite phase, unreacted Ga_2O_3 and $Sr_5(PO_4)_3(OH)$, Figure 4.5.

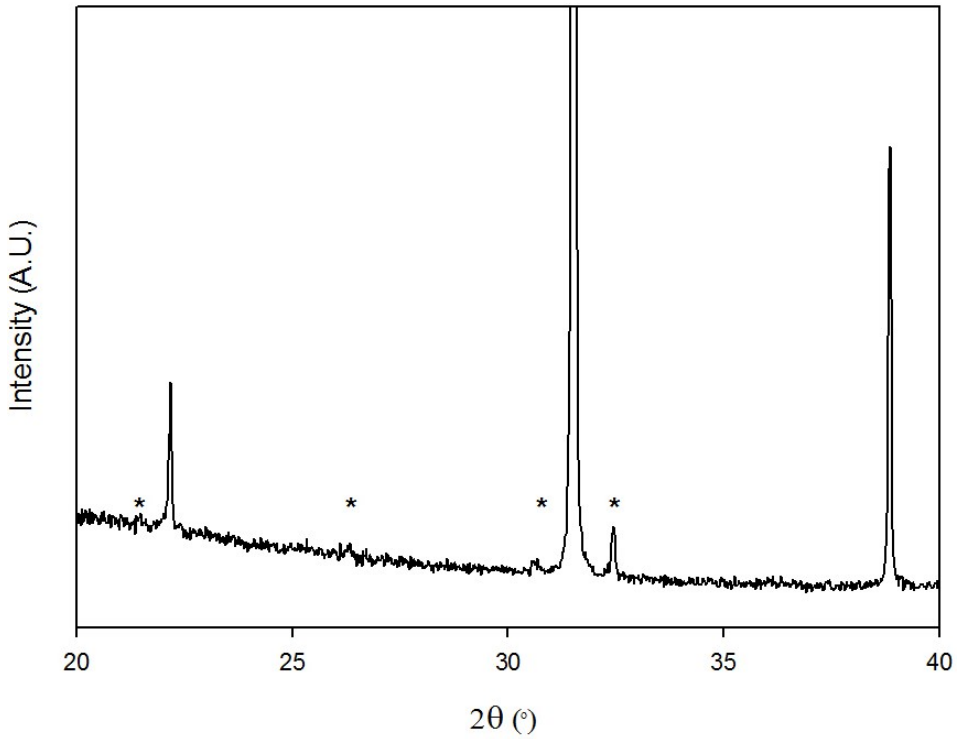

Figure 4.5 Powder X-ray diffraction pattern of attempted synthesis of "$Sr_2Sc_{1.4}Ga_{0.3}P_{0.3}O_{5.3}$" with impurity peaks indicated

Gallium doping was then attempted for 5% and 10% phosphate doped compositions and resulted in the following single phases $Sr_2Sc_{0.9}GaP_{0.1}O_{5.1}$ and $Sr_2Sc_{1.1}Ga_{0.7}P_{0.2}O_{5.2}$, Figure 4.6. For higher gallium contents, the gallium rich phase $Sr_3Ga_2O_6$ formed, and at lower gallium contents other phosphate impurities were present, Figure 4.7. The lower phosphate content required for increased gallium content is in agreement with the results seen for phosphate doped $Ba_2Sc_{2-y}Ga_yO_5$, and is most likely due to the preference of gallium as well as the phosphate to prefer a lower coordination than octahedral in these systems.[15]

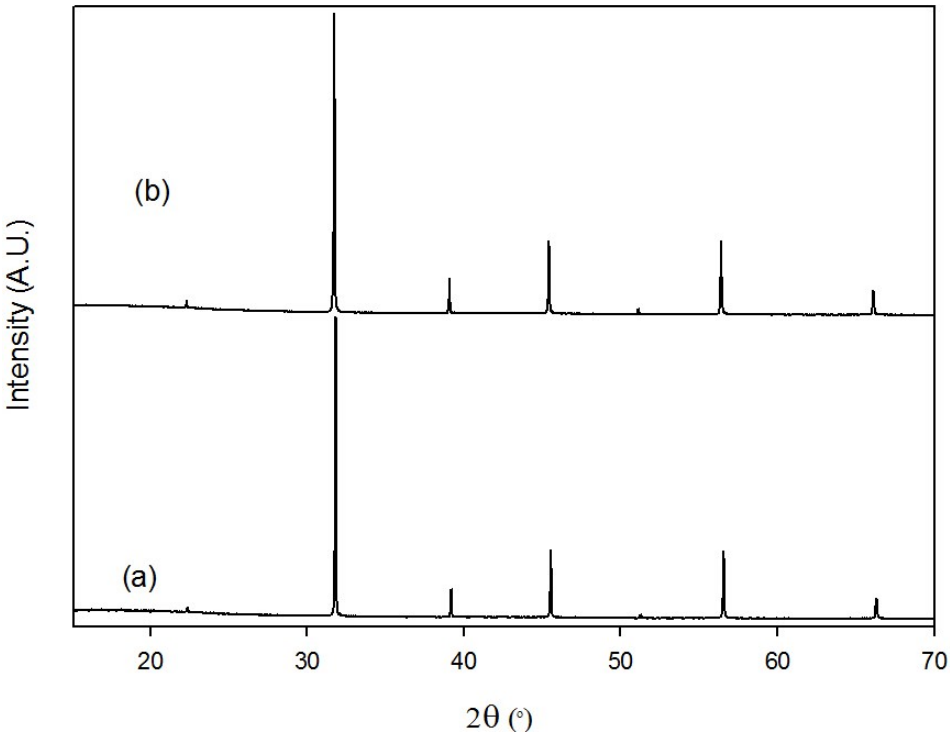

Figure 4.6 Powder X-ray diffraction pattern of (a) $Sr_2Sc_{0.9}GaP_{0.1}O_{5.1}$ and (b) $Sr_2Sc_{1.1}Ga_{0.7}P_{0.2}O_{5.2}$

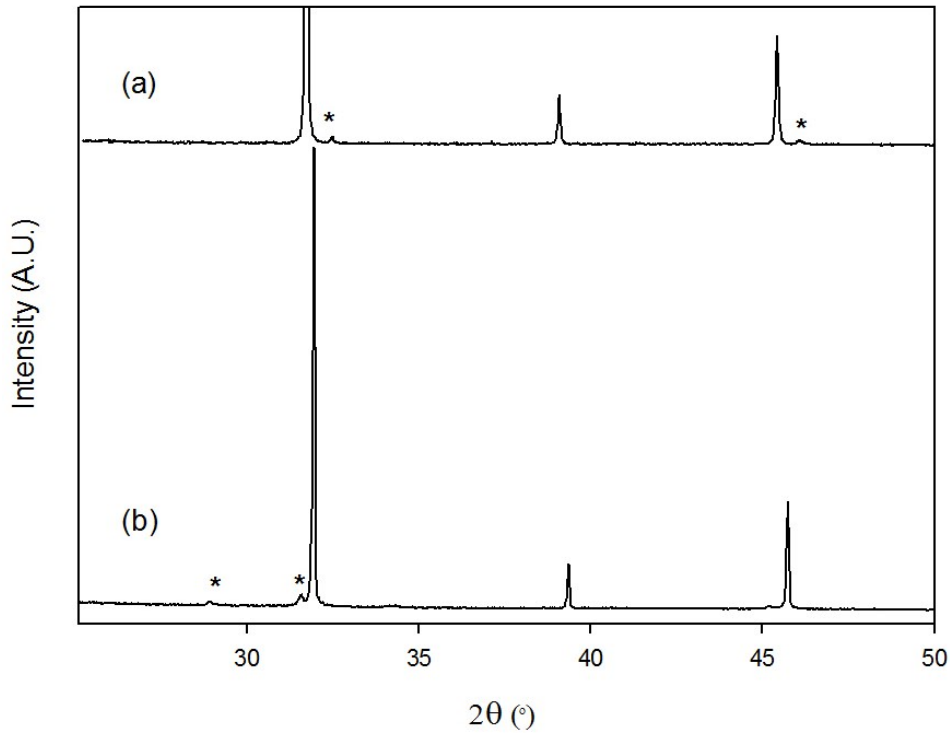

Figure 4.7 Powder X-ray diffraction pattern of attempted synthesis of (a) "$Sr_2Sc_{1.1}Ga_{0.7}P_{0.1}O_{5.1}$" and (b) "$Sr_2Sc_{0.6}Ga_{1.3}P_{0.1}O_{5.1}$" with impurity peaks indicated

As for $Sr_2Sc_{1.5}P_{0.5}O_{5.5}$, Rietveld refinement using the GSAS suite of programs was carried out to determine the lattice parameters. The same structural model, space group *P m -3 m*, was used with the gallium placed on the *1a* site along with scandium and phosphorus in the

weighed out stoichiometric amounts. The refinement gave a good agreement with the collected powder X-ray diffraction data. The following lattice parameters were obtained, Table 4.2, and compared with $Sr_2Sc_{1.5}P_{0.5}O_{5.5}$, and the visual fit representation and complete description of the refined model of $Sr_2Sc_{1.1}Ga_{0.7}P_{0.2}O_{5.2}$ are shown in Figure 4.8 and Table 4.3.

Table 4.2 Lattice parameters for phosphate doped $SrSc_{2-y}Ga_yO_5$

Composition	a (Å)
$Sr_2Sc_{1.5}P_{0.5}O_{5.5}$	4.03361(7)
$Sr_2Sc_{1.1}Ga_{0.7}P_{0.2}O_{5.2}$	4.00462(2)
$Sr_2Sc_{0.9}GaP_{0.1}O_{5.1}$	3.99485(4)

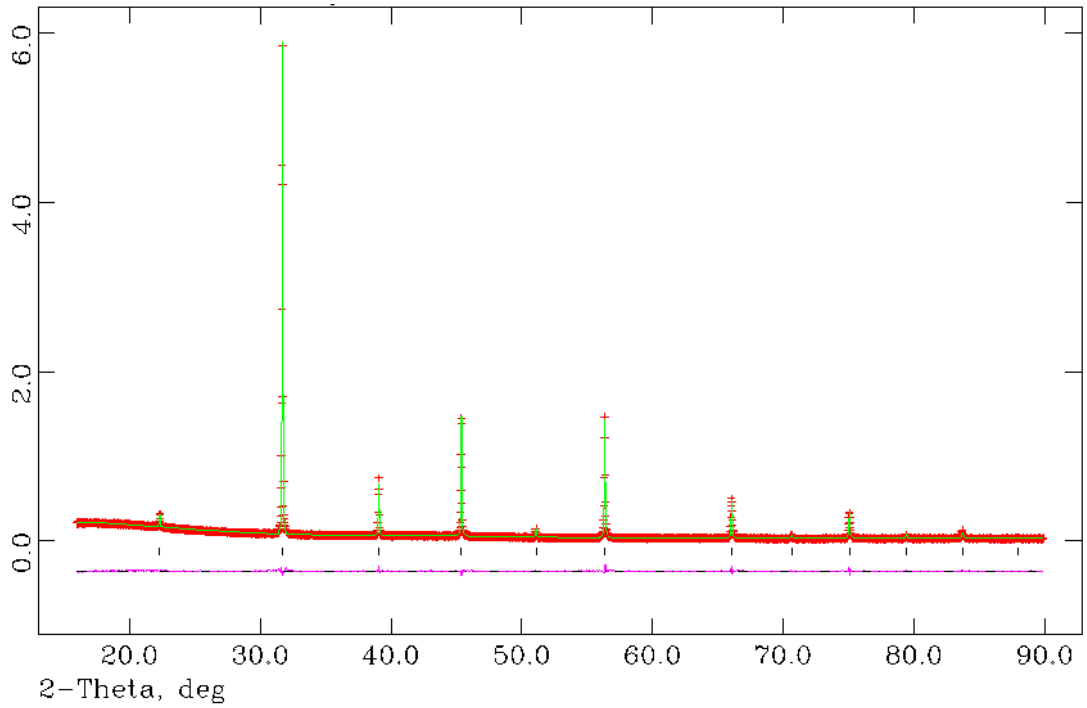

Figure 4.8 Observed, calculated and difference plots for structural refinement of $Sr_2Sc_{1.1}Ga_{0.7}P_{0.2}O_{5.2}$ using X-ray powder diffraction data

Table 4.3 Structural detail for $Sr_2Sc_{1.1}Ga_{0.7}P_{0.2}O_{5.2}$

	Site	x	y	z	Fraction	100 U ($Å^2$)
Sr	1b	0.5	0.5	0.5	1	2.81(4)
Sc	1a	0	0	0	0.55	3.31(6)
Ga	1a	0	0	0	0.35	3.31(6)
P	1a	0	0	0	0.1	3.31(6)
O	3d	0.5	0	0	0.867	7.7(1)
Space Group = *P m -3 m*, a = 4.00462(2) Å wR_p = 5.88%, R_p = 4.41%, χ^2 = 2.457						

The lattice parameter was found to decrease with increasing gallium content in agreement with the smaller ionic radius of gallium, 0.62 Å, compared to the scandium, 0.745 Å (coordination number equal to 6).[14] The exact coordination of the B site cations was unable to be determined due to the previously mentioned lack of sensitivity of oxygen to X-rays and other techniques such as neutron diffraction or solid state NMR would be required to resolve this.

4.3.1.1.2 Raman Spectroscopy

To confirm the presence of phosphate in $Sr_2Sc_{1.5}P_{0.5}O_{5.5}$, $Sr_2Sc_{0.9}GaP_{0.1}O_{5.1}$ and $Sr_2Sc_{1.1}Ga_{0.7}P_{0.2}O_{5.2}$, Raman data were collected on all samples, Figure 4.9. All three samples showed a band at around 940 cm^{-1}, associated with the internal stretching mode of phosphate, in agreement with the presence of phosphate.[16]

$Sr_2Sc_{1.5}P_{0.5}O_{5.5}$ also showed a small band at 415 cm^{-1}, due to the bending mode of phosphate, which was not seen for the other compositions. The Raman peaks resulting from phosphate in doped $Sr_2Sc_2O_5$ are broader and have a lower band height than those seen for the barium compositions which may explain why the band at 415 cm^{-1} is only seen for the composition with the greatest phosphate amount. As has been seen in previous studies of oxyanion doped systems the local structure is not perfectly cubic as broad peaks from 550 cm^{-1} to 800 cm^{-1} are seen.[17, 18] If the structure was perfectly cubic then these bands would not be seen, as all the

lattice sites would have inversion symmetry; however it should be noted that incorporating tetrahedral phosphate would remove this inversion symmetry at this particular site.

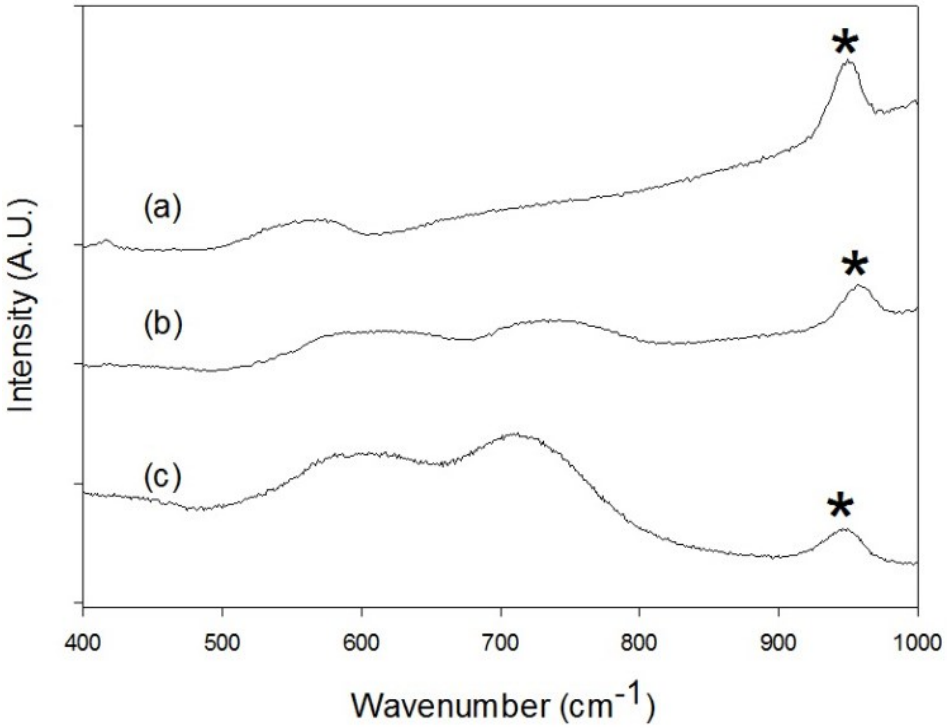

Figure 4.9 Raman spectra of (a) $Sr_2Sc_{1.5}P_{0.5}O_{5.5}$, (b) $Sr_2Sc_{0.9}GaP_{0.1}O_{5.1}$ and (c) $Sr_2Sc_{1.1}Ga_{0.7}P_{0.2}O_{5.2}$

4.3.1.1.3 Water Incorporation

The water contents of the hydrated samples were obtained using TGA analysis by measuring the mass loss upon heating, Table 4.4.

Table 4.4 Water content for $Sr_2Sc_{2-x-y}Ga_yP_xO_{5+x}$

Composition	% Mass Loss	Amount of water per formula unit
$Sr_2Sc_{1.5}P_{0.5}O_{5.5}$	0.18	0.03(1)
$Sr_2Sc_{0.9}GaP_{0.1}O_{5.1}$	0.23	0.05(1)
$Sr_2Sc_{1.1}Ga_{0.7}P_{0.2}O_{5.2}$	0.19	0.04(1)

The collected data showed that for $Sr_2Sc_{1.5}P_{0.5}O_{5.5}$, only a very small fraction of the oxygen vacancies could be filled in agreement with phosphate adopting a lower coordination,

tetrahedral rather than octahedral, and hence trapping vacancies around it, as observed by Shin *et al* and commented on in section 3.3.1.1.4.[19, 20]

Similarly for $Sr_2Sc_{2-x-y}Ga_yP_xO_{5+x}$ there were low levels of water incorporation, attributed also to a preference for gallium for a lower coordination than octahedral. Overall the water contents were slightly lower than for $Ba_2Sc_{2-x-y}Ga_yP_xO_{5+x}$.

4.3.1.2 Conductivity Measurements

Conductivity data were collected on $Sr_2Sc_{1.5}P_{0.5}O_{5.5}$ in dry and wet N_2 atmospheres to eliminate any p-type contribution to the conductivity and to observe if there is any protonic conduction. $Sr_2Sc_{1.5}P_{0.5}O_{5.5}$ showed a relatively high total conductivity with a significant protonic contribution, Figure 4.10, with a total conductivity of 4.82 x 10^{-5} S cm^{-1} and 4.01 x 10^{-4} S cm^{-1} at 500 °C and 800 °C respectively in dry N_2, while in wet N_2 the conductivities were higher at 3.10 x 10^{-4} and 6.00 x 10^{-4} S cm^{-1} at 500 °C and 800 °C respectively.

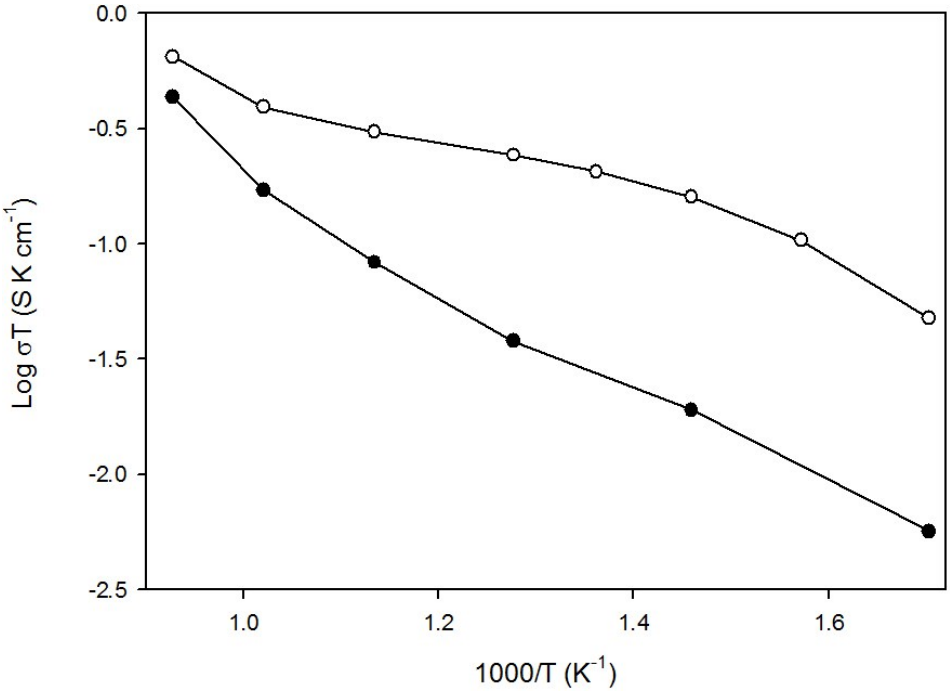

Figure 4.10 Conductivity data for $Sr_2Sc_{1.5}P_{0.5}O_{5.5}$ in dry (filled) and wet (empty) N_2

The values of the conductivities in both atmospheres were, however, found to be an order of magnitude lower than for $Ba_2Sc_{1.5}P_{0.5}O_{5.5}$ similar to the drop off in conductivity seen between doped barium and strontium cerates. In order to examine how the conductivity of the composition varies with decreasing phosphate content and increasing gallium content the conductivities of $Sr_2Sc_{0.9}GaP_{0.1}O_{5.1}$ and $Sr_2Sc_{1.1}Ga_{0.7}P_{0.2}O_{5.2}$ were also collected in dry and wet N_2, Table 4.5 and Figure 4.11.

Table 4.5 Total conductivity data for $Sr_2Sc_{2-x-y}Ga_yP_xO_{5+x}$

Sample (nominal composition)	Conductivity (S cm^{-1})			
	500 °C		800 °C	
	Dry N_2	Wet N_2	Dry N_2	Wet N_2
$Sr_2Sc_{1.1}Ga_{0.7}P_{0.2}O_{5.2}$	8.65 x 10^{-6}	1.73 x 10^{-5}	9.00 x 10^{-5}	1.15 x 10^{-4}
$Sr_2Sc_{0.9}GaP_{0.1}O_{5.1}$	1.40 x 10^{-6}	3.03 x 10^{-6}	4.91 x 10^{-5}	4.95 x 10^{-5}

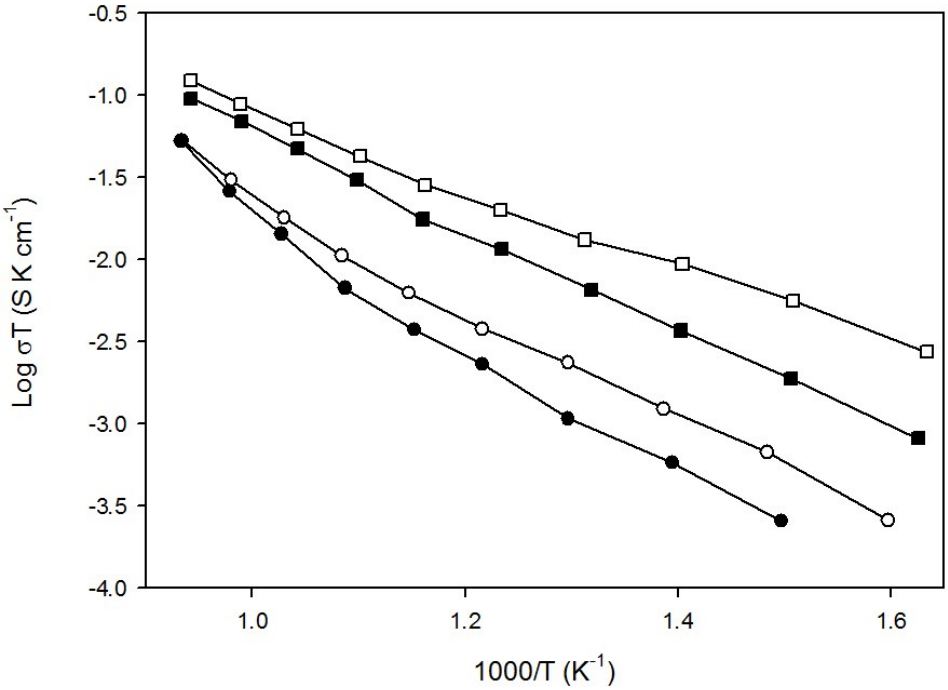

Figure 4.11 Conductivity data for $Sr_2Sc_{0.9}GaP_{0.1}O_{5.1}$ (circle) and $Sr_2Sc_{1.1}Ga_{0.7}P_{0.2}O_{5.2}$ (square) in dry (filled) and wet (empty) N_2

The collected data indicates that conductivity decreases with increasing gallium content, similar to the barium based systems.

As a p-type contribution to the conductivity was seen for oxyanion doped $Ba_2Sc_{2-y}Ga_yO_5$ in high $p(O_2)$, all the strontium compositions were also examined in a dry O_2 atmosphere, an example shown in Figure 4.12.

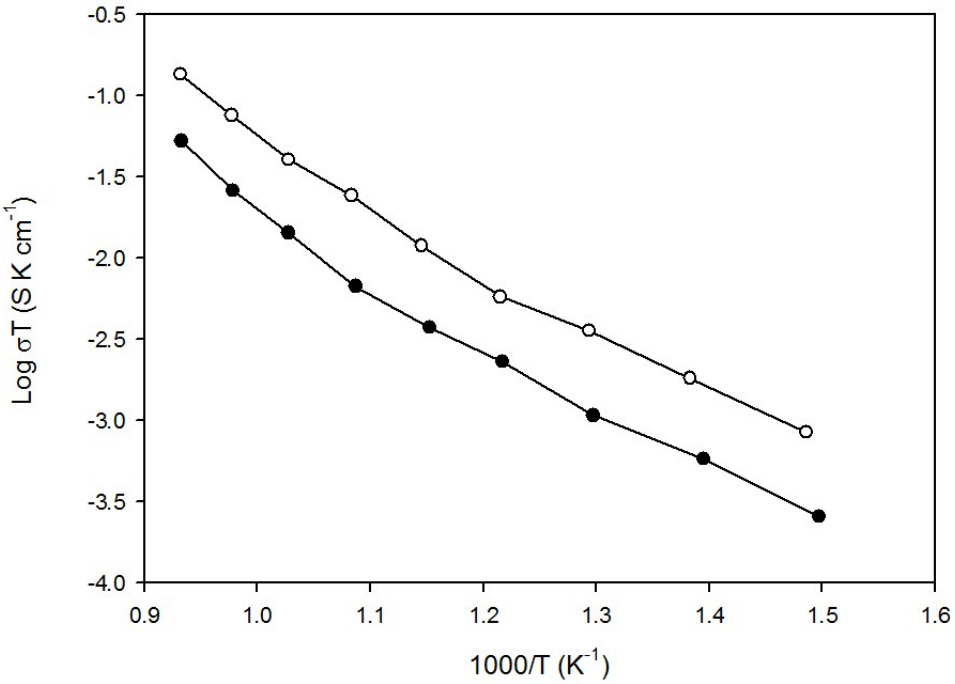

Figure 4.12 Conductivity data for $Sr_2Sc_{0.9}GaP_{0.1}O_{5.1}$ in dry N_2 (filled) and dry O_2 (empty)

All the compositions exhibited a p-type contribution to the conductivity due to the incorporation of oxygen into the vacancies according to the equation $V_O^{\bullet\bullet} + O_O^x + \frac{1}{2}O_2 \leftrightarrow 2O_O^{\bullet}$.

4.3.1.3 CO_2 Stability

The first experiment examining the CO_2 stability, across the operating temperatures used in SOFCs, was to heat the samples to 1000 °C at a rate of 10 °C min^{-1} in a 1:1 mix of flowing CO_2 and N_2. All the compositions exhibited no mass gain under these conditions. Thus $Sr_2Sc_{1.5}P_{0.5}O_{5.5}$ showed a superior stability compared to $Ba_2Sc_{1.5}P_{0.5}O_{5.5}$, which gained mass after 800 °C using these experimental conditions. However this may be due to a slower reaction rate of $Sr_2Sc_{1.5}P_{0.5}O_{5.5}$ compared to $Ba_2Sc_{1.5}P_{0.5}O_{5.5}$ as seen for $SrCeO_3$ compared to

$BaCeO_3$.[3] The high stability of the gallium containing compositions was in agreement with the stabilities seen for the higher gallium content $Ba_2Sc_{2-x-y}Ga_yP_xO_{5+x}$ compositions.

The second experiment involved heating the samples at 800 °C for 12 hours under flowing dry and wet CO_2, and using powder XRD to determine if partial decomposition had occurred. The powder XRD patterns for $Sr_2Sc_{1.5}P_{0.5}O_{5.5}$ and $Sr_2Sc_{1.1}Ga_{0.7}P_{0.2}O_{5.2}$ after treatment in dry CO_2 are shown in Figure 4.13.

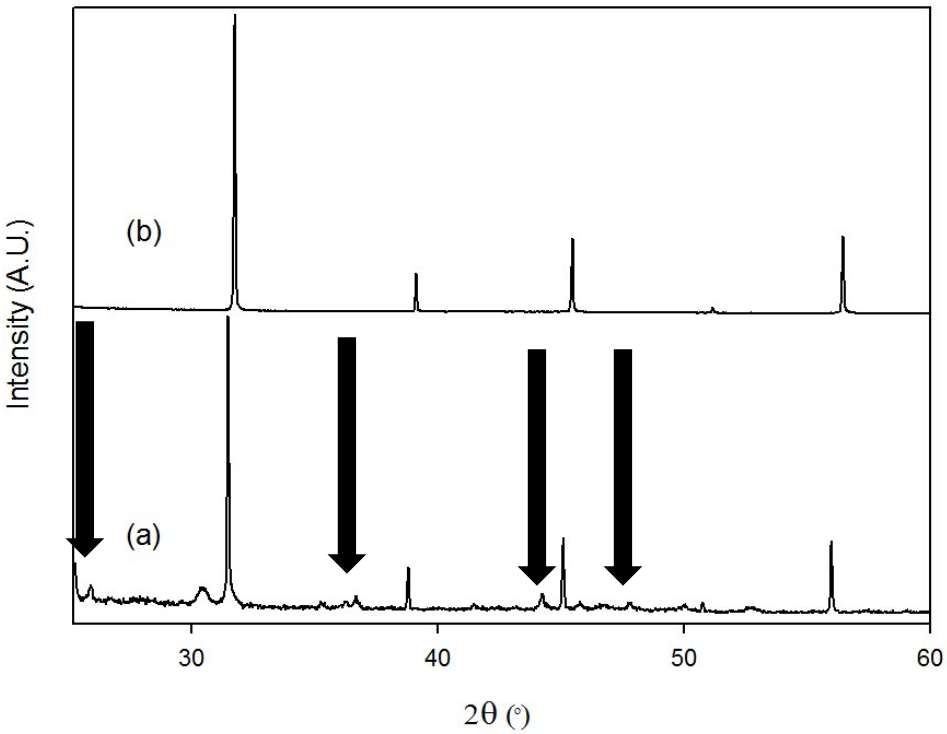

Figure 4.13 Powder XRD patterns of (a) $Sr_2Sc_{1.5}P_{0.5}O_{5.5}$ and (b) $Sr_2Sc_{1.1}Ga_{0.7}P_{0.2}O_{5.2}$ after heat treatment at 800 °C for 12 hours under flowing dry CO_2 with peaks due to $SrCO_3$ indicated

The gallium containing compositions showed complete stability to CO_2 at 800 °C as no $SrCO_3$ was present in the XRD patterns. In contrast $Sr_2Sc_{1.5}P_{0.5}O_{5.5}$ was found to not be stable to CO_2 at this temperature, as $SrCO_3$ alongside other phases formed indicating that, as seen for $Ba_2Sc_{2-x-y}Ga_yP_xO_{5+x}$, the gallium improved the CO_2 stability. Data were then collected under flowing wet CO_2 for the lowest gallium content composition to examine the effect of an even more extreme environment, with the powder XRD pattern shown in Figure 4.14.

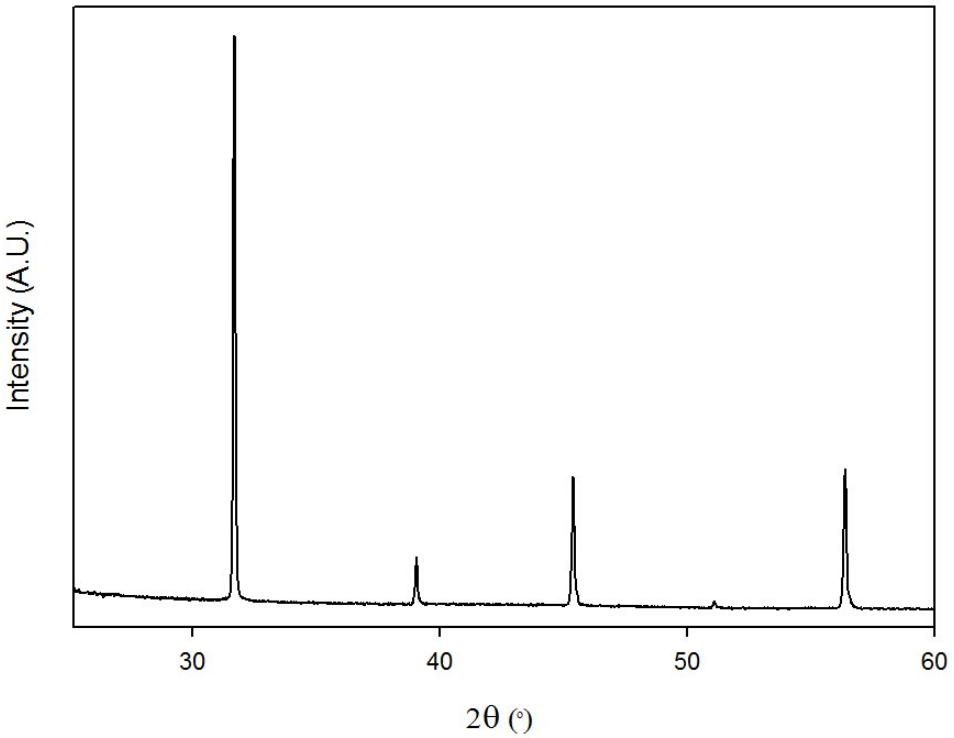

Figure 4.14 Powder XRD pattern of $Sr_2Sc_{1.1}Ga_{0.7}P_{0.2}O_{5.2}$ after heat treatment at 800 °C for 12 hours under flowing wet CO_2

The collected data showed that $Sr_2Sc_{1.1}Ga_{0.7}P_{0.2}O_{5.2}$ was also stable with respect to CO_2 under these extremely harsh conditions. The conditions used in these experiments are much harsher than those found in proton conducting SOFCs and show that these compositions have high stabilities and are far superior to other perovskite proton conductors, such as $BaCe_{0.9}Y_{0.1}O_{2.95}$ in this respect.[19]

4.3.2 Sulfate Doping

4.3.2.1 Structural Characterisation

4.3.2.1.1 Powder X-ray Diffraction

Following on from the preparation of the phosphate doped analogues, sulfate doping was attempted in $Sr_2Sc_2O_5$. This proved unsuccessful for all levels of sulfate doping, Figure 4.15, as unreacted starting materials, SrO and Sc_2O_3, were present along with sulfate impurities as well as peaks for other strontium scandate phases.

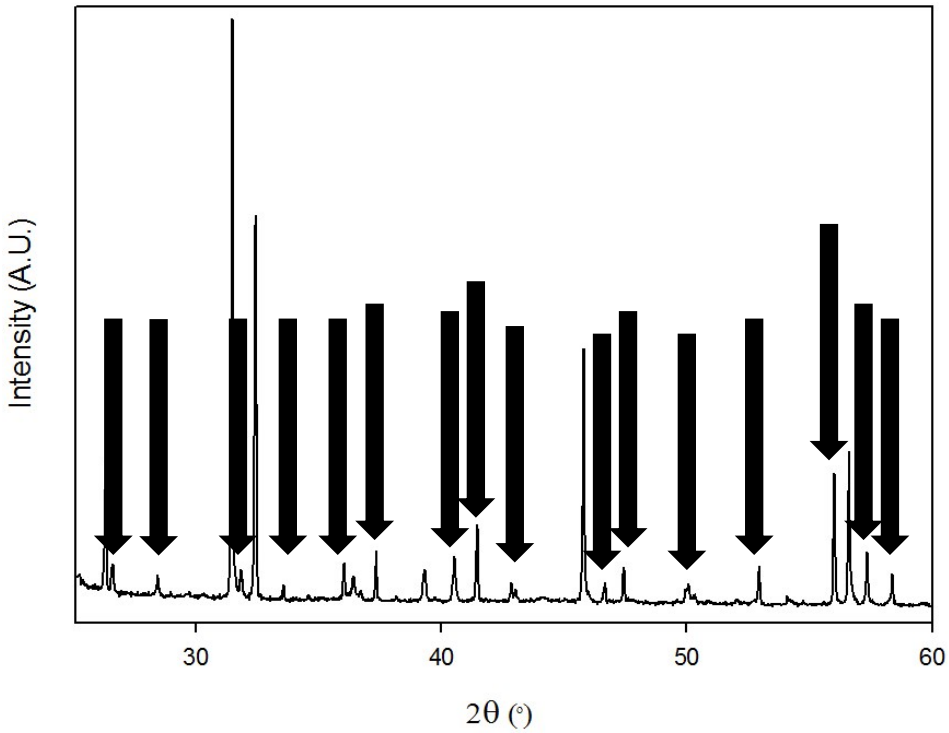

Figure 4.15 Powder X-ray diffraction pattern for attempted synthesis of "$Sr_2Sc_{1.6}S_{0.4}O_{5.6}$" with SrO, Sc_2O_3 peaks indicated

The preparation of sulfate doped $Sr_2Sc_{2-y}Ga_yO_5$ was then attempted. The compositions $Sr_2Sc_{0.9}GaS_{0.1}O_{5.15}$, $Sr_2Sc_{0.6}Ga_{1.3}S_{0.1}O_{5.15}$ and $Sr_2Sc_{0.8}GaS_{0.2}O_{5.3}$ resulted in cubic perovskite phases with no impurities present, Figure 4.16. At lower levels of gallium unidentified impurities were present, Figure 4.17, and higher gallium contents were not attempted due to the previously shown negative effect of gallium on the conductivity.

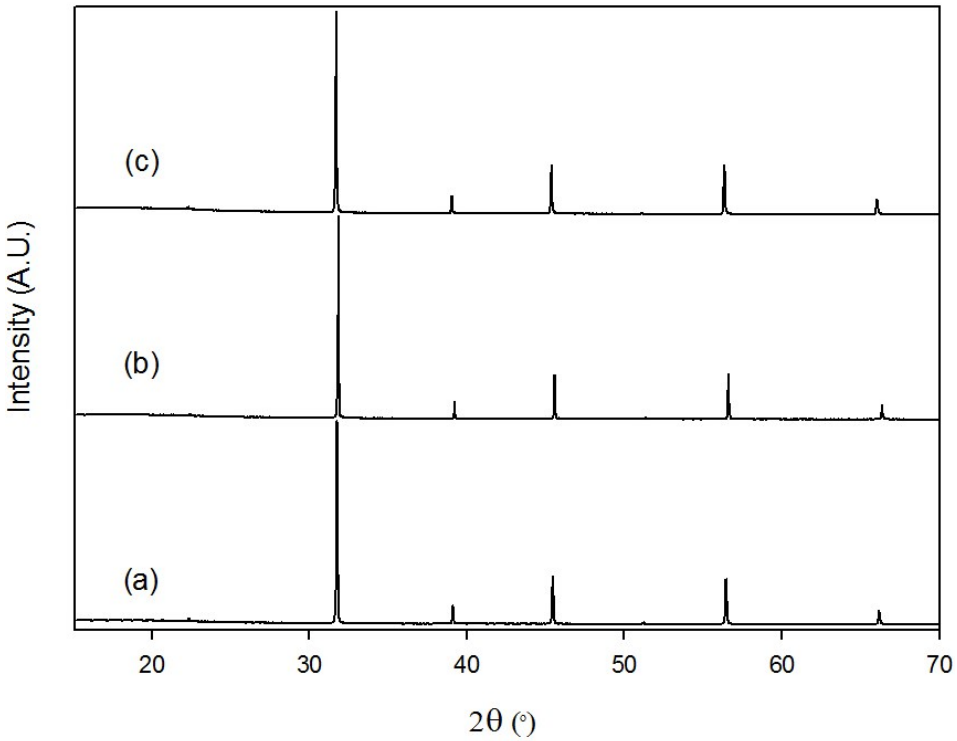

Figure 4.16 Powder X-ray diffraction pattern patterns for (a) $Sr_2Sc_{0.9}GaS_{0.1}O_{5.15}$, (b) $Sr_2Sc_{0.6}Ga_{1.3}S_{0.1}O_{5.15}$ and (c) $Sr_2Sc_{0.8}GaS_{0.2}O_{5.3}$

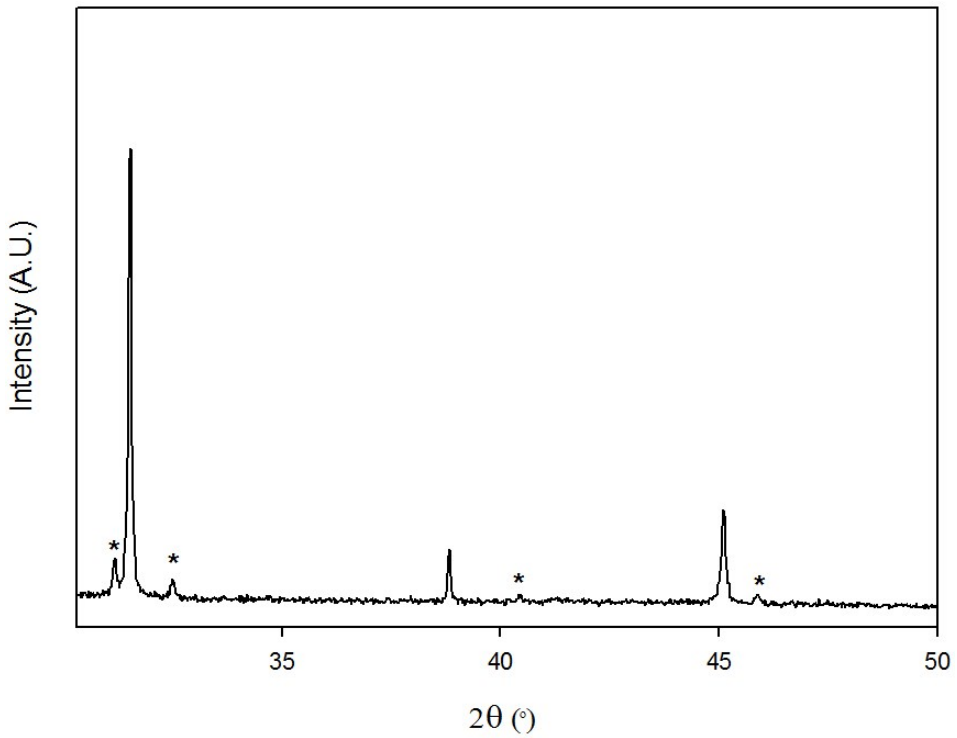

Figure 4.17 Powder X-ray diffraction pattern of attempted synthesis of "$Sr_2Sc_{1.4}Ga_{0.4}S_{0.2}O_{5.3}$" with impurity peaks indicated

Rietveld refinement with the GSAS suite of programs was used to obtain lattice parameters for the pure compositions. A structural model with space group *P m -3 m* was used with the

gallium, scandium and sulfur placed on the *1a* site using the weighed out stoichiometric amounts for the occupancies. The oxygen content was also fixed at the expected value. The refinement gave a good agreement with the collected powder X-ray diffraction and the following lattice parameters were obtained, Table 4.6, with the visual representation and the complete description of the refined model of $Sr_2Sc_{0.9}GaS_{0.1}O_{5.15}$ shown in Figure 4.18 and Table 4.7.

Table 4.6 Lattice parameters for sulfate doped $SrSc_{2-y}Ga_yO_5$

Composition	a (Å)
$Sr_2Sc_{0.9}GaS_{0.1}O_{5.15}$	4.00124(5)
$Sr_2Sc_{0.8}GaS_{0.2}O_{5.3}$	4.00854(3)
$Sr_2Sc_{0.6}Ga_{1.3}S_{0.1}O_{5.15}$	3.99136(4)

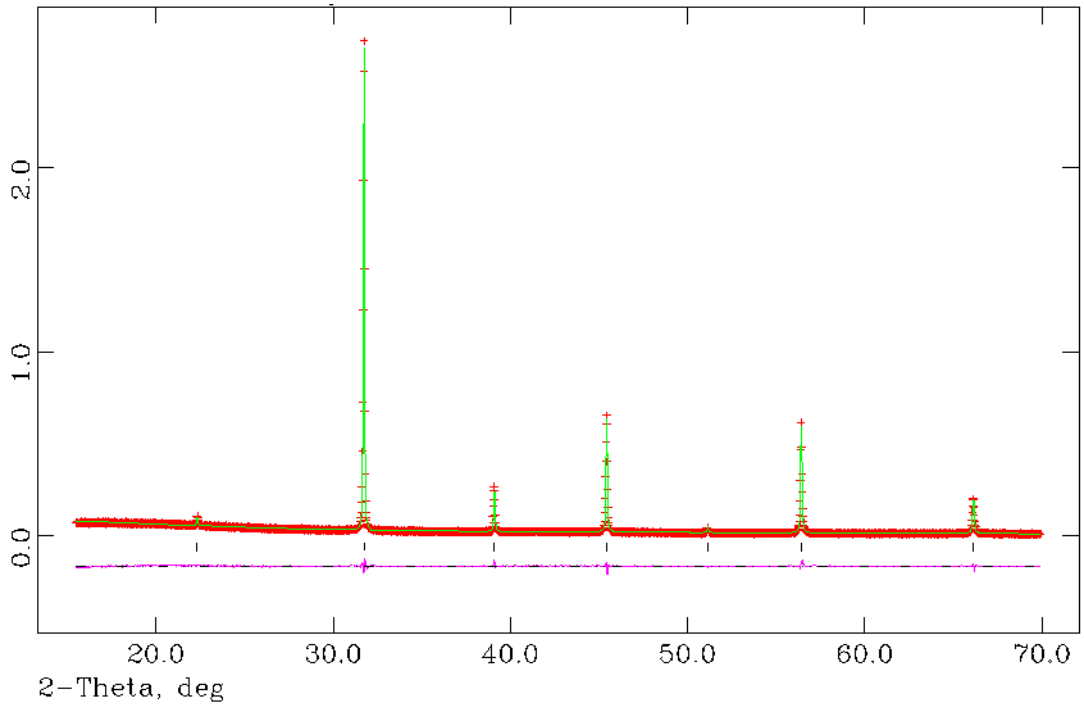

Figure 4.18 Observed, calculated and difference plots for structural refinement of $Sr_2Sc_{0.9}GaS_{0.1}O_{5.15}$ using X-ray powder diffraction data

Table 4.7 Structural detail for $Sr_2Sc_{0.9}GaS_{0.1}O_{5.15}$

	Site	x	y	z	Fraction	100 U ($Å^2$)
Sr	1b	0.5	0.5	0.5	1	3.04(8)
Sc	1a	0	0	0	0.45	3.57(9)
Ga	1a	0	0	0	0.5	3.57(9)
S	1a	0	0	0	0.05	3.57(9)
O	3d	0.5	0	0	0.858	8.9(2)
Space Group = *P m -3 m*, a = 4.00124(5) Å wR_p = 5.70%, R_p = 4.84%, χ^2 = 1.945						

The lattice parameter was found to decrease with increased gallium content in agreement with gallium having a smaller ionic radius, 0.62 Å, compared to scandium, 0.745 Å.[14] Increasing the sulfate content was found to increase the lattice parameter despite S^{6+} having a smaller ionic radius than Ga^{3+} and Sc^{3+}; this is most likely due to the increased oxygen content required with increased sulfate content as also suggested for the $Ba_2Sc_{2-x-y}Ga_ySxO_{5+3x/2}$ compositions.[14] To resolve the coordination of the individual cations on the *1a* site solid state NMR studies are required due to the lack of sensitivity of oxygen to X-rays and the presence of multiple cations on the B site.

4.3.2.1.2 Raman Spectroscopy

To provide confirmation that sulfate was incorporated into the structure, Raman data were collected, Figure 4.19.

All the compositions contained a peak at around 990 cm^{-1} (symmetric stretch) consistent with the presence of sulfate, however as seen for the phosphate compositions this band was very broad and this broadness may be the reason that the lower intensity peaks at 450 cm^{-1} (symmetric bend) and 610 cm^{-1} (asymmetric bend) are not seen.[21] The broad peaks seen from 500 cm^{-1} to 800 cm^{-1} also show that the local structure in these perovskites is not cubic.

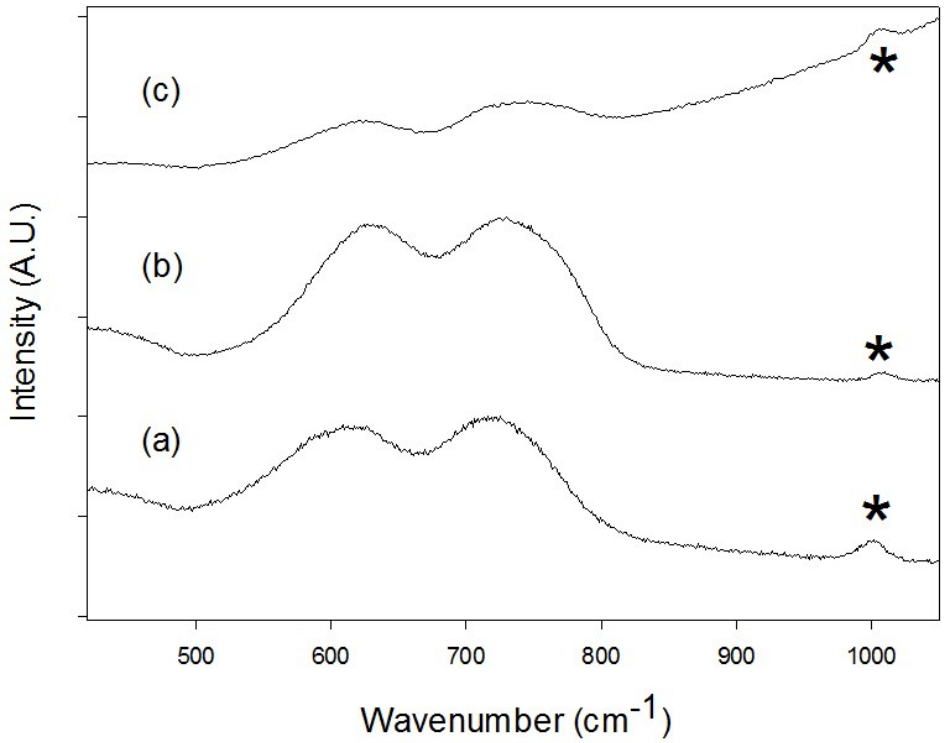

Figure 4.19 Raman spectra of (a) $Sr_2Sc_{0.9}GaS_{0.1}O_{5.15}$, (b) $Sr_2Sc_{0.6}Ga_{1.3}S_{0.1}O_{5.15}$ and (c) $Sr_2Sc_{0.8}GaS_{0.2}O_{5.3}$ with peak showing the presence of sulfate indicated

4.3.2.1.3 Water Incorporation

The amount of water incorporated into the compositions was calculated from the mass loss of the hydrated samples from TGA studies, Table 4.8.

Table 4.8 Water content for $Sr_2Sc_{2-x-y}Ga_yS_xO_{5+3x/2}$

Composition	% Mass Loss	Amount of water per formula unit
$Sr_2Sc_{0.9}GaS_{0.1}O_{5.15}$	0.14	0.03(1)
$Sr_2Sc_{0.6}Ga_{1.3}S_{0.1}O_{5.15}$	0.19	0.04(1)
$Sr_2Sc_{0.8}GaS_{0.2}O_{5.3}$	0.12	0.02(1)

All compositions showed limited water incorporation, indicating that not all the oxygen vacancies could be filled consistent with the results for the related phosphate doped systems.

4.3.2.2 Conductivity Measurements

Conductivities were collected in dry and wet N_2 atmospheres to remove any p-type contribution to the conductivity, and to determine if there was a protonic contribution to the

conductivity. Data was collected for all the compositions and all showed a reasonable ionic conductivity as well as a protonic contribution at low temperatures, although this contribution was significantly lower than that seen for the phosphate doped compositions, Table 4.9, Figure 4.20 and Figure 4.21. At high temperatures $Sr_2Sc_{0.9}GaS_{0.1}O_{5.15}$ and $Sr_2Sc_{0.6}Ga_{1.3}S_{0.1}O_{5.15}$ exhibited no difference between conductivities collected in wet and dry conditions showing there was no protonic contribution to the conductivity at this temperature.

Table 4.9 Bulk conductivity data for $Sr_2Sc_{2-x-y}Ga_yS_xO_{5+3x/2}$

Sample (nominal composition)	Conductivity (S cm^{-1})			
	500 °C		800 °C	
	Dry N_2	Wet N_2	Dry N_2	Wet N_2
$Sr_2Sc_{0.9}GaS_{0.1}O_{5.15}$	6.26 x 10^{-6}	1.16 x 10^{-5}	9.59 x 10^{-5}	1.01 x 10^{-4}
$Sr_2Sc_{0.6}Ga_{1.3}S_{0.1}O_{5.15}$	7.31 x 10^{-6}	1.16 x 10^{-5}	6.05 x 10^{-4}	6.46 x 10^{-4}
$Sr_2Sc_{0.8}GaS_{0.2}O_{5.3}$	5.04 x 10^{-6}	1.02 x 10^{-5}	8.05 x 10^{-5}	9.60 x 10^{-5}

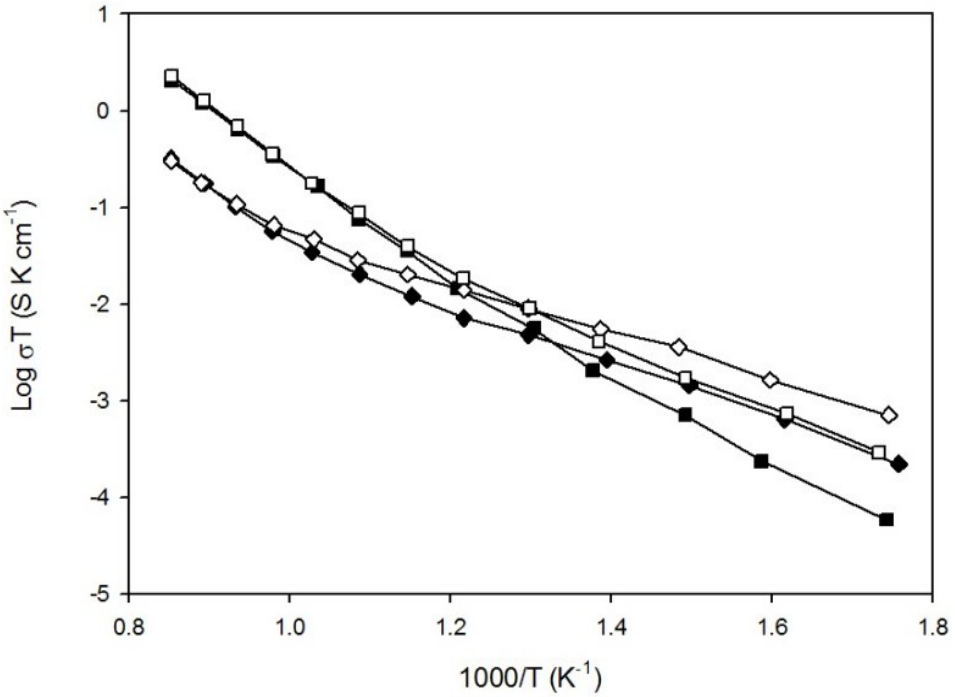

Figure 4.20 Conductivity data for $Sr_2Sc_{0.9}GaS_{0.1}O_{5.15}$ (diamond) and $Sr_2Sc_{0.6}Ga_{1.3}S_{0.1}O_{5.15}$ (square) in dry (filled) and wet (empty) N_2

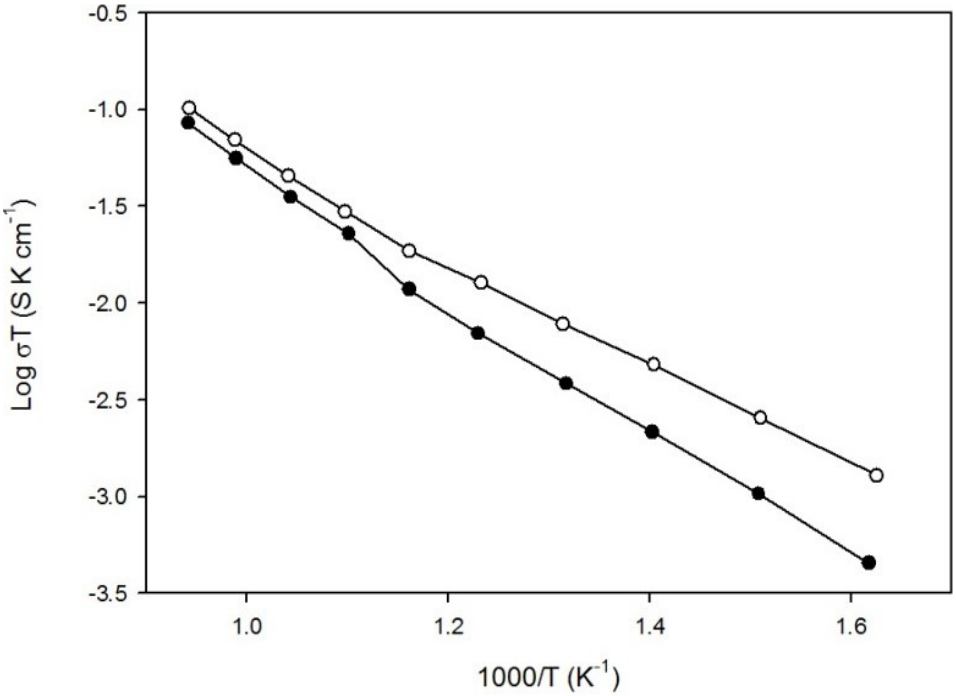

Figure 4.21 Conductivity data for $Sr_2Sc_{0.8}GaS_{0.2}O_{5.3}$ (circle) in dry (filled) and wet (empty) N_2

Unlike for the phosphate doped compositions there was an improvement in the conductivity upon increasing gallium content, and this was also opposite to that observed for oxyanion doped $Ba_2Sc_{2-y}Ga_yO_5$. The origin of this small improvement requires further investigation. The effect of sulfate on the conductivity was also analysed as two different compositions shared the same gallium content, and this showed that on increasing the sulfate content the conductivity decreased slightly. This is in agreement with the sulfate trapping the oxygen vacancies due to its tetrahedral coordination. There was also a much smaller difference between the dry and wet conductivities which is most likely due to the low water contents of these sulfate containing compositions.

The conductivities were then measured in a dry O_2 atmosphere to observe if there was any p-type conductivity, Figure 4.22.

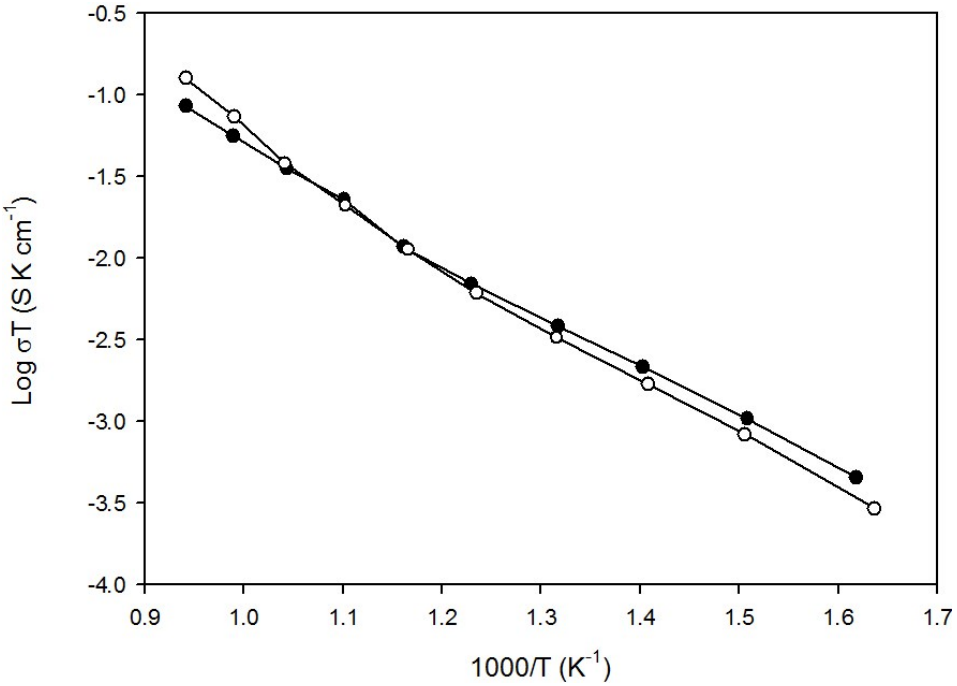

Figure 4.22 Conductivity data for $Sr_2Sc_{0.8}GaS_{0.2}O_{5.3}$ in dry N_2 (filled) and dry O_2 (empty)

While a small enhancement was seen at elevated temperatures in dry O_2, consistent with a p-type contribution, the conductivity at lower temperatures was slightly lowered. This requires further study, but may be related to the presence of a small amount of water in the "dry" gases.

4.3.2.3 CO_2 Stability

As with the phosphate doped samples, two experiments were carried out to determine the CO_2 stability of the sulfate doped compositions. The first involved using TGA studies to observe if a mass gain occurred (formation of $SrCO_3$) on heating from room temperature to 1000 °C at a heating rate of 10 °C min^{-1} under a flowing 1:1 mix of N_2 and CO_2. All the compositions showed no mass gain under these conditions.

The second experiment involved heating the compositions under flowing dry and wet CO_2, and using powder XRD to observe if any decomposition had occurred. All the compositions showed no formation of $SrCO_3$ after heating under flowing dry CO_2 at 800 °C, Figure 4.23.

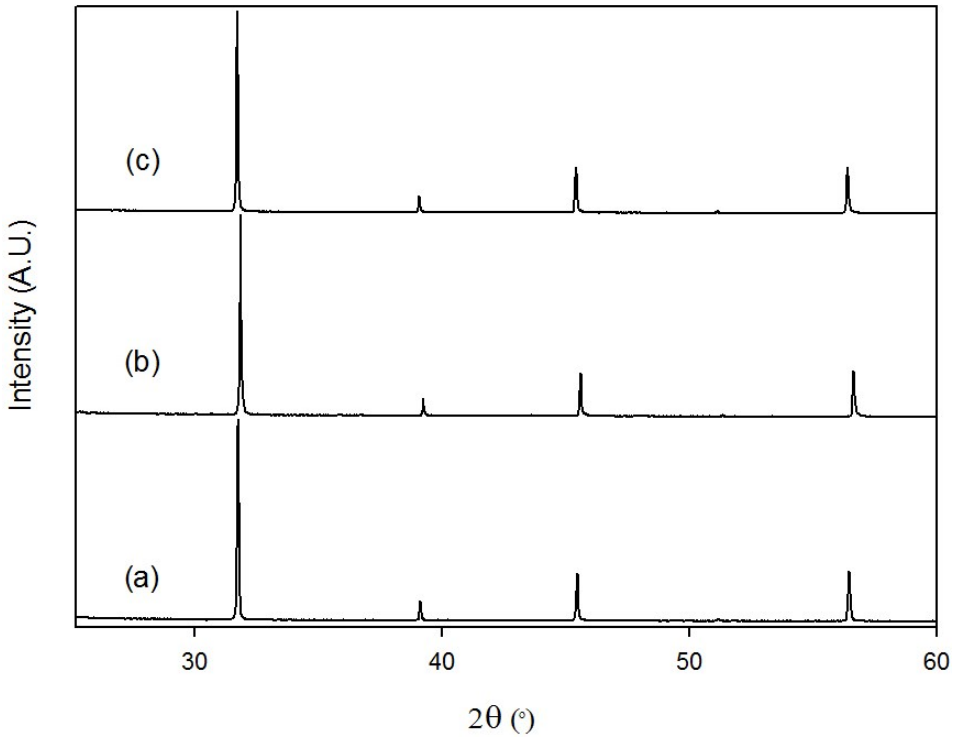

Figure 4.23 XRD patterns for ((a) $Sr_2Sc_{0.9}GaS_{0.1}O_{5.15}$, (b) $Sr_2Sc_{0.6}Ga_{1.3}S_{0.1}O_{5.15}$ and (c) $Sr_2Sc_{0.8}GaS_{0.2}O_{5.3}$ after heating in dry CO_2 at 800 °C for 12h

The composition with the lowest gallium content was then heated under flowing wet CO_2 to mimic even more extreme conditions, Figure 4.24.

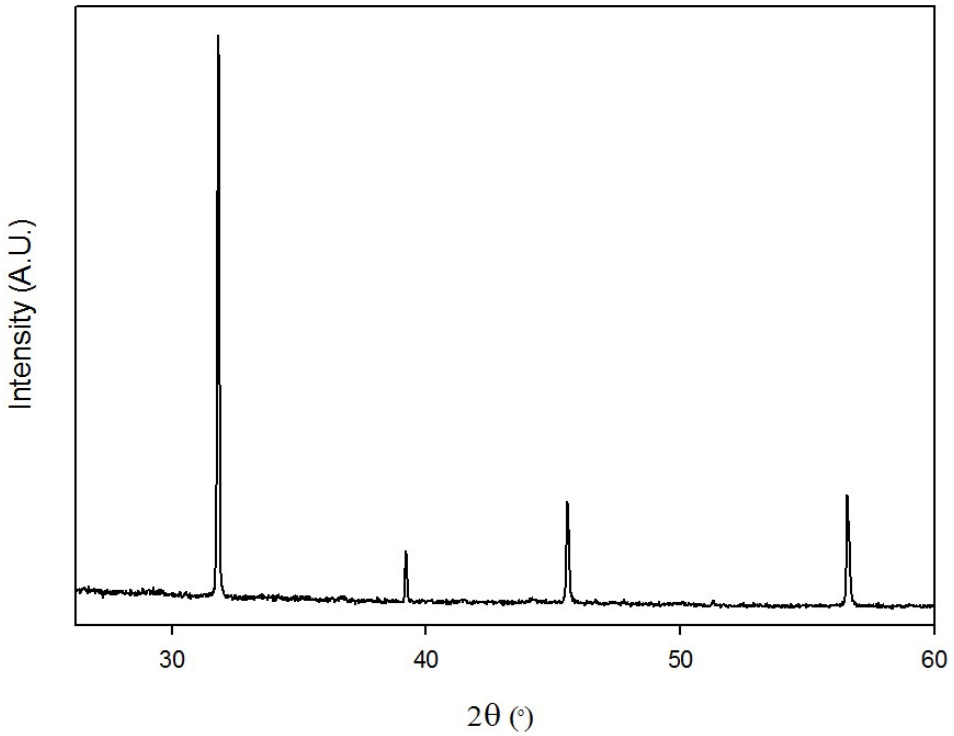

Figure 4.24 Powder XRD pattern of $Sr_2Sc_{0.8}GaS_{0.2}O_{5.3}$ after heat treatment at 800 °C for 12 hours under flowing wet CO_2

After treatment at these conditions $Sr_2Sc_{0.8}GaS_{0.2}O_{5.3}$ showed no sign of any degradation indicating that it shows excellent stability towards CO_2 as for the equivalent phosphate doped systems.

4.4 Conclusions

Powder X-ray diffraction data on a range of $Sr_2Sc_{2-x-y}Ga_yP_xO_{5+x}$ and $Sr_2Sc_{2-x-y}Ga_yS_xO_{5+3x/2}$ samples showed that they adopt a cubic perovskite structure with a space group *P m -3 m* and a lattice parameter in the range 3.99 Å to 4.04 Å. Raman data contained peaks that confirmed the presence of phosphate and sulfate. The water contents of hydrated samples were measured and shown to be low, attributed to the resistance of gallium and the oxyanions to accommodate water into the oxide ion vacancies around them.

The conductivities of the samples were determined and all compositions exhibited a relatively high conductivity but is inferior to $BaCe_{0.9}Y_{0.1}O_{2.95}$ with a protonic contribution and is lower than the barium based analogues; in addition increasing the gallium was generally found to lower the conductivity.

The CO_2 stabilities were measured and it was found that increasing the gallium content improved the relative stability, such that at operating temperatures for proton conducting SOFCs the gallium containing compositions were found to be completely stable with respect to CO_2. However applications in this respect would be limited by the lower conductivities compared to current generation acceptor doped $Ba(Zr/Ce)O_3$ systems.

4.5 References

1. H. Iwahara, *Solid State Ion.*, 1988, **28**, 573-578.
2. H. Uchida, A. Yasuda and H. Iwahara, *Denki Kagaku*, 1989, **57**, 153-156.
3. W. Zajac, D. Rusinek, K. Zheng and J. Molenda, *Central European Journal of Chemistry*, 2013, **11**, 471-484.
4. J. M. Porras-Vazquez, T. F. Kemp, J. V. Hanna and P. R. Slater, *J. Mater. Chem.*, 2012, **22**, 8287-8293.
5. J. M. Porras-Vazquez, E. R. Losilla, P. J. Keenan, C. A. Hancock, T. F. Kemp, J. V. Hanna and P. R. Slater, *Dalton Transactions*, 2013, **42**, 5421-5429.
6. J. M. Porras-Vazquez, T. Pike, C. A. Hancock, J. F. Marco, F. J. Berry and P. R. Slater, *Journal of Materials Chemistry A*, 2013, **1**, 11834-11841.
7. J. M. Porras-Vazquez and P. R. Slater, *Fuel Cells*, 2012, **12**, 1056-1063.
8. J. M. Porras-Vazquez and P. R. Slater, *J. Power Sources*, 2012, **209**, 180-183.
9. C. A. Hancock and P. R. Slater, *Dalton Transactions*, 2011, **40**, 5599-5603.
10. C. A. Hancock, R. C. T. Slade, J. R. Varcoe and P. R. Slater, *J. Solid State Chem.*, 2011, **184**, 2972-2977.
11. A. M. Abakumov, M. G. Rozova, B. P. Pavlyuk, M. V. Lobanov and E. V. Antipov, *J. Solid State Chem.*, 2001, **160**, 353-361.
12. S. V. Chernov, Y. A. Dobrovolsky, S. Y. Istomin, E. V. Antipov, J. Grins, G. Svensson, N. V. Tarakina, A. M. Abakumov, G. Van Tendeloo, S. G. Eriksson and S. M. H. Rahman, *Inorganic Chemistry*, 2012, **51**, 1094-1103.
13. A. C. Larson and R. B. Von Dreele, (1994), Los Alomos National Laboratory, Los Alomos NM.
14. R. D. Shannon, *Acta Crystallographica Section A*, 1976, **32**, 751-767.
15. L. J. Gillie, H. M. Palmer, A. J. Wright, J. Hadermann, G. Van Tendeloo and C. Greaves, *Journal of Physics and Chemistry of Solids*, 2004, **65**, 87-93.
16. K. Popa, R. J. M. Konings, O. Benes, T. Geisler and A. F. Popa, *Thermochimica Acta*, 2006, **451**, 1-4.
17. A. Mancini, J. F. Shin, A. Orera, P. R. Slater, C. Tealdi, Y. Ren, K. L. Page and L. Malavasi, *Dalton Transactions*, 2012, **41**, 50-53.
18. R. B. Cervera, S. Miyoshi, Y. Oyama, Y. E. Elammari, T. Yagi and S. Yamaguchi, *Chem. Mat.*, 2013, **25**, 1483-1489.
19. J. F. Shin, K. Joubel, D. C. Apperley and P. R. Slater, *Dalton Transactions*, 2012, **41**, 261-266.
20. J. F. Shin, A. Orera, D. C. Apperley and P. R. Slater, *J. Mater. Chem.*, 2011, **21**, 874-879.
21. P. Vargas Jentzsch, B. Kampe, V. Ciobota, P. Rosch and J. Popp, *Spectrochimica acta. Part A, Molecular and biomolecular spectroscopy*, 2013, **115**, 697-708.

Chapter 5 Synthesis and Characterisation of Phosphate Doped $BaCe_{1-x}(Y/Yb/In)_xO_{3-x/2}$

5.1 Introduction

Acceptor doped $BaCeO_3$ is a high temperature proton conductor in wet atmospheres that has attracted considerable interest as an electrolyte for proton conducting SOFCs since this property was discovered by Iwahara *et al*.[1-4] Substitution of cerium with a trivalent cation, for example Yb, Pr, Nd, Sm, Eu, Gd, Tb, Dy, Ho, Er, Tm, Lu and In, was found to introduce oxygen vacancies into the structure that could be filled with water according to the following equation.[5-17]

$$V_O^{\bullet\bullet} + O_O^x + H_2O \leftrightarrow 2\ OH_O^{\bullet}$$

The major drawback for doped $BaCeO_3$ is its instability to CO_2 atmospheres at fuel cell operating temperatures, 500-800 °C, as it forms $BaCO_3$ under these conditions.[18] To overcome this, co-doping with zirconium has been attempted, which while improving the stability in CO_2 atmospheres was found to decrease the conductivity.[19]

As noted previously by Soares *et al*., the effect of P additions in $BaCeO_3$ is also of relevance, since phosphate esters have been used as dispersants to prevent nanoparticle agglomeration in the preparation of related perovskite materials.[20] In this work it was shown that $(1 - x)BaY_{0.15}Zr_{0.85}O_{2.925}$:$xP_2O_5$ mixtures contained the presence of $Ba_3(PO_4)_2$ impurities which had a negative effect on the conductivity. However this particular study effectively takes compositions that would be A site deficient as P_2O_5 is added to $BaY_{0.15}Zr_{0.85}O_{2.925}$, which could explain the presence of phosphate impurities.[21-23]

Therefore in this chapter phosphate doping for cerium was attempted in $BaCe_{1-x}(Y/Yb/In)_xO_{3-x/2}$ with the aim of preparing single phase samples, in order to investigate if there was an improvement in the stability of the composition to CO_2, as seen for phosphate doped $Ba_2Sc_2O_5$, while retaining the high proton conductivities observed for $BaCe_{1-x}(Y/Yb/In)_xO_{3-x/2}$.[23]

5.2 Experimental Procedure

$BaCO_3$ (≥99%), CeO_2 (99.9%), Y_2O_3 (99.99%), Yb_2O_3 (99.99%), In_2O_3 (99.9%) and $NH_4H_2PO_4$ (≥98%) were used to prepare $Ba_2Ce_{2-y}Y_yP_xO_{6-y/2+x/2}$, $Ba_2Ce_{2-y}Yb_yP_xO_{6-y/2+x/2}$ and $Ba_2Ce_{2-y}In_yP_xO_{6-y/2+x/2}$ samples using the standard ceramic synthesis method. A small (3%) excess of $BaCO_3$ was employed, in order to overcome Ba loss at elevated temperatures as has been seen in other studies synthesising similar Ba containing phases.[22] The powders were intimately ground in an agate pestle and mortar and heated initially to 1000 °C for 12 hours. They were then ball-milled (350 rpm for 1 hour, Fritsch Pulverisette 7 Planetary Mill) and reheated to 1400 °C for 12 hours. The resulting powders were then ball-milled (350 rpm for 1 hour, Fritsch Pulverisette 7 Planetary Mill) a second time and pressed as pellets (1.3 cm diameter) and heated again at 1400 °C for 12 hours. The pellets were covered in sample powder and the crucible was covered with a lid to limit the amount of Ba loss during the sintering process. Powder X-ray diffraction (Bruker D8 diffractometer with Cu $K\alpha_1$ radiation) was used to demonstrate phase purity as well as for preliminary structure determination once a pure phase was obtained. For the latter, the GSAS suite of programs was used.[24]

Raman spectroscopy measurements were made in order to provide further evidence for the successful incorporation of phosphate. These measurements utilised a Renishaw inVia Raman microscope with excitation using a Cobolt Samba CW 532 nm DPSS Laser.

The samples were hydrated by heating up to 800 °C under flowing wet N_2 and then slow cooling (0.4 °C min^{-1}). The water contents of hydrated samples were determined from thermogravimetric analysis (Netzsch STA 449 F1 Jupiter Thermal Analyser). Samples were heated at 10 °C min^{-1} to 1000 °C in N_2, and the water content was determined from the observed mass loss.

For the conductivity measurements, the sintered pellets (>80%) were coated with Pt paste, and then heated to 800 °C for 1 hour to ensure bonding to the pellet. Conductivities were then measured by AC impedance measurements (Hewlett Packard 4192A impedance analyser) in the range from 0.1 to 1.3 x 10^3 kHz. Measurements were made in dry N_2 and wet N_2 (in which the gas was bubbled at room temperature through water) to identify any protonic contribution to the conductivity. Measurements were also made in dry O_2 to determine if there was a p-type electronic contribution to the conductivity. The impedance spectra typically showed the overlapping of bulk and grain boundary components making separation of the bulk and grain boundary components difficult, Figure 5.1. Therefore conductivities are reported as the total conductivity.

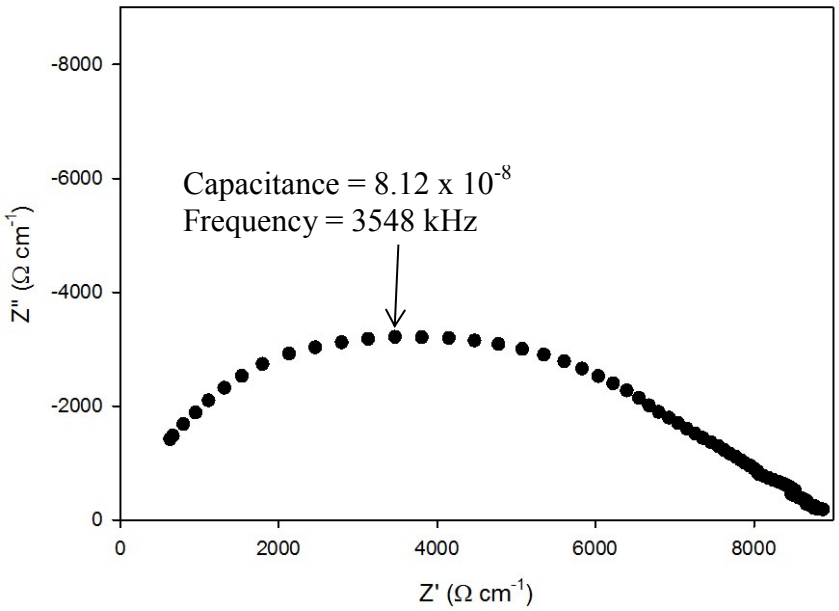

Figure 5.1 Impedance spectra for $BaCe_{0.75}In_{0.2}P_{0.05}O_{2.925}$ at 590 °C in dry N_2

The CO_2 stability of the samples was determined using thermogravimetric analysis (Netzsch STA 449 F1 Jupiter Thermal Analyser). Samples were heated at 10°C min^{-1} to 1000°C in 1:1 CO_2 and N_2 mixture to determine at what temperature CO_2 pick up occurred.

5.3 Results and Discussion

5.3.1 $BaCe_{1-y-x}Y_yP_xO_{3-y/2+x/2}$

5.3.1.1 Structural Determination

5.3.1.1.1 Powder X-ray Diffraction

Initial results found that for low levels of yttrium ($y < 0.2$) it was not possible to introduce phosphate into $BaCe_{1-y}Y_yO_{3-y/2}$ in agreement with the results found by Soares *et al*. on P_2O_5 additions to $BaY_{0.15}Zr_{0.85}O_{2.925}$.[20] For example the attempted synthesis of $BaY_{0.1}Ce_{0.8}P_{0.1}O_3$ was found to contain $Ba_{10}(PO_4)_6(OH)_2$, Figure 5.2. The presence of this impurity can most probably be related to the need for significant oxygen vacancies to accommodate phosphate,

as phosphate adopts a tetrahedral coordination, and this stoichiometry nominally contains no oxygen vacancies.

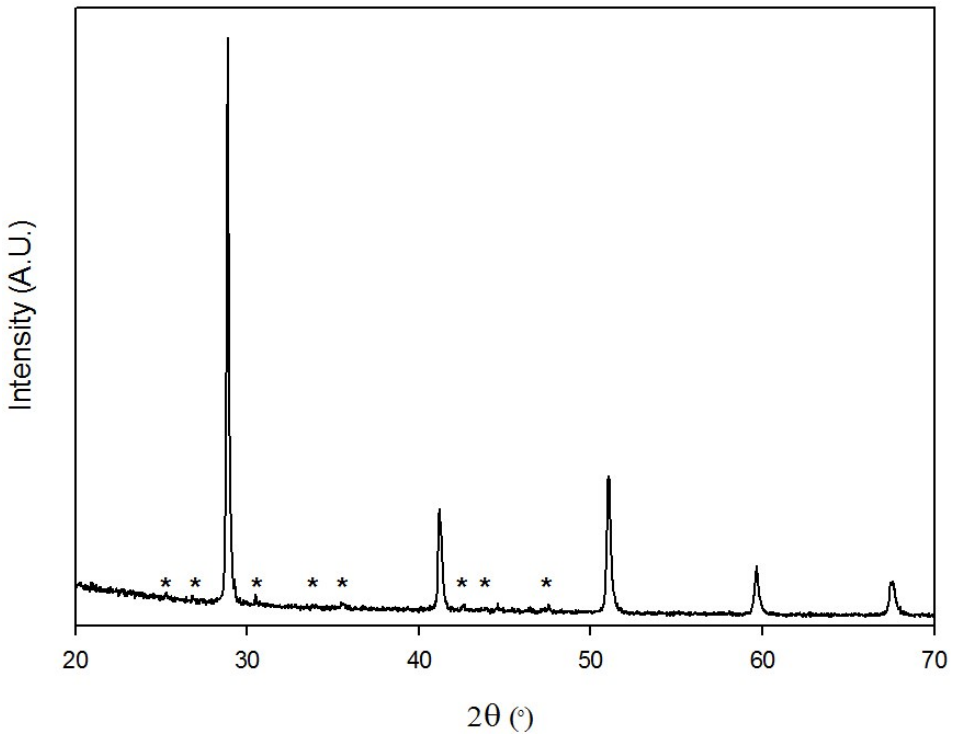

Figure 5.2 Powder X-ray diffraction data for attempted synthesis of "$BaY_{0.1}Ce_{0.8}P_{0.1}O_3$" with peaks for $Ba_{10}(PO_4)_6(OH)_2$ indicated

In agreement with this conclusion, increasing the yttrium content resulted in the formation of single phase phosphate doped samples due to the increased number of oxygen vacancies, showing that phosphate can be successfully doped directly onto the B-site. Therefore the results indicated that provided the yttrium content is sufficiently high, phosphate can be incorporated into this system. The powder X-ray diffraction patterns, Figure 5.3, showed single phase compositions for (x= 0.05, y= 0.2, 0.25, 0.3; x= 0.1, y= 0.3).

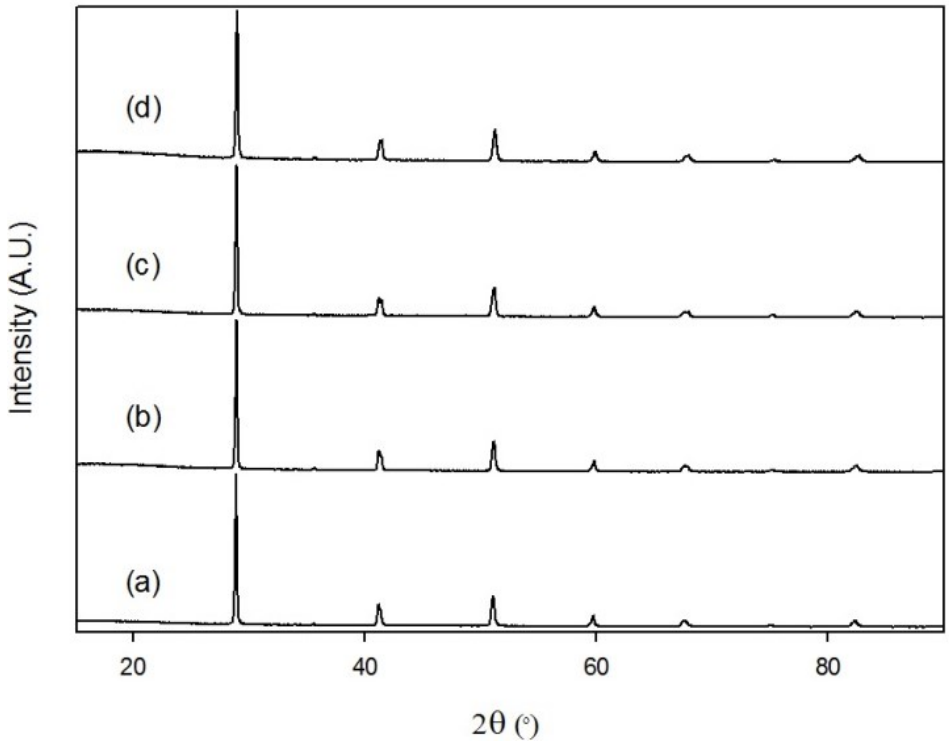

Figure 5.3 Powder X-ray diffraction data of (a) $BaCe_{.75}Y_{0.2}P_{0.05}O_{2.925}$, (b) $BaCe_{0.7}Y_{0.25}P_{0.05}O_{2.9}$, (c) $BaCe_{0.65}Y_{0.3}P_{0.05}O_{2.875}$ and (d) $BaCe_{0.6}Y_{0.3}P_{0.1}O_{2.9}$

Higher yttrium contents were attempted but single phase compositions could not be obtained, for example the attempted synthesis of $BaCe_{0.5}Y_{0.4}P_{0.1}O_{2.85}$ resulted in the formation of the yttrium rich phase $Ba_3Y_4O_9$, Figure 5.4, alongside a doped barium cerate.

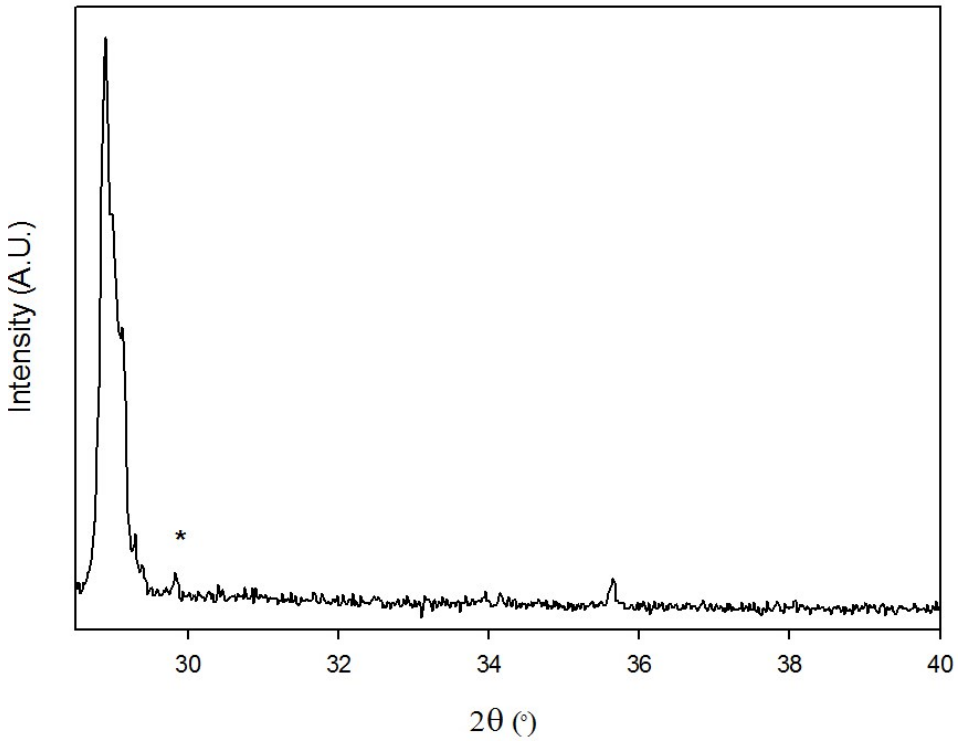

Figure 5.4 Powder X-ray diffraction data of attempted synthesis of "$BaCe_{0.5}Y_{0.4}P_{0.1}O_{2.85}$" with impurity peak indicated

Rietveld refinement was carried out on the pure phases to determine the lattice parameters and obtain structural information using the GSAS suite of programs.[24] A structural model using space group *P m c n*, as reported by Knight *et al*. was used.[25] The cerium, yttrium and phosphorus were placed on the *4b* site using the expected stoichiometric amounts. The oxygen sites had their fractional occupancies set to the correct amount for the oxidation states of the cations. The work carried out by Knight *et al*. showed that the oxygen vacancies preferentially occupied the O(2) site, however due to the coordination of the phosphate and the lack of sensitivity of oxygen to X-rays, in these refinements the oxygen vacancies were split across both oxygen sites. The refinements gave good agreement with the collected X-ray diffraction patterns and showed a decreasing lattice parameter with increasing yttrium and phosphate content. The decrease in lattice parameter with increasing yttrium content is unexpected due to the smaller size of Ce^{4+} (0.87 Å) compared to Y^{3+} (0.9 Å).[26] Previous work by Wu *et al*. had reported that B-site trivalent dopants could be partially substituted onto the

barium site and so further refinements investigating this possibility were carried out.[27] Such a refinement did suggest reduced X-ray scattering at the Ba-site consistent with partial yttrium substitution, although another possibility is simply the presence of A site vacancies. These factors will be discussed further in section 5.3.1.1.3. The following lattice parameters were obtained and compared with $BaCe_{0.8}Y_{0.2}O_{2.9}$, Table 5.1, with the observed, calculated and difference profiles for $BaCe_{0.7}Y_{0.25}P_{0.05}O_{2.9}$ and the complete description of the refined model shown in, Figure 5.5 and Table 5.2.

Table 5.1 Lattice parameters for $BaCe_{1-y-x}Y_yP_xO_{3-y/2+x/2}$

Composition	a (Å)	b (Å)	c (Å)	Unit Cell Volume (Å^3)
$BaCe_{0.8}Y_{0.2}O_{2.9}$	8.9137(9)	6.1815(6)	6.1793(7)	340.48(8)
$BaCe_{0.75}Y_{0.2}P_{0.05}O_{2.925}$	8.7431(3)	6.1998(2)	6.2186(2)	337.09(2)
$BaCe_{0.7}Y_{0.25}P_{0.05}O_{2.9}$	8.7363(3)	6.1978(2)	6.2188(2)	336.73(2)
$BaCe_{0.65}Y_{0.3}P_{0.05}O_{2.875}$	8.7302(4)	6.1969(3)	6.2191(2)	336.46(3)
$BaCe_{0.6}Y_{0.3}P_{0.1}O_{2.9}$	8.7240(5)	6.1856(3)	6.2061(3)	334.90(3)

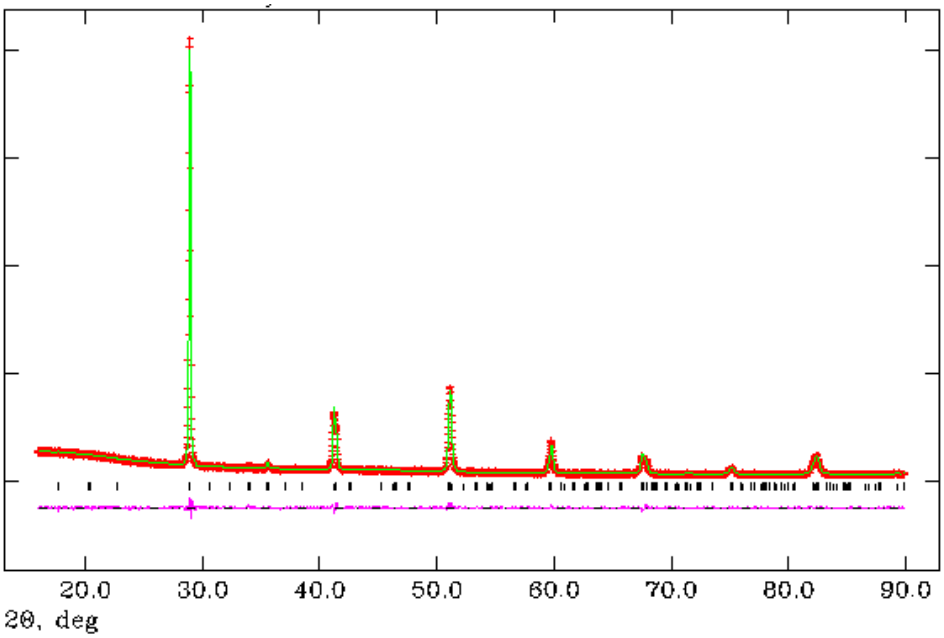

Figure 5.5 Observed, calculated and difference plots for structural refinement of $BaCe_{0.7}Y_{0.25}P_{0.05}O_{2.9}$ using X-ray powder diffraction data

Table 5.2 Structural detail for $BaCe_{0.7}Y_{0.25}P_{0.05}O_{2.9}$

	Site	x	y	z	Fraction	100 U ($Å^2$)
Ba	4c	0.25	0	0	1	2.6(1)
Ce	4b	0	0.5	0	0.7	1.4(1)
Y	4b	0	0.5	0	0.25	1.4(1)
P	4b	0	0.5	0	0.05	1.4(1)
O	4c	0.25	0.4	0	0.9667	4.5(3)
O	8d	0.5	0	0	0.9667	4.5(3)
Space Group = *P m c n*, a = 8.7363(3) Å, b = 6.1978(2) Å, c = 6.2188(2) Å, unit cell volume = 336.73(2) $Å^3$ wR_p = 4.37%, R_p = 3.81%, χ^2 = 1.611						

As mentioned previously, the lattice parameters decrease with increased yttrium doping despite the larger ionic size of yttrium compared with cerium, due to either some yttrium or A site vacancies on the barium site, most likely associated with barium loss during the high temperature synthesis. The collected data also shows that on increasing phosphate doping the lattice parameter decreases, consistent with phosphorus having a smaller ionic radius (0.17 Å) compared to cerium (0.87 Å).[26]

5.3.1.1.2 Raman Spectroscopy

To provide confirmation of the presence of phosphate in the compositions, Raman spectroscopy data were collected on all the pure phosphate doped compositions and $BaCe_{0.8}Y_{0.2}O_{2.9}$, Figure 5.6.

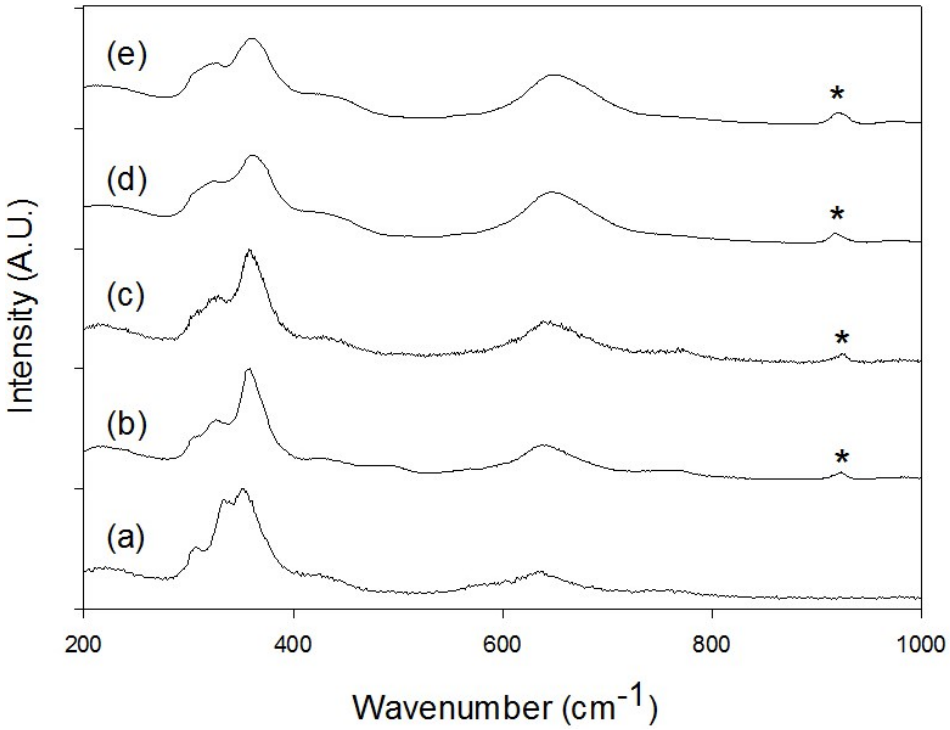

Figure 5.6 Raman spectra of (a) $BaCe_{0.8}Y_{0.2}O_{2.9}$, (b) $BaCe_{0.75}Y_{0.2}P_{0.05}O_{2.925}$, (c) $BaCe_{0.7}Y_{0.25}P_{0.05}O_{2.9}$, (d) $BaCe_{0.65}Y_{0.3}P_{0.05}O_{2.875}$ and (e) $BaCe_{0.6}Y_{0.3}P_{0.1}O_{2.9}$ with the main peak showing the presence of phosphate indicated

The data showed that all the phosphate containing compositions had a band at ~940 cm^{-1}, the internal stretching mode of phosphate, which was not seen in the $BaCe_{0.8}Y_{0.2}O_{2.9}$ data, consistent with the incorporation of phosphate.[28] The series of bands in the range 300-375 cm^{-1} are assigned to bending modes of O-Ce/Y-O and the band at 630 cm^{-1} is attributed to the Ce/Y-O stretching mode of the perovskite.[29, 30] The band due to the bending mode of phosphate, 415 cm^{-1}, was not seen due to the low intensity of the Raman bands due to phosphate, compared with the bands due to bending modes of O-Ce/Y-O.

5.3.1.1.3 Water Incorporation

The water uptake of the hydrated samples were determined from the resulting mass loss from TGA studies with the data shown in Table 5.3.

Table 5.3 Water content for $BaCe_{1-y-x}Y_yP_xO_{3-y/2+x/2}$

Composition	% Mass Loss	Amount of water per formula unit
$BaCe_{0.8}Y_{0.2}O_{2.9}$	0.58	0.10(1)
$BaCe_{0.75}Y_{0.2}P_{0.05}O_{2.925}$	0.15	0.03(1)
$BaCe_{0.7}Y_{0.25}P_{0.05}O_{2.9}$	0.68	0.11(1)
$BaCe_{0.65}Y_{0.3}P_{0.05}O_{2.875}$	0.56	0.09(1)
$BaCe_{0.6}Y_{0.3}P_{0.1}O_{2.9}$	0.33	0.05(1)

The results indicate that for 2 of the phases, $BaCe_{0.8}Y_{0.2}O_{2.9}$ and $BaCe_{0.7}Y_{0.25}P_{0.05}O_{2.9}$, all the oxygen vacancies could be filled. However, as noted earlier, it is possible that there could be some yttrium content on the A cation site or some A site deficiency. Given the fact that partial yttrium substitution on the A site would significantly reduce the oxygen vacancy content and hence the water incorporation, the observed water contents could indicate that the lower X-ray scattering for the barium site is due to A site cation vacancies. Increasing the phosphate content was found to reduce the water content in agreement with the tetrahedral coordination of phosphate limiting the vacancies that can be filled, as seen by Shin *et al*. for phosphate doped $Ba_2(In/Sc)O_5$ and in work covered in the previous chapters.[22, 23]

5.3.1.2 Conductivity Measurements

Conductivity data were collected on all the single phase compositions in N_2 atmospheres, to remove any p-type conduction, and comparing wet and dry conditions to determine if any proton conduction was present. All compositions showed a high total conductivity with a protonic contribution; the conductivities of $BaCe_{0.8}Y_{0.2}O_{2.9}$ are also included for comparison, Table 5.4, Figure 5.7 and Figure 5.8.

Table 5.4 Total conductivity data for $BaCe_{1-y-x}Y_yP_xO_{3-y/2+x/2}$

Sample (nominal composition)	Conductivity (S cm^{-1})			
	500 °C		800 °C	
	Dry N_2	Wet N_2	Dry N_2	Wet N_2
$BaCe_{0.8}Y_{0.2}O_{2.9}$	3.7×10^{-3}	3.7×10^{-3}	2.4×10^{-2}	1.9×10^{-2}
$BaCe_{0.75}Y_{0.2}P_{0.05}O_{2.925}$	1.4×10^{-3}	1.7×10^{-3}	4.9×10^{-3}	5.9×10^{-3}
$BaCe_{0.7}Y_{0.25}P_{0.05}O_{2.9}$	1.4×10^{-3}	2.1×10^{-3}	6.0×10^{-3}	7.3×10^{-3}
$BaCe_{0.65}Y_{0.3}P_{0.05}O_{2.875}$	2.0×10^{-3}	2.5×10^{-3}	6.8×10^{-3}	8.2×10^{-3}
$BaCe_{0.6}Y_{0.3}P_{0.1}O_{2.9}$	1.2×10^{-3}	1.4×10^{-3}	3.3×10^{-3}	4.1×10^{-3}

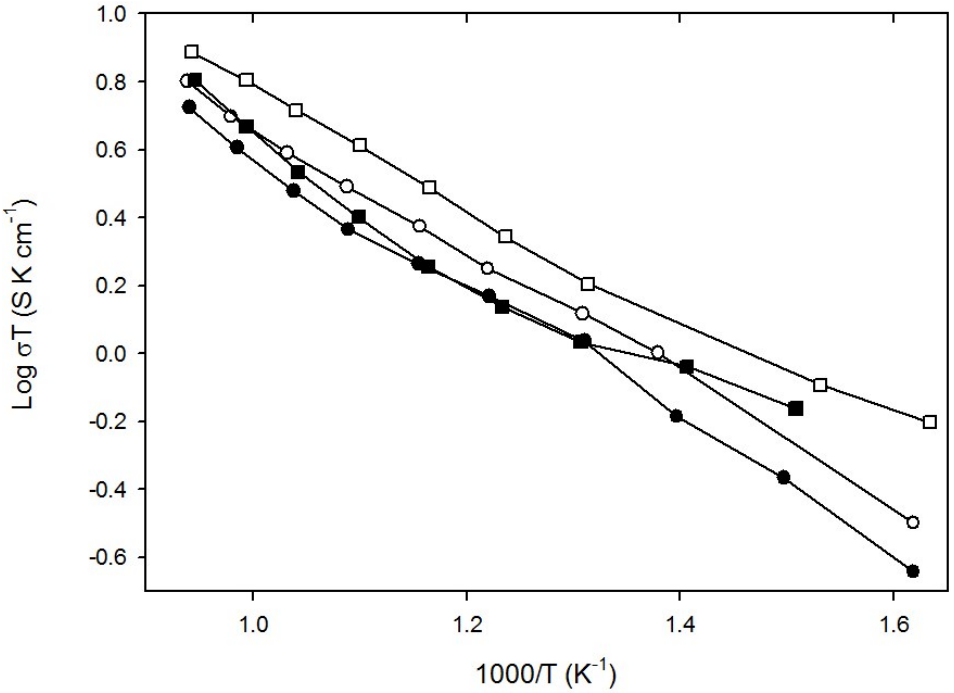

Figure 5.7 Conductivity data for $BaCe_{0.75}Y_{0.2}P_{0.05}O_{2.925}$ (circle) and $BaCe_{0.7}Y_{0.25}P_{0.05}O_{2.9}$ (square) in dry (filled) and wet (empty) N_2

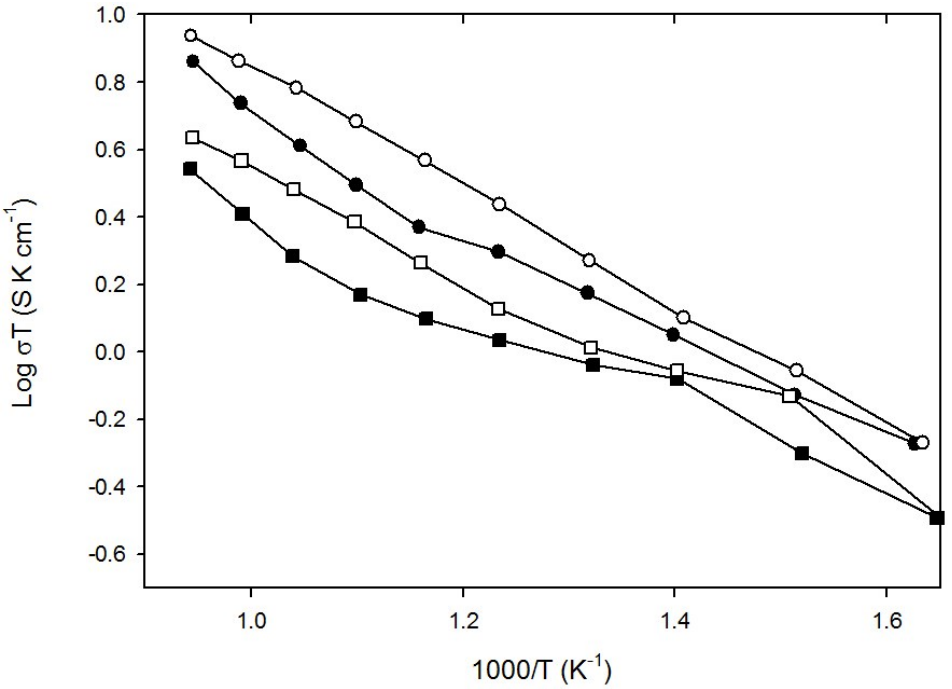

Figure 5.8 Conductivity data for $BaCe_{0.65}Y_{0.3}P_{0.05}O_{2.875}$ (circle) and $BaCe_{0.6}Y_{0.3}P_{0.1}O_{2.9}$ (square) in dry (filled) and wet (empty) N_2

The collected data showed that increasing the phosphate content lowered the conductivity as found for the $Ba_2Sc_{2-x-y}Ga_yP_xO_{5+x}$ series, due to the reduction in the number of mobile oxygen vacancies caused by the tetrahedral coordination of phosphate. All the compositions exhibited lower ionic conductivities than non-phosphate containing $BaCe_{0.8}Y_{0.2}O_{2.9}$ suggesting that phosphate doping is not a successful strategy for improving the oxide or proton conductivity of $BaCeO_3$ in contrast with the results found for phosphate doped $Ba_2In_2O_5$.[21] However this comparison with $BaCe_{0.8}Y_{0.2}O_{2.9}$ may not be fair due to the difference in oxygen coordination around the B cation site. The data also showed that increasing the yttrium content improved the conductivity in agreement with the increased number of oxygen vacancies improving the ionic conductivity. The level of phosphate doping was found not to affect the activation energy as the activation energies in wet N_2 were in the range 0.30 to 0.37 eV similar to the activation energy of yttrium doped barium cerate, $BaCe_{0.8}Y_{0.2}O_{2.9}$ (0.44 eV).[31] To determine if a p-type contribution to the conductivity is present the conductivities of the samples were also examined in a dry O_2 atmosphere and an example is shown in Figure 5.9.

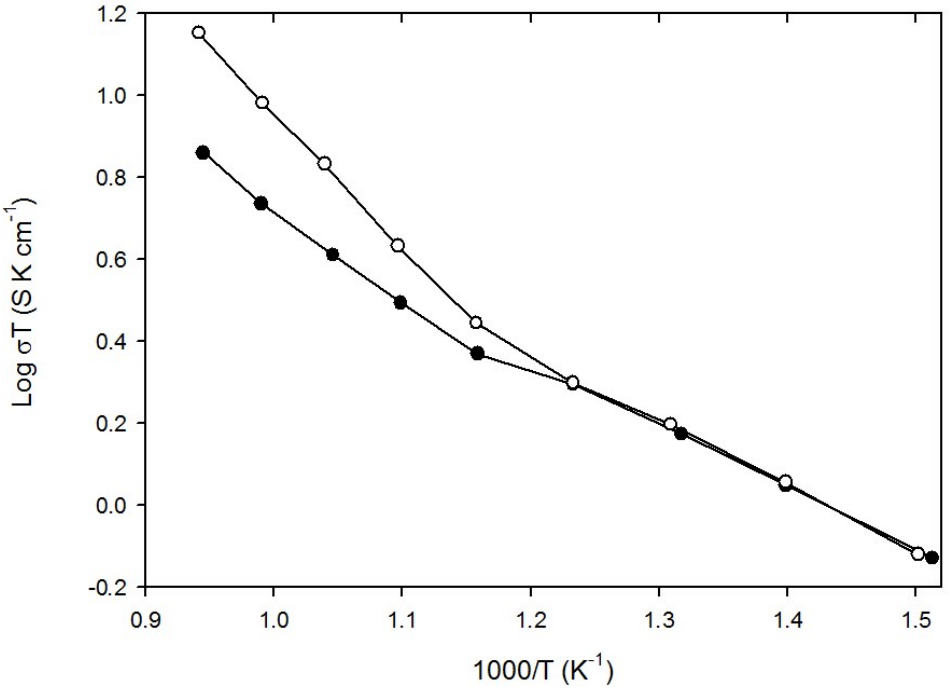

Figure 5.9 Conductivity data between 400 °C and 800 °C for $BaCe_{0.65}Y_{0.3}P_{0.05}O_{2.875}$ in dry N_2 (filled circle) and dry O_2 (empty circle)

The collected data confirmed the presence of a p-type contribution to the conductivity at elevated temperatures as seen for both the $Ba_2Sc_{2-x-y}Ga_yP_xO_{5+x}$ and $Sr_2Sc_{2-x-y}Ga_yP_xO_{5+x}$ series. The origin of this conductivity is due to the creation of holes according the equation $V_O^{\bullet\bullet} + O_O^x + 0.5O_2 \leftrightarrow 2O_O^{\bullet}$.

5.3.1.3 CO_2 Stability

Due to the aforementioned lack of stability of doped barium cerate to CO_2 atmospheres, the stability of these phosphate doped compositions was examined using TGA analysis to determine whether the phosphate doping improved this stability. The temperature of mass gain in a CO_2 atmosphere is shown in Table 5.5.

Table 5.5 Temperature for uptake of CO_2 for $BaCe_{1-y-x}Y_yP_xO_{3-y/2+x/2}$ from TGA studies up to 1000 °C

Composition	Temperature of Mass Gain
$BaCe_{0.8}Y_{0.2}O_{2.9}$	450 °C
$BaCe_{0.75}Y_{0.2}P_{0.05}O_{2.925}$	450 °C
$BaCe_{0.7}Y_{0.25}P_{0.05}O_{2.9}$	450 °C
$BaCe_{0.65}Y_{0.3}P_{0.05}O_{2.875}$	450 °C
$BaCe_{0.6}Y_{0.3}P_{0.1}O_{2.9}$	450 °C

These data showed that there were no improvements in the stability of $BaCe_{1-y-x}Y_yP_xO_{3-y/2+x/2}$, as all compositions showed a mass gain at 450 °C under a flowing 1:1 N_2:CO_2 mixture.

5.3.2 $BaCe_{1-y}Yb_yO_{3-y/2}$

5.3.2.1 Structural Determination

5.3.2.1.1 Powder X-ray Diffraction

As phosphate doping of the yttrium containing compositions was not possible for low yttrium contents, the initial compositions examined for the $BaCe_{1-y-x}Yb_yP_xO_{3-y/2+x/2}$ series were the same stoichiometry that resulted in pure phases for yttrium doping, i.e. x= 0.05, y= 0.2, 0.25, 0.3; x= 0.1, y= 0.3). All these compositions resulted in single phase samples, Figure 5.10.

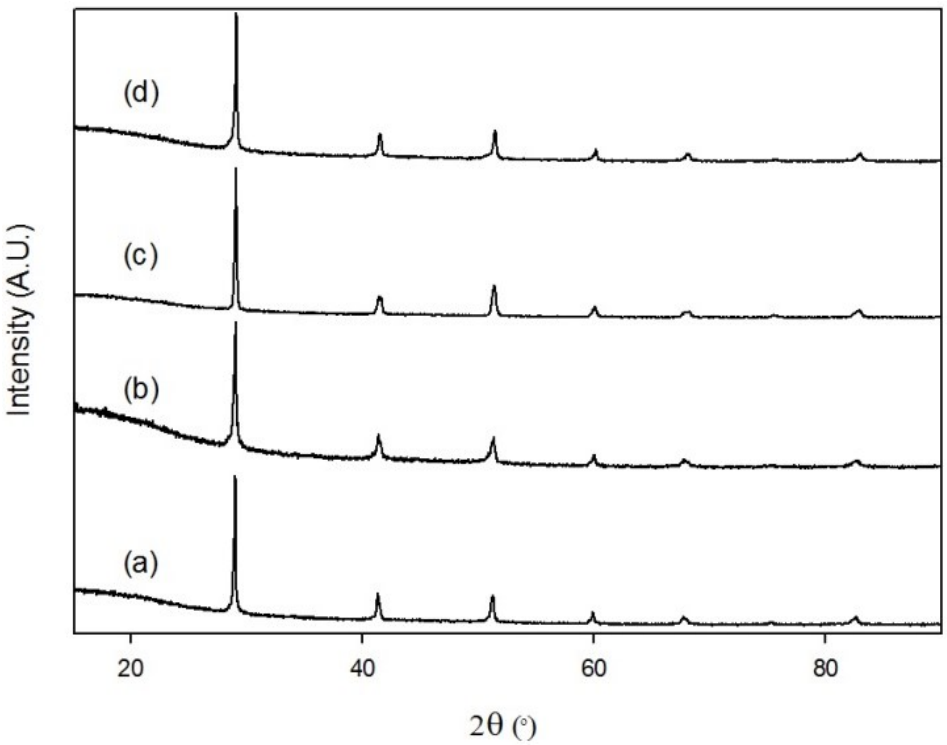

Figure 5.10 Powder X-ray diffraction data of (a) $BaCe_{.75}Yb_{0.2}P_{0.05}O_{2.925}$, (b) $BaCe_{0.7}Yb_{0.25}P_{0.05}O_{2.9}$, (c) $BaCe_{0.65}Yb_{0.3}P_{0.05}O_{2.875}$ and (d) $BaCe_{0.6}Yb_{0.3}P_{0.1}O_{2.9}$

Higher ytterbium contents were attempted but, as in the case for the yttrium doped analogues, impurity phases, in this case $Ba_3Yb_4O_9$, alongside a doped barium cerate phase were found to form, Figure 5.11.

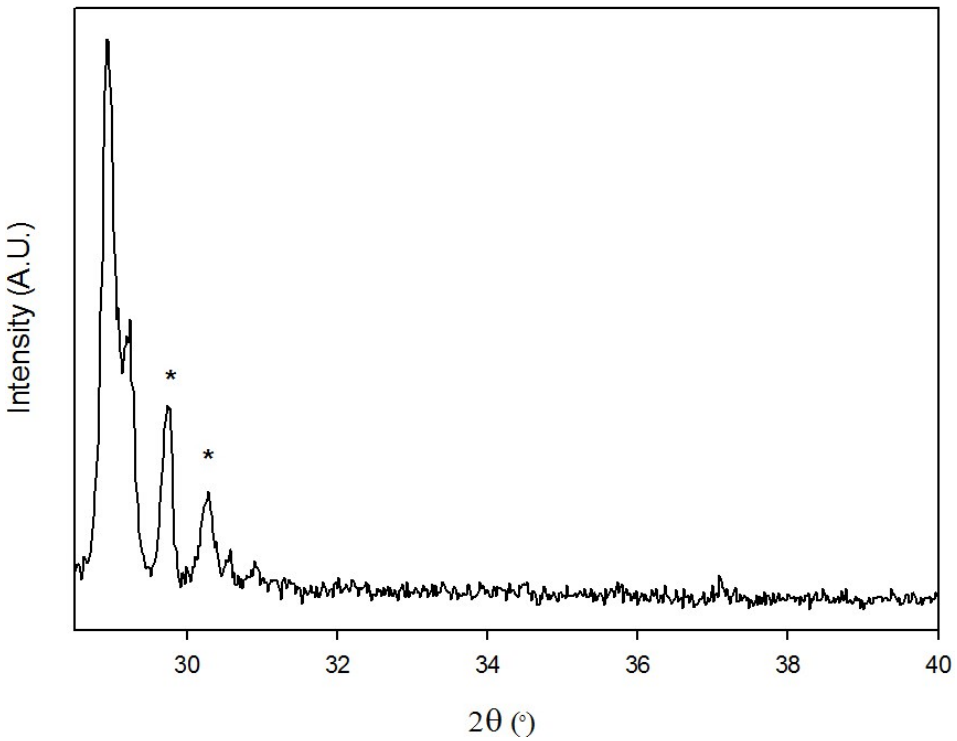

Figure 5.11 Powder X-ray diffraction data of attempted synthesis of "$BaCe_{0.5}Yb_{0.4}P_{0.1}O_{2.85}$" with impurity peaks indicated

Some further work showed that it was possible to synthesise an endmember phase, believed to be $BaYb_{0.75}P_{0.25}O_{2.75}$, containing only ytterbium and phosphorus on the B site, but it has so far not been possible to prepare this phase pure, with significant $Ba_3Yb_4O_9$ impurities observed, Figure 5.12. Further work including lower temperature synthesis routes are required to overcome this problem.

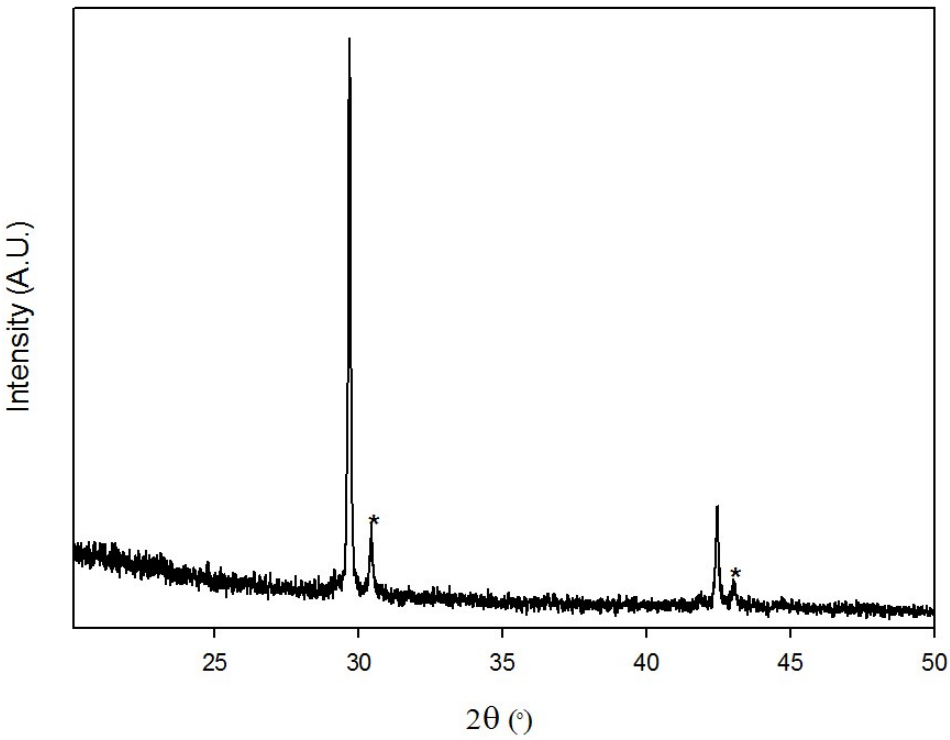

Figure 5.12 Powder X-ray diffraction data of attempted synthesis of "$BaYb_{0.75}P_{0.25}O_{2.75}$" with $Ba_3Yb_4O_9$ peak indicated

Rietveld refinement using the GSAS suite of programs was carried out on the pure phases.[24] The same structural model, as for the yttrium phase, was used in these refinements, with space group *P m c n*. Cerium, ytterbium and phosphorus were placed on the *4b* site using the expected stoichiometry as the fractional occupancies. The oxygen occupancy was set to the calculated amount from the cation oxidation states, with the vacancies split across both oxygen sites as for the yttrium compositions, and not refined due to the lack of sensitivity of oxygen to X-rays. The refinements gave good agreement with the collected X-ray diffraction patterns and the following lattice parameters were obtained, Table 5.6, with the observed, calculated and difference profiles and the complete description of the refined structural model of $BaCe_{0.65}Yb_{0.3}P_{0.05}O_{2.875}$ shown in Figure 5.13 and Table 5.7.

Table 5.6 Lattice parameters for $BaCe_{1-y-x}Yb_yP_xO_{3-y/2+x/2}$

Composition	a (Å)	b (Å)	c (Å)	Unit Cell Volume (Å^3)
$BaCe_{0.8}Yb_{0.2}O_{2.9}$	8.8637(5)	6.1677(4)	6.1682(4)	337.214
$BaCe_{0.75}Yb_{0.2}P_{0.05}O_{2.925}$	8.7267(6)	6.1815(4)	6.2113(4)	335.06(5)
$BaCe_{0.7}Yb_{0.25}P_{0.05}O_{2.9}$	8.718(1)	6.174(1)	6.213(1)	334.4(1)
$BaCe_{0.65}Yb_{0.3}P_{0.05}O_{2.875}$	8.6973(5)	6.1714(4)	6.1964(3)	332.59(4)
$BaCe_{0.6}Yb_{0.3}P_{0.1}O_{2.9}$	8.697(1)	6.1578(6)	6.1892(6)	331.49(7)

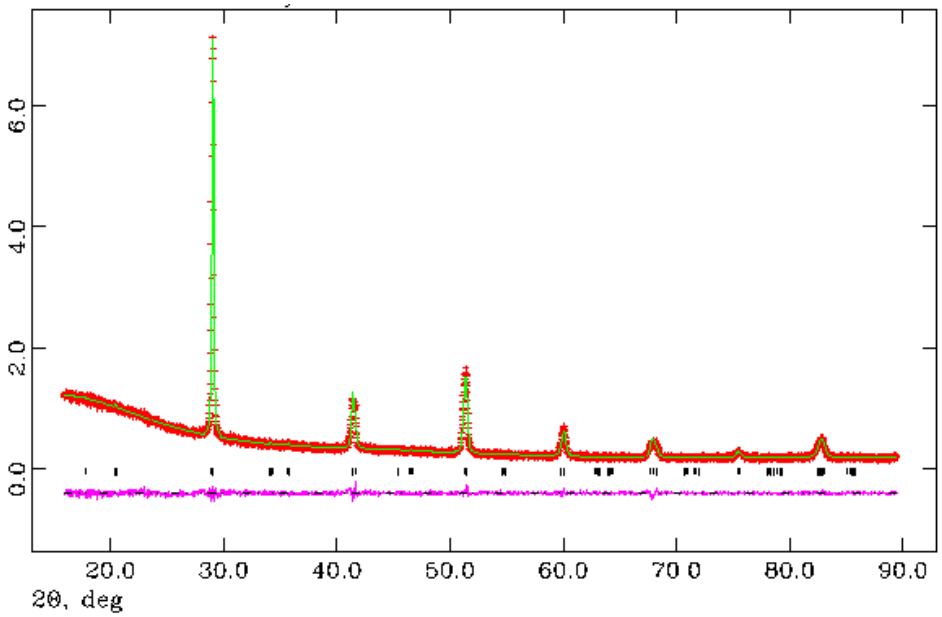

Figure 5.13 Observed, calculated and difference plots for structural refinement of $BaCe_{0.65}Yb_{0.3}P_{0.05}O_{2.875}$ using X-ray powder diffraction data

Table 5.7 Structural detail for $BaCe_{0.65}Yb_{0.3}P_{0.05}O_{2.875}$

	Site	x	y	z	Fraction	100 U (Å^2)
Ba	4c	0.25	0	0	1	1.6(2)
Ce	4b	0	0.5	0	0.65	1.4(2)
Yb	4b	0	0.5	0	0.3	1.4(2)
P	4b	0	0.5	0	0.05	1.4(2)
O	4c	0.25	0.4	0	0.9583	2.9(5)
O	8d	0.5	0	0	0.9583	2.9(5)
Space Group = *P m c n*, a = 8.6973(5) Å, b = 6.1714(4) Å, c = 6.1964(3) Å, unit cell volume = 332.59(4) Å^3 wR_p = 5.31%, R_p = 4.56%, χ^2 = 1.248						

The collected data showed that the lattice parameter decreased on increased ytterbium and phosphorus content. This is in agreement with both phosphorus (0.17 Å) and ytterbium (0.868 Å) having a smaller ionic radius than cerium (0.87 Å).[26] As cerium and ytterbium have very

close ionic radii the difference in cell volume between the compositions can also be attributed to the increased amount of oxygen vacancies as the ytterbium content is increased. In addition Wu *et al*. found that ytterbium could be doped onto the barium site if the composition was barium deficient, however further refinements on these samples suggested this not to be happening with these samples; as whenever ytterbium was placed onto the barium site negative occupancies for ytterbium were obtained and no barium deficiency was inferred.[27]

5.3.2.1.2 Raman Spectroscopy

To confirm the presence of phosphate in $BaCe_{1-y-x}Yb_yP_xO_{3-y/2+x/2}$ Raman spectroscopy data were collected on all the pure compositions, as well as $BaCe_{0.8}Yb_{0.2}O_{2.9}$ for comparison, Figure 5.14.

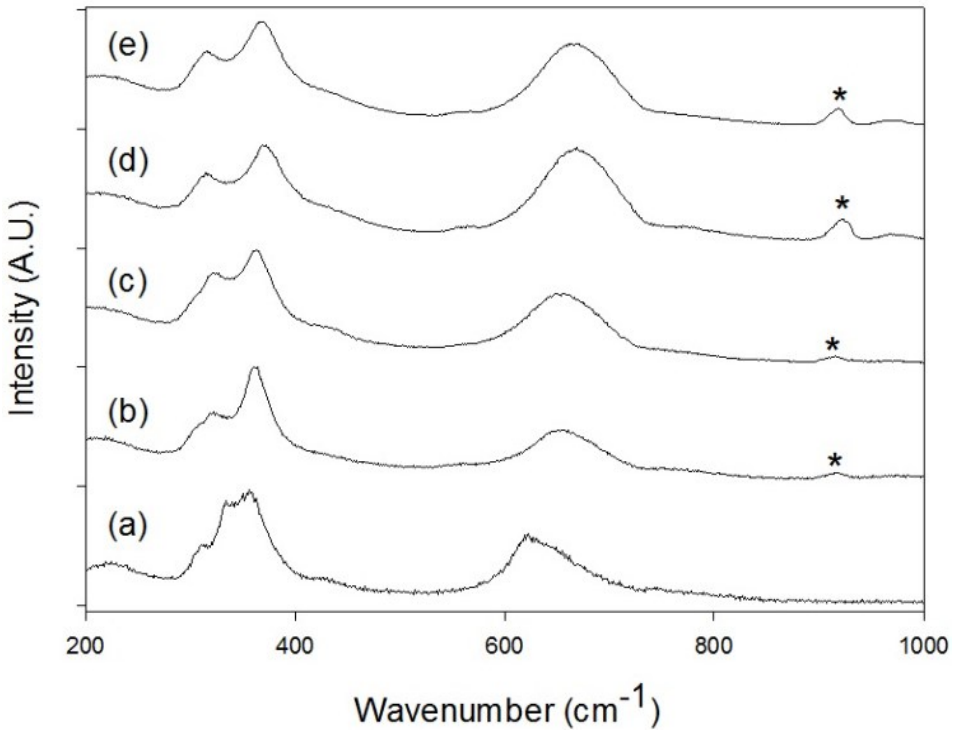

Figure 5.14 Raman spectra of (a) $BaCe_{0.8}Yb_{0.2}O_{2.9}$, (b) $BaCe_{0.75}Yb_{0.2}P_{0.05}O_{2.925}$, (c) $BaCe_{0.7}Yb_{0.25}P_{0.05}O_{2.9}$, (d) $BaCe_{0.65}Yb_{0.3}P_{0.05}O_{2.875}$ and (e) $BaCe_{0.6}Yb_{0.3}P_{0.1}O_{2.9}$ with the main peak showing the presence of phosphate indicated

All the phosphate containing compositions had a band at ~940 cm^{-1} which was not seen in $BaCe_{0.8}Yb_{0.2}O_{2.9}$. This band is due to the internal stretching mode of phosphate and thus confirms the presence of phosphate.[28] The bands seen between 300 and 375 cm^{-1} are caused

by bending modes of O-Ce/Yb-O and the band at 630 cm^{-1} is caused by stretching mode of Ce/Yb-O.[29, 30]

5.3.2.1.3 Water Incorporation

The amount of water in the structure was calculated by measuring the mass loss from hydrated samples under heating in flowing N_2, Table 5.8.

Table 5.8 Water content for $BaCe_{1-y-x}Yb_yP_xO_{3-y/2+x/2}$

Composition	% Mass Loss	Amount of water per formula unit
$BaCe_{0.8}Yb_{0.2}O_{2.9}$	0.47	0.09(1)
$BaCe_{0.75}Yb_{0.2}P_{0.05}O_{2.925}$	0.22	0.04(1)
$BaCe_{0.7}Yb_{0.25}P_{0.05}O_{2.9}$	0.31	0.06(1)
$BaCe_{0.65}Yb_{0.3}P_{0.05}O_{2.875}$	0.31	0.06(1)
$BaCe_{0.6}Yb_{0.3}P_{0.1}O_{2.9}$	0.21	0.04(1)

The collected data showed that for the phosphate containing compositions not all the vacancies could be filled as found for the yttrium doped samples due to the tetrahedral coordination of phosphate. The water content was found to decrease with increasing phosphate content, consistent with phosphate having a tetrahedral coordination, such that some of the oxygen vacancies cannot be filled. Increasing the ytterbium content was found to increase the amount of water due to the increased number of oxygen vacancies on ytterbium doping. The ytterbium containing samples also had slightly lower water contents than the yttrium containing samples, which may also correlate with a lack of barium site vacancies.

5.3.2.2 Conductivity Measurements

Conductivity measurements were recorded using AC impedance measurements in wet and dry N_2 for the pure compositions of $BaCe_{1-y-x}Yb_yP_xO_{3-y/2+x/2}$. All compositions showed a high total conductivity with a protonic contribution in wet atmospheres, Table 5.9, Figure 5.15 and Figure 5.16.

Table 5.9 Total conductivity data for $BaCe_{1-y-x}Yb_yP_xO_{3-y/2+x/2}$

Sample (nominal composition)	Conductivity (S cm^{-1})			
	500 °C		800 °C	
	Dry N_2	Wet N_2	Dry N_2	Wet N_2
$BaCe_{0.8}Yb_{0.2}O_{2.9}$	2.7×10^{-3}	2.8×10^{-3}	1.1×10^{-2}	1.1×10^{-2}
$BaCe_{0.75}Yb_{0.2}P_{0.05}O_{2.925}$	8.6×10^{-4}	2.0×10^{-3}	6.4×10^{-3}	7.2×10^{-3}
$BaCe_{0.7}Yb_{0.25}P_{0.05}O_{2.9}$	1.7×10^{-3}	2.5×10^{-3}	1.2×10^{-2}	1.2×10^{-2}
$BaCe_{0.65}Yb_{0.3}P_{0.05}O_{2.875}$	8.5×10^{-4}	1.6×10^{-3}	4.3×10^{-3}	4.6×10^{-3}
$BaCe_{0.6}Yb_{0.3}P_{0.1}O_{2.9}$	4.4×10^{-4}	6.3×10^{-4}	2.6×10^{-3}	2.8×10^{-3}

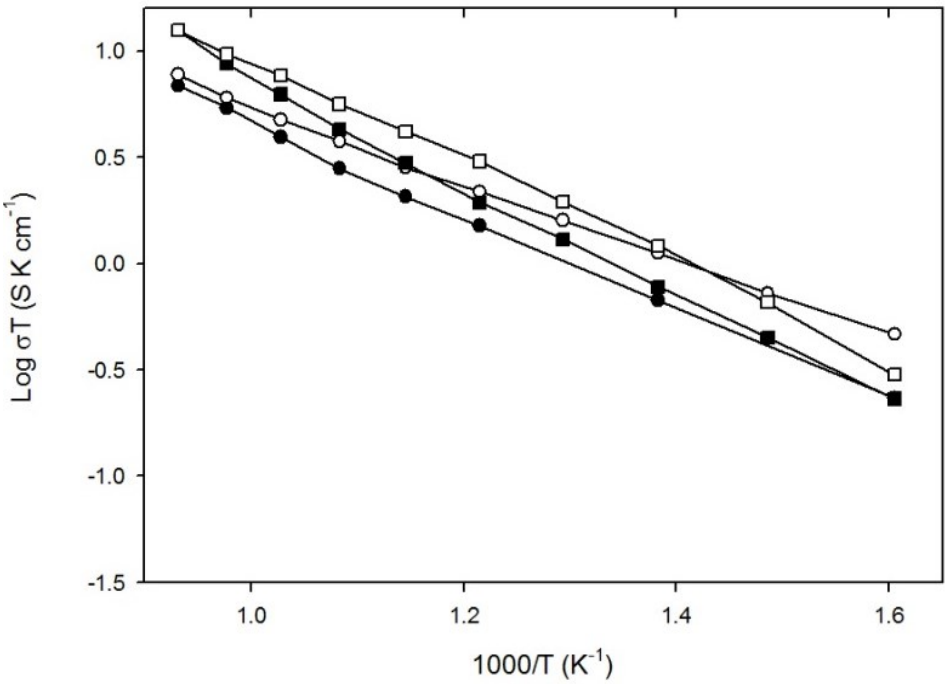

Figure 5.15 Conductivity data for $BaCe_{0.75}Yb_{0.2}P_{0.05}O_{2.925}$ (circle) and $BaCe_{0.7}Yb_{0.25}P_{0.05}O_{2.9}$ (square) in dry (filled) and wet (empty) N_2

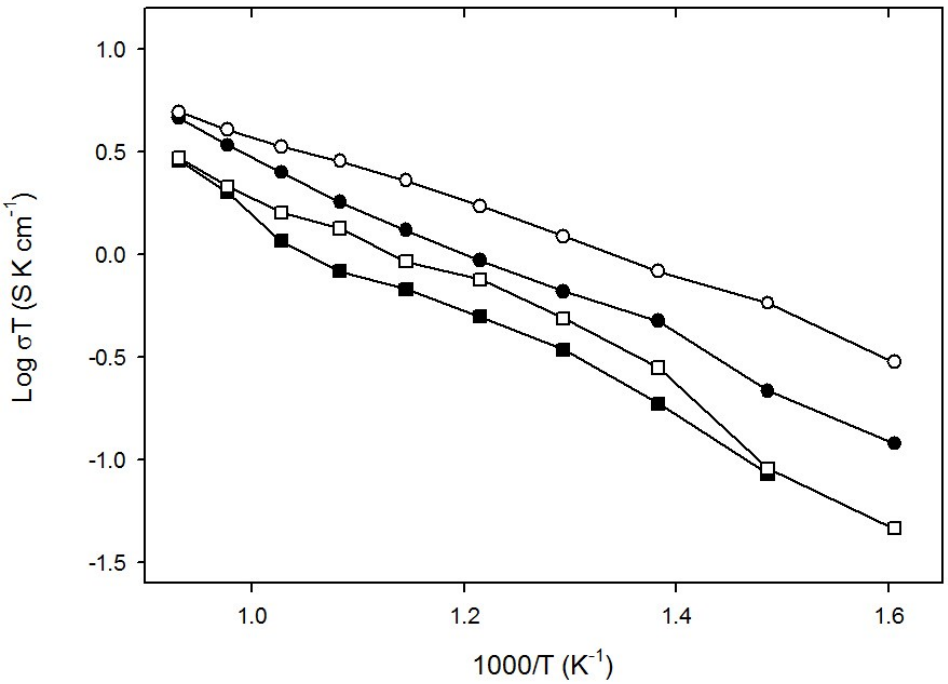

Figure 5.16 Conductivity data for $BaCe_{0.65}Yb_{0.3}P_{0.05}O_{2.875}$ (circle) and $BaCe_{0.6}Yb_{0.3}P_{0.1}O_{2.9}$ (square) in dry (filled) and wet (empty) N_2

The collected data shows that increasing the phosphate content lowers the conductivity in agreement with phosphate lowering the amount of mobile oxygen vacancies, with $BaCe_{0.7}Yb_{0.25}P_{0.05}O_{2.9}$ having the highest conductivity of the doped samples. The activation energies in wet N_2 were in the range 0.35 to 0.53 eV similar to the activation energy of 0.39 eV in air of $BaCe_{0.85}Yb_{0.15}O_{2.925}$.[32] These activation energies indicate that the mechanism of conduction in the synthesised samples is the same as that of $BaCe_{0.85}Yb_{0.15}O_{2.925}$.

To determine if there was a p-type contribution to the conductivity, measurements were also made in dry O_2, and an example is shown in Figure 5.17. These data showed that there was a p-type contribution to the conductivity at elevated temperatures, as seen for the yttrium doped analogues.

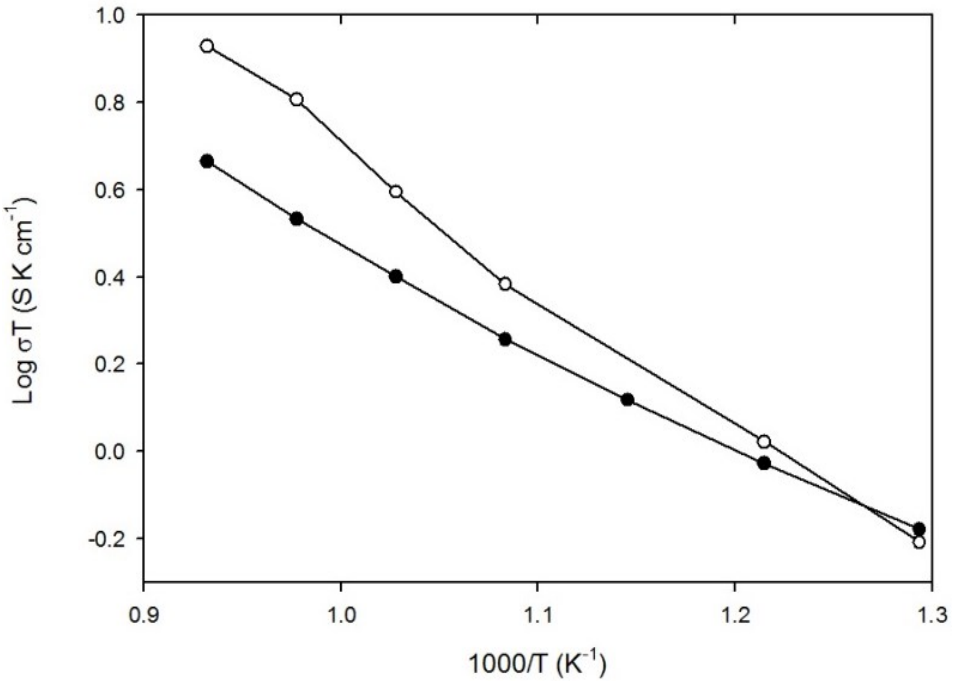

Figure 5.17 Conductivity data between 400 °C and 800 °C for $BaCe_{0.65}Yb_{0.3}P_{0.05}O_{2.875}$ in dry N_2 (filled circle) and dry O_2 (empty circle)

5.3.2.3 CO_2 Stability

As for the yttrium doped samples, TGA studies were carried out to determine the CO_2 stability by identifying the temperature of mass gain under a flowing mix of 1:1 CO_2:N_2, with the results shown in Table 5.10.

Table 5.10 Temperature for uptake of CO_2 for $BaCe_{1-y-x}Yb_yP_xO_{3-y/2+x/2}$ from TGA studies up to 1000 °C

Composition	Temperature of Mass Gain
$BaCe_{0.8}Yb_{0.2}O_{2.9}$	450 °C
$BaCe_{0.75}Yb_{0.2}P_{0.05}O_{2.925}$	450 °C
$BaCe_{0.7}Yb_{0.25}P_{0.05}O_{2.9}$	450 °C
$BaCe_{0.65}Yb_{0.3}P_{0.05}O_{2.875}$	500 °C
$BaCe_{0.6}Yb_{0.3}P_{0.1}O_{2.9}$	500 °C

The collected data showed that unlike the yttrium case, there was an improvement in the CO_2 stability with increased trivalent doping on the B-site, although the improvements were small. The phosphate appeared to have no effect on the CO_2 stability.

5.3.3 $BaCe_{1-y}In_yO_{3-y/2}$

5.3.3.1 Structural Determination

5.3.3.1.1 Powder X-ray Diffraction

After phosphate doping into yttrium and ytterbium doped barium cerate phosphate, the $BaCe_{1-y}In_yO_{3-y/2}$ series was examined, as phosphate doping had proven successful for $Ba_2In_2O_5$, and also proven to improve the CO_2 stability in this system.[21, 33] The same stoichiometries as for the yttrium and ytterbium doped samples were used, so as to make a direct comparison between the dopants (x= 0.05, y= 0.2, 0.25, 0.3; x= 0.1, y= 0.3). These compositions resulted in the formation of single phase orthorhombic perovskites, Figure 5.18.

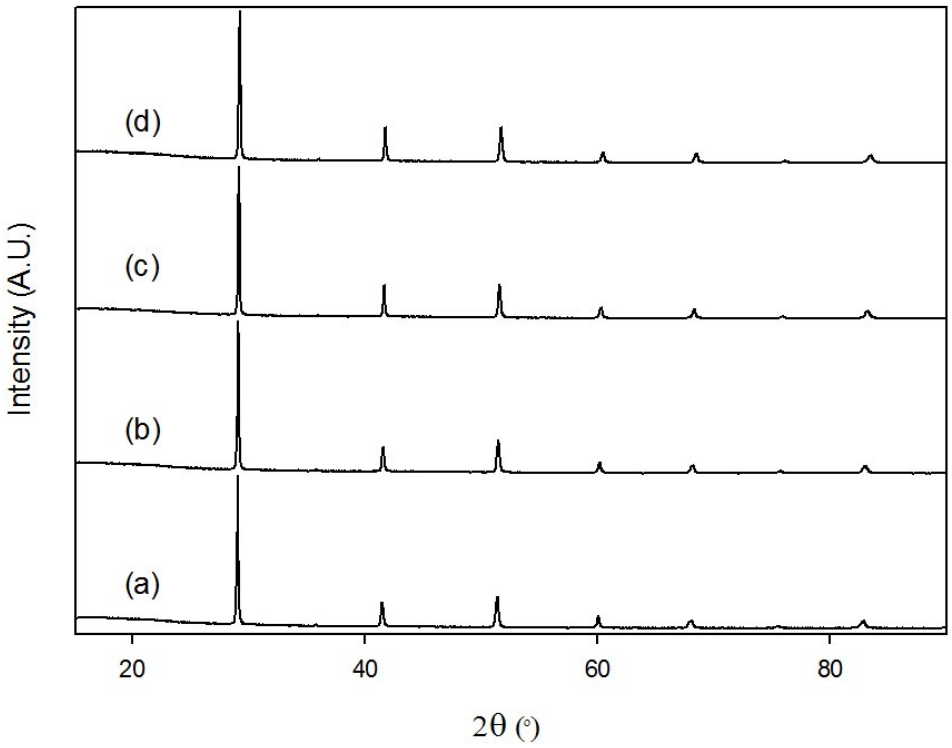

Figure 5.18 Powder X-ray diffraction data of (a) $BaCe_{.75}In_{0.2}P_{0.05}O_{2.925}$, (b) $BaCe_{0.7}In_{0.25}P_{0.05}O_{2.9}$, (c) $BaCe_{0.65}In_{0.3}P_{0.05}O_{2.875}$ and (d) $BaCe_{0.6}In_{0.3}P_{0.1}O_{2.9}$

Rietveld refinement was carried out on these phases using the GSAS suite of program. Chupakhina *et al*. used the space group *P b n m* for $BaCe_{1-x}In_xO_{3-x/2}$ however this space group differs from *P m c n* via a simple transformation, (*P m c n* to *P b n m* is represented by a to c,

b to a and c to b) so the space group *P m c n* was used in line with the other series analysed in this chapter.[34] The indium, cerium and phosphorus were all placed on the *4b* site with the expected stoichiometry used for the occupancy. The oxygen vacancies were split across both oxygen sites with the fractional occupancy set to the correct amount for the cation oxidation states, and the oxygen occupancies were not refined due to the lack of sensitivity of oxygen to X-rays. The refinement gave good agreement with the collected X-ray diffraction patterns and the following lattice parameters were obtained, Table 5.11, with the observed, calculated and difference profiles and the complete description of the refined model of $BaCe_{0.7}In_{0.25}P_{0.05}O_{2.9}$ shown in Figure 5.19 and Table 5.12.

Table 5.11 Lattice parameters for $BaCe_{1-y-x}In_xP_xO_{3-y/2+x/2}$

Composition	a (Å)	b (Å)	c (Å)	Unit Cell Volume (Å^3)
$BaCe_{0.8}In_{0.2}O_{2.9}$	8.7204(2)	6.1899(2)	6.2094(1)	335.17(2)
$BaCe_{0.75}In_{0.2}P_{0.05}O_{2.925}$	8.7131(2)	6.1935(1)	6.1697(2)	332.95(2)
$BaCe_{0.7}In_{0.25}P_{0.05}O_{2.9}$	8.7002(3)	6.1592(2)	6.1799(2)	331.16(2)
$BaCe_{0.65}In_{0.3}P_{0.05}O_{2.875}$	8.6896(3)	6.1450(2)	6.1634(2)	329.12(1)
$BaCe_{0.6}In_{0.3}P_{0.1}O_{2.9}$	8.6674(4)	6.1482(3)	6.1283(3)	326.57(2)

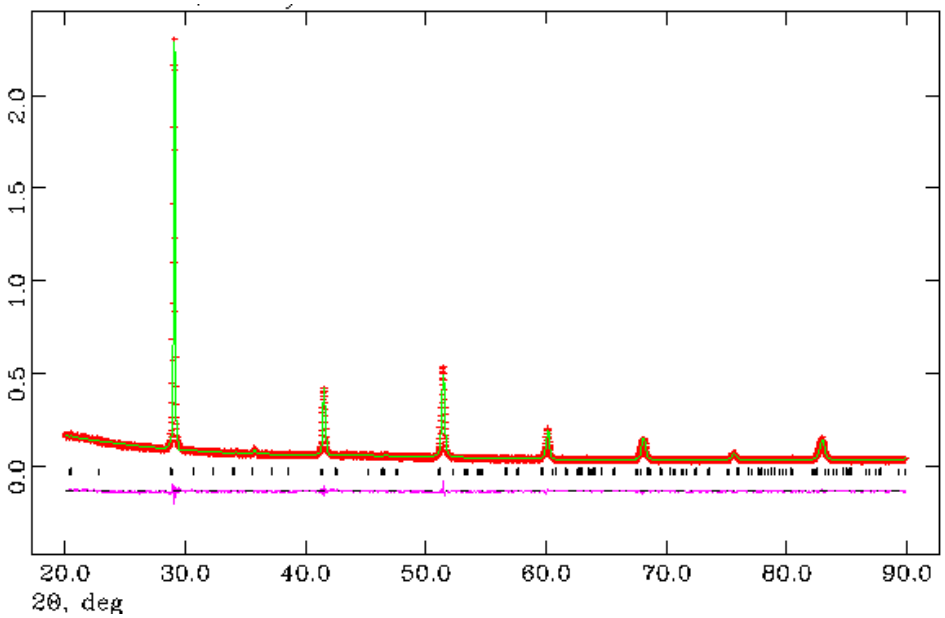

Figure 5.19 Observed, calculated and difference plots for structural refinement of $BaCe_{0.7}In_{0.25}P_{0.05}O_{2.9}$ using X-ray powder diffraction data

Table 5.12 Structural detail for $BaCe_{0.7}In_{0.25}P_{0.05}O_{2.9}$

	Site	x	y	z	Fraction	100 U ($Å^2$)
Ba	4c	0.25	0	0	1	2.2(1)
Ce	4b	0	0.5	0	0.7	0.8(1)
In	4b	0	0.5	0	0.25	0.8(1)
P	4b	0	0.5	0	0.05	0.8(1)
O	4c	0.25	0.4	0	0.9667	2.4(3)
O	8d	0	0.75	0.25	0.9667	2.4(3)
Space Group = *P m c n*, a = 8.7002(3) Å, b = 6.1592(2) Å, c = 6.1799(2) Å, unit cell volume = 331.16(2) $Å^3$ wR_p = 4.52%, R_p = 3.96%, χ^2 = 1.706						

The data from the refinements show that the lattice parameters decrease with an increase in indium and phosphorus content, in agreement with the smaller ionic radii of indium (0.8 Å for 6 coordinate) and phosphorus (0.38 Å for 4 coordinate) compared to cerium (0.87 Å for 6 coordinate).[26] Due to the smaller size of indium compared to ytterbium and yttrium it was not thought that indium could doped onto the barium site and further refinements confirmed this, with no change in barium site occupancy when this was refined.

5.3.3.1.2 Raman Spectroscopy

To confirm the presence of phosphate in the compositions, Raman spectroscopy was carried out on all the phases, as well as $BaCe_{0.8}In_{0.2}O_{2.9}$ for comparison, Figure 5.20.

All the phosphate containing compositions contained a band at ~940 cm^{-1}, which was not seen in $BaCe_{0.8}In_{0.2}O_{2.9}$. This band is due to the internal stretching mode of phosphate confirming the presence of phosphate in these systems.[28] These phosphate bands look to be two different peaks, which may relate to different environments, e.g. close to either cerium or indium. The bands seen between 300 and 375 cm^{-1} are caused by bending modes of O-In/Ce-O and the band at 630 cm^{-1} is caused by stretching mode of In/Ce-O.[29, 30] These bands broaden with increased indium content which may be due to the composition becoming more cubic as found by Giannici *et al*. for high indium contents in indium doped barium cerate.[17]

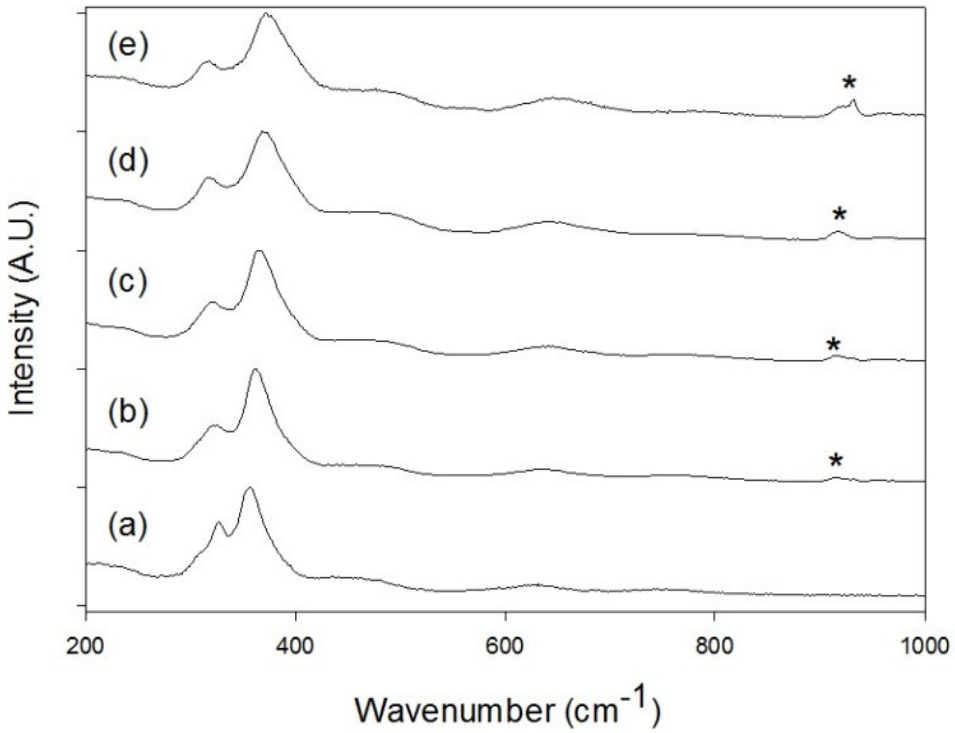

Figure 5.20 Raman spectra of (a) $BaCe_{0.8}In_{0.2}O_{2.9}$, (b) $BaCe_{0.75}In_{0.2}P_{0.05}O_{2.925}$, (c) $BaCe_{0.7}In_{0.25}P_{0.05}O_{2.9}$, (d) $BaCe_{0.65}In_{0.3}P_{0.05}O_{2.875}$ and (e) $BaCe_{0.6}In_{0.3}P_{0.1}O_{2.9}$ with the main peak showing the presence of phosphate indicated

5.3.3.1.3 Water Incorporation

The water contents of the hydrated samples were determined using TGA studies from the mass loss under heating, Table 5.13.

Table 5.13 Water content for $BaCe_{1-y-x}In_yP_xO_{3-y/2+x/2}$

Composition	% Mass Loss	Amount of water per formula unit
$BaCe_{0.8}In_{0.2}O_{2.9}$	0.25	0.04(1)
$BaCe_{0.75}In_{0.2}P_{0.05}O_{2.925}$	0.20	0.04(1)
$BaCe_{0.7}In_{0.25}P_{0.05}O_{2.9}$	0.18	0.03(1)
$BaCe_{0.65}In_{0.3}P_{0.05}O_{2.875}$	0.13	0.02(1)
$BaCe_{0.6}In_{0.3}P_{0.1}O_{2.9}$	0.23	0.04(1)

The collected data shows that not all the oxygen vacancies could be filled, as found for the ytterbium doped samples. The levels of water incorporation were slightly lower than those found for the yttrium and ytterbium analogues, which implies a greater degree of oxygen

vacancy trapping occurring for these indium containing samples. There was no obvious effect of phosphate content on the water incorporation.

5.3.3.2 Conductivity Measurements

Conductivity data were collected as for the yttrium/ytterbium doped samples. All compositions showed a conductivity that was lower than that seen for the yttrium and ytterbium analogues, with a protonic contribution in wet atmospheres and are compared with $BaCe_{0.8}In_{0.2}O_{2.9}$ in Table 5.14, with the plots shown in Figure 5.21 and Figure 5.22.

Table 5.14 Total conductivity data for $BaCe_{1-y-x}In_yP_xO_{3-y/2+x/2}$

Sample (nominal composition)	Conductivity (S cm^{-1})			
	500 °C		800 °C	
	Dry N_2	Wet N_2	Dry N_2	Wet N_2
$BaCe_{0.8}In_{0.2}O_{2.9}$	7.4×10^{-5}	5.3×10^{-4}	1.6×10^{-3}	2.4×10^{-3}
$BaCe_{0.75}In_{0.2}P_{0.05}O_{2.925}$	1.8×10^{-5}	2.5×10^{-4}	2.8×10^{-4}	8.7×10^{-4}
$BaCe_{0.7}In_{0.25}P_{0.05}O_{2.9}$	1.4×10^{-4}	2.4×10^{-4}	1.3×10^{-3}	1.3×10^{-3}
$BaCe_{0.65}In_{0.3}P_{0.05}O_{2.875}$	2.1×10^{-5}	2.4×10^{-4}	6.2×10^{-4}	1.2×10^{-3}
$BaCe_{0.6}In_{0.3}P_{0.1}O_{2.9}$	8.5×10^{-6}	1.1×10^{-4}	2.3×10^{-4}	4.7×10^{-4}

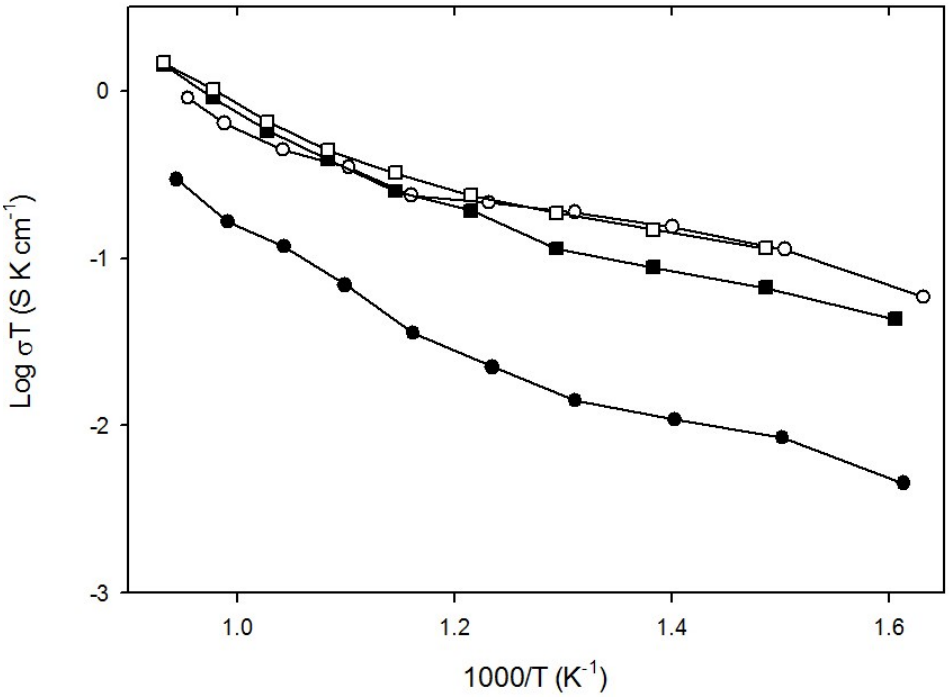

Figure 5.21 Conductivity data for $BaCe_{0.75}In_{0.2}P_{0.05}O_{2.925}$ (circle) and $BaCe_{0.7}In_{0.25}P_{0.05}O_{2.9}$ (square) in dry (filled) and wet (empty) N_2

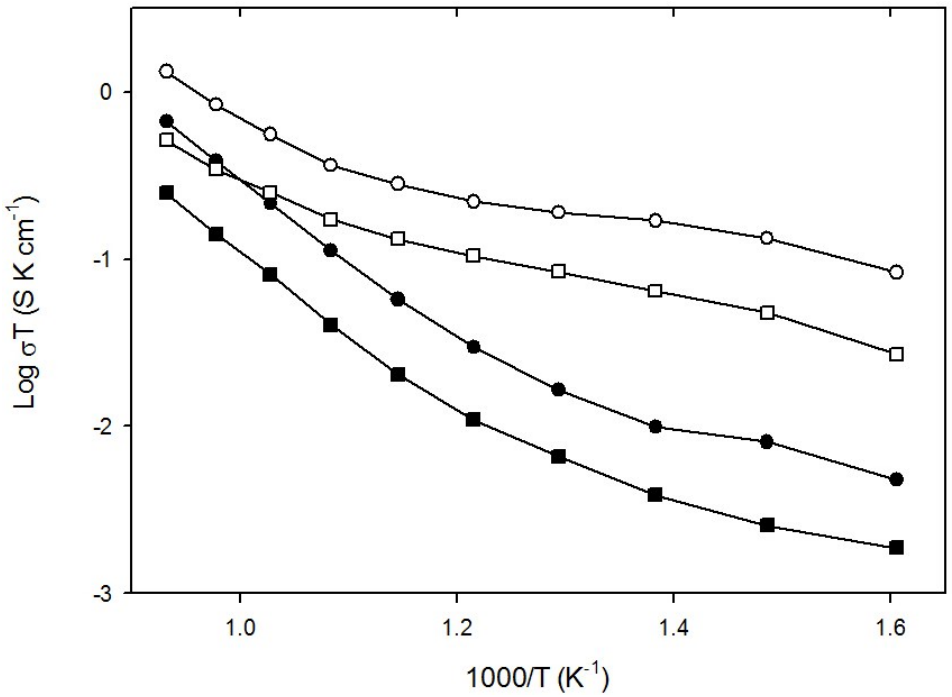

Figure 5.22 Conductivity data for $BaCe_{0.65}In_{0.3}P_{0.05}O_{2.875}$ (circle) and $BaCe_{0.6}In_{0.3}P_{0.1}O_{2.9}$ (square) in dry (filled) and wet (empty) N_2

The conductivity data shows that increasing the phosphate content lowers the conductivity, as found for the yttrium and ytterbium analogues, which is attributed to the decreasing amount of mobile oxygen vacancies on phosphate doping. The results showed the highest

conductivity of the phosphate doped samples was for $BaCe_{0.7}In_{0.25}P_{0.05}O_{2.9}$, similar to the results found for ytterbium doping. This may be due to increased vacancy trapping occurring around the indium, as indium can adopt a lower coordination as seen in $Ba_2In_2O_5$. EXAFS could be used to determine the local structure as used by Nguyen *et al* and O'Dell *et al*.[36, 37] The activation energies in wet N_2 were in the range 0.30 to 0.39 eV similar to the activation energies found for other proton conducting perovskites.

To determine whether there is a p-type contribution to the conductivity as found for the yttrium and ytterbium analogues, conductivity measurements were also carried out in dry O_2, an example of which is shown in Figure 5.23. The conductivity measurements in a dry O_2 atmosphere showed there was a p-type contribution to the conductivity for all the compositions at elevated temperatures.

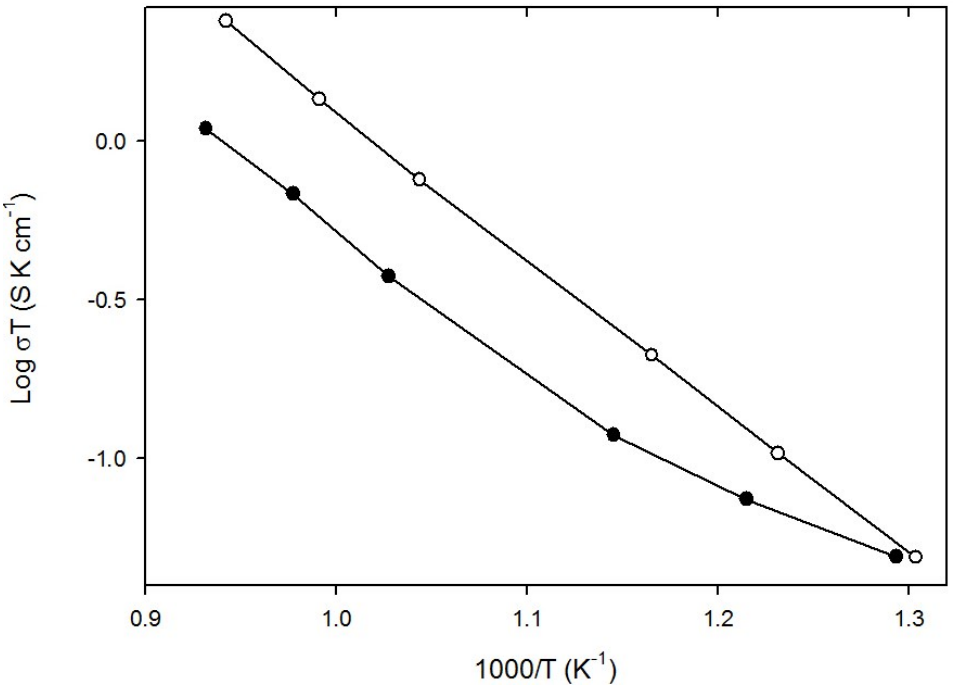

Figure 5.23 Conductivity data between 500 °C and 800 °C for $BaCe_{0.65}In_{0.3}P_{0.05}O_{5.875}$ in dry N_2 (filled circle) and dry O_2 (empty circle)

5.3.3.3 CO_2 Stability

The CO_2 stabilities of $BaCe_{1-y}In_yP_xO_{3-y/2+x/2}$ were measured using TGA by observing the temperature of mass gain under a flowing 1:1 mix of CO_2:N_2, Table 5.15.

Table 5.15 Temperature for uptake of CO_2 for $BaCe_{1-y-x}In_yP_xO_{3-y/2+x/2}$ from TGA studies up to 1000 °C

Composition	Temperature of Mass Gain
$BaCe_{0.8}In_{0.2}O_{2.9}$	450 °C
$BaCe_{0.75}In_{0.2}P_{0.05}O_{2.925}$	525 °C
$BaCe_{0.7}In_{0.25}P_{0.05}O_{2.9}$	550 °C
$BaCe_{0.65}In_{0.3}P_{0.05}O_{2.875}$	550 °C
$BaCe_{0.6}In_{0.3}P_{0.1}O_{2.9}$	575 °C

The collected data shows that increasing the phosphorus content was found to improve the stability of the compositions to CO_2 atmospheres in agreement with the data found for phosphate doped $Ba_2Sc_2O_5$ and $Ba_2In_2O_5$.[21, 35] Indium doping was also found to improve the stability of the compositions to CO_2 unlike in the case of yttrium doping. Further work would be required to clarify this, but the CO_2 stability could be affected by different degrees of local order between the trivalent dopants and the phosphate group, and in this respect computer modelling studies may provide some insight. These data show that while lowering the conductivity, indium and phosphate doping are found to improve the stability of barium cerate.

5.4 Conclusions

The collected data show that it is possible to dope phosphate into various trivalent doped barium cerate compositions provided enough oxygen vacancies are present to accommodate the tetrahedral phosphate group. All the compositions had a cell volume between 326 and 338 $Å^3$ and adopted a perovskite structure with a space group *P m c n*. Raman spectroscopy data showed the presence of phosphate in all the compositions as a band at ~940 cm^{-1}, internal stretching mode of phosphate, was seen in these compositions but not found in the non-

phosphate analogues. The water contents of hydrated samples were measured and showed that in general not all the oxygen vacancies could be filled which can explained by the requirement for tetrahedral coordination of phosphate. Similarly for the indium doped samples, the water contents were lower than expected and potentially some oxygen vacancy trapping is occurring around indium, although further work is required to confirm if this is the case. In this respect, modelling studies would be of interest to examine the energetics of the hydration reaction around the cerium and trivalent dopants.

All the compositions exhibited a high conductivity with a protonic contribution, although the values were lower than their non-phosphate analogues, suggesting that phosphorus doping is detrimental to the conductivity in these systems. The indium containing compositions had the lowest conductivity which could potentially also be due to some oxygen vacancy trapping occurring around the indium, consistent with the lower water contents of these samples.

The stabilities of the samples to CO_2 were also measured, with little improvement for the $BaCe_{1-y-x}Y_yP_xO_{3-y/2+x/2}$ and $BaCe_{1-y-x}Yb_yP_xO_{3-y/2+x/2}$, while for the $BaCe_{1-y-x}In_yP_xO_{3-y/2+x/2}$ series a small improvement in CO_2 stability was observed.

Overall reduced conductivities indicate that phosphate doping in $BaCeO_3$ is not a viable option to improve the performance of these systems for fuel cell applications.

5.5 References

1. H. Iwahara, H. Uchida, K. Ono and K. Ogaki, *J. Electrochem. Soc.*, 1988, **135**, 529-533.
2. T. Norby, *Solid State Ion.*, 1999, **125**, 1-11.
3. K. D. Kreuer, *Solid State Ion.*, 1997, **97**, 1-15.
4. A. Orera and P. R. Slater, *Chem. Mat.*, 2010, **22**, 675-690.
5. S. Yamaguchi and N. Yamada, *Solid State Ion.*, 2003, **162**, 23-29.
6. M. Y. Wang and L. G. Qiu, *Chin. J. Chem. Phys.*, 2008, **21**, 286-290.
7. N. V. Sharova and V. P. Gorelov, *Russ. J. Electrochem.*, 2005, **41**, 1001-1007.
8. E. Gorbova, V. Maragou, D. Medvedev, A. Demin and P. Tsiakaras, *J. Power Sources*, 2008, **181**, 207-213.
9. N. Maffei, L. Pelletier, J. P. Charland and A. McFarlan, *J. Power Sources*, 2006, **162**, 165-167.
10. C. Chen and G. L. Ma, *J. Alloy. Compd.*, 2009, **485**, 69-72.
11. N. I. Matskevich and T. A. Wolf, *J. Chem. Thermodyn.*, 2010, **42**, 225-228.
12. W. B. Wang, J. W. Liu, Y. D. Li, H. T. Wang, F. Zhang and G. L. Ma, *Solid State Ion.*, 2010, **181**, 667-671.
13. M. Y. Wang, L. G. Qiu and G. L. Ma, *Chin. J. Chem.*, 2007, **25**, 1273-1277.
14. J. L. Yin, X. W. Wang, J. H. Xu, H. T. Wang, F. Zhang and G. L. Ma, *Solid State Ion.*, 2011, **185**, 6-10.
15. L. G. Qiu and M. Y. Wang, *Chin. J. Chem. Phys.*, 2010, **23**, 707-712.
16. N. I. Matskevich, T. Wolf, M. Y. Matskevich and T. I. Chupakhina, *Eur. J. Inorg. Chem.*, 2009, 1477-1482.
17. F. Giannici, A. Longo, A. Balerna, K. D. Kreuer and A. Martorana, *Chem. Mat.*, 2007, **19**, 5714-5720.
18. M. J. Scholten, J. Schoonman, J. C. Vanmiltenburg and H. A. J. Oonk, *Solid State Ion.*, 1993, **61**, 83-91.
19. K. H. Ryu and S. M. Haile, *Solid State Ion.*, 1999, **125**, 355-367.
20. H. S. Soares, X. Zhang, I. Antunes, J. R. Frade, G. C. Mather and D. P. Fagg, *J. Solid State Chem.*, 2012, **191**, 27-32.
21. J. F. Shin, L. Hussey, A. Orera and P. R. Slater, *Chemical Communications*, 2010, **46**, 4613-4615.
22. J. F. Shin, A. Orera, D. C. Apperley and P. R. Slater, *J. Mater. Chem.*, 2011, **21**, 874-879.
23. J. F. Shin, K. Joubel, D. C. Apperley and P. R. Slater, *Dalton Transactions*, 2012, **41**, 261-266.
24. A. C. Larson and R. B. Von Dreele, (1994), Los Alomos National Laboratory, Los Alomos NM.
25. K. S. Knight, M. Soar and N. Bonanos, *J. Mater. Chem.*, 1992, **2**, 709-712.
26. R. D. Shannon, *Acta Crystallographica Section A*, 1976, **32**, 751-767.
27. J. Wu, L. P. Li, W. T. P. Espinosa and S. T. Haile, *J. Mater. Res.*, 2004, **19**, 2366-2376.
28. K. Popa, R. J. M. Konings, O. Benes, T. Geisler and A. F. Popa, *Thermochimica Acta*, 2006, **451**, 1-4.
29. T. Scherban, R. Villeneuve, L. Abello and G. Lucazeau, *Solid State Ion.*, 1993, **61**, 93-98.
30. C. J. Zhang and H. L. Zhao, *Solid State Ion.*, 2012, **206**, 17-21.

31. P. Sawant, S. Varma, B. N. Wani and S. R. Bharadwaj, *Int. J. Hydrog. Energy*, 2012, **37**, 3848-3856.
32. Y. J. Gu, Z. G. Liu, J. H. Ouyang, F. Y. Yan and Y. Zhou, *Electrochim. Acta*, 2013, **105**, 547-553.
33. J. F. Shin and P. R. Slater, *J. Power Sources*, 2011, **196**, 8539-8543.
34. T. I. Chupakhina, N. I. Matskevich, G. V. Bazuev, N. A. Ovechkina, V. R. Galakhov, M. Raeckers and M. Neumann, *Russ. J. Inorg. Chem.*, 2010, **55**, 1002-1009.
35. A. D. Smith, J. F. Shin and P. R. Slater, *J. Solid State Chem.*, 2013, **198**, 247-252.
36. H. K. D. Nguyen, T. N. Don, G. Sankar, R. A. Catlow, *Catalysis Comm.*, 2012, **25**, 125-129
37. L. A. Dell, S. L. P. Savin, A. V. Chadwick, M. E. Smith, *J. Nanoparticle Research*, 2008, **10**, 1263-1270

Chapter 6 Synthesis and Characterisation of Oxyanion Doped $Ba_2Sn_{1-x}Ti_x(Y/Yb)O_{5.5}$

6.1 Introduction

$Ba_2SnYO_{5.5}$ was first reported by Paulose *et al*., who discovered it as an impurity phase in the yttrium barium copper tin oxide system.[1] They reported that this phase possessed a perovskite-type structure with a doubled unit cell (8.42 Å) and claimed that it could only be stabilised using impurity phases, in their case CuO. Later Murugaraj *et al*. investigated the potential of $Ba_2SnYO_{5.5}$ as a proton conducting electrolyte for proton conducting SOFCs due to its high number of oxygen vacancies.[2] They found the sample could be made single phase with no impurity phase needed to stabilise it. It crystallised as a cubic perovskite with a doubled unit cell with some degree of Sn/Y ordering on the B cation site. The sample exhibited a similar conductivity to doped $BaCeO_3$ and was found to be stable with respect to carbonate formation. However the structure was found to change in reducing atmospheres forming the brownmillerite structure.

Wang *et al*. extended this work on $Ba_2SnYO_{5.5}$ and reported that it formed a single cubic perovskite phase with no ordering of the tin and yttrium and a lattice parameter of 4.241 Å.[3] They confirmed the high conductivity and CO_2 stability of this phase and found that the sample was a p-type conductor in high $p(O_2)$ atmospheres.

In this chapter the possibility to dope oxyanions (borate, phosphate and sulfate) into $Ba_2SnYO_{5.5}$ has been investigated, along with titanium and ytterbium doping, in the hope of retaining the high ionic conductivity whilst improving the stability of the phase to reducing atmospheres.

6.2 Experimental Procedure

Oxyanion doped $Ba_2Sn_{1-x}Ti_x(Y/Yb)O_{5.5}$ was synthesised using the standard ceramic synthesis method. Stoichiometric amounts of $BaCO_3$ (≥99%), SnO_2 (99.9%), Y_2O_3 (99.99%), Yb_2O_3 (99.99%), TiO_2 (99.7%), $NH_4H_2PO_4$ (≥98%), H_3BO_3 (99.5+%), SiO_2 (99.6%) and $(NH_4)_2SO_4$ (99+%) were ground together in an agate pestle and mortar and heated at 1000 °C for 12 hours. A 3% excess of $BaCO_3$ was used to overcome Ba loss at elevated temperatures and eliminate Ba deficient impurities as has been seen in other studies.[4] The mixtures were then ball-milled (350 rpm for 1 hour, Fritsch Pulverisette 7 Planetary Mill) and reheated to 1400 °C for 12 hours. The resulting powders were then ball-milled (350 rpm for 1 hour, Fritsch Pulverisette 7 Planetary Mill) a second time and pressed into pellets using a 13 mm die set and heated at 1400 °C for 12 hours. The crucibles had lids placed on them to lower Ba loss during the sintering process. When powder X-ray diffraction (Bruker D8 diffractometer with Cu-$K\alpha_1$ radiation) confirmed the presence of a single phase, the GSAS suite of programs was used to obtain unit cell parameters.[5]

Raman spectroscopy measurements were carried out to confirm the presence of the oxyanion in the compositions. These measurements utilised a Renishaw inVia Raman microscope with excitation using a Cobolt Samba CW532 nm DPSS laser.

For conductivity measurements the sintered pellets were coated on either side with platinum paste, platinum electrodes were attached to both faces, and the sample was then heated at 800°C for 1 hour to ensure bonding to the pellet. The conductivities were then measured in a temperature range of 350 °C to 800 °C by AC impedance measurements (Hewlett Packard 4192A impedance analyser) in the range 0.1 to 10^3 kHz with ac signal amplitude of 100 mV. Measurements were carried out in dry and wet N_2 (in which gas was bubbled at room

temperature through water) to identify any protonic contribution to the conductivity. Measurements were also made in dry O_2 to determine if there was a p-type contribution to the conductivity. Some of the impedance spectra showed two overlapping semicircles indicative of an overlapping of bulk and grain boundary arcs whereas others, especially at lower temperatures could be resolved, Figure 6.1. The conductivity reported represents the total (bulk and grain boundary) conductivity. The differences in densities of the samples was taken into consideration in the calculations used for the final conductivity data.

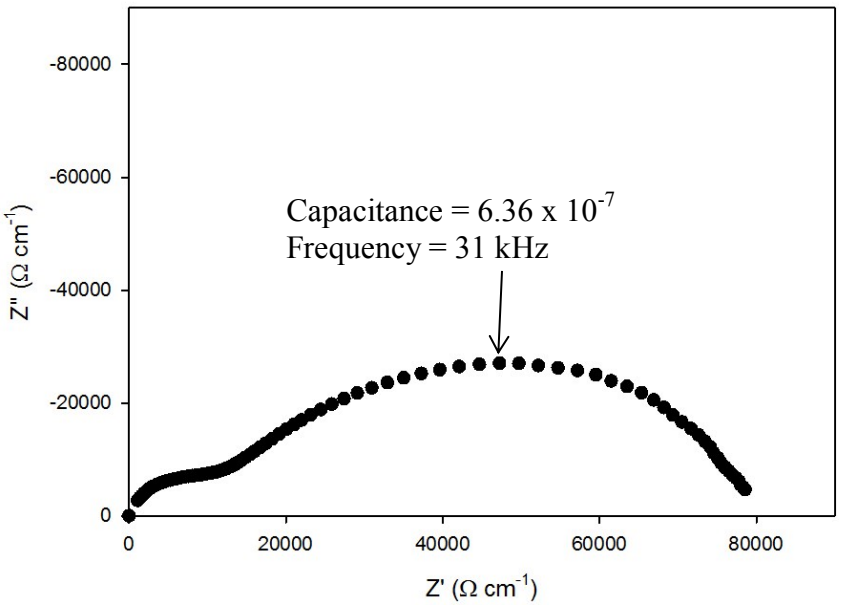

Figure 6.1 Impedance spectrum for $Ba_2Sn_{0.8}YS_{0.2}O_{5.7}$ at 350 °C in dry N_2

The CO_2 stabilities of the phases were determined using 2 methods. The first was thermogravimetric analysis with a Netzsch STA 449 F1 Jupiter Thermal Analyser. Samples were heated at 10 °C min^{-1} to 1000°C in a 1:1 CO_2 and N_2 mixture to determine at what temperature CO_2 pick up occurred. The second method involved heating the samples at 800 $^{\circ}$C for 12 hours in a tube furnace under flowing CO_2 gas. The samples were then analysed for partial decomposition by X-ray diffraction.

The stability to reducing atmospheres was determined by heating the samples at 1000 °C for 36 hours under a flowing 10%/90% H_2 nitrogen mix and then analyzing the samples by X-ray diffraction for the presence of extra peaks indicative of the brownmillerite structure or partial decomposition.

The water incorporation was not able to be calculated accurately since at the temperatures at which water loss occurred an additional mass loss was observed, most likely due to oxygen loss.

6.3 Results and Discussion

6.3.1 Oxyanion doped $Ba_2SnYO_{5.5}$

6.3.1.1 Structural Determination

6.3.1.1.1 Powder X-ray Diffraction

The initial compositions were prepared by doping with an oxyanion (borate, phosphate and sulfate) content of 10% to replace either the tin or yttrium on the B site. Phosphate and sulfate doping for tin resulted in the formation of a single phase cubic perovskite. The XRD patterns are shown in Figure 6.2 and compared with $Ba_2SnYO_{5.5}$ which formed a non-ordered cubic perovskite phase as found by Wand *et al*.[3] For borate doped compositions, small additional peaks were observed due to Y_2O_3, Figure 6.3. All the phases that involved oxyanion doping for yttrium resulted in the formation of a cubic phase alongside additional peaks due to the formation of $Ba_3Sn_2O_7$ as an impurity phase (albeit at low levels for the sulfate doped composition), Figure 6.4. Higher levels of phosphate and sulfate doping for tin were not attempted due to the fact that this would significantly decrease the number of oxygen vacancies, and it is these oxygen vacancies that are required for the ionic conduction.

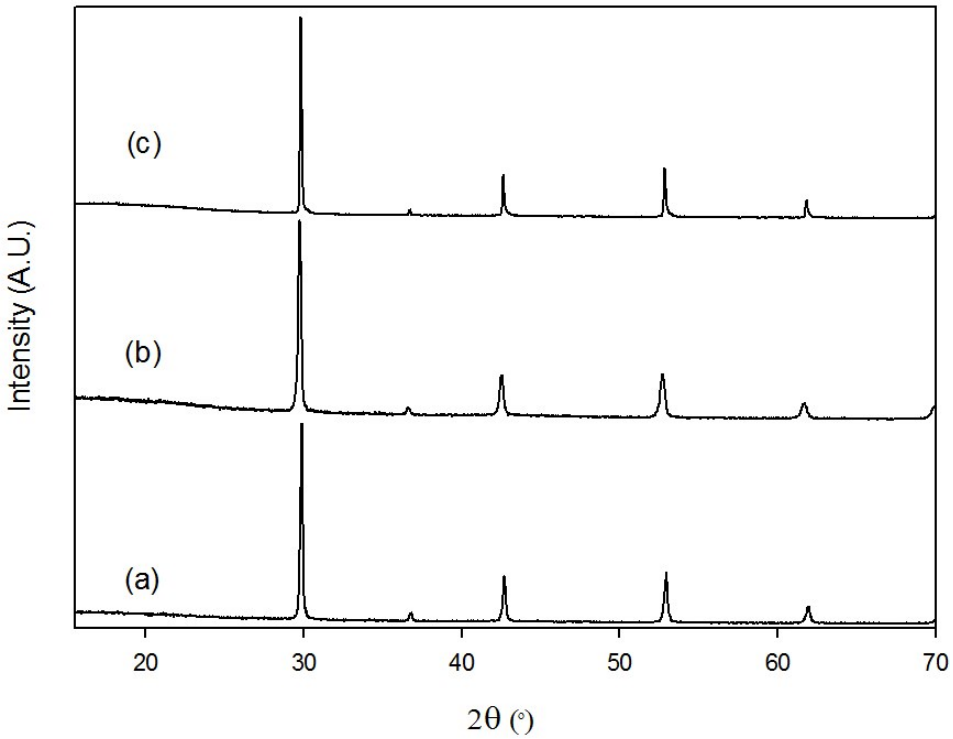

Figure 6.2 Powder X-ray diffraction data of (a) $Ba_2Sn_{0.8}YP_{0.2}O_{5.6}$, (b) $Ba_2Sn_{0.8}YS_{0.2}O_{5.7}$ and (c) $Ba_2SnYO_{5.5}$

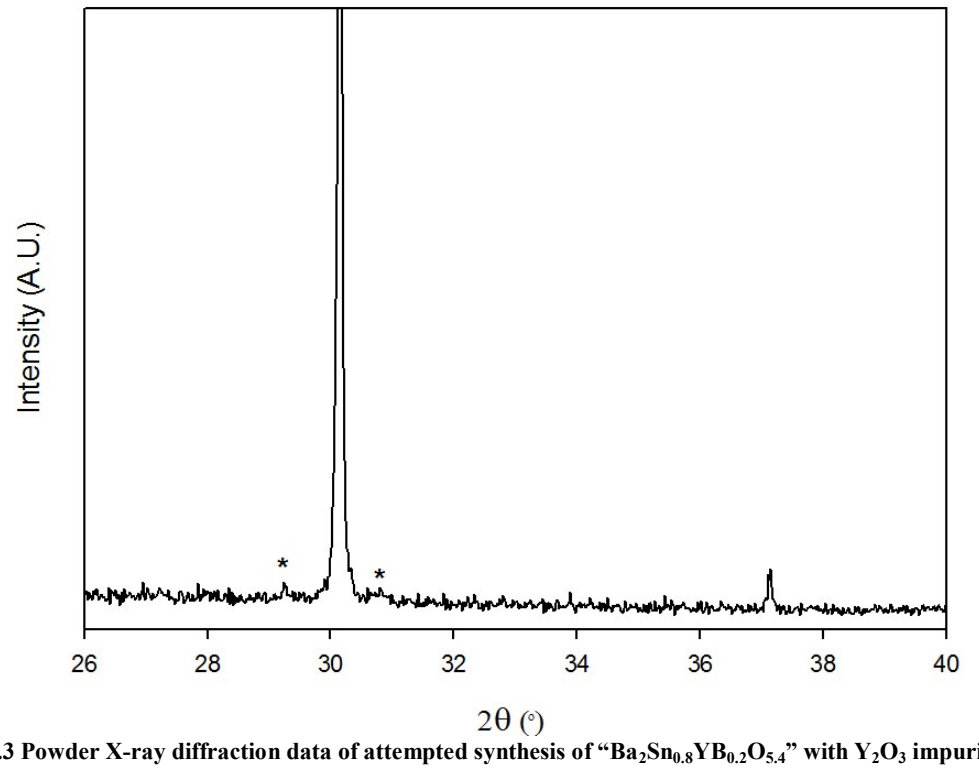

Figure 6.3 Powder X-ray diffraction data of attempted synthesis of "$Ba_2Sn_{0.8}YB_{0.2}O_{5.4}$" with Y_2O_3 impurity peaks indicated

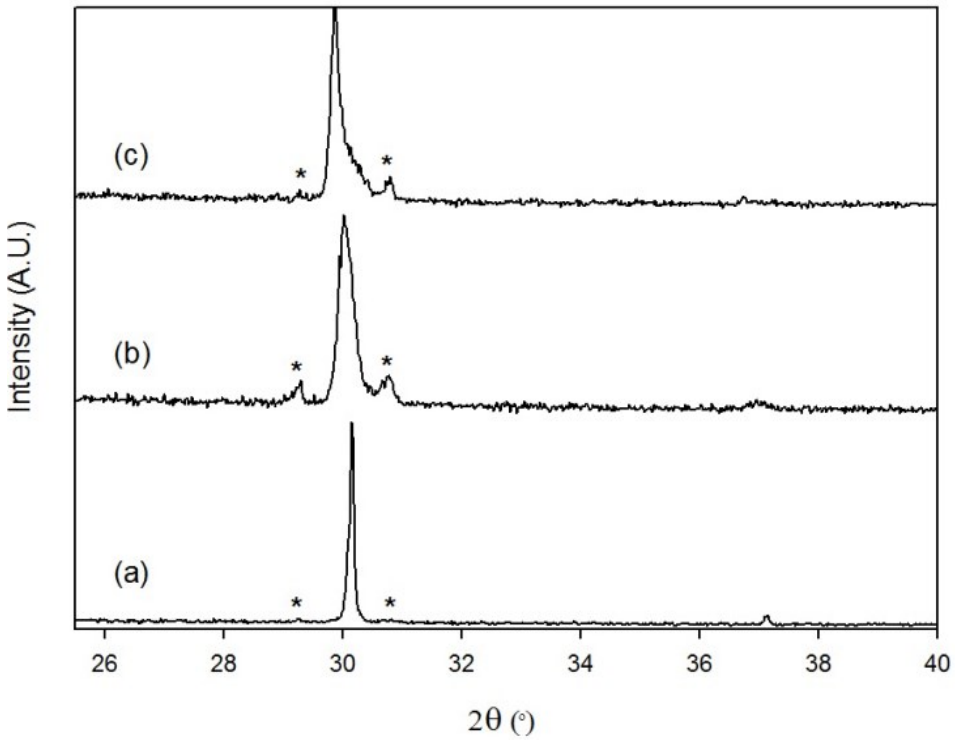

Figure 6.4 Powder X-ray diffraction data for the attempted synthesis of (a) "$Ba_2SnY_{0.8}B_{0.2}O_{5.4}$", (b) "$Ba_2SnY_{0.8}P_{0.2}O_{5.6}$" and (c) "$Ba_2SnY_{0.8}S_{0.2}O_{5.7}$" with $Ba_3Sn_2O_7$ impurity peaks indicated

The three pure phases synthesised were analysed further to determine the lattice parameters using the GSAS suite of programs.[5] Space group *P m -3 m* was used in agreement with the results found by Wang *et al*. and for other oxyanion doped compositions studied in this thesis.[3] The tin, yttrium and the oxyanion were placed on the *1a* site using the expected stoichiometry from the weighed out amounts. The oxygen content was set to the expected value from the oxidation states of the cations and was not refined due to the lack of sensitivity of oxygen to X-rays. The refinement gave a good agreement with the collected powder X-ray diffraction data. The following lattice parameters were obtained, Table 6.1, with the visual representation of the observed, calculated and difference profiles for $Ba_2Sn_{0.8}YP_{0.2}O_{5.6}$ shown in Figure 6.5 with the full structural data in Table 6.2.

Table 6.1 Lattice parameters for $BaSn_{1-x}YX_xO_{5.5+z}$

Composition	a (Å)
$Ba_2SnYO_{5.5}$	4.24507(8)
$Ba_2Sn_{0.8}YP_{0.2}O_{5.6}$	4.2442(1)
$Ba_2Sn_{0.8}YS_{0.2}O_{5.7}$	4.2597(1)

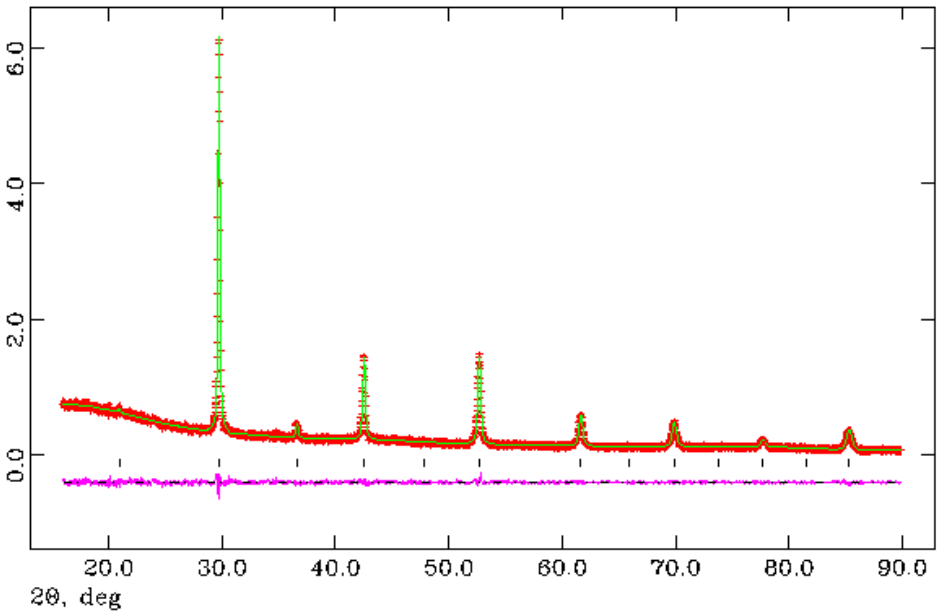

Figure 6.5 Observed, calculated and difference plots for structural refinement of $Ba_2Sn_{0.8}YS_{0.2}O_{5.7}$ using X-ray powder diffraction data

Table 6.2 Structural detail for $Ba_2Sn_{0.8}YS_{0.2}O_{5.7}$

	Site	x	y	z	Fraction	100 U ($Å^2$)
Ba	1b	0.5	0.5	0.5	1	2.9(1)
Sn	1a	0	0	0	0.4	0.7(1)
Y	1a	0	0	0	0.5	0.7(1)
S	1a	0	0	0	0.1	0.7(1)
O	3d	0.5	0	0	0.95	2.9(3)
Space Group = *P m -3 m*, a = 4.2597(1) Å wR_p = 5.02%, R_p = 4.63%, χ^2 = 1.168						

The calculated lattice parameters showed changes on phosphate and sulfate doping consistent with successful doping. For phosphate doping a decrease was observed, with an increase observed on sulfate doping. The decrease in lattice parameter on phosphate doping can be correlated with the smaller size of P^{5+} (0.17 Å) compared to Sn^{4+} (0.69 Å), which outweighs the effect of the increased oxygen content.[6] The increase in lattice parameter on sulfate doping

may be due to the higher charge of sulfate, leading to a larger increase in the oxygen content, and this increased oxygen content outweighs the effect of the smaller size of S^{6+} (0.12 Å) compared to Sn^{4+}.

6.3.1.1.2 Raman Spectroscopy

To confirm the presence of the oxyanions in the compositions, Raman spectroscopy data were collected for $Ba_2Sn_{0.8}YP_{0.2}O_{5.6}$ and $Ba_2Sn_{0.8}YS_{0.2}O_{5.7}$ and compared with $Ba_2SnYO_{5.5}$, Figure 6.6.

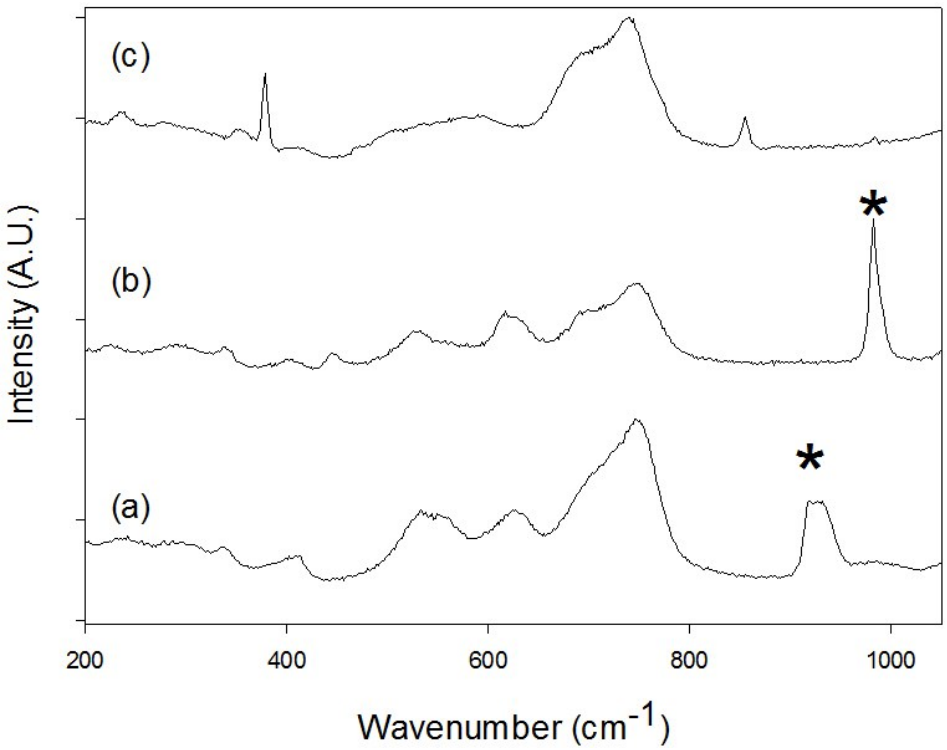

Figure 6.6 Raman spectra of (a) $Ba_2Sn_{0.8}YP_{0.2}O_{5.6}$, (b) $Ba_2Sn_{0.8}YS_{0.2}O_{5.7}$ and (c) $Ba_2SnYO_{5.5}$ with bands due to oxyanions indicated

The collected data showed a peak at 940 cm^{-1} for $Ba_2Sn_{0.8}YP_{0.2}O_{5.6}$ and a peak at 990 cm^{-1} for $Ba_2Sn_{0.8}YS_{0.2}O_{5.7}$; these peaks are due to the stretching mode of phosphate for the former and sulfate for the latter.[7, 8] As these peaks were not visible for $Ba_2SnYO_{5.5}$ they confirmed the presence of oxyanions, however in this undoped phase additional peaks were seen at 390 cm^{-1}

and 880 cm^{-1} potentially due to an impurity phase; although this phase was not seen in the powder XRD pattern.

The spectra of all the compositions show the presence of a range of Raman active bands; these bands should not be Raman active if the composition was a perfect cubic perovskite as the lattice sites all have inversion symmetry. As these bands are present, this indicates that the structure for all the compositions is not locally cubic and further studies, for example total scattering experiments are required to investigate in more detail this local structure.

6.3.1.2 Conductivity Measurements

Conductivity measurements were collected in dry and wet N_2 on all the samples, and compared with $Ba_2SnYO_{5.5}$. All the compositions showed a high total conductivity with an enhancement in wet atmospheres, indicative of a protonic contribution, Table 6.3 and Figure 6.7.

Table 6.3 Total conductivity data for $Ba_2Sn_{1-x}YX_xO_{5.5+z}$

Sample (nominal composition)	Conductivity (S cm^{-1})			
	500 °C		800 °C	
	Dry N_2	Wet N_2	Dry N_2	Wet N_2
$Ba_2SnYO_{5.5}$	1.0×10^{-4}	3.2×10^{-4}	7.4×10^{-4}	8.1×10^{-4}
$Ba_2Sn_{0.8}YP_{0.2}O_{5.6}$	4.8×10^{-5}	1.2×10^{-4}	2.8×10^{-4}	6.8×10^{-4}
$Ba_2Sn_{0.8}YS_{0.2}O_{5.7}$	4.3×10^{-5}	1.2×10^{-4}	2.3×10^{-4}	5.7×10^{-4}

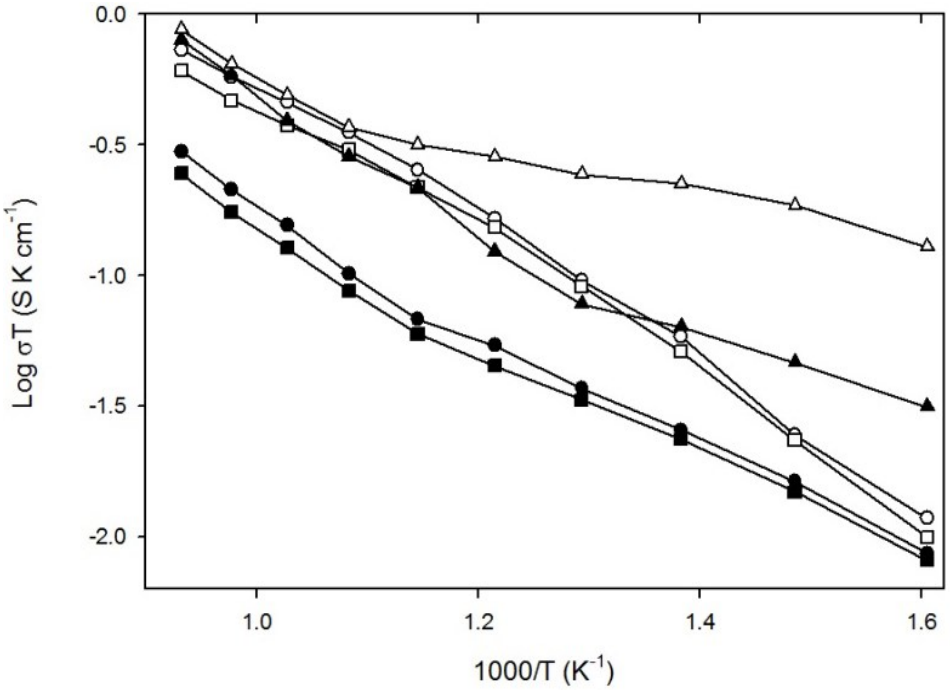

Figure 6.7 Conductivity data for $Ba_2Sn_{0.8}YP_{0.2}O_{5.6}$ (circle), $Ba_2Sn_{0.8}YS_{0.2}O_{5.7}$ (square) and $Ba_2SnYO_{5.5}$ (triangle) in dry (filled) and wet (empty) N_2

The collected conductivity data showed that on oxyanion doping the conductivity decreased. This can be correlated with the lower number of oxygen vacancies due to the higher oxidation states of phosphorus and sulfur compared to tin, and the tetrahedral coordination of the oxyanions, which can lead to trapping of oxide ion vacancies. The difference between the conductivities of the oxyanion doped compositions in wet and dry N_2 increases with temperature whereas for $Ba_2SnYO_{5.5}$ the difference decreases; further work is required to understand why this is occurring.

As a p-type contribution to the conductivity was seen by Wang *et al*. measurements were carried out in dry O_2 to determine if there was also a p-type contribution to the conductivity in the oxyanion doped samples, Figure 6.8.

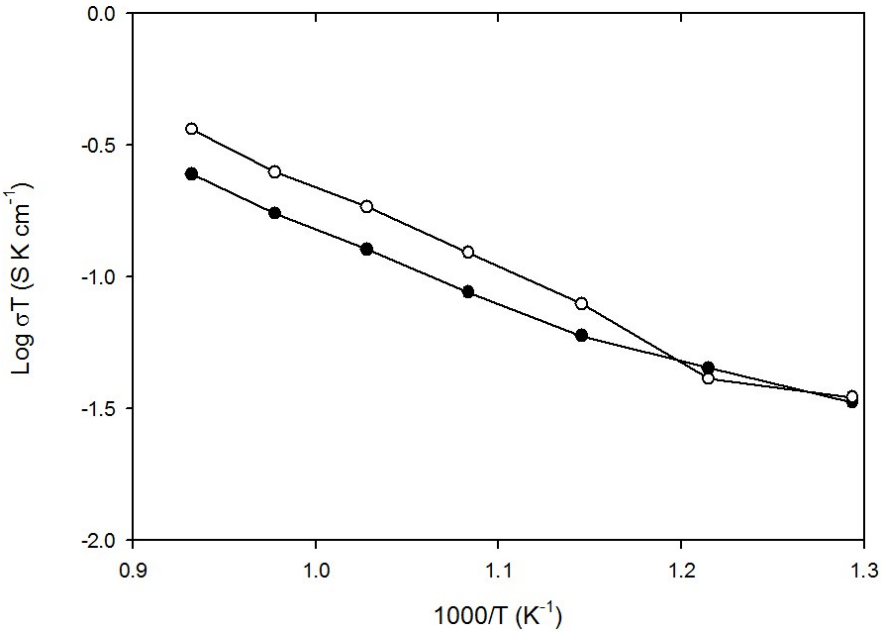

Figure 6.8 Conductivity data for $Ba_2Sn_{0.8}YP_{0.2}O_{5.6}$ in dry N_2 (filled circle) and dry O_2 (empty circle)

The collected data showed that all samples exhibited a p-type contribution to the conductivity at elevated temperatures, as found for the other electrolyte compositions in this thesis, due to oxygen incorporation into the vacancies according to $V_O^{\bullet\bullet} + O_O^x + \frac{1}{2}O_2 \leftrightarrow 2O_O^{\bullet}$.

6.3.1.3 Chemical Stability

6.3.1.3.1 CO_2 Stability

The first experiment to test the CO_2 stability was to use TGA to monitor the temperature at which mass gain, formation of $BaCO_3$, occurred under heating to 1000 °C at 10 °C min^{-1} under a flowing mix of 1:1 CO_2:N_2. None of the compositions showed any mass gain under these conditions.

The second experiment carried out involved heating the samples at 800 °C for 12 hours under flowing CO_2 and then using powder XRD to observe if any decomposition had taken place, Figure 6.9.

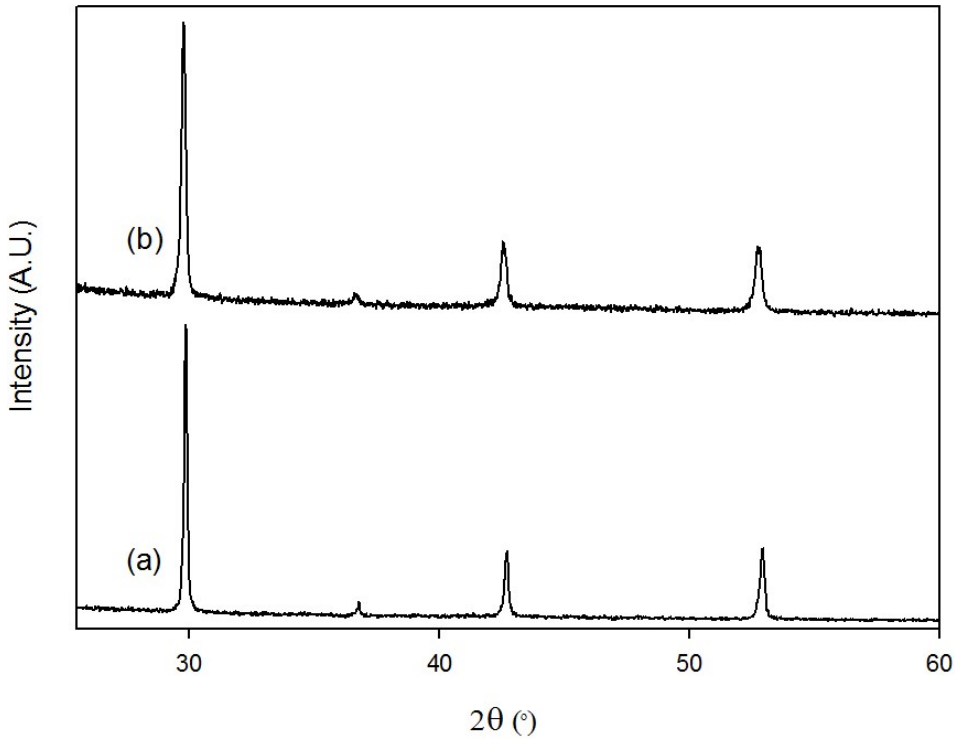

Figure 6.9 Powder X-ray diffraction data (a) $Ba_2Sn_{0.8}YbP_{0.2}O_{5.6}$ and (b) $Ba_2Sn_{0.8}YbS_{0.2}O_{5.7}$ after heating for 12 hours at 800 °C under flowing CO_2

The XRDs show that the compositions are completely stable with respect to CO_2 at standard operating temperatures for proton conducting SOFCs at this temperature, with no sign of $BaCO_3$ formation.

6.3.1.3.2 Stability to Reducing Atmospheres

Murugaraj *et al*. found that under reducing conditions there is a change in the structure of $Ba_2SnYO_{5.5}$ leading to oxygen vacancy ordering and the formation of the brownmillerite structure, the same structure as $Ba_2In_2O_5$.[2, 9] Therefore $Ba_2Sn_{0.8}YP_{0.2}O_{5.6}$, $Ba_2Sn_{0.8}YS_{0.2}O_{5.7}$ and $Ba_2SnYO_{5.5}$ were heated under flowing 10% H_2 in N_2 at 1000 °C for 36 hours and powder XRD was used to observe if there had been any change in the structure, .

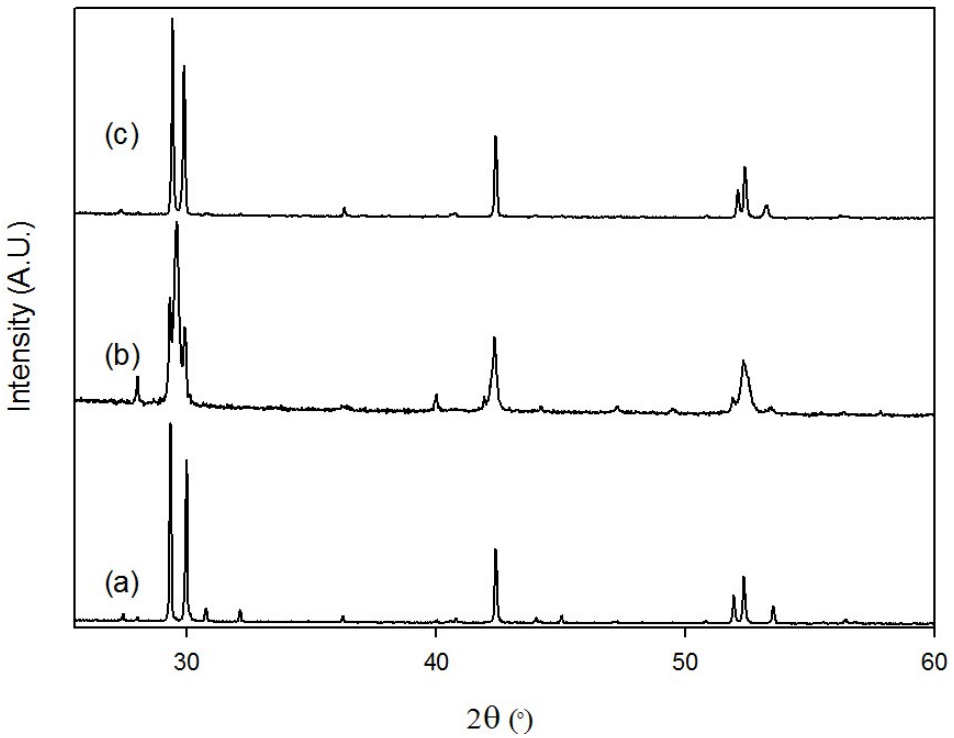

Figure 6.10 Powder X-ray diffraction patterns of (a) $Ba_2SnYO_{5.5}$, (b) $Ba_2Sn_{0.8}YS_{0.2}O_{5.7}$ and (c) $Ba_2Sn_{0.8}YP_{0.2}O_{5.6}$ after heating under 10% H_2 for 36 hours

The collected data showed that the structure of all three compositions changed to brownmillerite from a cubic perovskite, although the sulfate composition did not seem undergo complete change, with evidence for a mixed perovskite/ brownmillerite phase.

6.3.2 Oxyanion doped $Ba_2SnYbO_{5.5}$

6.3.2.1 Structural Determination

6.3.2.1.1 Powder X-ray Diffraction

Following on from examining oxyanion doped $Ba_2SnYO_{5.5}$, it was decided to attempt oxyanion doping of $Ba_2SnYbO_{5.5}$. $Ba_2SnYbO_{5.5}$ has not been previously examined but oxyanion doping of ytterbium doped barium cerate had proven successful in the previous chapter. Initial compositions involved 10% oxyanion (borate, phosphate and sulfate) doping for tin as proved successful for phosphate and sulfate doping of $Ba_2SnYO_{5.5}$ (section 6.3.1).

Powder XRD patterns of the compositions after synthesis showed the formation of cubic perovskites for all the attempted oxyanion doped phases, Figure 6.11.

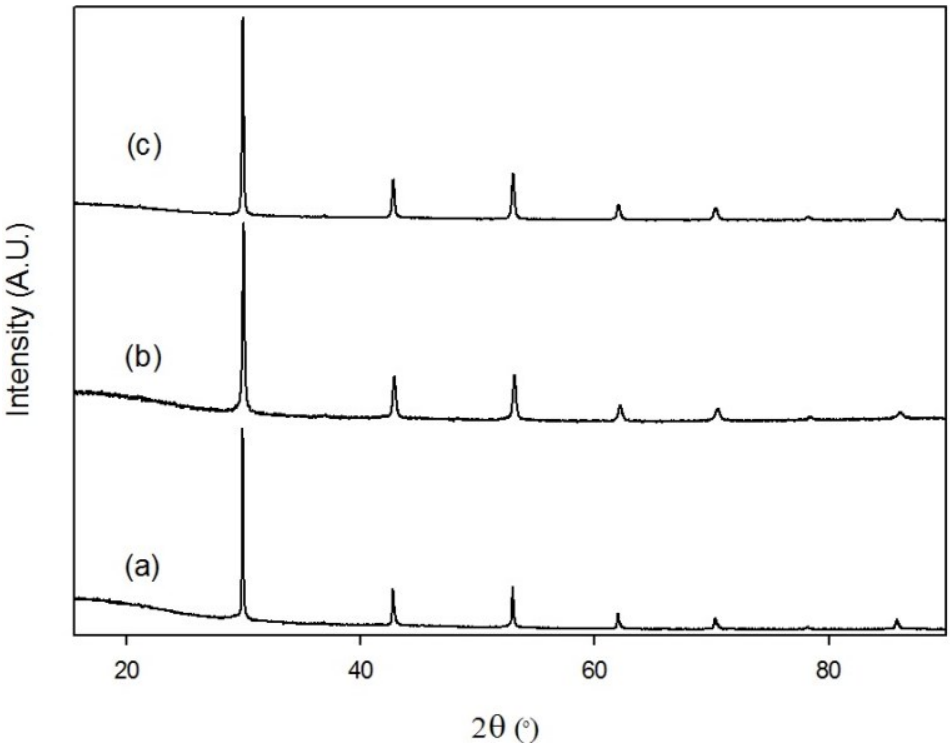

Figure 6.11 Powder X-ray diffraction data of (a) $Ba_2Sn_{0.8}YbB_{0.2}O_{5.4}$, (b) $Ba_2Sn_{0.8}YbP_{0.2}O_{5.6}$ and (c) $Ba_2Sn_{0.8}YbS_{0.2}O_{5.7}$

Higher oxyanion contents were not attempted but following on from the successful incorporation of boron, silicon doping was also attempted, which had proven successful for $Ba_2In_2O_5$. While the attempted silicon doped composition resulted in the formation of a cubic perovskite phase, there was also the formation of Ba_2SiO_4 as an impurity phase, Figure 6.12, and so this system was not examined further.

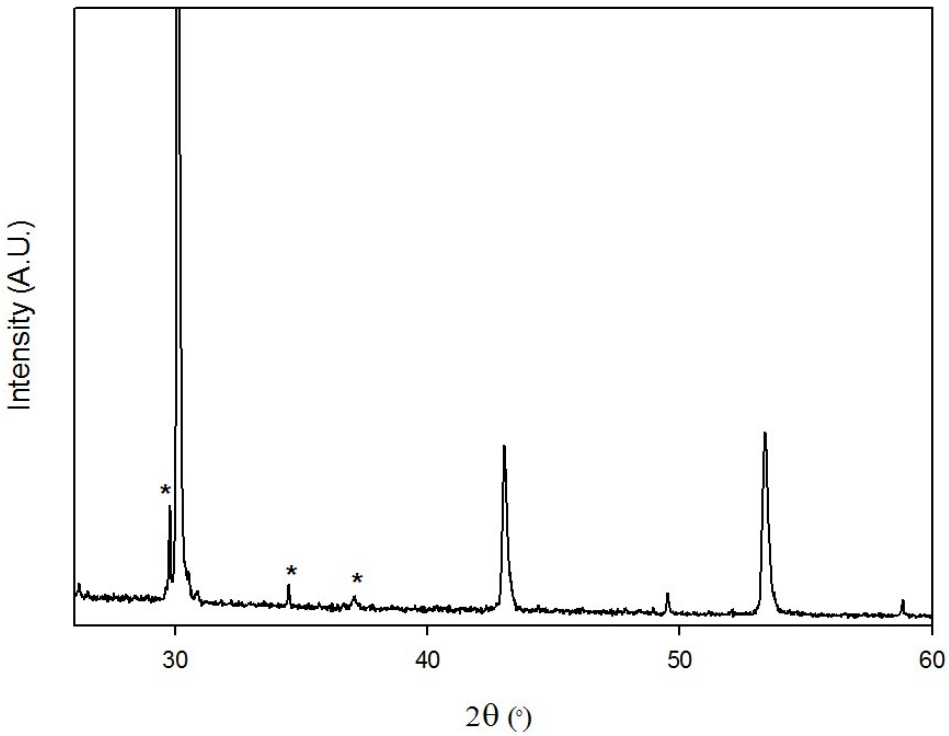

Figure 6.12 Powder X-ray diffraction data for attempted synthesis of "$Ba_2Sn_{0.8}YbSi_{0.2}O_{5.5}$" with impurity peaks indicated

Oxyanion doping for ytterbium was not attempted as oxyanion doping for yttrium had proven unsuccessful, Figure 6.4.

Rietveld refinement was carried out on the three single phase compositions using the GSAS suite of programs in order to obtain the lattice parameters.[5] The same space group, *P m -3 m*, was used as for the yttrium analogues. The tin, ytterbium, phosphorus, sulfur and boron were placed on the *1a* site using the expected stoichiometries and these occupancies were not refined. The oxygen content was set to the expected amount from the cation oxidation states and the occupancy and atomic positions were not refined. The refinement gave a good agreement with the collected powder X-ray diffraction data. The following lattice parameters were obtained, Table 6.4, with the visual representation and the complete description of the refined model of $Ba_2Sn_{0.8}YbS_{0.2}O_{5.7}$ shown in Figure 6.13 and Table 6.5 respectively.

Table 6.4 Lattice parameters for $Ba_2Sn_{1-x}YbX_xO_{5.5+z}$

Composition	a (Å)
$Ba_2Sn_{0.8}YbB_{0.2}O_{5.4}$	4.2389(1)
$Ba_2Sn_{0.8}YbP_{0.2}O_{5.6}$	4.2290(1)
$Ba_2Sn_{0.8}YbS_{0.2}O_{5.7}$	4.23936(6)

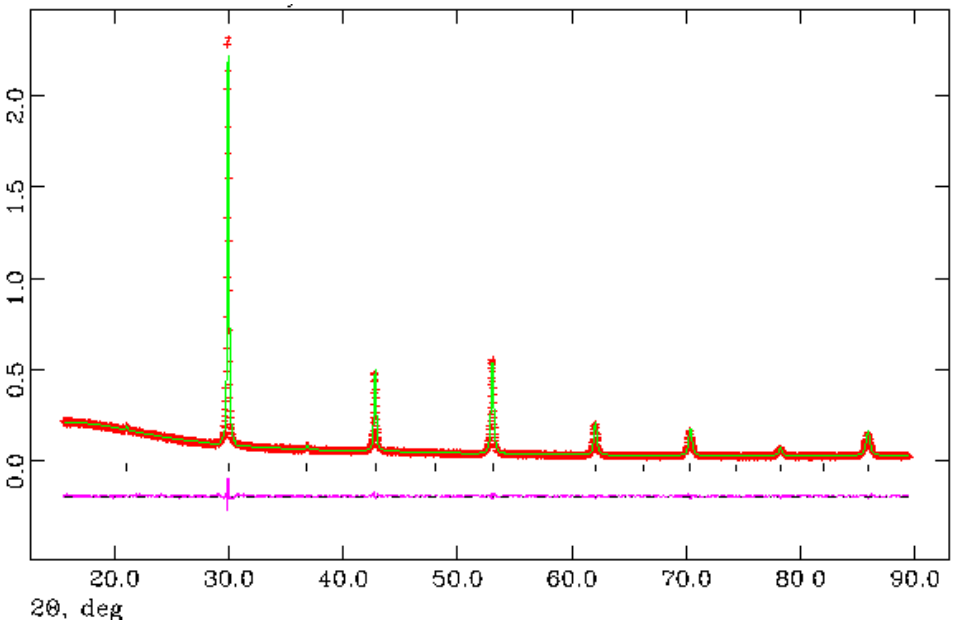

Figure 6.13 Observed, calculated and difference plots for structural refinement of $Ba_2Sn_{0.8}YbS_{0.2}O_{5.7}$ using X-ray powder diffraction data

Table 6.5 Structural detail for $Ba_2Sn_{0.8}YbS_{0.2}O_{5.7}$

	Site	x	y	z	Fraction	100 U (Å^2)
Ba	1b	0.5	0.5	0.5	1	1.94(9)
Sn	1a	0	0	0	0.4	0.87(8)
Yb	1a	0	0	0	0.5	0.87(8)
S	1a	0	0	0	0.1	0.87(8)
O	3d	0.5	0	0	0.95	3.1(2)
Space Group = *P m -3 m*, a = 4.23936(6) Å wR_p = 4.00%, R_p = 3.60%, χ^2 = 1.477						

The compositions had a smaller lattice parameter than their yttrium analogues, consistent with the fact that Y^{3+} (0.9 Å) has a larger ionic radius than Yb^{3+} (0.868 Å).[6] The lattice parameter was larger for $Ba_2Sn_{0.8}YbS_{0.2}O_{5.7}$ than $Ba_2Sn_{0.8}YbP_{0.2}O_{5.6}$, as seen for the yttrium analogues, due to the lower number of oxygen vacancies in the sulfur composition. $Ba_2Sn_{0.8}YbB_{0.2}O_{5.4}$ has a larger lattice parameter than $Ba_2Sn_{0.8}YbP_{0.2}O_{5.6}$ despite having a smaller ionic size and a

larger number of oxygen vacancies and further work probing the local structure of these compositions is required to explain this.

6.3.2.1.2 Raman Spectroscopy

To confirm the presence of oxyanions in the samples, Raman spectroscopy studies were carried out on all the compositions, Figure 6.14.

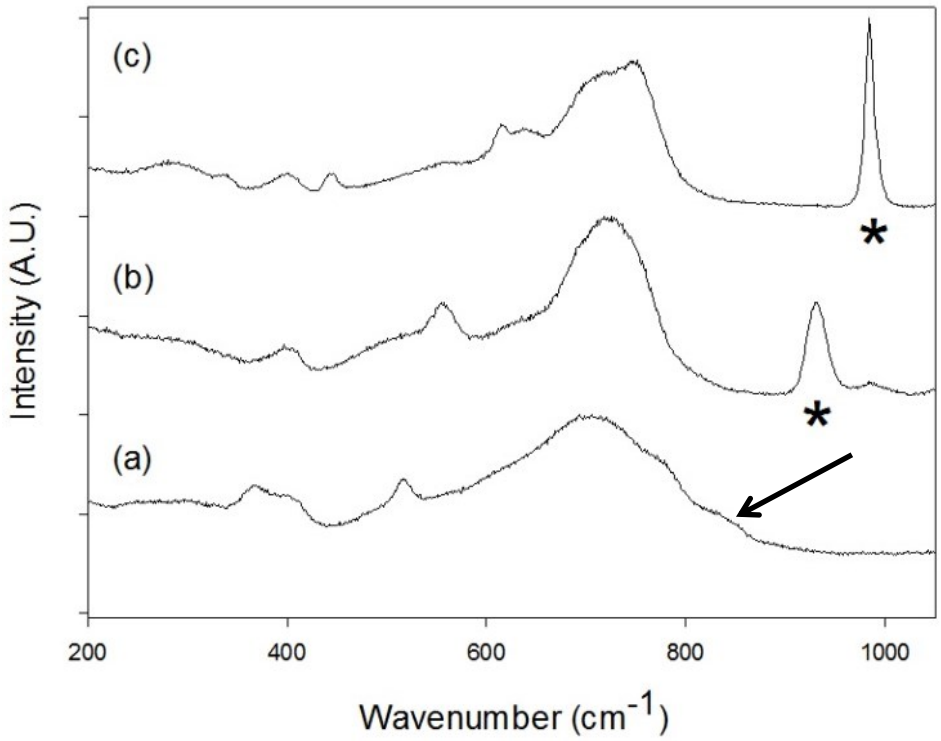

Figure 6.14 Raman spectra of (a) $Ba_2Sn_{0.8}YbB_{0.2}O_{5.4}$, (b) $Ba_2Sn_{0.8}YbP_{0.2}O_{5.6}$ and (c) $Ba_2Sn_{0.8}YbS_{0.2}O_{5.7}$ with bands due to oxyanions indicated

The Raman spectra of $Ba_2Sn_{0.8}YbP_{0.2}O_{5.6}$ and $Ba_2Sn_{0.8}YbS_{0.2}O_{5.7}$ show the presence of a band at 940 cm^{-1} for the former, due to the internal stretching mode of phosphate, and 990 cm^{-1} for the latter, the symmetric stretch of sulfate, confirming their presence.[7, 8] The spectra of $Ba_2Sn_{0.8}YbP_{0.2}O_{5.6}$ also contains a peak at 415 cm^{-1} due to a bending mode of phosphate and $Ba_2Sn_{0.8}YbS_{0.2}O_{5.7}$ has two additional peaks at 450 cm^{-1}, symmetric bend of sulfate, and 610 cm^{-1}, asymmetric bend of sulfate.[7, 8] The spectra of $Ba_2Sn_{0.8}YbB_{0.2}O_{5.4}$ does not contain a separate clearly observed peak from borate doping, however there is a shoulder at 835 cm^{-1}

which could be attributed to the symmetric stretch of borate consistent with the incorporation of borate in the structure.[10]

There are additional bands present, as seen for the yttrium compositions, which mean that the structure is locally not cubic.

6.3.2.2 Conductivity Measurements

Conductivity measurements were collected in dry and wet N_2 to observe if there is a protonic contribution in wet atmospheres to the conductivity. All the compositions showed a high conductivity with a protonic contribution, Table 6.6 and Figure 6.15.

Table 6.6 Total conductivity data for $Ba_2Sn_{1-x}YbX_xO_{5.5+z}$

Sample (nominal composition)	Conductivity (S cm^{-1})			
	500 °C		800 °C	
	Dry N_2	Wet N_2	Dry N_2	Wet N_2
$Ba_2Sn_{0.8}YbB_{0.2}O_{5.4}$	1.4×10^{-4}	5.4×10^{-4}	1.0×10^{-3}	8.4×10^{-4}
$Ba_2Sn_{0.8}YbP_{0.2}O_{5.6}$	1.3×10^{-5}	6.0×10^{-5}	3.4×10^{-4}	4.6×10^{-4}
$Ba_2Sn_{0.8}YbS_{0.2}O_{5.7}$	2.9×10^{-5}	1.1×10^{-4}	1.2×10^{-3}	1.4×10^{-3}

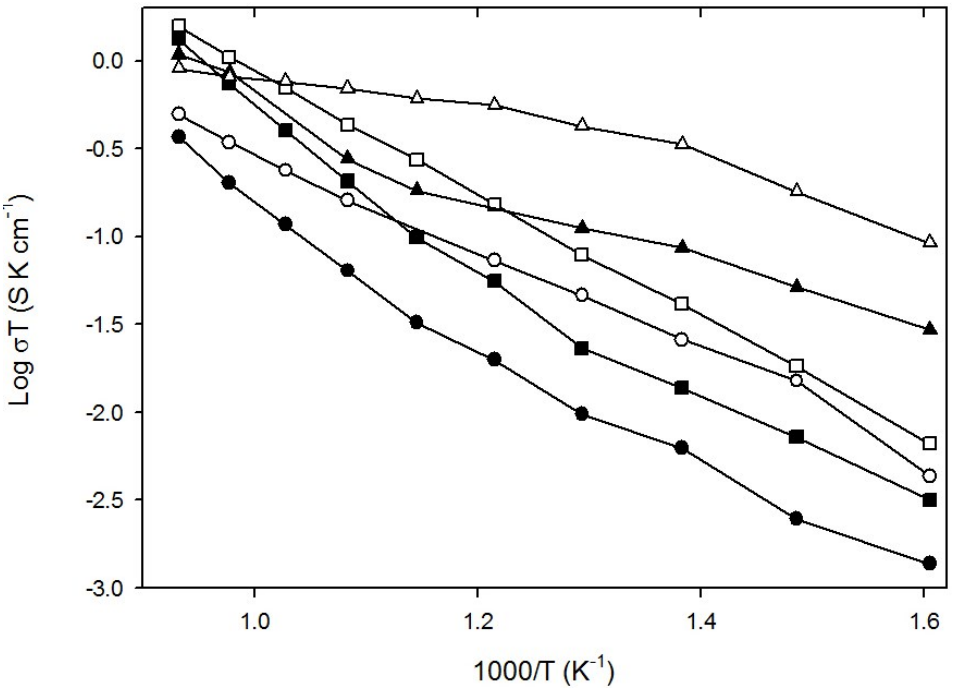

Figure 6.15 Conductivity data for $Ba_2Sn_{0.8}YbB_{0.2}O_{5.4}$ (triangle), $Ba_2Sn_{0.8}YbP_{0.2}O_{5.6}$ (circle) and $Ba_2Sn_{0.8}YbS_{0.2}O_{5.7}$ (square) in dry (filled) and wet (empty) N_2

$Ba_2Sn_{0.8}YbP_{0.2}O_{5.6}$ had the lowest conductivity of the three compositions, however this could be attributed due to the poor sinterability of this composition (60%) compared to the other two (~75%) and heat treatments at a higher temperature failed to resolve this issue. $Ba_2Sn_{0.8}YbB_{0.2}O_{5.4}$ had the best conductivity at lower temperatures however at higher temperatures it had a similar conductivity to the sulfate doped composition. The conductivities at 800 °C for the sulfate and borate samples were found to be superior to $Ba_2SnYO_{5.5}$.

As a p-type contribution to the conductivity was seen for other samples in this thesis the conductivity of the samples were collected in dry O_2 and compared with the results from dry N_2, the data for $Ba_2Sn_{0.8}YbS_{0.2}O_{5.7}$ are shown in Figure 6.16.

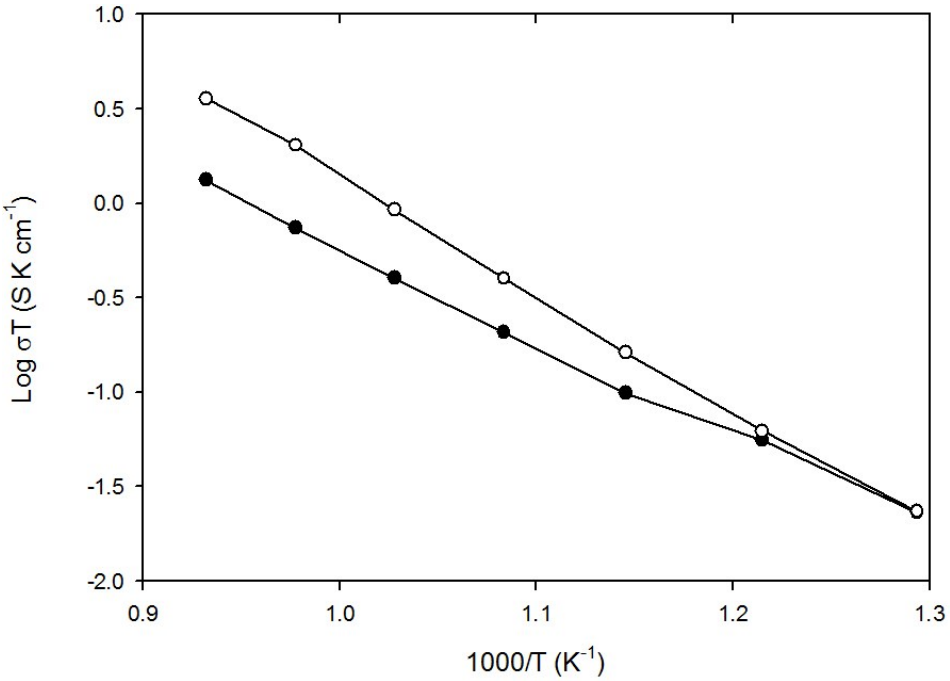

Figure 6.16 Conductivity data for $Ba_2Sn_{0.8}YbS_{0.2}O_{5.7}$ in dry N_2 (filled circle) and dry O_2 (empty circle)

All the compositions showed a p-type contribution to the conductivity due to the introduction of holes from the filling of the oxygen vacancies by oxygen according to the equation in section 6.3.1.2.

6.3.2.3 Chemical Stability

6.3.2.3.1 CO_2 Stability

As CO_2 stability is an issue for perovskite proton conducting electrolytes for proton conducting SOFCs, two experiments to determine the samples stability were carried out. The first of which involved heating the samples (10 °C min^{-1}) under a flowing mix of 1:1 CO_2:N_2 to 1000 °C and observing using TGA at what temperature mass gain occurred. All these compositions showed no mass gain under these conditions.

The second experiment involved heating the samples at 800 °C in a furnace for 12 hours under flowing CO_2 and examining the powder XRD patterns for partial decomposition, Figure 6.17.

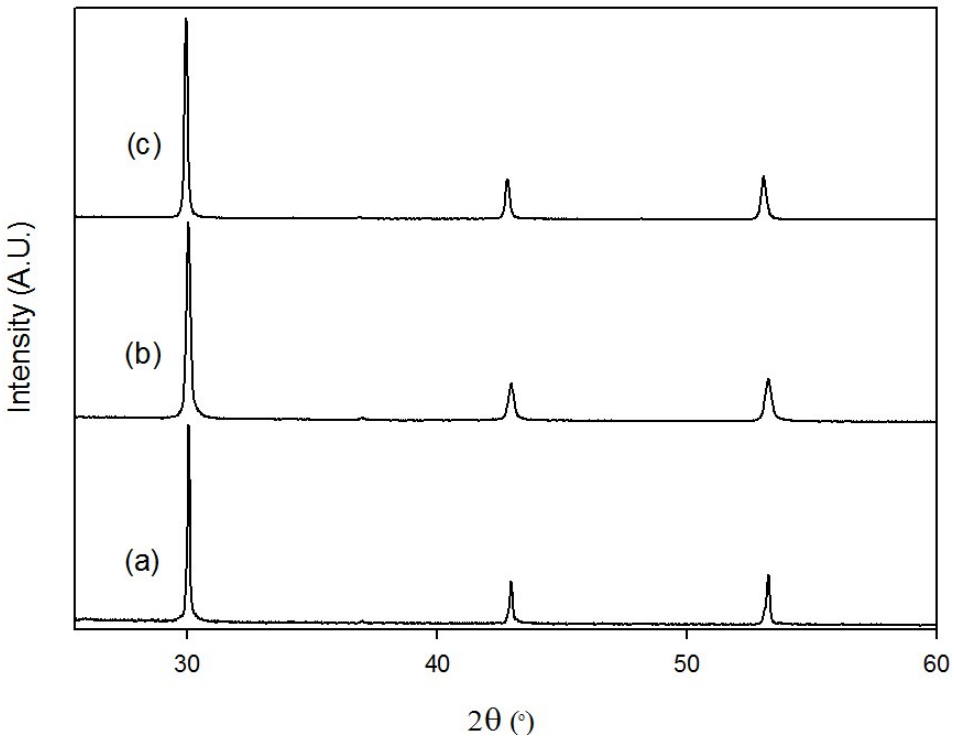

Figure 6.17 Powder X-ray diffraction data (a) $Ba_2Sn_{0.8}YbB_{0.2}O_{5.4}$, (b) $Ba_2Sn_{0.8}YbP_{0.2}O_{5.6}$ and (c) $Ba_2Sn_{0.8}YbS_{0.2}O_{5.7}$ after heating for 12 hours at 800 °C under flowing CO_2

The collected data shows that all the compositions are completely stable to CO_2 under these conditions.

6.3.2.3.2 Stability to Reducing Atmospheres

As the yttrium containing compositions all showed a change in structure upon heating in a reducing atmosphere the ytterbium compositions were also heated at 1000 °C for 36 hours under flowing 10%/90% H_2 in N_2 and the powder XRD patterns were examined for partial decomposition/ structural change, Figure 6.18.

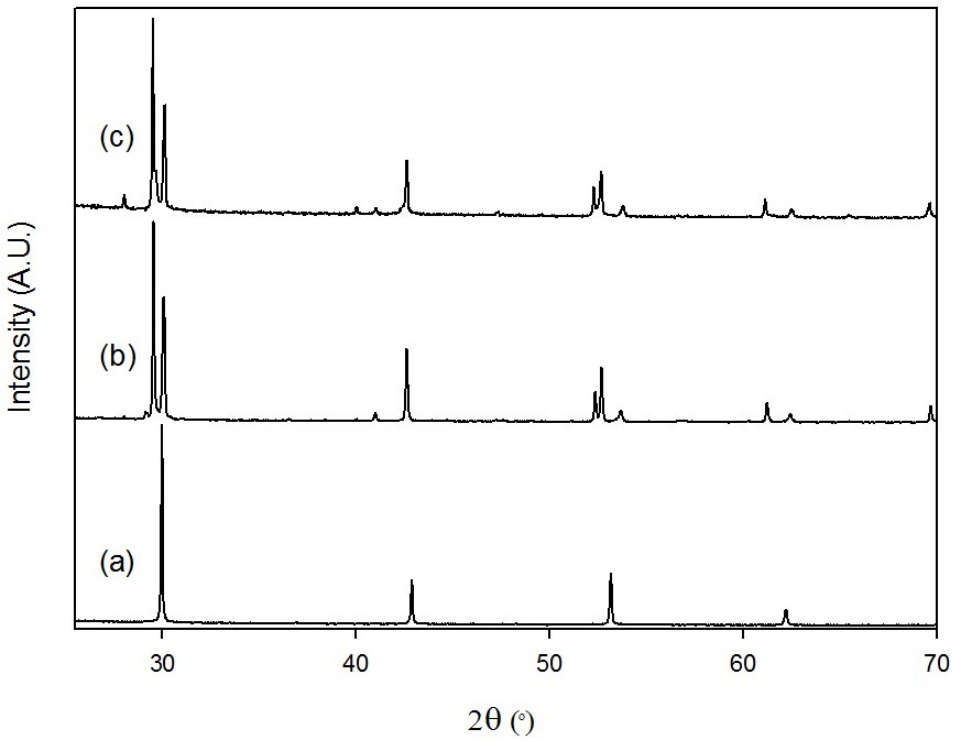

Figure 6.18 Powder X-ray diffraction patterns of (a) $Ba_2Sn_{0.8}YbB_{0.2}O_{5.4}$, (b) $Ba_2Sn_{0.8}YbP_{0.2}O_{5.6}$ and (c) $Ba_2Sn_{0.8}YbS_{0.2}O_{5.7}$ after heating under 10% H_2 for 36 hours

$Ba_2Sn_{0.8}YbP_{0.2}O_{5.6}$ and $Ba_2Sn_{0.8}YbS_{0.2}O_{5.7}$ formed a brownmillerite structure under these conditions as seen for the yttrium analogues. However $Ba_2Sn_{0.8}YbB_{0.2}O_{5.4}$ was found to be completely stable under these conditions as it retained the cubic structure and showed no change of this structure to a brownmillerite phase. This shows that $Ba_2Sn_{0.8}YbB_{0.2}O_{5.4}$ not only retains the high conductivity seen for $Ba_2SnYO_{5.5}$, but it also has a better chemical stability and suggests that $Ba_2Sn_{0.8}YbB_{0.2}O_{5.4}$ has superior properties as an electrolyte in an SOFC. Further work is required to investigate the conductivity of this phase in H_2/N_2

6.3.3 Oxyanion doped $Ba_2Sn_{1-x}Ti_xYO_{5.5}$

6.3.3.1 Structural Determination

6.3.3.1.1 Powder X-ray Diffraction

Titanium doping for tin was attempted to observe how this affects the properties of the $Ba_2SnYO_{5.5}$ series. Initial doping was carried out at the 10% and 20% levels for tin giving

compositions $Ba_2Sn_{0.8}Ti_{0.2}YO_{5.5}$ and $Ba_2Sn_{0.6}Ti_{0.4}YO_{5.5}$ with the XRD patterns shown in Figure 6.19.

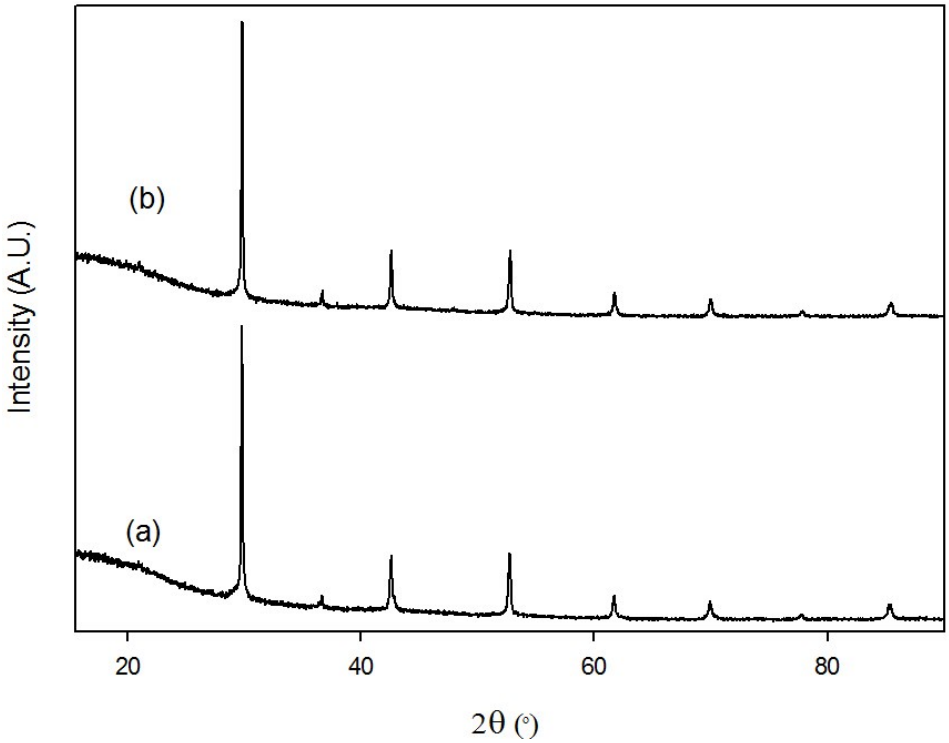

Figure 6.19 Powder X-ray diffraction patterns of (a) $Ba_2Sn_{0.8}Ti_{0.2}YO_{5.5}$ and (b) $Ba_2Sn_{0.6}Ti_{0.4}YO_{5.5}$

Higher titanium contents were also attempted, Figure 6.20, however this resulted in the presence of Ba_2TiO_4 impurity alongside the cubic perovskite phase, showing that titanium could not be incorporated above the 20% level.

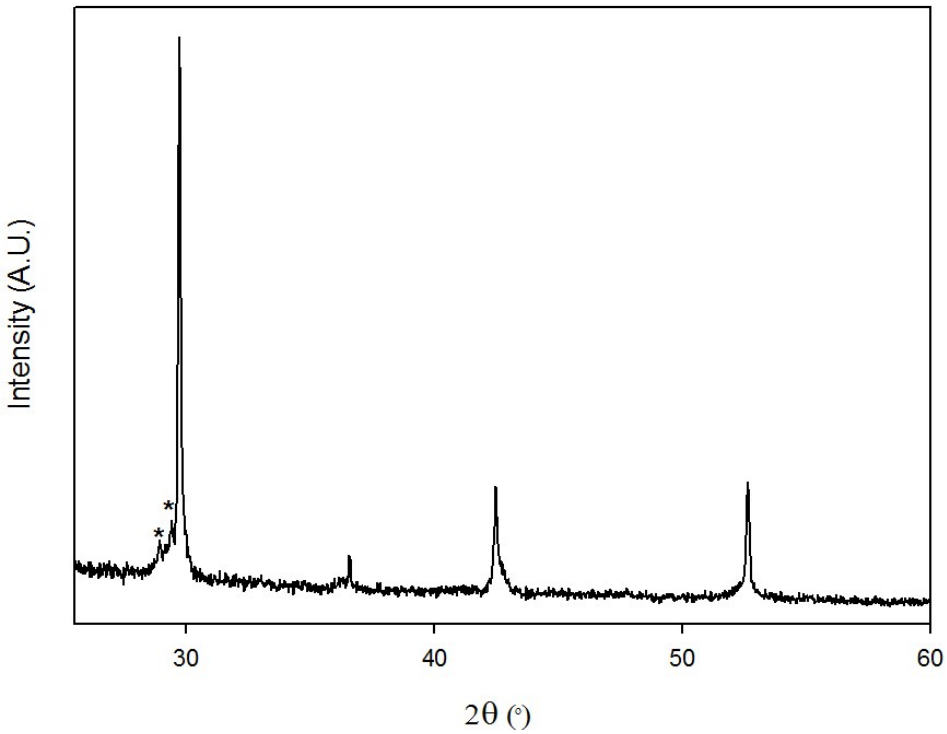

Figure 6.20 Powder X-ray diffraction pattern for the attempted synthesis of "$Ba_2Sn_{0.4}Ti_{0.6}YO_{5.5}$" with the peaks related to Ba_2TiO_4 indicated

After demonstrating that titanium could be incorporated successfully into the $Ba_2SnYO_{5.5}$ this work was extended to doping oxyanions into this phase. Initial oxyanion doping was carried out with 10% titanium and oxyanion content for borate, phosphate and sulfate, giving the following compositions $Ba_2Sn_{0.6}Ti_{0.2}YB_{0.2}O_{5.4}$, $Ba_2Sn_{0.6}Ti_{0.2}YP_{0.2}O_{5.6}$ and $Ba_2Sn_{0.6}Ti_{0.2}YS_{0.2}O_{5.7}$. These stoichiometries resulted in the formation of pure cubic perovskites although some peak broadening occurred at the base of the peaks in $Ba_2Sn_{0.6}Ti_{0.2}YS_{0.2}O_{5.7}$, Figure 6.21.

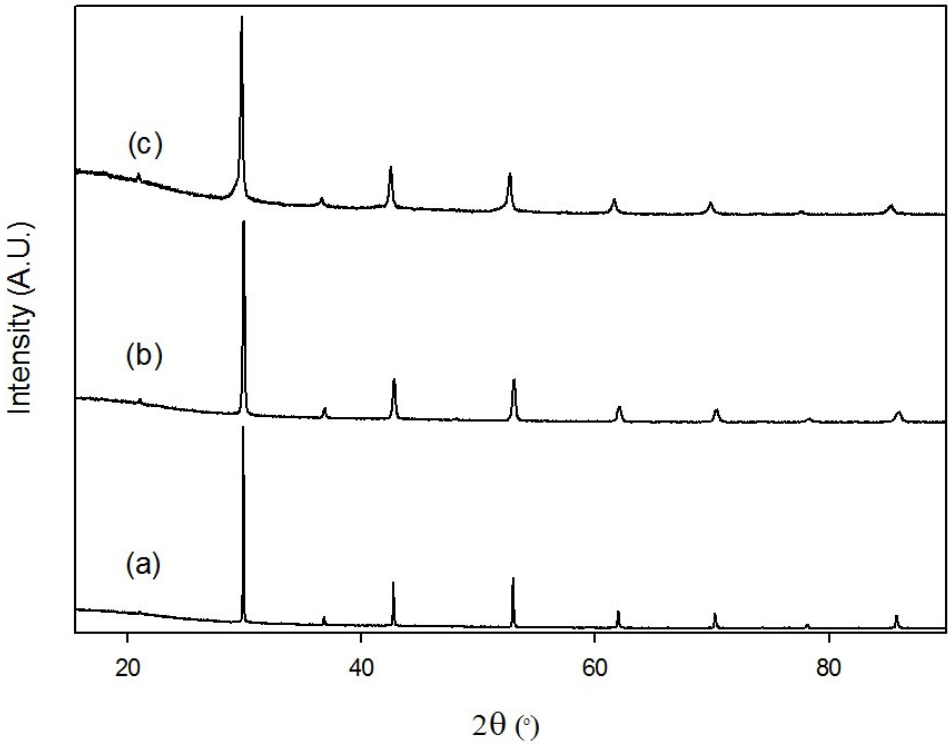

Figure 6.21 Powder X-ray diffraction data of (a) $Ba_2Sn_{0.6}Ti_{0.2}YB_{0.2}O_{5.4}$, (b) $Ba_2Sn_{0.6}Ti_{0.2}YP_{0.2}O_{5.6}$ and (c) $Ba_2Sn_{0.6}Ti_{0.2}YS_{0.2}O_{5.7}$

As with $Ba_2SnYbO_{5.5}$ silicon doping was attempted and resulted in the formation of Ba_2SiO_4 impurity alongside a cubic perovskite phase, Figure 6.22, so this phase was not analysed further.

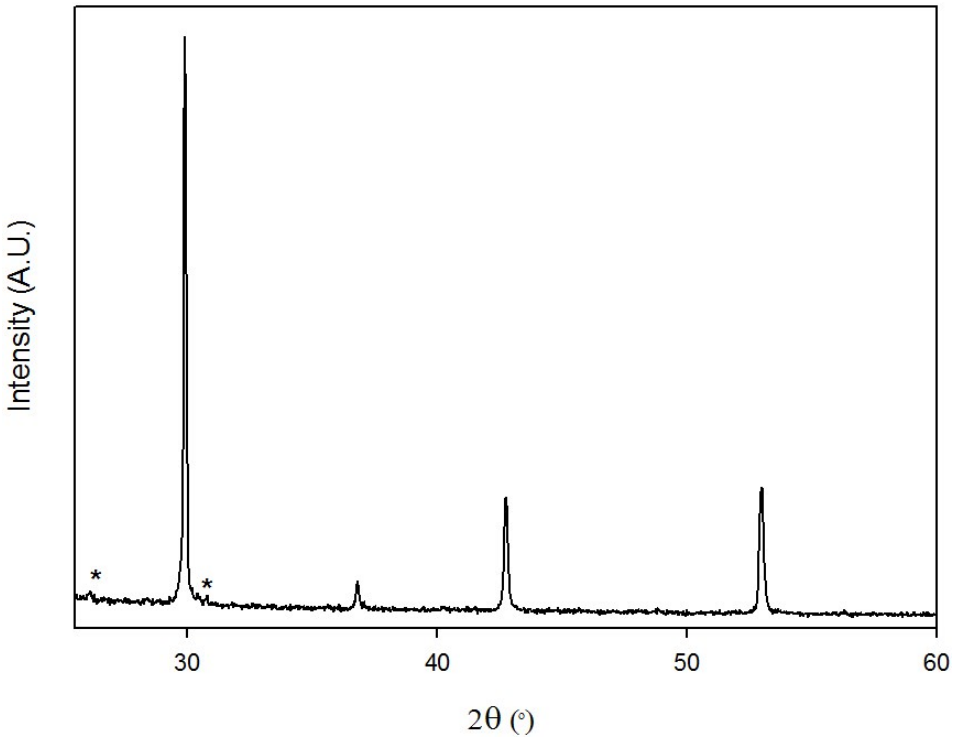

Figure 6.22 Powder X-ray diffraction data for attempted synthesis of "$Ba_2Sn_{0.6}Ti_{0.2}YSi_{0.2}O_{5.5}$" with Ba_2SiO_4 impurity peaks indicated

Rietveld refinement was carried out on the single phase samples synthesised using the GSAS suite of programs to determine the lattice parameters. A structural model with space group *P m -3 m* was used with the tin, yttrium, titanium and respective oxyanion placed on the *1a* site with the expected stoichiometry from the weighed out amounts. The oxygen content was set to the expected amount from the cation oxidation states. The refinements gave good agreement with the collected data and the following lattice parameters were obtained, Table 6.7, and the observed, calculated and difference profiles for $Ba_2Sn_{0.6}Ti_{0.2}YB_{0.2}O_{5.4}$ shown in Figure 6.23 along with the complete structural details for this phase in Table 6.8.

Table 6.7 Lattice parameters of $Ba_2Sn_{1-x-y}Ti_yYX_xO_{5.5+z}$

Composition	a (Å)
$Ba_2Sn_{0.8}Ti_{0.2}YO_{5.5}$	4.2599(1)
$Ba_2Sn_{0.6}Ti_{0.4}YO_{5.5}$	4.2551(1)
$Ba_2Sn_{0.6}Ti_{0.2}YB_{0.2}O_{5.4}$	4.24051(4)
$Ba_2Sn_{0.6}Ti_{0.2}YP_{0.2}O_{5.6}$	4.23406(9)
$Ba_2Sn_{0.6}Ti_{0.2}YS_{0.2}O_{5.7}$	4.2612(9)

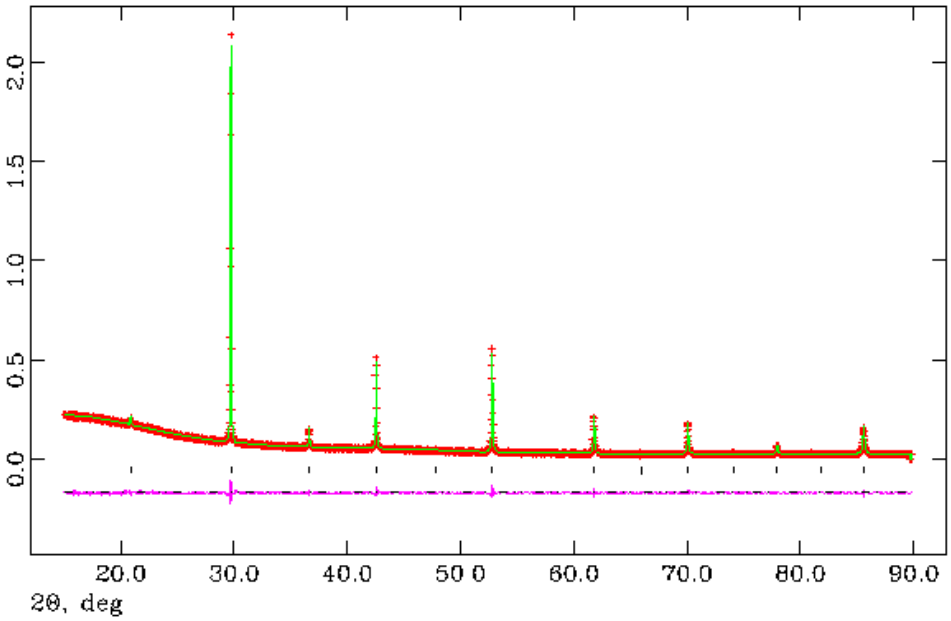

Figure 6.23 Observed, calculated and difference plots for structural refinement of $Ba_2Sn_{0.6}Ti_{0.2}YB_{0.2}O_{5.4}$ using X-ray powder diffraction data

Table 6.8 Structural detail for $Ba_2Sn_{0.6}Ti_{0.2}YB_{0.2}O_{5.4}$

	Site	x	y	z	Fraction	100 U ($Å^2$)
Ba	1b	0.5	0.5	0.5	1	2.49(9)
Sn	1a	0	0	0	0.3	0.05(9)
Ti	1a	0	0	0	0.1	0.05(9)
Y	1a	0	0	0	0.5	0.05(9)
B	1a	0	0	0	0.1	0.05(9)
O	3d	0.5	0	0	0.9	4.1(3)
Space Group = *P m -3 m*, a = 4.24051(4) Å wR_p = 5.72%, R_p = 4.99%, χ^2 = 1.413						

The cell parameter data showed some unusual variation with titanium content and oxyanion doping which require further study to rationalise.

6.3.3.1.2 Raman Spectroscopy

To provide further confirmation that the oxyanions are incorporated in the structure Raman spectroscopy data were collected on all the pure samples, Figure 6.24 and Figure 6.25.

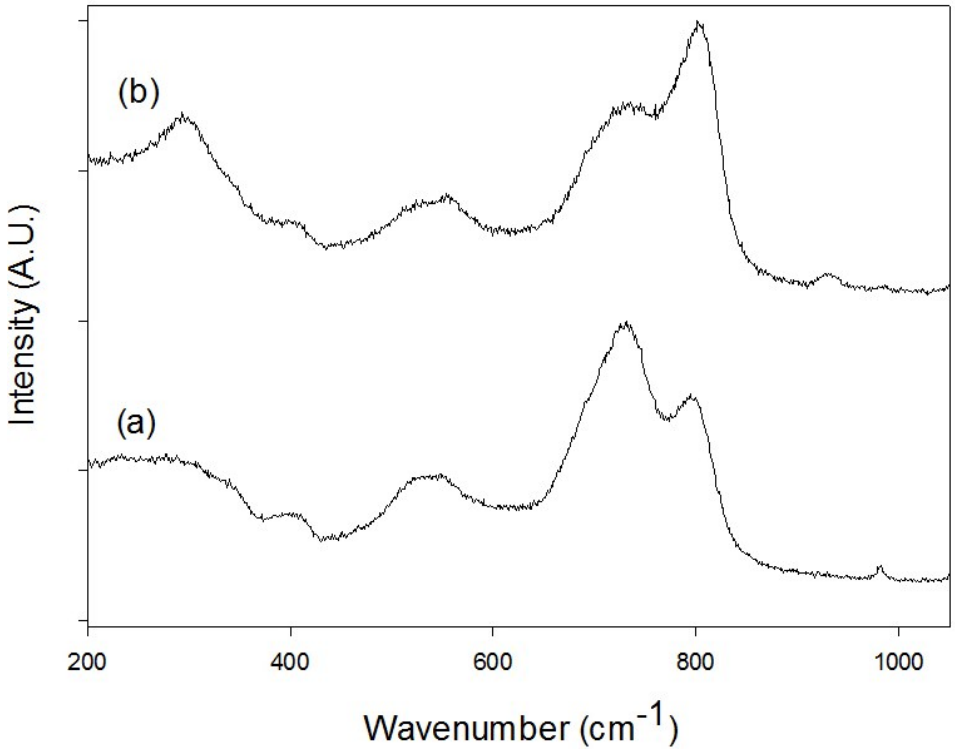

Figure 6.24 Raman spectra of (a) $Ba_2Sn_{0.8}Ti_{0.2}YO_{5.5}$ and (b) $Ba_2Sn_{0.6}Ti_{0.4}YO_{5.5}$

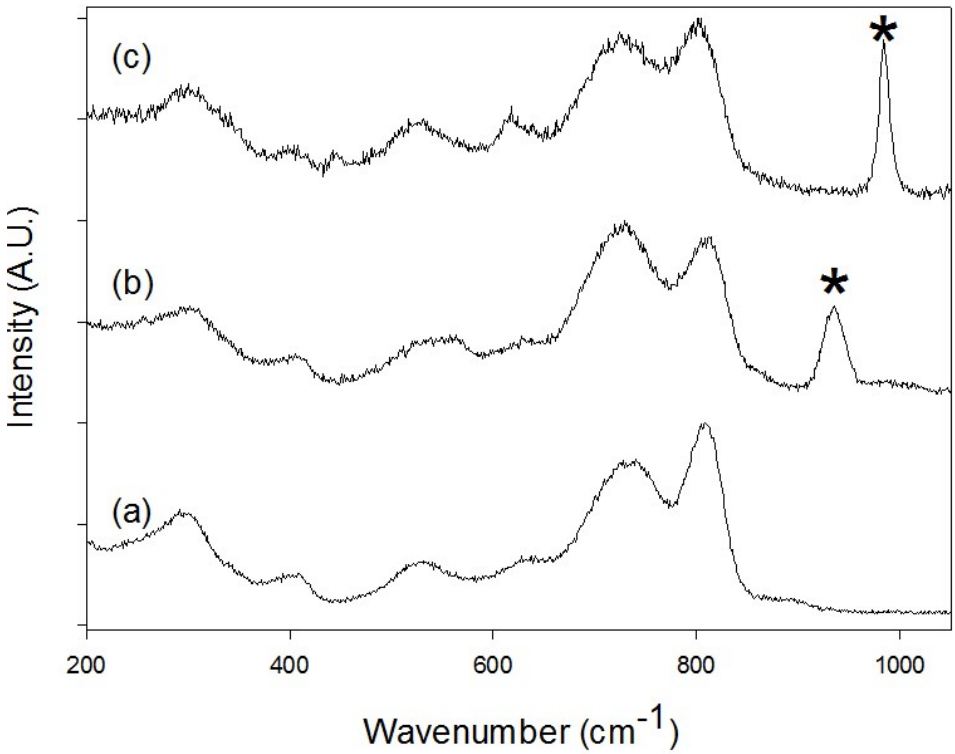

Figure 6.25 Raman spectra of (a) $Ba_2Sn_{0.6}Ti_{0.2}YB_{0.2}O_{5.4}$, (b) $Ba_2Sn_{0.6}Ti_{0.2}YP_{0.2}O_{5.6}$ and (c) $Ba_2Sn_{0.6}Ti_{0.2}YS_{0.2}O_{5.7}$ with bands due to phosphate and sulfate indicated

The Raman spectra of the compositions with no oxyanions showed no peaks present due to oxyanions, with the exception of a small peak at 990 cm^{-1} that may indicate the presence of a

small amount of carbonate in $Ba_2Sn_{0.8}Ti_{0.2}YO_{5.5}$. The phosphate composition showed a peak at 940 cm^{-1} due to the internal stretching mode of phosphate and the sulfate composition showed a peak at 990 cm^{-1} due to the symmetric stretch of sulfate, confirming the presence of both oxyanions in their respective compositions. $Ba_2Sn_{0.6}Ti_{0.2}YB_{0.2}O_{5.4}$ showed no large peak at 835 cm^{-1} due to the symmetric stretch of tetrahedral borate, however on closer inspection a shoulder at 835 cm^{-1} on the band at 810 cm^{-1} was observed when compared with the spectrum for $Ba_2Sn_{0.8}Ti_{0.2}YO_{5.5}$, Figure 6.26, consistent with the incorporation of borate.[10]

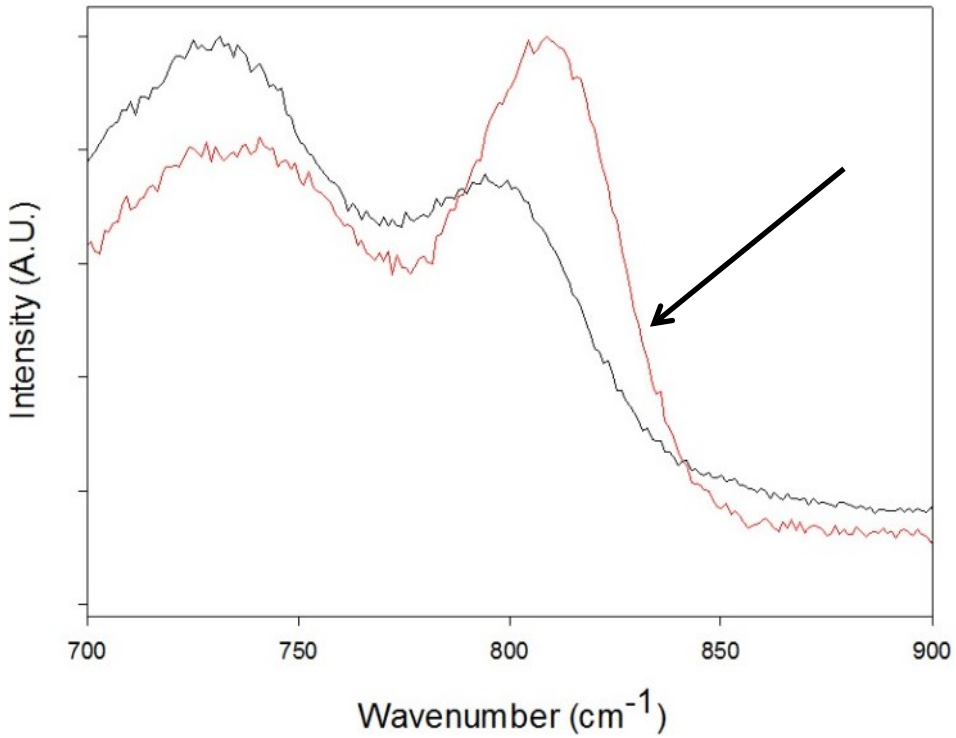

Figure 6.26 Raman spectra of $Ba_2Sn_{0.8}Ti_{0.2}YO_{5.5}$ (black) and $Ba_2Sn_{0.6}Ti_{0.2}YB_{0.2}O_{5.4}$ (red) with the shoulder due to borate indicated

As for the other compositions examined in this chapter, the presence of bands in the Raman spectra indicate that the local structure is not cubic, despite powder XRD showing an average cubic cell.

6.3.3.2 Conductivity Measurements

Conductivity measurements were carried out on all the pure compositions in dry and wet N_2. All the compositions exhibited a high conductivity with a significant protonic contribution in wet N_2, Table 6.9, Figure 6.27 and Figure 6.28. At 800 °C the resistance of the composition $Ba_2Sn_{0.6}Ti_{0.2}YP_{0.2}O_{5.6}$ was unable to be resolved however at 750 °C the conductivity was 7.8 x 10^{-5}.

Table 6.9 Total conductivity data for $Ba_2Sn_{1-x-y}Ti_yYX_xO_{5.5+z}$

Sample (nominal composition)	Conductivity (S cm^{-1})			
	500 °C		800 °C	
	Dry N_2	Wet N_2	Dry N_2	Wet N_2
$Ba_2Sn_{0.8}Ti_{0.2}YO_{5.5}$	3.5 x 10^{-5}	1.8 x 10^{-4}	5.3 x 10^{-4}	5.1 x 10^{-4}
$Ba_2Sn_{0.6}Ti_{0.4}YO_{5.5}$	3.8 x 10^{-5}	1.6 x 10^{-4}	5.7 x 10^{-4}	5.6 x 10^{-4}
$Ba_2Sn_{0.6}Ti_{0.2}YB_{0.2}O_{5.4}$	1.1 x 10^{-4}	4.9 x 10^{-4}	1.1 x 10^{-3}	7.2 x 10^{-4}
$Ba_2Sn_{0.6}Ti_{0.2}YP_{0.2}O_{5.6}$	5.7 x 10^{-6}	2.4 x 10^{-5}	-	1.5 x 10^{-4}
$Ba_2Sn_{0.6}Ti_{0.2}YS_{0.2}O_{5.7}$	3.3 x 10^{-5}	1.7 x 10^{-4}	4.7 x 10^{-4}	6.1 x 10^{-4}

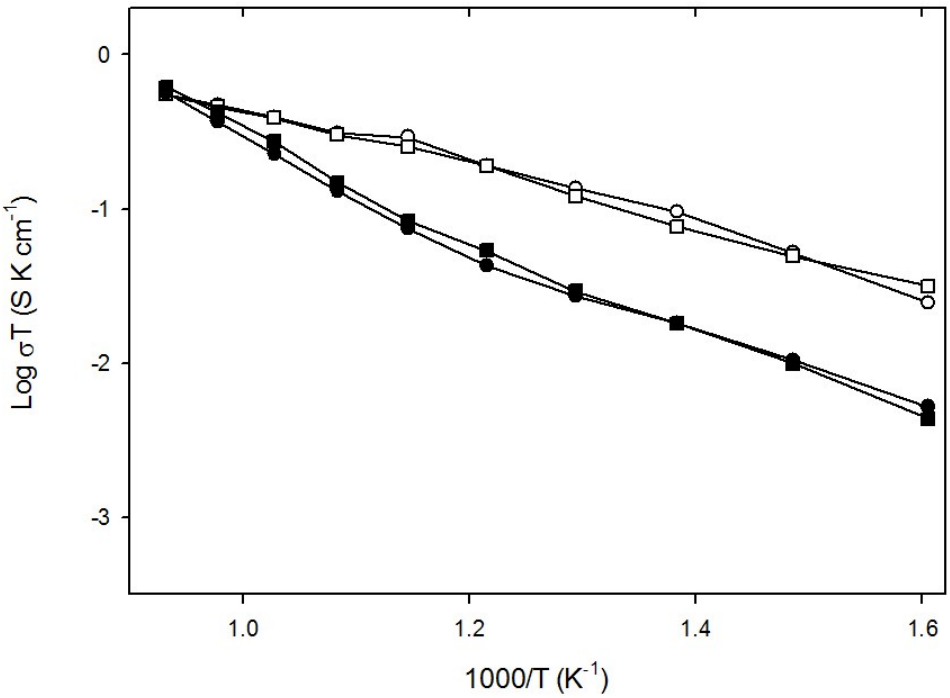

Figure 6.27 Conductivity data for $Ba_2Sn_{0.8}Ti_{0.2}YO_{5.5}$ (circle) and $Ba_2Sn_{0.6}Ti_{0.4}YO_{5.5}$ (square) in dry (filled) and wet (empty) N_2

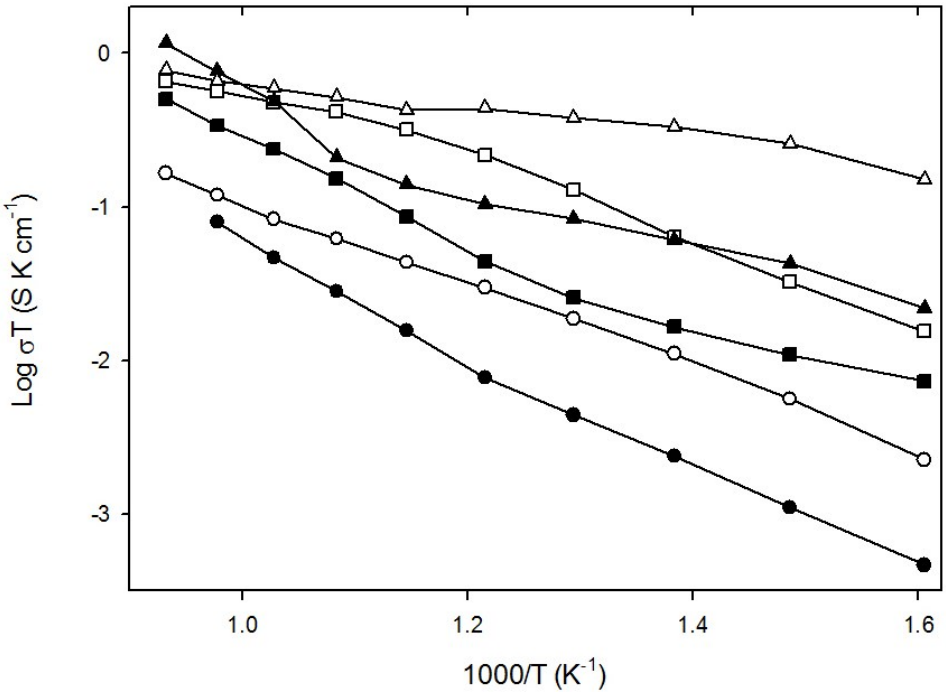

Figure 6.28 Conductivity data for $Ba_2Sn_{0.6}Ti_{0.2}YB_{0.2}O_{5.4}$ (triangle), $Ba_2Sn_{0.6}Ti_{0.2}YP_{0.2}O_{5.6}$ (circle) and $Ba_2Sn_{0.6}Ti_{0.2}YS_{0.2}O_{5.7}$ (square) in dry (filled) and wet (empty) N_2

The data for the conductivities found that doping with titanium for tin had little effect on the conductivity values, most likely due to only a small change in the lattice parameter and no change in the amount of oxygen vacancies. As seen for the oxyanion doped ytterbium compositions, $Ba_2Sn_{0.6}Ti_{0.2}YP_{0.2}O_{5.6}$ had a lower conductivity than its sulfate and borate analogues; however with these samples there was no difference in the densities of the pellets suggesting that the phosphate compositions for both series have an inherently lower conductivity. The origin of this needs further investigation.

As the other series investigated have shown a p-type contribution to the conductivity the conductivities of the samples were collected in dry O_2 and compared with the results collected in dry N_2, the data for $Ba_2Sn_{0.6}Ti_{0.2}YP_{0.2}O_{5.6}$ are shown in Figure 6.29.

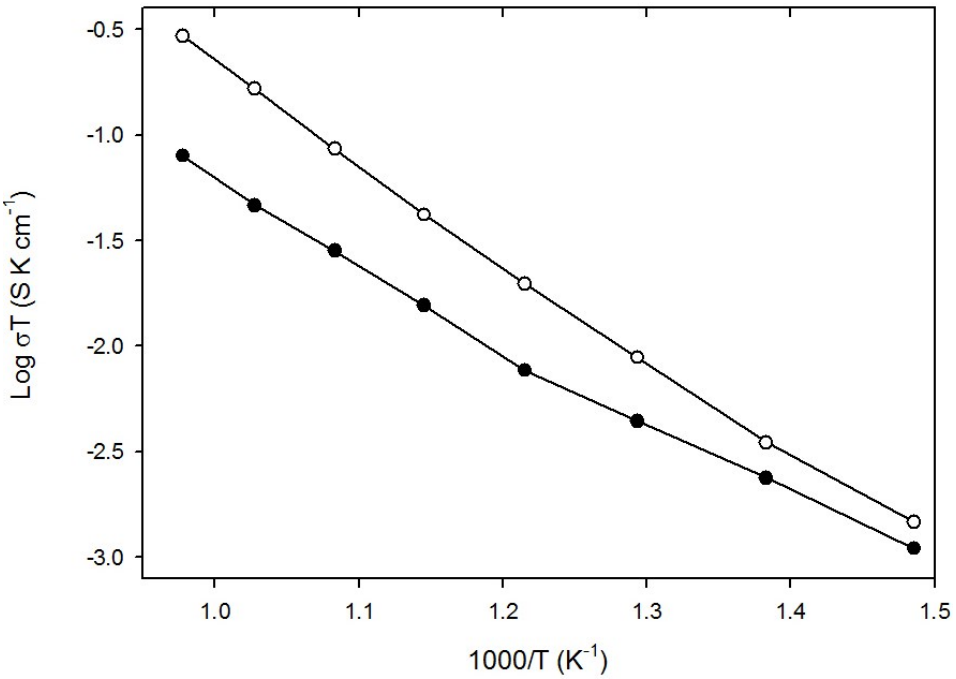

Figure 6.29 Conductivity data for $Ba_2Sn_{0.6}Ti_{0.2}YP_{0.2}O_{5.6}$ in dry N_2 (filled circle) and dry O_2 (empty circle)

All the compositions showed a p-type contribution to the conductivity at elevated temperatures due to oxygen incorporation according to the equation shown in section 6.3.1.2.

6.3.3.3 Chemical Stability

6.3.3.3.1 CO_2 Stability

The first experiment using TGA studies showed that none of the titanium compositions gained mass under a flowing 1:1 mix of CO_2 and N_2 up to 1000 °C, similar to the results for the other series in this chapter.

Similarly XRD analysis showed no evidence for decomposition after heating for 12 hours at 800 °C under flowing CO_2, Figure 6.30 and Figure 6.31.

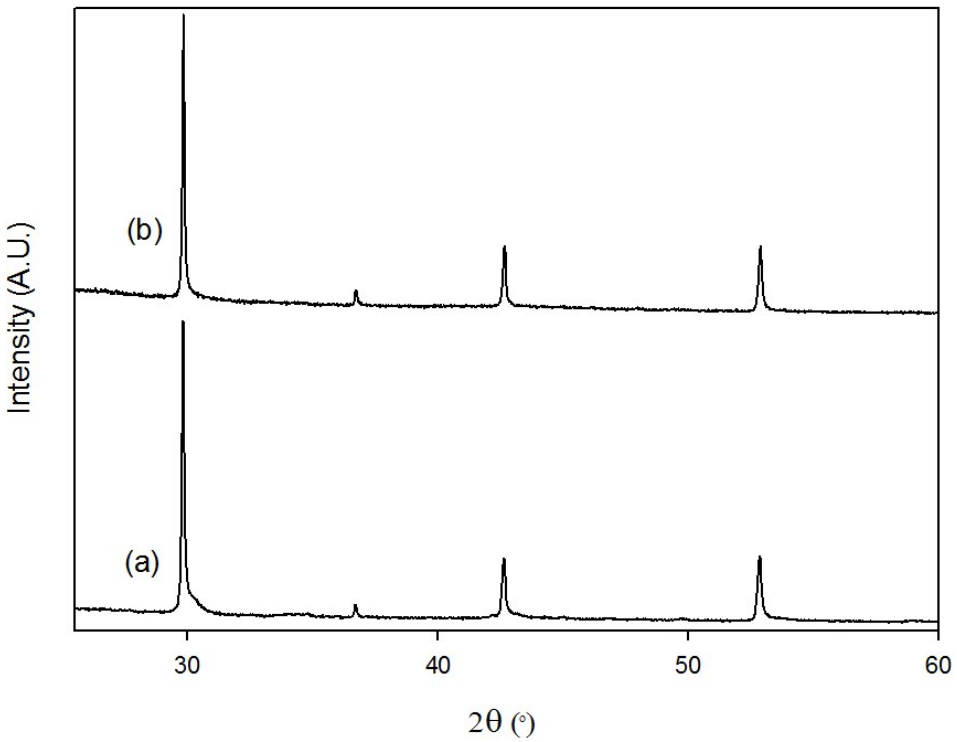

Figure 6.30 Powder X-ray diffraction patterns of (a) $Ba_2Sn_{0.8}Ti_{0.2}YO_{5.5}$ and (b) $Ba_2Sn_{0.6}Ti_{0.4}YO_{5.5}$ after heating for 12 hours at 800 °C under flowing CO_2

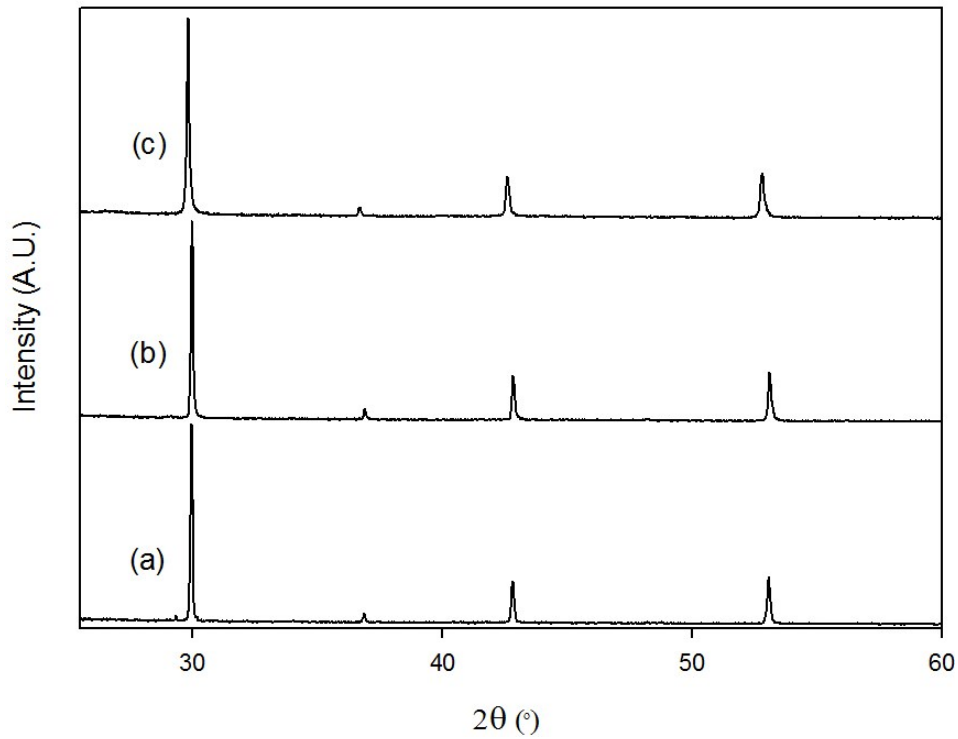

Figure 6.31 Powder X-ray diffraction data of (a) $Ba_2Sn_{0.6}Ti_{0.2}YB_{0.2}O_{5.4}$, (b) $Ba_2Sn_{0.6}Ti_{0.2}YP_{0.2}O_{5.6}$ and (c) $Ba_2Sn_{0.6}Ti_{0.2}YS_{0.2}O_{5.7}$ after heating for 12 hours at 800 °C under flowing CO_2

6.3.3.3.2 Stability to Reducing Atmospheres

As all the previous samples, apart from $Ba_2Sn_{0.8}YbB_{0.2}O_{5.4}$, showed a change in structure when heated in a reducing atmosphere, the titanium containing samples were also heated at 1000 °C for 36 hours under H_2/N_2, and powder XRD was used to examine if there was any brownmillerite formation, Figure 6.32 and Figure 6.33.

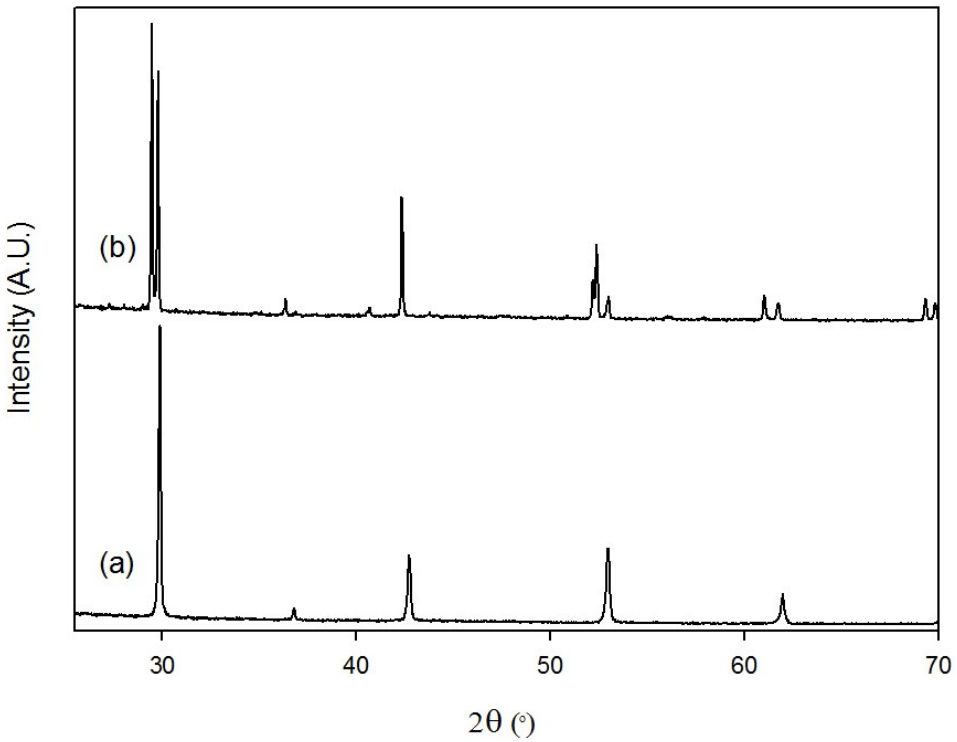

Figure 6.32 Powder X-ray diffraction patterns of (a) $Ba_2Sn_{0.8}Ti_{0.2}YO_{5.5}$ and (b) $Ba_2Sn_{0.6}Ti_{0.4}YO_{5.5}$ after heating under 10% H_2 for 36 hours

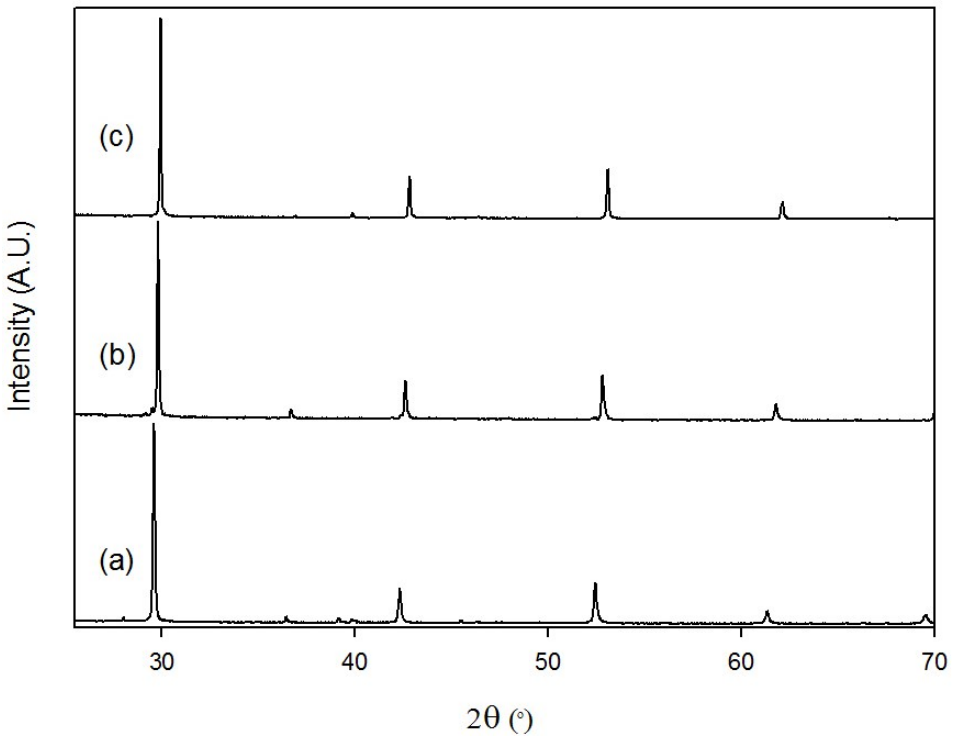

Figure 6.33 Powder X-ray diffraction data of (a) $Ba_2Sn_{0.6}Ti_{0.2}YB_{0.2}O_{5.4}$, (b) $Ba_2Sn_{0.6}Ti_{0.2}YP_{0.2}O_{5.6}$ and (c) $Ba_2Sn_{0.6}Ti_{0.2}YS_{0.2}O_{5.7}$ after heating under 10% H_2 for 36 hours

The data show that compositions with a titanium content of 10% were able to retain the cubic structure under the reaction conditions used. However increasing the titanium content to 20% was found to cause brownmillerite formation under reducing conditions.

$Ba_2Sn_{0.6}Ti_{0.2}YB_{0.2}O_{5.4}$ and $Ba_2Sn_{0.6}Ti_{0.2}YS_{0.2}O_{5.7}$ were shown to retain the cubic cell, however there is a change in the lattice parameter (the unit cell becomes larger) as the peaks shift to lower angle relative to the phosphate compositions, and also the appearance of small peaks that do not appear in the cubic structure. These small peaks match the peaks seen by Murugaraj *et al*. suggesting that there may be some Sn/Y ordering occurring in these samples, although this needs further investigation.[2]

6.4 Conclusions

Powder X-ray diffraction data collected on $Ba_2Sn_{1-x}YX_xO_{5.5+z}$, $Ba_2Sn_{1-x}YbX_xO_{5.5+z}$ and $Ba_2Sn_{1-x-y}Ti_yYX_xO_{5.5+z}$ showed that the compositions that formed a single phase had the space

group *P m -3 m* and a lattice parameter in the range 4.22 Å to 4.27 Å. The lattice parameter was found to decrease with increasing titanium, phosphate and borate content, but was found to increase on sulfate doping.

Raman spectroscopy was carried out on all the samples and confirmed the presence of oxyanions in the structure. The presence of peaks in the Raman spectra showed that the structures were locally not cubic.

The conductivities were collected and all the compositions showed a high conductivity with a significant protonic contribution in wet atmospheres. Titanium doping was found to have little effect on the conductivity, while the oxyanion doped compositions were found to have a lower conductivity, most likely due to a lower number of oxygen vacancies and/or trapping of the oxygen vacancies by the oxyanions.

All the samples were found to be stable with respect to CO_2.

Doping with phosphate and sulfate was found not to prevent the change to the brownmillerite structure on heating in reducing conditions; however on borate doping an improved stability was observed. Doping with 10% titanium was also found to lead to no change of the cubic structure but increasing this level did lead to brownmillerite formation when heated under reducing conditions.

The collected data suggests that these compositions do have potential for use as electrolytes in proton conducting SOFCs, due to their improved stability alongside their high proton conductivities. Further work is however needed to measure the conductivities of these systems under H_2 and improve their sintering characteristics.

6.5 References

1. K. V. Paulose, P. Murugaraj, J. Koshy and A. D. Damodaran, *Japanese Journal of Applied Physics*, 1992, **31**, 1323-1325.
2. P. Murugaraj, K. D. Kreuer, T. He, T. Schober and J. Maier, *Solid State Ion.*, 1997, **98**, 1-6.
3. Y. Z. Wang, A. Chesnaud, E. Bevillon and G. Dezanneau, *Solid State Ion.*, 2012, **214**, 45-55.
4. J. F. Shin, A. Orera, D. C. Apperley and P. R. Slater, *J. Mater. Chem.*, 2011, **21**, 874-879.
5. A. C. Larson and R. B. Von Dreele, (1994), Los Alomos National Laboratory, Los Alomos NM.
6. R. D. Shannon, *Acta Crystallographica Section A*, 1976, **32**, 751-767.
7. K. Popa, R. J. M. Konings, O. Benes, T. Geisler and A. F. Popa, *Thermochimica Acta*, 2006, **451**, 1-4.
8. P. Vargas Jentzsch, B. Kampe, V. Ciobota, P. Rosch and J. Popp, *Spectrochimica acta. Part A, Molecular and biomolecular spectroscopy*, 2013, **115**, 697-708.
9. J. B. Goodenough, J. E. Ruizdiaz and Y. S. Zhen, *Solid State Ion.*, 1990, **44**, 21-31.
10. R. L. Frost and Y. F. Xi, *Spectroc. Acta Pt. A-Molec. Biomolec. Spectr.*, 2013, **103**, 151-155.

Chapter 7 Synthesis and Characterisation of $(Ca/Sr)_2MnFe_{1-x}Si_xO_{6-\delta}$

7.1 Introduction

Perovskite structures have dominated recent research into new electrode materials for Solid Oxide Fuel Cells (SOFCs) due to their generally high electronic conductivities and good catalytic performance. Traditionally the substitution of the A-site cation, e.g. Sr for La, has been the focus of doping studies.[1-5] In this work an alternative strategy is carried out, where silicon is doped onto the B site as the silicate unit. Previous work has shown that on silicon doping, $SrMnO_3$ adopts a cubic perovskite structure (for > 15% doping) whereas the undoped analogue has a hexagonal perovskite structure.[6] This work was then extended to silicon doped $Sr_{1-y}Ca_yMnO_3$, and the doping strategy was again found to improve the conductivity by stabilising the more highly conducting cubic phase, due to the generation of oxygen vacancies associated with silicon preferentially adopting a tetrahedral coordination, which led to the partial reduction of Mn^{4+} to give mixed valence Mn^{3+}/Mn^{4+}.[7, 8]

Silicon doping has also been carried out on $SrFeO_{3-\delta}$, which was shown to adopt a cubic unit cell on doping, whereas the undoped composition had a tetragonal unit cell.[9] It was found that the silicon doped compositions showed an improvement in conductivity and electrode performance. This introduction of silicon to improve the conductivity is interesting as silicon is usually considered detrimental to the conductivity of SOFC materials as it has been reported to congregate at the grain boundaries to give insulating siliceous phases decreasing the conductivity and lowering performance.[10-16]

In this chapter we extend these silicon doping studies to examine the mixed Mn/Fe systems $(Sr_{1-y}Ca_y)_2MnFeO_{6-\delta}$ to attempt to make new low-cost cathode materials (non rare-earth

containing materials). Previous work carried out on undoped $Ca_2MnFeO_{6-\delta}$ found that it formed a cubic perovskite phase.[17] This work was extended to other compositions, $(Sr_{1-y}Ca_y)_2MnFeO_{6-\delta}$ by Nakahara *et al*., and for y = 0.8, 0.9 and 1 a brownmillerite structure was observed, unlike the earlier study by Coates *et al*., while for lower values of y, a cubic perovskite structure was observed.[18] In this latter work there was no clear trend in conductivity with composition according to the authors. The iron in $Ca_2MnFeO_{6-\delta}$ was found to occupy the tetrahedral site and manganese the octahedral site. This formation of the brownmillerite phase for $Ca_2MnFeO_{6-\delta}$ was confirmed through further work by Ramezanipour *et al*, and further studies by this group also found that $CaSrMnFeO_{6-\delta}$ formed an oxygen vacancy ordered phase.[19, 20] In this chapter $Ca_2MnFeO_{6-\delta}$, $SrCaMnFeO_{6-\delta}$ and $Sr_2MnFeO_{6-\delta}$ were prepared and doped with silicon to examine the effect on structure and conductivity.

7.2 Experimental Procedure

$(Ca/Sr)_2MnFe_{1-x}Si_xO_{6-\delta}$ were synthesised using a standard ceramic synthesis method. Stoichiometric amounts of $CaCO_3$ (99%), $SrCO_3$ (99.9%), MnO_2 (99%), Fe_2O_3 (99%) and SiO_2 (99.6%) were ground together in an agate pestle and mortar and then heated at a temperature of 1000 °C for 12 hours. The samples were then reground and fired at 1250 °C for 12 hours. The resulting samples were then reground a second time, and pressed into a pellet using a 13mm die set and a force of 10000 kg cm^{-2}, before heating at 1250 °C for 4 hours. The sample was then cooled to 350 °C and held at this temperature for 12 hours to ensure full oxygenation. When powder X-ray diffraction data (Bruker D8 diffractometer with Cu-$K\alpha_1$ radiation) confirmed the presence of a single phase, the GSAS suite of programs was used to obtain unit cell parameters.[21]

Oxygen contents were estimated using thermogravimetric analysis on a Netzsch STA 449 F1 Jupiter Thermal Analyser by heating the samples at 10 °C min^{-1} up to 1200 °C under N_2 and then held at this temperature for 30 minutes to reduce the iron and manganese oxidation states to 3+, and thus allow the average metal oxidation state and the original oxygen content to be calculated from the mass loss.

Conductivity data were collected using the 4 probe dc method. 4 platinum electrodes were attached to the sample pellets using platinum paste and then heated at 800 °C for 60 minutes. The samples were heated at 350 °C for 12 hours in air to ensure similar oxygenation conditions. Conductivity measurements were taken from 800 °C to 350 °C at 50°C intervals.

In order to examine the potential of these materials for use as a SOFC cathode material, chemical compatibility studies were performed with CGO. The compatibility studies examined a 1:1 mixture of the sample and CGO, which were thoroughly mixed. The mixture was then heated at 900 °C for 24 hours and then examined by XRD to determine if any reaction had occurred.

To elucidate the potential of these materials as SOFC cathodes, symmetrical electrodes were coated on both sides of dense CGO (CGO10 Sigma Aldrich) pellets (sintered at 1500 °C for 12 hours) using a suspension of the electrode and Decoflux™ (WB41 Zschimmer and Schwartz) as binder material. The symmetrical cells were fired at 900 °C for 1 hour in air. Afterwards platinum paste was painted on both sides and platinum electrodes were attached and then heated at 800 °C for 60 minutes. Area-specific resistance (ASR) values were then obtained under symmetrical air atmosphere in a two electrode configuration in a temperature range of 350 °C to 800 °C by AC impedance measurements (PSM 1735 NumertriQ 35MHz

phase sensitive multimeter) in the range 0.0001 to 10^3 kHz with AC signal amplitude of 100 mV, Figure 7.1.

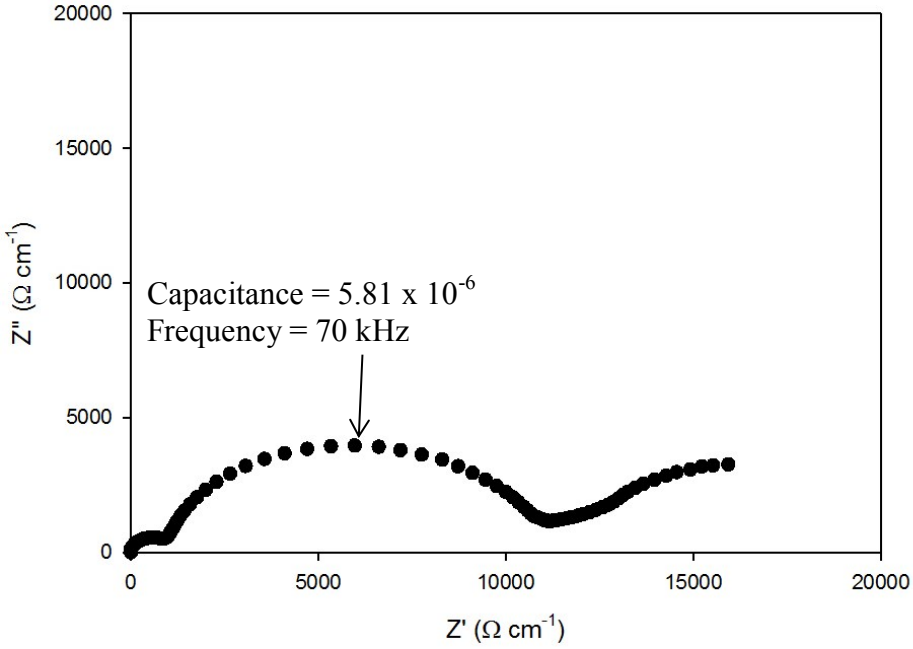

Figure 7.1 Impedance spectrum for $CaSrMnFe_{0.95}Si_{0.05}O_{6-\delta}$ at 350 °C in air

7.3 Structural Determination

7.3.1 $Ca_2MnFe_{1-x}Si_xO_{6-\delta}$

7.3.1.1 Powder X-ray Diffraction

Powder X-ray diffraction data were collected and indicated the formation of a cubic perovskite with a space group *P m -3 m* consistent with the formation of single phase $Ca_2MnFe_{1-x}Si_xO_{6-\delta}$ (for x = 0.05, 0.1, 0.2 and 0.4), Figure 7.2. At higher values of x an impurity phase, which was unable to be assigned (but believed to be a calcium silicon oxide phase), is formed alongside the cubic perovskite phase, Figure 7.3. This impurity phase did not disappear with further heat treatments.

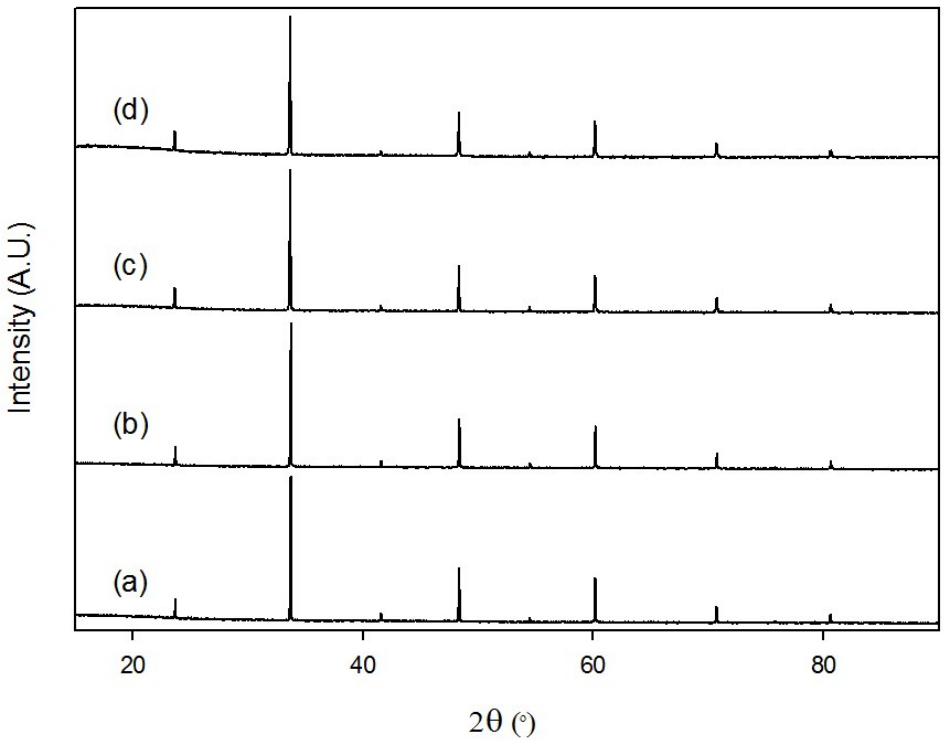

Figure 7.2: Powder X-ray diffraction data of (a) $Ca_2MnFe_{0.95}Si_{0.05}O_{6-\delta}$, (b) $Ca_2MnFe_{0.9}Si_{0.1}O_{6-\delta}$, (c) $Ca_2MnFe_{0.8}Si_{0.2}O_{6-\delta}$ and (d) $Ca_2MnFe_{0.6}Si_{0.4}O_{6-\delta}$

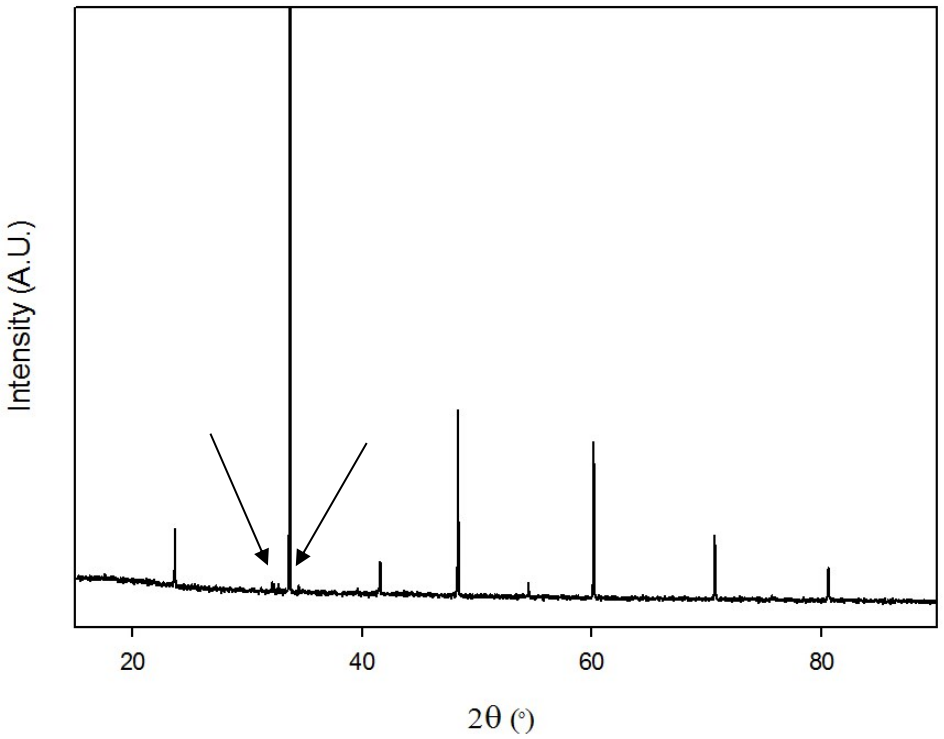

Figure 7.3: Powder X-ray diffraction data of "$Ca_2MnFe_{0.5}Si_{0.5}O_{6-\delta}$" with impurity peaks indicated

The synthesis of undoped $Ca_2MnFeO_{6-\delta}$ was also examined and resulted in the formation of a perovskite phase according to the powder XRD pattern, Figure 7.4.

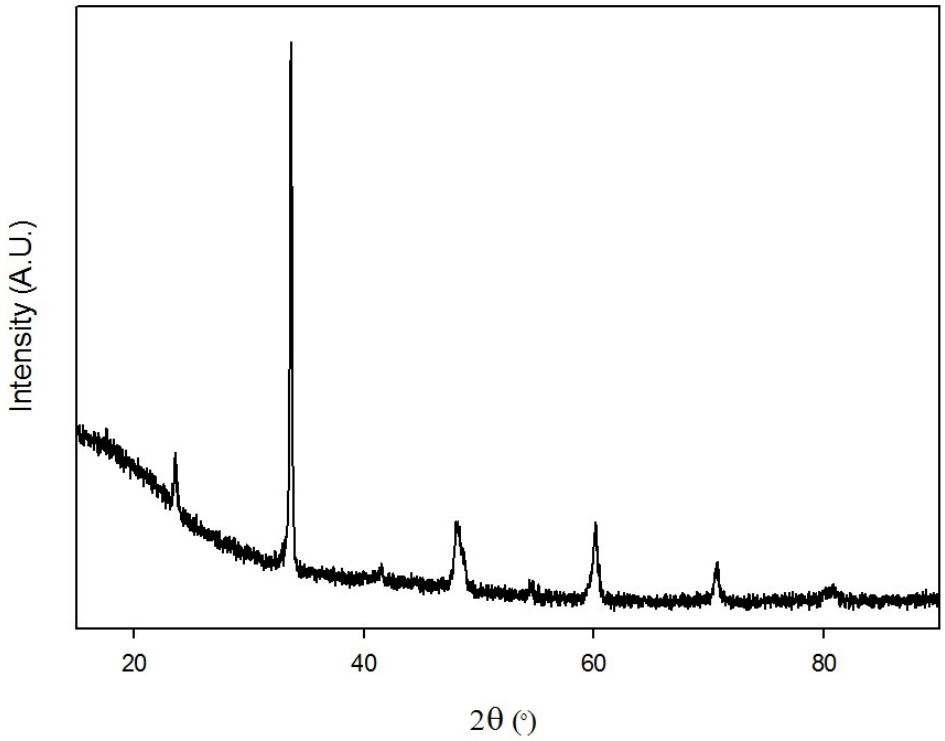

Figure 7.4: Powder X-ray diffraction data of $Ca_2MnFeO_{6-\delta}$

The collected data suggested the formation of a cubic perovskite in agreement with Coates *et al*. rather than the later published work by Nakahara *et al*. and Ramezanipour *et al*., this difference in structure may be caused by differences in the oxidation state of manganese/iron, in particular there was a low temperature anneal in the present study to maximise the oxygen content.[18-20] Despite the appearance of a peaks relating to a cubic phase there was some peak broadening occurring compared to the silicon doped compositions, potentially indicating a small deviation from cubic symmetry.

7.3.1.2 Thermogravimetric Analysis

Thermogravimetric analysis (TGA) was carried out to determine the oxygen content and hence the average B-site metal cation oxidation states for $Ca_2MnFe_{1-x}Si_xO_{6-\delta}$, Table 7.1 by observing the mass loss under heating in a N_2 atmosphere.

Table 7.1 Oxygen content and B-site metal oxidation state of $Ca_2MnFe_{1-x}Si_xO_{6-\delta}$

X	% Mass Loss	Oxygen Content	Average B-site Metal Oxidation State
0	2.52	5.44	3.44
0.05	1.86	5.34	3.33
0.1	1.92	5.38	3.35
0.2	1.71	5.39	3.32
0.4	1.57	5.46	3.33

$Ca_2MnFeO_{6-\delta}$ was found to have an average B-site metal oxidation state of 3.5 consistent with manganese not being reduced to Mn^{3+} and thus preventing the formation of the brownmillerite structure, as Nakahara *et al*. found the average B-site metal oxidation state in brownmillerite-type $Ca_2MnFeO_{6-\delta}$ to be 3.06.[18] On addition of silicon the average B-site metal oxidation state was found to decrease, although all the silicon doped samples had similar average Mn/Fe oxidation states.[7]

While the silicon reduces the average transition metal oxidation state, it does not form the brownmillerite structure, as the overall oxygen content remains significantly above 5.

7.3.1.3 Rietveld Refinement

A structural model with a space group of *P m -3 m* was successfully refined, using the GSAS suite of programs, against the collected diffraction patterns of the pure phases. The manganese, iron and silicon were all placed on the *1a* site using the expected stoichiometric amounts. The oxygen content was set to the amount calculated from the TGA analysis. Lattice parameters and goodness of fit parameters are presented in Table 7.2. The refined data for $Ca_2MnFe_{0.8}Si_{0.2}O_{5.39}$ are shown in Table 7.3, with the profiles showing observed, calculated and difference plots in Figure 7.5.

Table 7.2 Cell and goodness of fit parameters for $Ca_2MnFe_{1-x}Si_xO_{6-\delta}$

x	a (Å)	wR_p	R_p	χ^2
0	3.7789(7)	4.45%	3.60%	1.655
0.05	3.77171(5)	3.05%	2.40%	1.063
0.1	3.77162(4)	3.04%	2.38%	1.200
0.2	3.77399(4)	3.87%	3.07%	1.144
0.4	3.77584(4)	4.21%	3.32%	1.099

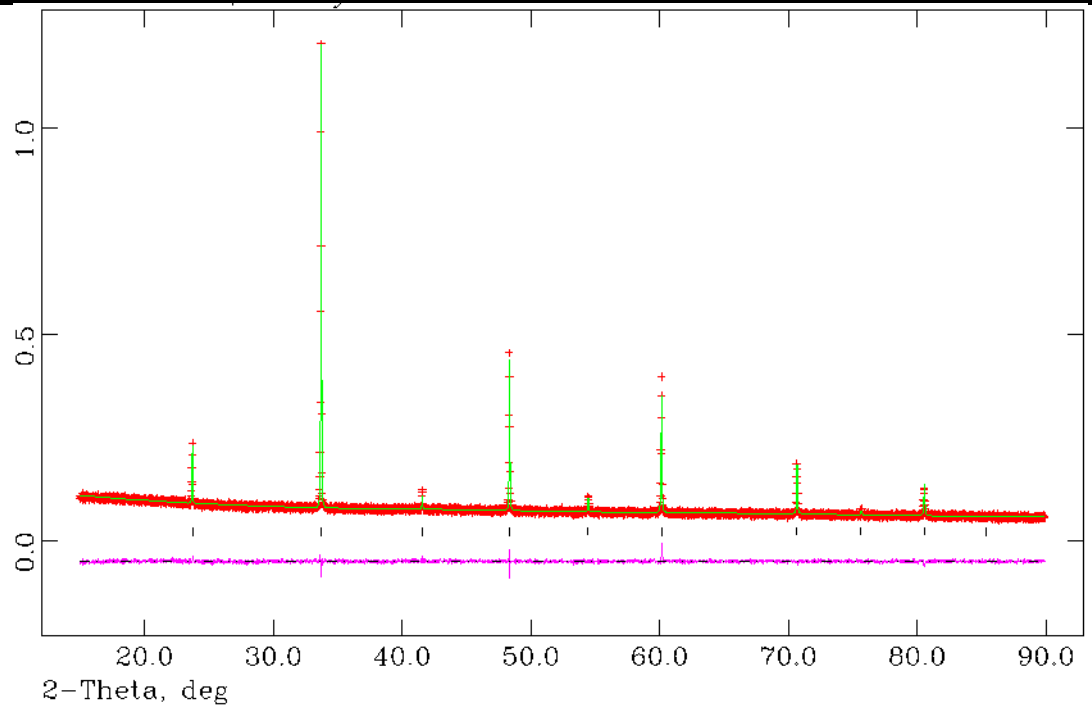

Figure 7.5 Observed, calculated and difference plots for structural refinement of $Ca_2MnFe_{0.8}Si_{0.2}O_{5.39}$ using X-ray powder diffraction data

Table 7.3 Structural detail for $Ca_2MnFe_{0.8}Si_{0.2}O_{5.39}$

	Site	x	y	z	Fraction	100 U (Å^2)
Ca	1b	0.5	0.5	0.5	1	2.1(1)
Mn	1a	0	0	0	0.5	0.75(1)
Fe	1a	0	0	0	0.4	0.75(1)
Si	1a	0	0	0	0.1	0.75(1)
O	3d	0.5	0	0	0.898	5.5(2)
Space Group = *P m -3 m*, a = 3.77399(4) Å wR_p = 3.87%, R_p = 3.07%, χ^2 = 1.173						

The lattice parameter was found to decrease from $Ca_2MnFeO_{6-\delta}$ to the 1st silicon doped compositions although with further increases in silicon content the data shows an increase in lattice parameter in disagreement with the smaller ionic size of silicon (0.26 Å) compared to

manganese (Mn^{3+} 0.645 Å and Mn^{4+} 0.53 Å) and iron (Fe^{3+} 0.645 Å, Fe^{4+} 0.585 Å).[22] As the oxidation state stays constant with increased silicon doping this increase cannot be explained by a reduction of Mn^{4+} and Fe^{4+} to the larger Mn^{3+} and Fe^{3+} ions. However the oxygen content has increased on increasing silicon content reducing the amount of oxygen vacancies in the system and therefore this maybe the origin for the small increase in the lattice parameter.

7.3.2 $CaSrMnFe_{1-x}Si_xO_{6-\delta}$

7.3.2.1 Powder X-ray Diffraction

Powder X-ray diffraction data were collected and show the formation of a cubic perovskite phase with a space group of *P m -3 m* for $CaSrMnFe_{1-x}Si_xO_{6-\delta}$, where x = 0.05, 0.1 0.2 and 0.25, Figure 7.6. Higher values of x were not attempted due to the decrease in conductivity seen as the silicon content increased past 0.2, section 7.4.2.1.

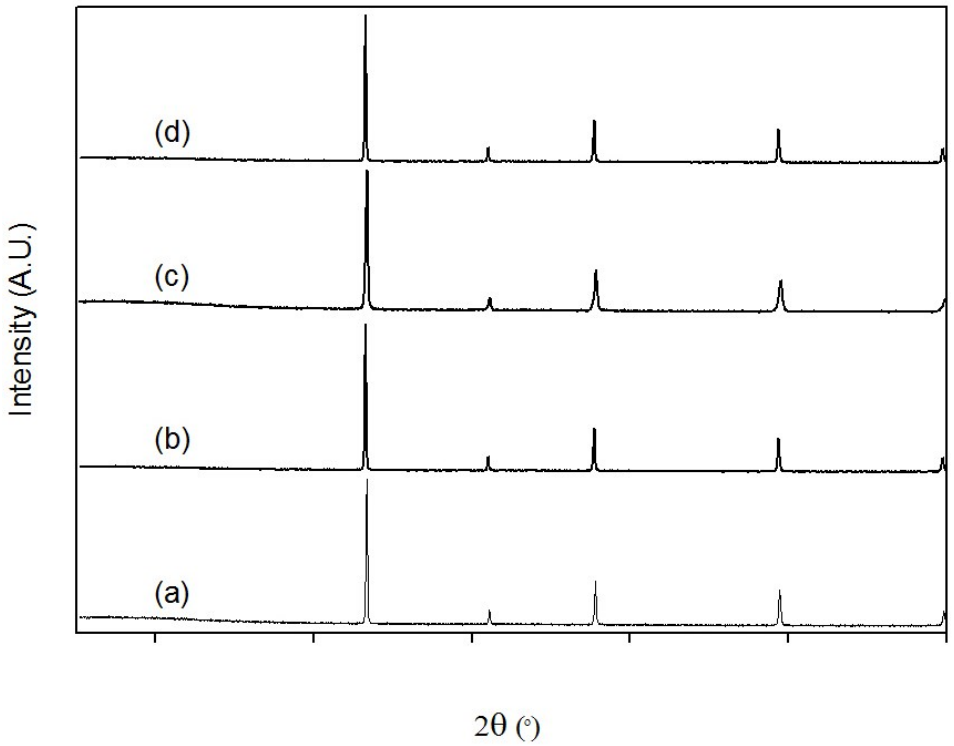

Figure 7.6: Powder X-ray diffraction data of (a) $CaSrMnFe_{0.95}Si_{0.05}O_{6-\delta}$, (b) $CaSrMnFe_{0.9}Si_{0.1}O_{6-\delta}$, (c) $CaSrMnFe_{0.8}Si_{0.2}O_{6-\delta}$ and (d) $CaSrMnFe_{0.75}Si_{0.25}O_{6-\delta}$

Undoped $CaSrMnFeO_{6-\delta}$ was also synthesised and was found to adopt a cubic perovskite phase, Figure 7.7, in agreement with the results found by Nakahara *et al*.[18]

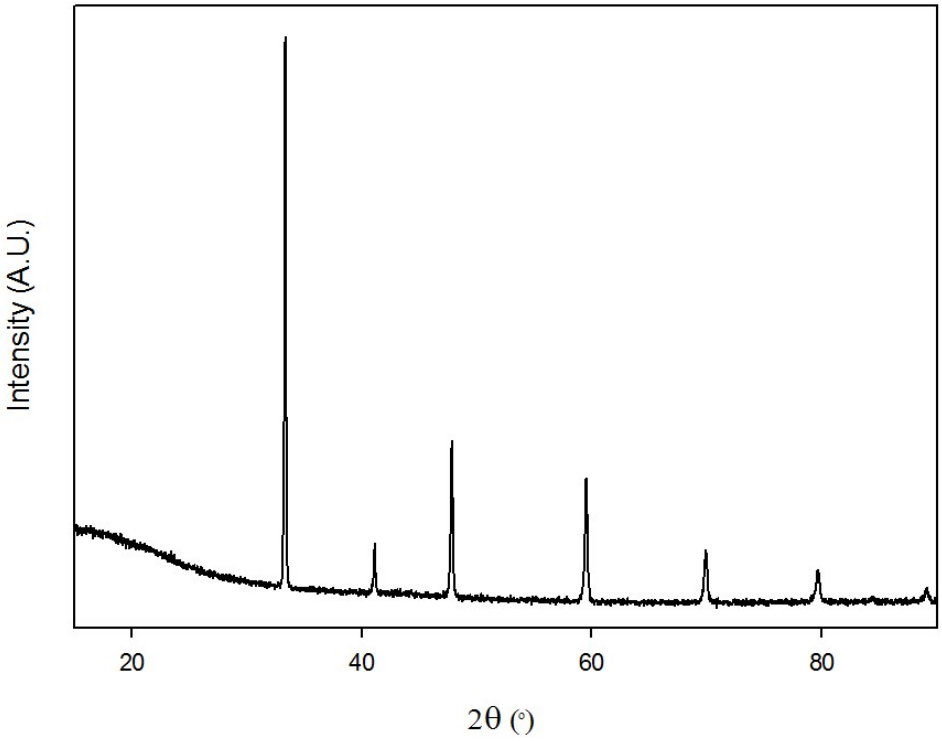

Figure 7.7 Powder X-ray diffraction data of $CaSrMnFeO_{6-\delta}$

7.3.2.2 Thermogravimetric Analysis

Thermogravimetric analysis was carried out on the compositions to determine the oxygen content, from which the average B-site metal cation oxidation state could be calculated, the results of which are shown in Table 7.4, indicating no systematic trend in oxygen content on silicon doping.

Table 7.4 Oxygen content and B-site metal oxidation state of $CaSrMnFe_{1-x}Si_xO_y$

x	% Mass Loss	Oxygen Content	Average B-site Metal Oxidation State
0	2.27	5.46	3.46
0.05	2.46	5.53	3.51
0.1	2.15	5.48	3.46
0.2	1.63	5.42	3.36
0.25	1.72	5.47	3.39

7.3.2.3 Rietveld Refinement

A structural model with space group *P m -3 m* was refined using GSAS against the collected powder X-ray diffraction data. As with the $Ca_2MnFe_{1-x}Si_xO_{6-\delta}$ compositions the manganese, iron and silicon were all put onto the 1a site with the expected stoichiometric amounts. The calcium and strontium were put onto the 1b site with the occupancies set at 0.5, and the oxygen fractional occupancy was set to the value calculated from the TGA data. The cell parameter data from these refinements are shown in Table 7.5. The refined structural data of $CaSrMnFe_{0.8}Si_{0.2}O_{5.42}$ are shown in Table 7.6, with the profiles showing observed, calculated and difference plots in Figure 7.8.

Table 7.5 Cell and goodness of fit parameters for $CaSrMnFe_{1-x}Si_xO_y$

x	a (Å)	wR_p	R_p	χ^2
0	3.80826(9)	2.62%	2.03%	1.281
0.05	3.80942(5)	2.76%	2.10%	1.616
0.1	3.81074(5)	2.64%	2.06%	1.233
0.2	3.81263(4)	2.59%	2.04%	1.254
0.25	3.80908(6)	2.94%	2.30%	1.127

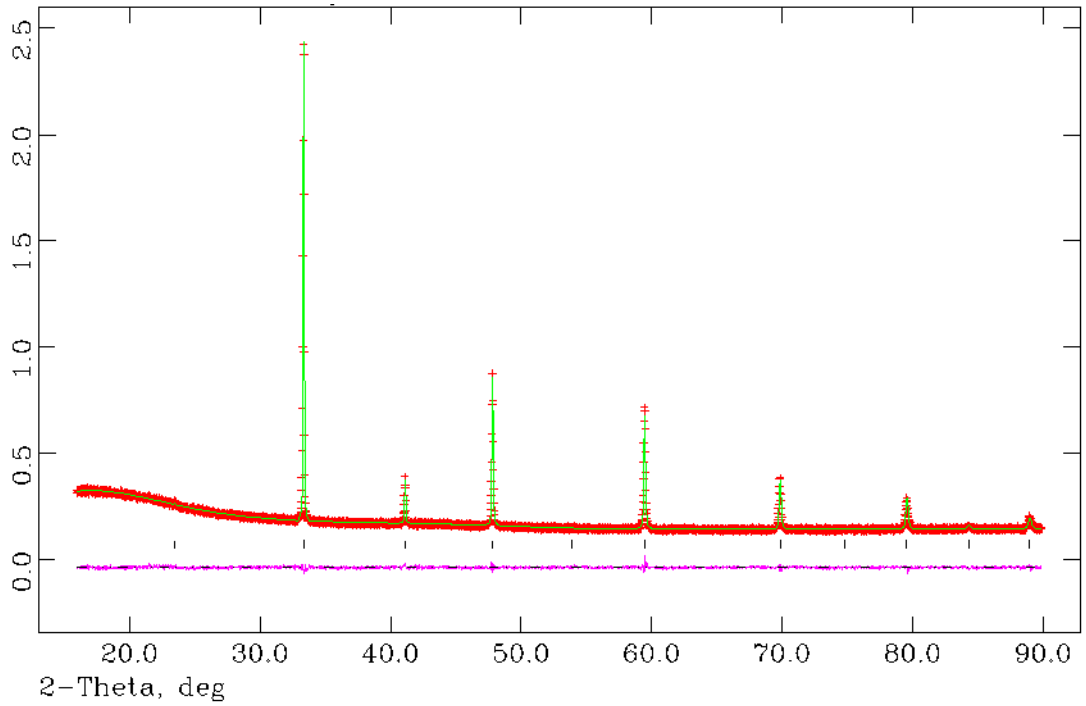

Figure 7.8 Observed, calculated and difference plots for structural refinement of $CaSrMnFe_{0.8}Si_{0.2}O_{5.42}$ using X-ray powder diffraction data

Table 7.6 Structural detail for $CaSrMnFe_{0.8}Si_{0.2}O_{5.42}$

	Site	x	y	z	Fraction	100 U ($Å^2$)
Ca	1b	0.5	0.5	0.5	0.5	0.33(8)
Sr	1b	0.5	0.5	0.5	0.5	0.33(8)
Mn	1a	0	0	0	0.5	0.70(9)
Fe	1a	0	0	0	0.4	0.70(9)
Si	1a	0	0	0	0.1	0.70(9)
O	3d	0.5	0	0	0.903	2.2(1)
Space Group = *P m -3 m*, a = 3.81263(4) Å wR_p = 2.59%, R_p = 2.04%, χ^2 = 1.254						

The lattice parameter was found to increase with increased silicon doping, with the exception of $CaSrMnFe_{0.75}Si_{0.25}O_{5.47}$, which had the lowest lattice parameter. Further work is required to investigate these samples in more detail to explain these results.

7.3.3 $Sr_2MnFe_{1-x}Si_xO_{6-\delta}$

7.3.3.1 Powder X-ray Diffraction

Powder XRD data were collected on $Sr_2MnFe_{1-x}Si_xO_{6-\delta}$ compositions for x = 0.05, 0.1 and 0.2, showing the formation of a pure cubic perovskite phase, Figure 7.9. Higher values of x were not investigated, due to a silicon content greater than 0.1 lowering the conductivity.

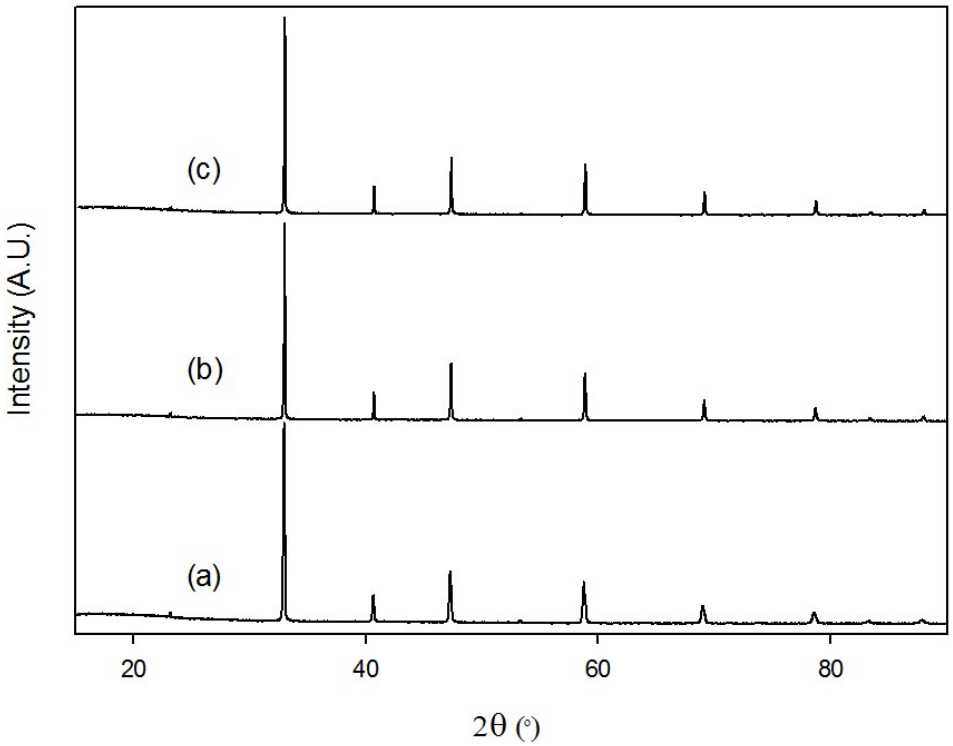

Figure 7.9: Powder X-ray diffraction data of (a) $Sr_2MnFe_{0.95}Si_{0.05}O_y$, (b) $Sr_2MnFe_{0.9}Si_{0.1}O_y$ and (c) $Sr_2MnFe_{0.8}Si_{0.2}O_y$

Undoped $Sr_2MnFeO_{6-\delta}$ was also successfully synthesised and formed a cubic perovskite phase, Figure 7.10, in agreement with the work of Nakahara *et al*.[18]

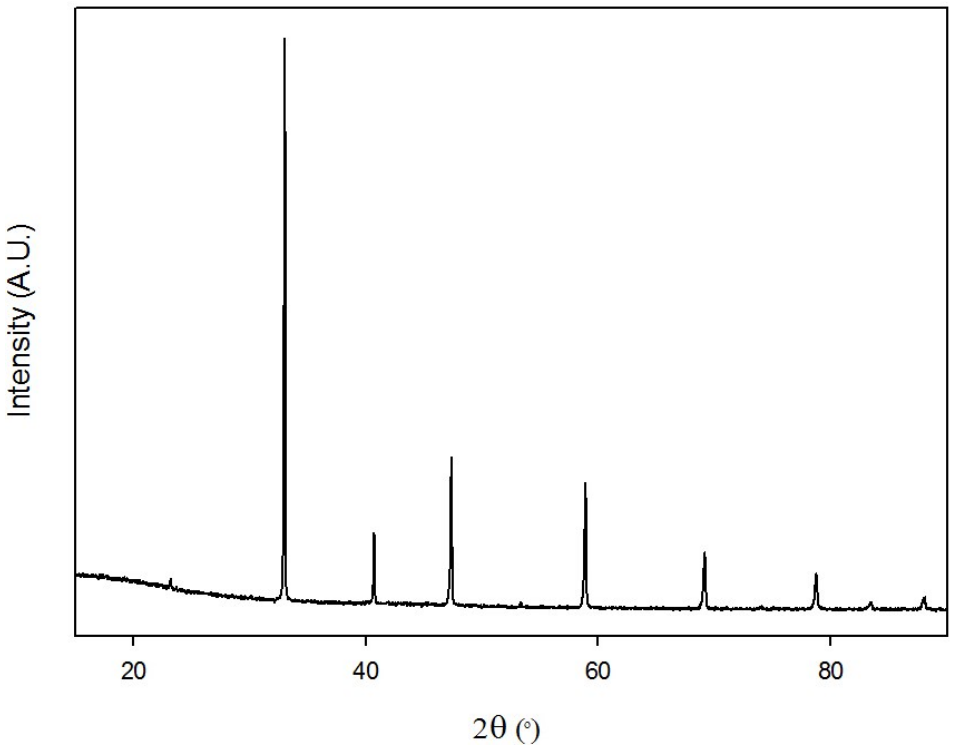

Figure 7.10 Powder X-ray diffraction data of $Sr_2MnFeO_{6-\delta}$

7.3.3.2 Thermogravimetric Analysis

To determine the average oxidation state of the B-site metal cations thermogravimetric analysis was carried out and the resulting mass loss was used to calculate the average oxidation state of the B-site metal cations, Table 7.7.

Table 7.7 Oxygen content and B-site metal oxidation state of $Sr_2MnFe_{1-x}Si_xO_{6-\delta}$

x	% Mass Loss	Oxygen Content	Average B-site Metal Oxidation State
0	2.22	5.52	3.52
0.05	1.91	5.47	3.46
0.1	2.10	5.54	3.51
0.2	1.41	5.42	3.36

On increasing the silicon doping there was no clear trend in the B-site metal oxidation state as the intermediate silicon content sample, $Sr_2MnFe_{0.9}Si_{0.1}O_{3.51}$, has the highest oxygen content and B-site metal oxidation state.

7.3.3.3 Rietveld Refinement

Rietveld analysis, using the GSAS suite of programs, was carried out on powder X-ray diffraction data of the silicon containing compositions using a model with a space group of *P m -3 m*. As for the previous series the manganese, iron and silicon were placed on the *1a* site using the expected stoichiometric amounts and the oxygen fractional occupancy set to the amount calculated from the TGA data. The unit cell lattice parameter and goodness of fit parameters are shown in Table 7.8. The refined structural data for $Sr_2MnFe_{0.8}Si_{0.2}O_{5.42}$ are shown in Table 7.9, with the profiles showing observed, calculated and difference plots in Figure 7.11.

Table 7.8 Cell and goodness of fit parameters for $Sr_2MnFe_{1-x}Si_xO_{6-\delta}$

x	a (Å)	wR_p	R_p	χ^2
0	3.84527(5)	3.44%	2.55%	2.125
0.05	3.84363(4)	3.66%	2.62%	1.836
0.1	3.85107(2)	3.40%	2.61%	1.345
0.2	3.85502(5)	4.26%	3.17%	1.762

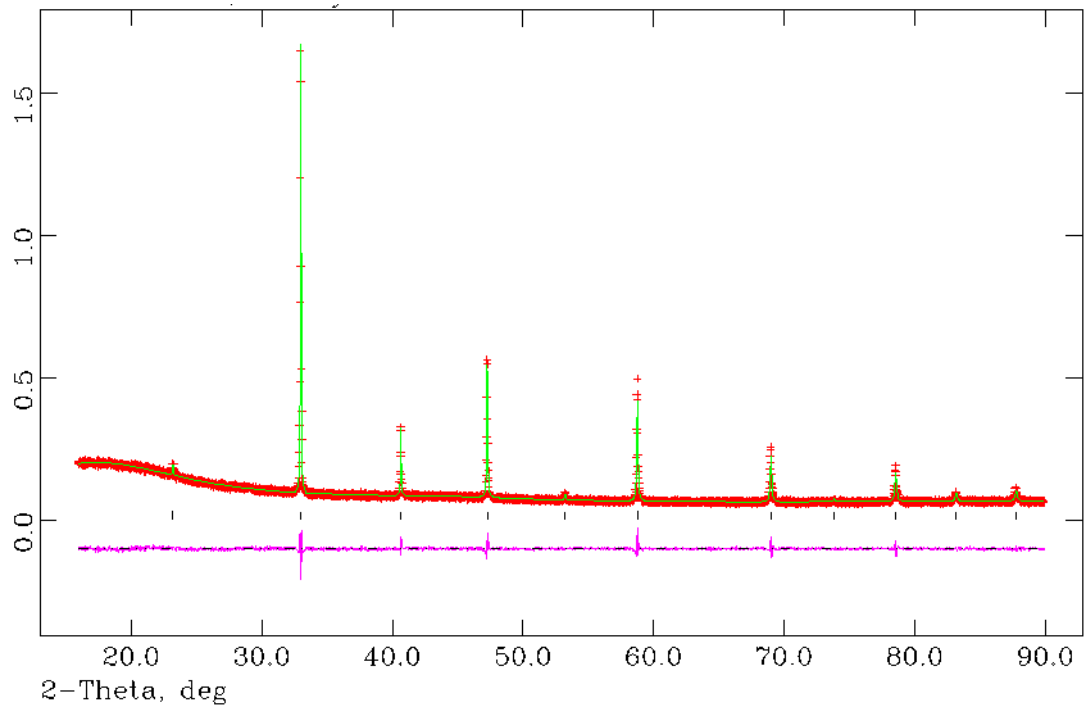

Figure 7.11 Observed, calculated and difference plots for structural refinement of $Sr_2MnFe_{0.8}Si_{0.2}O_{5.42}$ using X-ray powder diffraction data

Table 7.9 Structural detail for $Sr_2MnFe_{0.8}Si_{0.2}O_{5.42}$

	Site	x	y	z	Fraction	100 U (Å^2)
Sr	1b	0.5	0.5	0.5	1	0.30(7)
Mn	1a	0	0	0	0.5	0.6(1)
Fe	1a	0	0	0	0.4	0.6(1)
Si	1a	0	0	0	0.1	0.6(1)
O	3d	0.5	0	0	0.903	0.5(1)
Space Group = *P m -3 m*, a = 3.85502(5) Å wR_p = 4.26%, R_p = 3.17%, χ^2 = 1.761						

Initial silicon doping appears to lower the lattice parameter, in agreement with the smaller ionic radius of silicon; however the lattice parameter increases with further increasing silicon content as seen for the calcium analogues. This trend is unusual, and cannot be explained by

an increasing oxygen content or the oxidation state of the B-cation metals as there was no clear trend found for the TGA data of the $Sr_2MnFe_{1-x}Si_xO_y$ series. Therefore further investigation is required to explain these cell parameter variations.

7.4 Conductivity Measurements

7.4.1 $Ca_2MnFe_{1-x}Si_xO_{6-\delta}$

7.4.1.1 Conductivity Measurements

The conductivities of the silicon doped samples, along with undoped $Ca_2MnFeO_{6-\delta}$, were measured in air, Figure 7.12.

The data shows an improvement in the conductivity upon silicon doping up to $Ca_2MnFe_{0.9}Si_{0.1}O_{5.38}$, after which the conductivity decreased upon increasing silicon doping with the lowest conductivity observed for $Ca_2MnFe_{0.6}Si_{0.4}O_{5.46}$. The decrease in conductivity upon higher dopant levels is most likely due to the silicon disrupting the Mn/Fe-O network. The initial improvement upon silicon doping is potentially due to $Ca_2MnFeO_{6-\delta}$ having some local Mn/Fe or oxygen vacancy ordering, which disappears upon silicon doping.

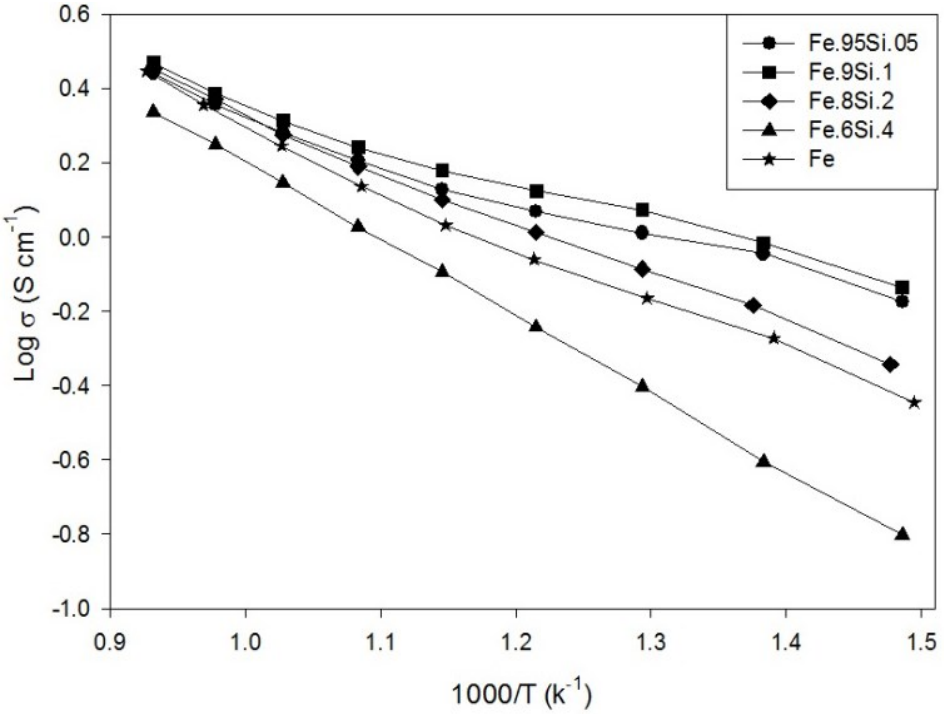

Figure 7.12: Temperature dependence of the electronic conductivity data for $Ca_2MnFe_{1-x}Si_xO_{6-\delta}$

7.4.1.2 Compatibility Tests

In order to determine if these materials could be used in high temperature SOFCs the compatibility of all the samples with CGO was measured with the results for $Ca_2MnFe_{0.9}Si_{0.1}O_{5.38}$ shown in Figure 7.13.

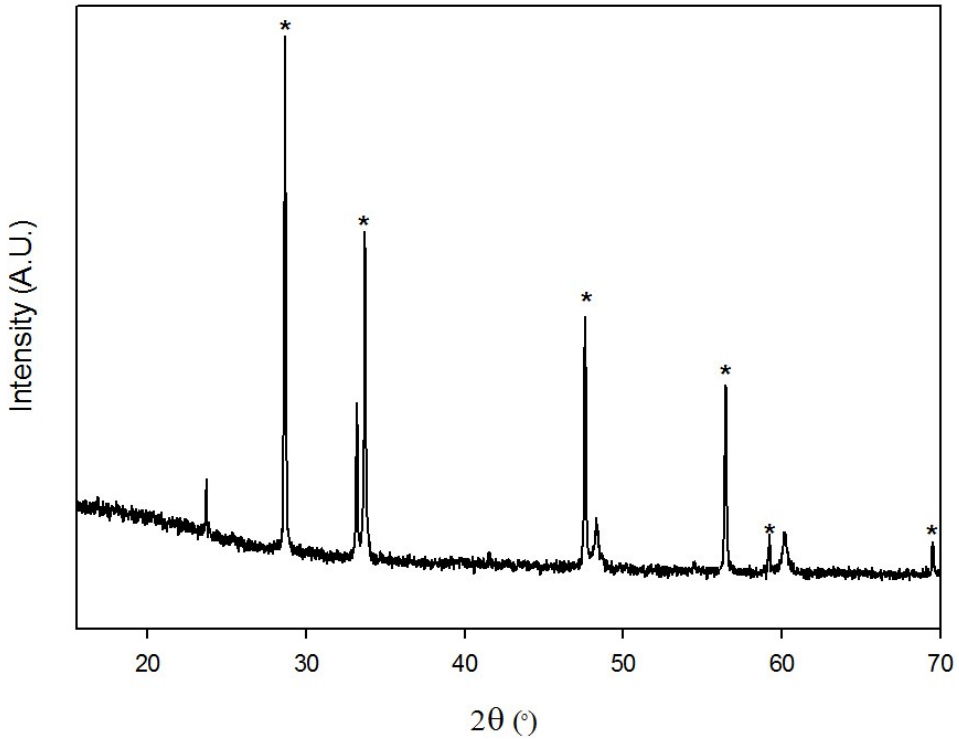

Figure 7.13 Powder X-ray diffraction pattern of $Ca_2MnFe_{0.9}Si_{0.1}O_{5.38}$ and CGO with CGO peaks indicated

The data show that at 900 °C the $Ca_2MnFe_{1-x}Si_xO_{6-\delta}$ series does not react with CGO and thus suggests that it could potentially be used as a cathode material with a CGO electrolyte.

7.4.1.3 Area Specific Resistance

To determine the cathode performance of these materials, they were deposited on a sintered CGO pellet as outlined in the experimental procedure. The area specific resistances were then collected and are shown in Figure 7.14 and Table 7.10.

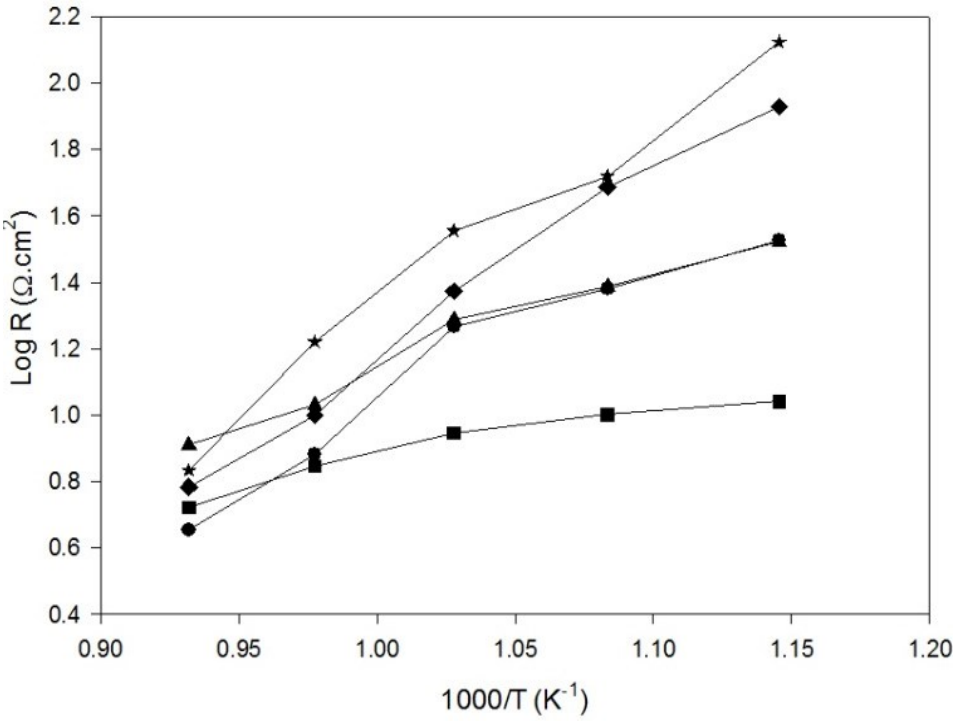

Figure 7.14 Temperature dependence of the area specific resistance of $Ca_2MnFeO_{6-\delta}$ (star), $Ca_2MnFe_{0.95}Si_{0.05}O_{5.34}$ (circle), $Ca_2MnFe_{0.9}Si_{0.1}O_{5.38}$ (square), $Ca_2MnFe_{0.8}Si_{0.2}O_{5.39}$ (diamond) and $Ca_2MnFe_{0.6}Si_{0.4}O_{5.46}$ (triangle)

Table 7.10 Area specific resistance of $Ca_2MnFe_{1-x}Si_xO_{6-\delta}$ at 700 °C

x	Area Specific Resistance (Ω cm^{-2})
0	35.9
0.05	18.5
0.1	8.8
0.2	23.6
0.4	19.4

$Ca_2MnFe_{0.9}Si_{0.1}O_{5.38}$ was found to have the lowest area specific resistances below 800 °C in agreement with it having the best conductivity at these temperatures. Undoped $Ca_2MnFeO_{6-\delta}$ had the worst area specific resistance showing that silicon improved the cathode performance in all the samples. The performance of $Ca_2MnFe_{0.6}Si_{0.4}O_{5.46}$ was better than the $Ca_2MnFe_{0.8}Si_{0.2}O_{5.39}$ samples despite the lower electronic conductivity, and further work is required to investigate why this is the case; possible explanations could be an improved oxide ion conductivity or electrode morphology, and so further studies including microscopy studies are warranted.

7.4.2 $CaSrMnFe_{1-x}Si_xO_{6-\delta}$

7.4.2.1 Conductivity Measurements

Conductivity measurements were carried out in air on the silicon doped samples, and compared with undoped $CaSrMnFeO_{6-\delta}$, Figure 7.15.

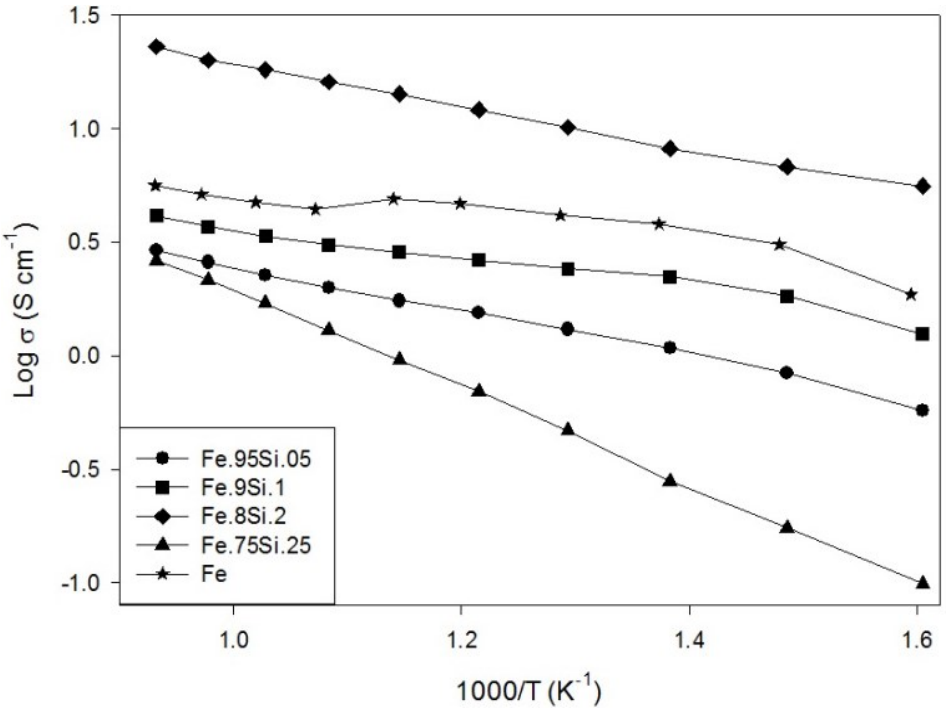

Figure 7.15 Temperature dependence of the electronic conductivity data for $CaSrMnFe_{1-x}Si_xO_{6-\delta}$

The collected data shows no obvious trend with increasing silicon content. The undoped system has a cubic perovskite structure and on initial silicon doping there is a reduction in conductivity. There is then an increase in conductivity for $CaSrMnFe_{0.8}Si_{0.2}O_{5.42}$ before a decrease for the highest silicon content. The unusual variations in conductivity warrant further study.

7.4.2.2 Compatibility Tests

To determine if these samples can be used as cathodes in SOFCs their compatibility with the electrolyte CGO was investigated with the data for $CaSrMnFe_{0.9}Si_{0.1}O_{5.48}$ after heating at 900 °C with CGO shown in Figure 7.16.

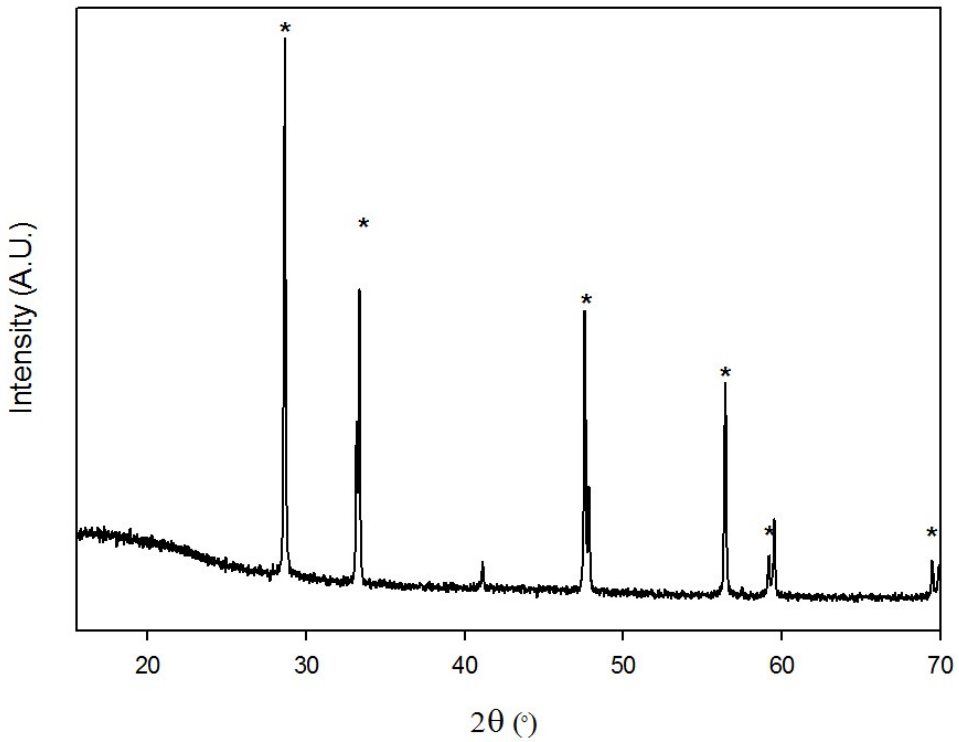

Figure 7.16 Powder X-ray diffraction pattern of $CaSrMnFe_{0.9}Si_{0.1}O_{5.48}$ and CGO with CGO peaks indicated

All the samples showed no reaction with CGO after heating at 900 °C indicating that these compositions are potentially suitable for use as cathode materials in a CGO SOFC.

7.4.2.3 Area Specific Resistance

The materials were deposited on CGO pellets as outlined in the experimental procedure section and their performance as cathode materials was analysed by measuring the area specific resistance data, Figure 7.17 and Table 7.11.

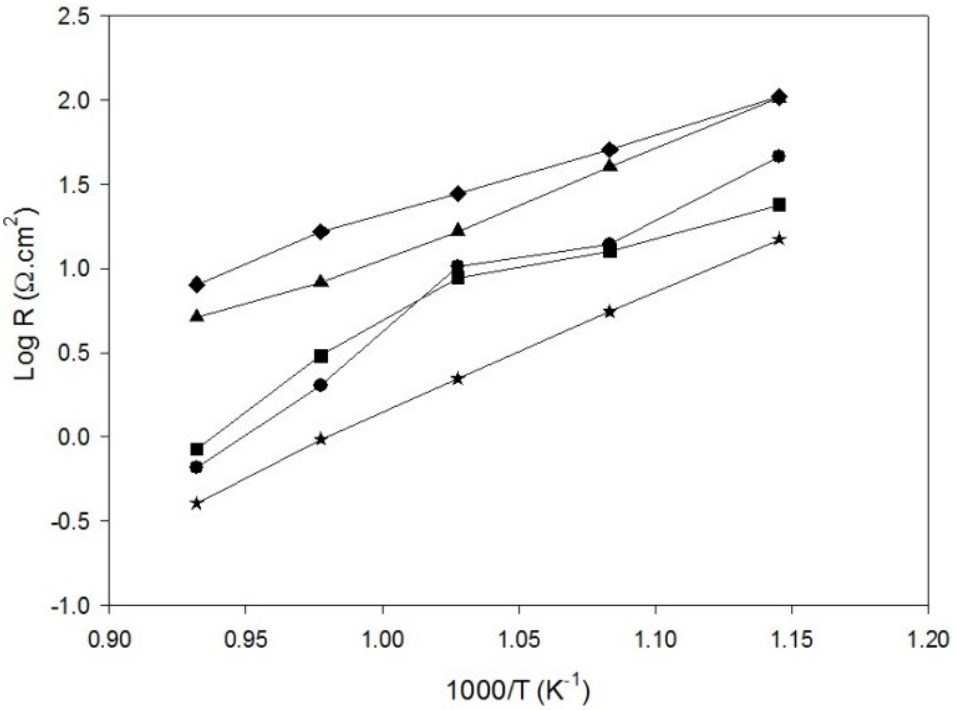

Figure 7.17 Temperature dependence of the area specific resistance of $CaSrMnFeO_y$ (star), $CaSrMnFe_{0.95}Si_{0.05}O_{5.53}$ (circle), $CaSrMnFe_{0.9}Si_{0.1}O_{5.48}$ (square), $CaSrMnFe_{0.8}Si_{0.2}O_{5.42}$ (diamond) and $CaSrMnFe_{0.75}Si_{0.25}O_{5.47}$ (triangle)

Table 7.11 Area specific resistance of $CaSrMnFe_{1-x}Si_xO_{6-\delta}$ at 700 °C

x	Area Specific Resistance (Ω cm^{-2})
0	2.21
0.05	10.3
0.1	8.8
0.2	27.9
0.25	16.6

In this case increasing the silicon content was found to increase the area specific resistance. Despite $CaSrMnFe_{0.8}Si_{0.2}O_{5.42}$ having the best conductivity it was found to have the highest area specific resistance across the temperature range measured. Further work is required to clarify these results; including microscopy studies to investigate changes in morphology as well as the possible presence of amorphous secondary phases.

7.4.3 $Sr_2MnFe_{1-x}Si_xO_{6-\delta}$

7.4.3.1 Conductivity Measurements

Conductivity measurements were carried out in air on the silicon doped samples and compared with undoped Sr_2MnFeO_y, Figure 7.18.

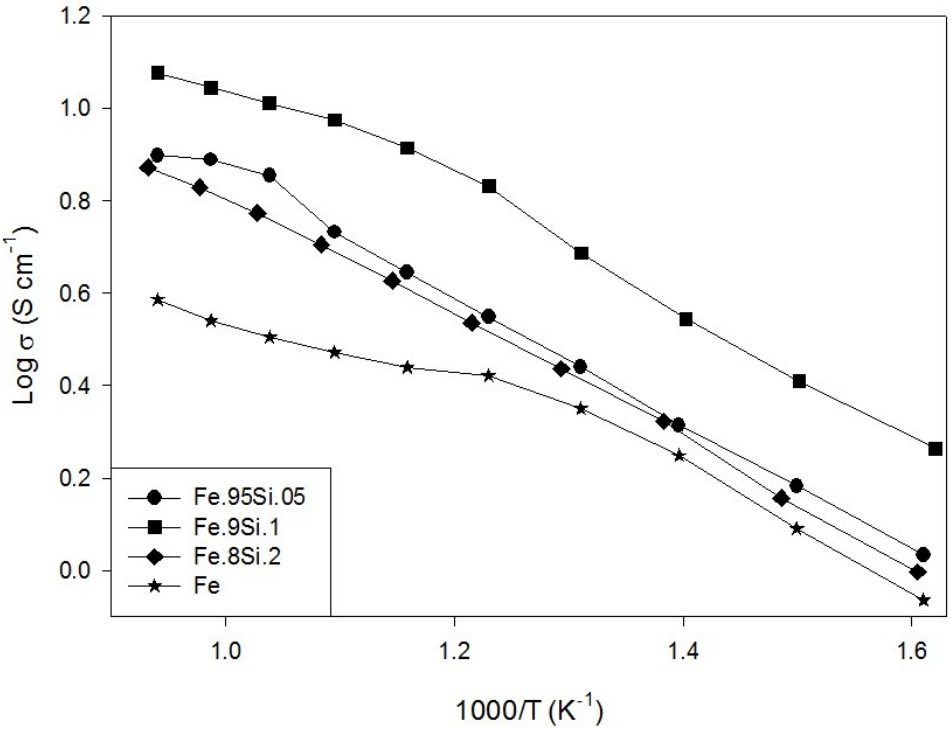

Figure 7.18 Temperature dependence of the electronic conductivity data for $Sr_2MnFe_{1-x}Si_xO_{6-\delta}$

The data showed that doping with silicon at low levels initially improves the conductivity before a decrease at higher levels, the latter attributed to the silicon disrupting the Mn/Fe-O pathways and so decreasing the conductivity. Nonetheless the conductivities of all the silicon doped systems were higher than the undoped system.

7.4.3.2 Compatibility Tests

To determine if these samples could be used as cathode materials their compatibility with CGO was analysed with the data for $Sr_2MnFe_{0.9}Si_{0.1}O_{5.54}$ shown in Figure 7.19.

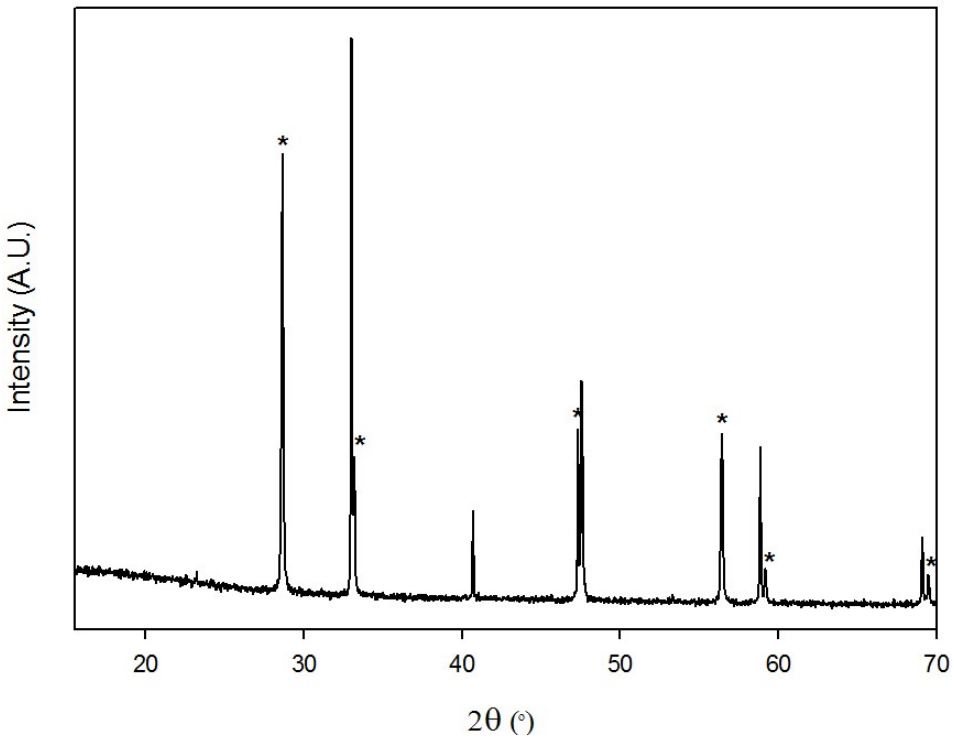

Figure 7.19 Powder X-ray diffraction pattern of $Sr_2MnFe_{0.9}Si_{0.1}O_{5.54}$ and CGO with CGO peaks indicated

The samples all showed no additional peaks, indicating no reaction between the perovskite and CGO, thus suggesting that the $Sr_2MnFe_{1-x}Si_xO_{6-\delta}$ series could be used as a cathode material with CGO as the electrolyte up to 900 °C.

7.4.3.3 Area Specific Resistance

To determine the cathode performance of the samples the area specific resistances of the samples were measured and compared with Sr_2MnFeO_y, Figure 7.20 and Table 7.12.

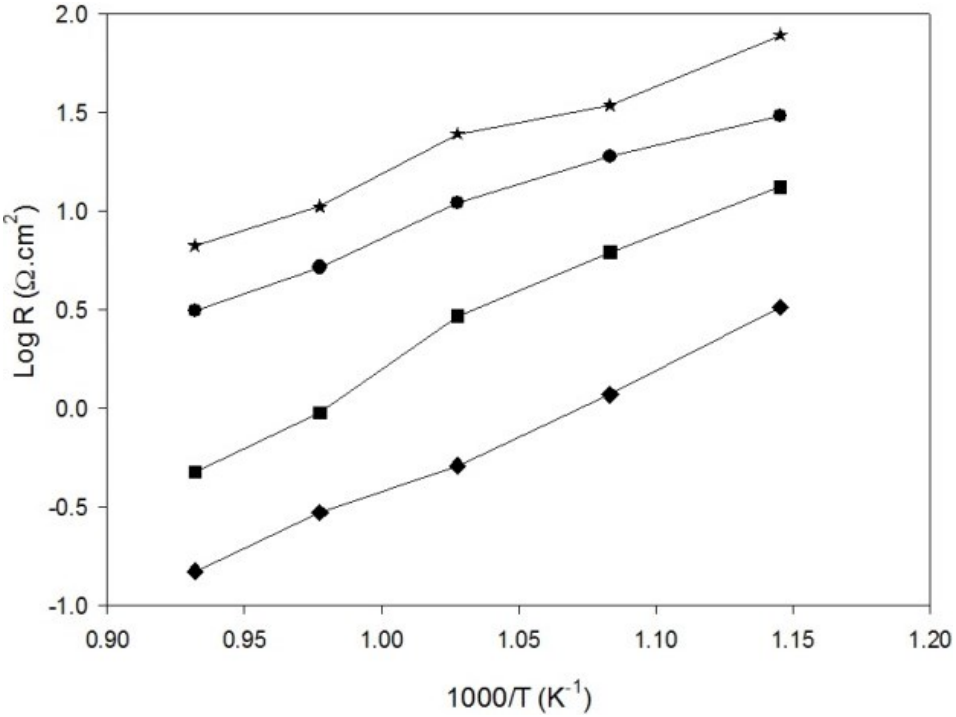

Figure 7.20 Temperature dependence of the area specific resistance of Sr_2MnFeO_y (star), $Sr_2MnFe_{0.95}Si_{0.05}O_{5.34}$ (circle), $Sr_2MnFe_{0.9}Si_{0.1}O_{5.38}$ (square) and $Sr_2MnFe_{0.8}Si_{0.2}O_{5.39}$ (diamond)

Table 7.12 Area specific resistance of $Sr_2MnFe_{1-x}Si_xO_{6-\delta}$ at 700 °C

x	Area Specific Resistance (Ω cm^{-2})
0	24.7
0.05	11.0
0.1	2.9
0.2	0.5

The collected ASR values were found to decrease with increasing silicon doping. Thus $Sr_2MnFe_{0.8}Si_{0.2}O_{5.39}$ has the lowest area specific resistance despite having an inferior electronic conductivity to $Sr_2MnFe_{0.9}Si_{0.1}O_{5.38}$, which may relate to either improved oxide ion conductivity or improved electrode morphology. Further work is needed to investigate these results in more detail to rationalise these observations.

7.5 Conclusions

Powder X-ray diffraction showed that silicon could be doped into $Ca_2MnFeO_{6-\delta}$, $CaSrMnFeO_{6-\delta}$ and $Sr_2MnFeO_{6-\delta}$ and resulted in the formation of cubic perovskites with space

group *P m -3 m*. Thermogravimetric analysis was used to determine the oxidation states of the manganese and iron and found that the compositions had mixed valences, average B-site cation oxidation state in the range 3.32 to 3.51. In this respect Mössbauer studies would be useful to determine the iron oxidation states and hence by inference the manganese oxidation state.

Conductivity measurements showed that for $Ca_2MnFeO_{6-\delta}$ and $Sr_2MnFeO_{6-\delta}$ there was a general improvement on initial silicon doping, with a decrease at higher silicon contents attributed to the silicon disrupted the Mn/Fe-O network. For the $CaSrMnFeO_{6-\delta}$ series there was no systematic trend in conductivity with increasing silicon content. These conductivities are however inferior to those found for other silicon doped electrode materials.

Chemical compatibility tests with CGO showed that all the samples showed no evidence for reaction with CGO at 900 °C.

The area specific resistances of the compositions on a CGO pellet were measured and showed some interesting results, with the lowest values observed for the $Sr_2MnFe_{1-x}Si_xO_{6-\delta}$ series. Further work is, however, required to examine these series in more detail; this would include different synthesis routes to yield higher surface area samples, as well as examining composite electrodes with a CGO electrolyte. Microscopy studies are also required to investigate the morphologies of the electrodes.

7.6 References

1. A. Orera and P. R. Slater, *Chem. Mat.*, 2010, **22**, 675-690.
2. A. J. Jacobson, *Chem. Mat.*, 2010, **22**, 660-674.
3. A. Lashtabeg and S. J. Skinner, *J. Mater. Chem.*, 2006, **16**, 3161-3170.
4. J. H. Kuo, H. U. Anderson and D. M. Sparlin, *J. Solid State Chem.*, 1990, **87**, 55-63.
5. H. Yokokawa, N. Sakai, T. Kawada and M. Dokiya, *Solid State Ion.*, 1990, **40-1**, 398-401.
6. C. A. Hancock and P. R. Slater, *Dalton Transactions*, 2011, **40**, 5599-5603.
7. J. M. Porras-Vazquez, E. R. Losilla, P. J. Keenan, C. A. Hancock, T. F. Kemp, J. V. Hanna and P. R. Slater, *Dalton Transactions*, 2013, **42**, 5421-5429.
8. J. M. Porras-Vazquez, T. F. Kemp, J. V. Hanna and P. R. Slater, *J. Mater. Chem.*, 2012, **22**, 8287-8293.
9. J. M. Porras-Vazquez, T. Pike, C. A. Hancock, J. F. Marco, F. J. Berry and P. R. Slater, *Journal of Materials Chemistry A*, 2013, **1**, 11834-11841.
10. D. Ivanova, E. Lima, A. Kovalevsky, F. M. L. Figueiredo, V. V. Kharton and F. M. B. Marques, *Ionics*, 2008, **14**, 349-356.
11. X. Guo and R. Waser, *Prog. Mater. Sci.*, 2006, **51**, 151-210.
12. M. J. Verkerk, A. J. A. Winnubst and A. J. Burggraaf, *J. Mater. Sci.*, 1982, **17**, 3113-3122.
13. S. P. S. Badwal and J. Drennan, *J. Mater. Sci.*, 1987, **22**, 3231-3239.
14. M. L. Mecartney, *J. Am. Ceram. Soc.*, 1987, **70**, 54-58.
15. S. P. S. Badwal and J. Drennan, *J. Mater. Sci.*, 1989, **24**, 88-96.
16. D. Ivanova, A. Kovalevsky, V. V. Kharton and F. M. B. Marques, *Boletin De La Sociedad Espanola De Ceramica Y Vidrio*, 2008, **47**, 201-206.
17. R. V. Coates and J. W. McMillan, *Journal of Applied Chemistry*, 1964, **14**, 346.
18. Y. Nakahara, S. Kato, M. Sugai, Y. Ohshima and K. Makino, *Mater. Lett.*, 1997, **30**, 163-167.
19. F. Ramezanipour, B. Cowie, S. Derakhshan, J. E. Greedan and L. M. D. Cranswick, *J. Solid State Chem.*, 2009, **182**, 153-159.
20. F. Ramezanipour, J. E. Greedan, L. M. D. Cranswick, V. O. Garlea, R. L. Donaberger and J. Siewenie, *J. Am. Chem. Soc.*, 2012, **134**, 3215-3227.
21. A. C. Larson and R. B. Von Dreele, (1994), Los Alomos National Laboratory, Los Alomos NM.
22. R. D. Shannon, *Acta Crystallographica Section A*, 1976, **32**, 751-767.

Chapter 8 Conclusions and Further Work

8.1 Conclusions

Phosphate and sulfate were shown to be successfully incorporated into $Ba_2Sc_{2-y}Ga_yO_5$ and adopted a cubic perovskite structure *P m -3 m*. The conductivities of selected samples were collected and showed a high ionic conductivity with a protonic contribution and the water occupancies were obtained and showed that not all the oxygen vacancies could be filled. The stabilities of the samples in CO_2 atmospheres was found to superior to doped barium cerate and improved with increasing gallium content.

This work was then extended to the strontium analogues which also adopted a cubic structure and a higher gallium content could be incorporated than for the barium series. The samples were found to be stable with respect to CO_2 at standard operating conditions for SOFCs. The conductivity data showed a lower ionic conductivity than seen for the barium series.

It was shown that phosphate could be doped into various trivalent doped barium cerate compositions and adopted a perovskite structure and that not all the oxygen vacancies could be filled with water. All the samples exhibited a high conductivity with a protonic contribution albeit lower than their non-phosphate analogues and there was no improvement seen in the CO_2 stability of the compositions apart from for the indium doped samples which showed an improvement with increasing indium content.

$Ba_2Sn_{1-x}YX_xO_{5.5+z}$, $Ba_2Sn_{1-x}YbX_xO_{5.5+z}$ and $Ba_2Sn_{1-x-y}Ti_yYX_xO_{5.5+z}$ were analysed and were found have formed a single phase with the cubic perovskite structure. The conductivities showed that on oxyanion doping the conductivity was lowered although on borate doping the stability of the system to reducing conditions was improved.

Silicon doping into $Ca_2MnFeO_{6-\delta}$, $CaSrMnFeO_{6-\delta}$ and $Sr_2MnFeO_{6-\delta}$ was shown to lead to the formation of single phase cubic perovskites with a mixed oxidation state on the B-site. The conductivities were generally found to improve with initial silicon doping and then decrease at higher silicon contents. Chemical compatibility tests were carried out with CGO and the compositions showed no reaction with CGO.

8.2 Further Work

To improve the understanding of the local structure of all the oxyanion doped electrolyte materials solid state NMR could be carried out. This would enable the oxygen atom positions to be determined and help explain some of the conductivity and water content results. Neutron powder diffraction could also be used on dry and wet samples to determine the vacancy positions and also the positions of protons in the hydrated samples. Modelling studies to examine the energetics of the hydration reaction around the cations would also be of interest.

The specific fuel cell performance of all the samples could be determined by running full fuel cell tests and therefore determine the viability of these materials for use in SOFCs.

The barium stannate samples conductivities under flowing H_2 should be collected to determine how reducing conditions affect the conductivity and working on improving their sintering characteristics and how this affects the performance.

The specific oxidation states of iron and manganese in $Ca_2MnFeO_{6-\delta}$, $CaSrMnFeO_{6-\delta}$ and $Sr_2MnFeO_{6-\delta}$ could be determined using Mössbauer spectroscopy. To improve the understanding of the area specific resistance tests microscopy could be used to investigate the morphologies of the samples. Also different synthesis methods to increase the amount of surface area or using composite electrodes, with CGO, could also be analysed.

Conference List

Solid State Christmas Conference	12/10	Poster
Workshop Prospects PCP 2011	09/11	Poster
MEGS II Christmas Conference	12/11	Poster
Grove Fuel Cells 2012	04/12	Poster
School of Chemistry Symposium	07/12	Poster
MEGS III Christmas Conference	12/12	Talk
Solid State Christmas Conference	12/12	Poster
Celebration of 60 years of Fuel Cell / Hydrogen Research @ University of Birmingham	01/13	Talk
SSI 19	06/13	Poster
School of Chemistry Symposium	07/13	Talk
PPCC 2013	07/13	Talk
MEGS Annual Conference 2013	09/13	Poster
H2FC SUPERGEN Researcher Conference	12/13	Poster
MEGS IV Christmas Conference	12/13	Poster

Publication List

Smith A D, Shin J F and Slater P R, *Synthesis and characterization of oxyanion (phosphate, sulphate) doped Ba2Sc2-yGayO5*, Journal of Solid State Chemistry, 2013, **198**, 247-252

Smith A D and Slater P R, *Investigation into the Incorporation of Phosphate into* $BaCe_{1-y}A_yO_{3-y/2}$ *(A = Y, Yb, In)*, Inorganics, 2014, **2**, 16-28

Smith A D, Hanna J V and Slater P R, *Synthesis and Characterization of Oxyanion (Phosphate, Sulfate) Doped* $Sr_2Sc_{2-y}Ga_yO_5$, in preparation

Smith A D, Keenan P J, Weston S and Slater P R, *Synthesis and Characterization of Phosphate Doped* $BaPr_{1-y}(Y/Yb)_yO_{3-\delta}$, in preparation

Smith A D and Slater P R, *Synthesis and Characterization of Oxyanion(Phosphate, Sulfate, Borate) Doped* $Ba_2Sn_{1-x}Ti_x(Y/Yb)O_{5.5}$, in preparation

Smith A D and Slater P R, *Synthesis and Characterization of Silicate Doped* $(Ca/Sr)_2MnFe_{1-x}Si_xO_{6-\delta}$, in preparation